Universiteit Antwerpen

Faculteit Wetenschappen
Departement Fysica

Effects of quantum confinement in nanoscale superconductors: from electronic density of states to vortex matter

---

Effecten ten gevolge van kwantum inperking in nanoschaal supergeleiders: van elektronische toestandsdichtheid tot vortex materie

---

Proefschrift voorgelegd tot het behalen van de graad van doctor in de wetenschappen aan de Universiteit Antwerpen te verdedigen door

Lingfeng Zhang

Promotors: Prof. Dr. François Peeters,
Dr. L. Covaci.

Antwerpen
April 2015

Members of the Jury:

Chairman
Prof. Dr. Jacques Tempere, Universiteit Antwerpen, Belgium.

Supervisors
Prof. Dr. François Peeters, Universiteit Antwerpen, Belgium,
Dr. Lucian Covaci, Universiteit Antwerpen, Belgium.

Members
Prof. Dr. Dirk Lamoen, Universiteit Antwerpen, Belgium,
Prof. Dr. Alejandro V. Silhanek, University of Liège, Belgium,
Prof. Dr. Andrea Perali, University of Camerino, Italy,
Prof. Dr. Tristan Cren, UPMC Univ Paris 6, France.

Contact Information

Lingfeng Zhang
G.U. 206
Groenenborgerlaan 171
2020 Antwerpen
Belgium
lingfeng.zhang@uantwerpen.be

Acknowledgements

First of all, I would like to express my sincere gratitude to my supervisors Dr. Lucian Covaci and Prof. François Peeters for giving me the opportunity to work on interesting research topics with them. Their broad knowledge and deep understanding of physics helped me to solve numerous scientific problems at many critical moments. Particularly, the guidance of Dr. Covaci was essential for my PhD study. Additional, I really enjoy working and discussing with him.

I would like to thank Prof. Milorad Milošević and Dr. G. R. Berdiyorov for the great collaboration and professional instructive suggestions to improve my works.

I would like to thank my thesis jury members: Prof. Jacques Tempere, Prof. Tristan Cren, Prof. Dirk Lamoen, Prof. Alejandro V. Silhanek and Prof. Andrea Perali, for reviewing my thesis and for asking great questions during the pre-defense. These questions guided and motivated me to better understand fundamental physics of superconductors.

I would like to thank all the CMT group members and staff members. Particularly, I want to thank our secretary Ms. Evans Hilde and Ms. Veronique Van Herck for all administrative support.

I also want to thank Prof. Shi-Ping Zhou and Prof. Ernst Helmut Brandt. Without their support and recommendation, I would not have had the chance to pursue my PhD in Belgium. Prof. Shi-Ping Zhou was the supervisor of my Bachelor's and Master's thesis. Through his guidance, I realized the beauty of physics, which is the motivation for me to learn physics.

Last but not least, I want to give my deepest appreciation to my wife, Dr. Liya Feng, and my parents for bringing happiness to me and for their long term support of my physics career.

Finally, I thank the Flemish Science Foundation (FWO-Vlaanderen) and the Methusalem funding of the Flemish Government for financial support.

Contents

List of Abbreviations

0D	Zero dimensional
1D	One dimensional
2D	Two dimensional
3D	Three dimensional
BCS	Bardeen-Cooper-Schrieffer
BdG	Bogoliubov-de Gennes
DOS	Density of states
GL	Ginzburg-Landau
GV	Giant vortex
LDOS	Local density of states
ML	Monolayer
OP	Order parameter
QPI	Quasiparticle interference
QSE	Quantum size effect
SEM	Scanning electron microscopy
SIC	striped incommensurate
STS	Scanning tunneling spectroscopy
STM	Scanning tunneling microscope
SQUID	Superconducting quantum interference device
TE	Tomasch effect
TEM	Transmission electron microscopy
V-aV	Vortex-antivortex
ZBC	Zero-bias conductance

Chapter 1

Introduction

1.1 Introduction to Superconductivity

Many materials show **exactly zero electrical resistance to direct current (DC)** and **expulsion of magnetic fields** when they are cooled below a characteristic critical temperature, T_c. This phenomenon is called **superconductivity**. Its history began in 1911 at Leiden University when Dutch physicist Heike Kamerlingh Onnes observed the disappearance of the electrical resistance in mercury [1, 2]. At that time, people had known that the resistance of metals decreased with falling temperature but people did not know what would happen at temperature approaching absolute zero (0 K). Some scientists, such as Lord Kelvin, predicted that the resistance would go up due to electrons being frozen. Other scientists, including Onnes and Dewar, predicted a steady decrease in resistance with falling temperature until reaching a minimum value at 0 K which allowed the current to flow with little or no resistance depending on purity. Being the first to liquefy helium by cooling it to 4.2 K in 1908, Onnes was able to study the electrical properties of metals at extremely low temperatures. He first investigated resistance of platinum and gold, but results were affected by impurities in the metals. Then, he studied mercury since very pure samples could be easily prepared by distillation. The experimental results for mercury and platinum are shown in Fig. 1.1. Much to his surprise, the resistance of the mercury sample suddenly disappeared at 4.2 K. In contrast, platinum showed a finite resistance even at very low temperatures. Due to its extraordinary electrical properties, Onnes believed that mercury had passed into a new state. He called it **su-**

perconductivity and the phase transition temperature is the "T_c". Due to this historical reason, mercury became the first superconductor. Since then, many other materials were found to exhibit superconductivity, each with a different T_c such as 6 K for lead and 4 K for tin. Due to his research, Onnes was awarded the Nobel Prize in Physics in 1913.

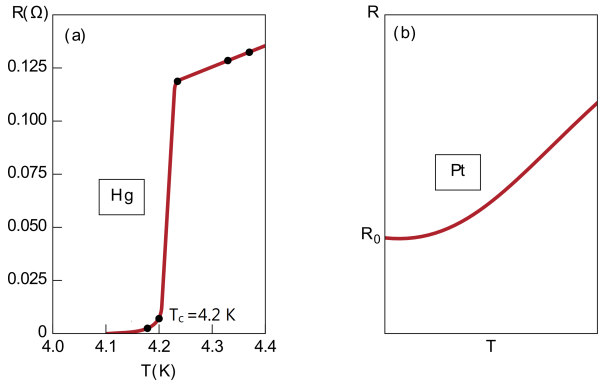

Figure 1.1: Plots of resistance versus temperature for (a) mercury (the original data published by Kamerlingh Onnes) and (b) platinum. Note that the resistance of mercury follows the path of a normal metal above the critical temperature, T_c, and then suddenly drops to zero at the critical temperature, which is $4.2K$ for mercury. In contrast, the data for platinum show a finite resistance R_0 even at very low temperatures. Taken from [3].

In order to verify if the resistance of a superconductor is exactly zero, Onnes performed an experiment to measure the decay time of a magnetically induced current in a superconducting ring. A year later the current was still flowing without significant current loss. It is called **persistent current** or **supercurrent**. Later, a more accurate experiment[4] showed that the decay time was more than 10^5 years and the resistance of a superconductor was less than $10^{-29}\Omega \cdot \mathrm{m}$. Meanwhile, the resistance of high-purity copper at $4.2K$ is $10^{-12}\Omega \cdot \mathrm{m}$. Thus, the **perfect conductivity** with zero electrical resistance to direct current (DC) is a fundamental characteristic of superconductivity.

A second fundamental characteristic is the **perfect diamagnetism**. It is also called **Meissner effect** since it was discovered by Meissner and Ochsenfeld in 1933. The effect is that a superconductor always *completely* expelled a weak magnetic field from its interior when cooled below T_c [5]. Moreover, such expulsion of magnetic field is independent of the history of cooling below

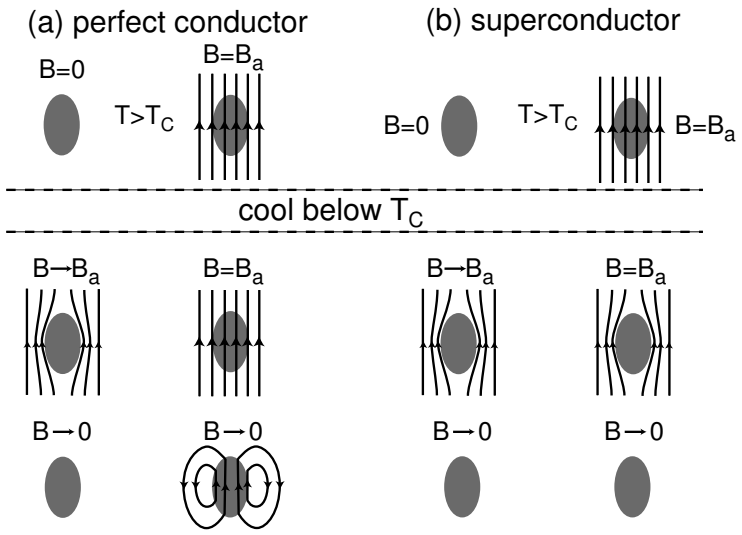

Figure 1.2: The Meissner effect is not merely a consequence of zero resistivity. (a) shows the behaviour of a 'perfect conductor', i.e. a material which merely has zero resistivity below T_c. For this material the magnetic field in the specimen below T_c depends on the presence and size of a magnetic field before cooling down below T_c. (b) shows the situation for a genuine superconductor which displays the Meissner effect. The interior of the specimen is field free below T_c, independent of the sample's history.

T_c and applying a magnetic field. As shown in Fig. 1.2(b). This effect distinguishes superconductivity from perfect conductivity. The reason is that the magnetic flux within a perfect conductor must be constant with time according to the Maxwell's equations as shown in Fig. 1.2(a). It means that **superconductivity is more than perfect conductivity** and the Meissner effect is a uniquely defining property of only superconductors.

The Meissner effect occurs only for weak magnetic fields. When the field is strong enough, the Meissner effect is destroyed. Based on how the destruction occurs, superconductors can be divided into two types. For the first type (**type-I superconductor**), superconductivity is abruptly destroyed when the magnetic field exceeds a certain temperature-dependent critical field, $H_c(T)$. The $H-T$ phase diagram only exhibits two states, the Meissner state and the normal state, as shown in Fig. 1.3(b). Most elemental superconductors are of type-I and show low critical fields and a simple magnetization curve [see Fig. 1.3(a)]. For the second type (**type-II supercon-**

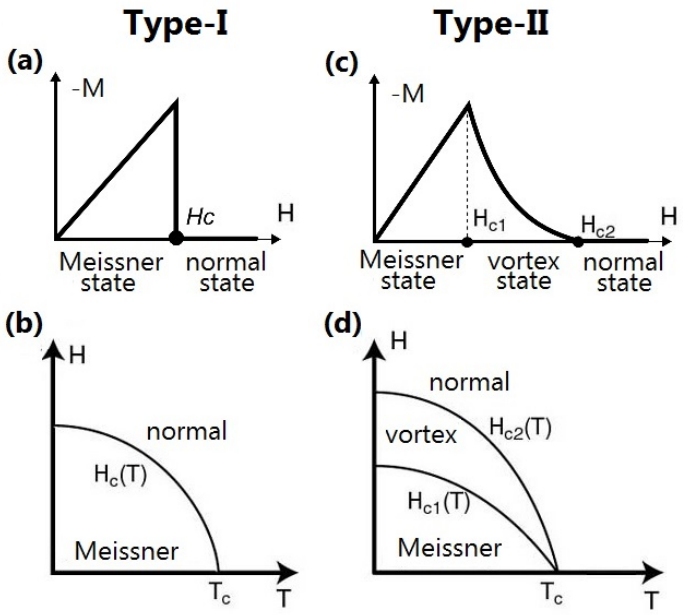

Figure 1.3: (a) A plot of magnetization versus applied field and (b) $H-T$ phase diagram for a type-I superconductor. (c) A plot of magnetization versus applied field and (d) $H-T$ phase diagram for a type-II superconductor.

ductor), there are two critical fields, the lower one $H_{c1}(T)$ and the higher one $H_{c2}(T)$ [see Fig. 1.3(c)]. When $H < H_{c1}(T)$, the superconductor shows the Meissner effect. When $H_{c1}(T) < H < H_{c2}(T)$, the flux partially penetrates the superconductor and the penetration gradually increases with increasing the field. When $H_{c2}(T)$ is reached, the flux totally penetrates the superconductor, which becomes the normal state. Thus, the magnetization curve of a type-II superconductor is more complex than a type-I superconductor. The phase diagram of a type-II superconductor is shown in Fig. 1.3(d). The phase between $H_{c1}(T)$ and $H_{c2}(T)$ is called the Shubnikov phase due to his first observation in 1934. However, the type-II superconductor was initially considered to be unphysical until 1957 when Abrikosov pointed out that the way the magnetic flux penetrated in the type-II superconductor was in the form of quantum vortices with a core in the normal state. The density of vortices increases with field until $H_{c2}(T)$ is reached, where the vortex cores (which are in the normal phase) overlap with one another, and the material

becomes a normal metal. Due to this reason, the Shubnikov phase is also called the vortex state or mixed state (a mixture of a normal and a superconducting state). Most materials of practical interest are of type-II due to the large H_{c2}. For example, it is often used to make coils to generate high magnetic fields.

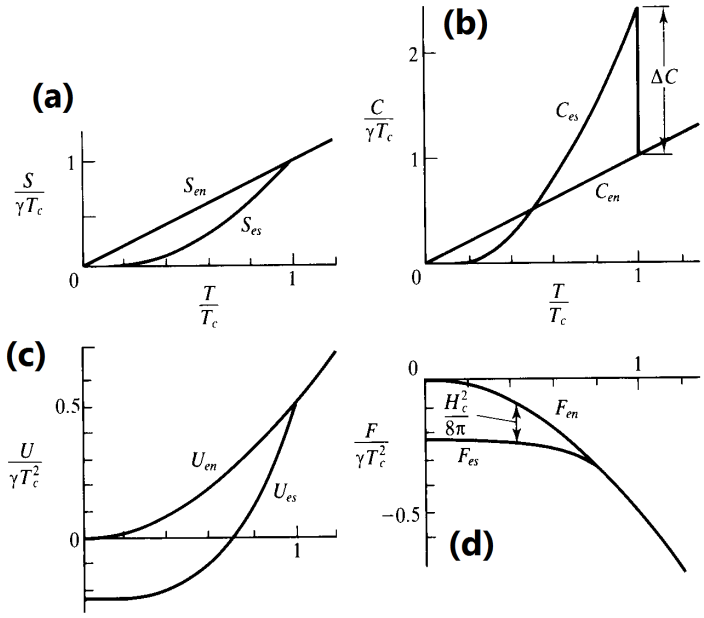

Figure 1.4: (a) Electronic entropy, (b) electronic specific heat, (c) internal energy and (d) free energy versus temperature for the superconducting state and normal state. Taken from [6].

From the phase diagram [see Figs. 1.3(b) and (d)], the superconducting state exhibits an equilibrium thermodynamical state. Gorter and Casimir developed the thermodynamical theory of superconductivity. The results are summarised in Fig. 1.4. First, the internal energy and free energy of the superconducting state is lower than the normal state when $T < T_c$. Second, the superconducting state is more ordered due to the lower entropy. Third, there is a jump in the heat capacity at T_c, indicating that the transition between the superconducting state and the normal state is a second order phase transition in the absence of the external magnetic field while a first order phase transition occurs in the presence of the field. They also proposed a two-fluid model for superconductors.

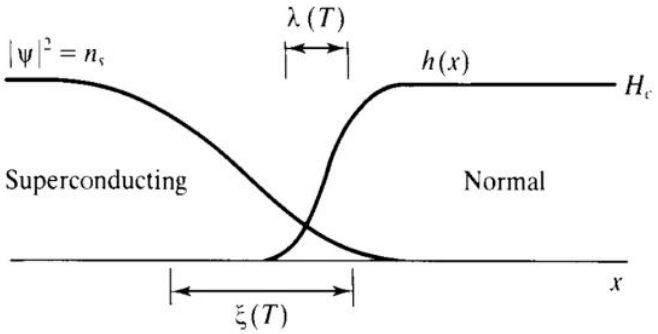

Figure 1.5: Variations of the square of the superconducting order parameter $\psi(x)$ and the external magnetic field $h(x)$ in the interface between the normal and superconducting domains. $\xi(T)$ and $\lambda(T)$ are the temperature dependent coherence length and magnetic field penetration depth, respectively. Taken from [6].

In 1935, the brothers Fritz and Heinz London developed the first theory of superconductivity in order to explain the Meissner effect. It is called the phenomenological London equations[7]. Starting from the Drude-Lorentz equation of motion for electrons in a metal, they derived these equations by incorporating Maxwell equations and imposing the condition $B = 0$ inside the superconductor. In this way, the equations successfully describe both perfect conductors and perfect diamagnetism. The perfect diamagnetism is explained by the screening supercurrent which flows to cancel the magnetic flux inside the superconductor. Consequently, the magnetic field does not vanish suddenly to zero at the boundary of the superconductor while it decays exponentially as shown in Fig. 1.5. The distance over which a magnetic field can penetrate into a superconductor and exponentially decay to $1/e$ times that of the magnetic field at the surface of the superconductor is called the London **penetration depth** λ. It is one of the most important characteristic length of a superconductor and typical values are on the order of 10 to 100 nm such as 37 nm for Pb and 110 nm for Cd.

However, the London equations yield a negative surface energy between adjacent superconducting and normal regions. This implied that when the superconductor is in an applied magnetic field, it would always maximize the area of the interface to decrease the total energy. This was a contradiction to experimental results. In 1953, Pippard proposed the non-local

generalisation of the London equations to overcome this problem. He introduced the **coherence length** ξ_0 in his theory, over which the supercurrent $\mathbf{j_s}$ and the super-electrons n_s does not change much. It is a intrinsic length scale for superconductor and the dimensionless parameter λ/ξ_0 decides if the superconductor is of type-I or type-II. Thus, both ξ_0 and λ are important characteristic lengths for superconductivity. Typically, ξ_0 is on the order of 100 nm such as 83 nm for Pb and 230 nm for Sn. It is worth to mention that the coherence length was also introduced independently by Ginzburg and Landau. These length scales are not identical. The Pippard length is temperature-independent while the Ginzburg-Landau length depends on temperature. The Pippard coherence length is related to the BCS coherence length.

In 1950, Vitaly Lazarevich Ginzburg and Lev Landau postulated a phenomenological theory of superconductivity to solve the negative surface energy problem of the London equations. The theory is called the **Ginzburg-Landau (GL) theory** [8] and was later proven to be a very powerful theory for superconductivity. By taking into account the two facts: 1) The appearance of superfluidity in liquid He takes place by a phase transition of the second kind which is similar to the appearance of superconductivity; 2) Superfluidity in liquid H_e^4 has been proven to be a Bose condensate system and can be described by a condensate wave function which is related to the number of condensate particles, n_0; they developed a theory based on Landau's theory of second-order phase transitions and they proposed a wave function as being the order parameter ψ. The physical meaning of the $|\psi|^2$ was regarded as the density of the superconducting electrons. This theory correctly features both characteristic lengths for the superconductor, i.e. the magnetic penetration depth λ and the coherence length ξ. This theory is also able to describe the destruction of superconductivity by temperature, magnetic field and current. Finally, the surface energy between the normal and superconducting phases depends on the dimensionless 'material' constant $\kappa = \lambda/\xi$, which is also called the GL parameter. When $\kappa < 1/\sqrt{2}$ ($\kappa > 1/\sqrt{2}$), the surface energy is positive (negative) leading to type-I (type-II) superconductors.

In the beginning, the GL theory did not receive much attention until: 1) in 1957 Abrikosov predicted the **vortex states** in type-II superconductors by solving the GL theory [9] and 2) in 1959 Gor'kov showed that the GL theory can be derived as some limiting form of the microscopic BCS theory [10]. He also showed that the order parameter ψ in the GL theory is pro-

portional to the energy gap in the BCS theory and the GL theory is only valid in the vicinity of T_c and the order parameter must be a slowly varying function. Nowadays, the GL theory is widely used in studying e.g. vortices in superconductors. Due to the pioneering contributions to the theory of superconductors and superfluids, Ginzburg and Abrikosov shared the Nobel Prize in Physics in 2003.

In 1957, a breakthrough was made when a complete microscopic theory of superconductivity was proposed by John Bardeen, Leon Cooper, and John Schrieffer, i.e., the **BCS theory** [11]. The ideas leading to the BCS theory includes: 1) the existence of a band gap separating the superconducting phase from the state of normal conduction; 2) the similarity to superfluidity; 3) the isotope effect, and 4) experimental results for the flux quantum suggesting two involved electrons. A key conceptual element in this theory is the pairing of electrons close to the Fermi level into **Cooper pairs** through an attractive interaction mediated by phonons. The pairs do not break, unless a certain minimum energy is provided. This energy provided the band gap. At low temperature, the pairs condensate into a boson-like state so that they move collectively and unperturbed through the crystal lattice since they cannot absorb energies smaller than the Cooper-pair binding energy. The BCS theory successfully described the dependence of the value of the energy gap Δ on temperature T; the variation of the critical magnetic field with temperature; the Meissner effect and the isotope effect. For this work, the authors were awarded the Nobel Prize in Physics in 1972.

In 1962, Brian Josephson made the important theoretical prediction that a supercurrent can flow between two pieces of superconductors separated by a thin layer of insulator [12]. He predicted two remarkable effects: 1) the DC Josephson effect: a current flows across the junction without resistance, and 2) the AC Josephson effect: the emission of electromagnetic radiation upon applying a voltage across the junction. This phenomenon is called the **Josephson effect**. This was verified by P. W. Anderson and A. H. Dayem in 1964 [13]. The effect is exploited in superconducting devices such as SQUIDs (superconducting quantum interference device), which is used in the most accurate available measurements of the magnetic flux quantum. Josephson was awarded the Nobel Prize in Physics for this work in 1973.

When superconductivity was thought to be settled, the discovery by Alex Müller and Georg Bednorz in 1986 revived the interest in superconductors tremendously. In this year, they discovered the first high-T_c superconductor, the layered copper oxide BaLaCuO with a T_c of about 35 K[14]. This tem-

perature is above the theoretical limit predicted by BCS theory, indicating unconventional superconductivity. In 1987, they were awarded the Nobel Prize in Physics "for their important breakthrough in the discovery of superconductivity in ceramic materials". Shortly, YBCO was discovered to be superconducting with a T_c of 90 K [15] and BSCCO with T_c equal to 105 K [16]. Up to now, the highest T_c was found to reach 164 K in $Hg-1223$ under high pressure [17]. Their T_c around the boiling temperature of liquid nitrogen, allowed for the use of a coolant much less expensive than helium. High-T_c superconductors are type-II superconductors. However, they can not be accounted for by the conventional BCS theory. The mechanism that causes superconductivity in high-T_c superconductors is one of the major unsolved problems of the theoretical condensed matter physics.

In 1994, Sr_2RuO_4 was found to display superconductivity with $T_c \approx 1$ K [18]. It has received considerable attentions because it is an unconventional p-wave spin-triplet superconductor [19]. Nearly all the superconductors known to date, either conventional or unconventional, are spin-singlet paired. Even the celebrated $d_{x^2-y^2}$ high-T_c order parameter involves singlet pairing. The best-known example of triplet pairing is not a superconductor at all, but a super-fluid, ^{3}He, in which the condensate consists of spin-triplet atomic Cooper pairs[20]. The electronic structures of Sr_2RuO_4 are consistent with the quasi-two-dimensional Fermi liquid at low temperatures ($T < 40$ K). The BCS theory and GL theory can be used to describe them.

In 2001, the discovery of superconductivity with a $T_c = 39$ K in magnesium diboride (MgB_2) [21] is another important event in the history of superconductivity. Although this compound was first synthesized in the 1950's [22], it was not found to be superconducting due to historical reasons. In 1970 superconductivity was discovered by Cooper et al.[23] in NbB_2 with critical temperature of 3.87 K. In systematic studies of the diborides MeB_2 (Me = Ti, Zr, Hf, V, Nb, Ta, Cr and Mo) in the late seventies Leyarovska et al. [24] found that only NbB_2 was showing superconductivity; in their studies MgB_2 was not investigated. Therefore, this unexpected property of this material was waiting for several decades to be discovered. The remarkable properties of MgB_2 open a new window in superconductivity for fundamental as well as applied research. MgB_2 was found to be a two-band BCS superconductor with a much higher critical temperature and a significantly smaller isotope effect [25]. The critical temperature of MgB_2 of 39 K enables the realization of electronic circuits based on this material to operate at $20-25$ K, achievable by a compact cryocooler, which gives a significant advantage for this

material as compared to the low-temperature superconductors [26]. Compared to the High-T_c superconductors, MgB_2 is simpler, cheaper, and more stable over time.

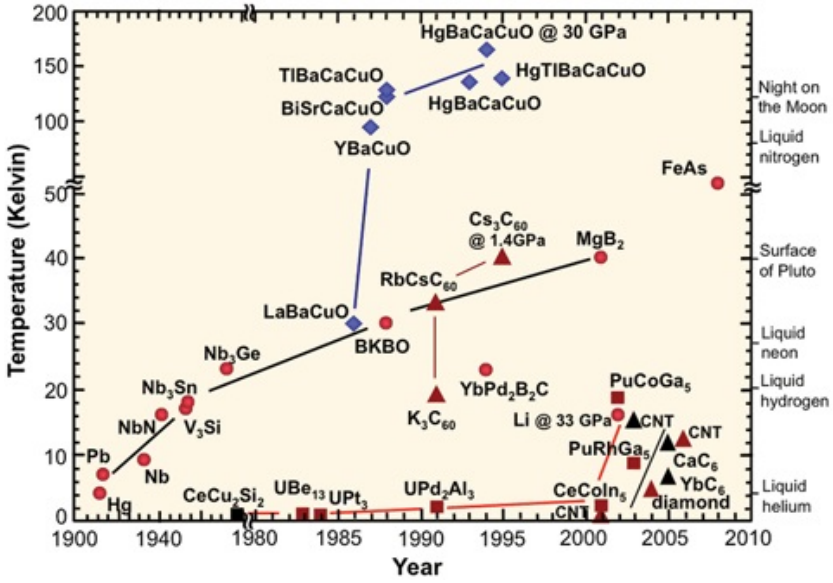

Figure 1.6: The chronology of discoveries of superconductors, and their critical temperatures. Credit: Wikipedia.

Recently, a new superconductor based on iron, LaFeOP, was discovered by a group at Tokyo Institute of Technology, Japan[27]. Iron, as a ferromagnet, was believed to preclude superconductivity because of the way ferromagnetism competes against Cooper-pair formation. Unexpectedly, however, the critical temperature was to stay at $4-6$ K irrespective of hole/electron-doping. A large increase in the T_c to 26 K was then found in $LaFe[O_{1-x}F_x]As$ [28]. The T_c of this material was further raised to 43 K under pressure. Much of the interest in theses new compounds are a consequence of the fact that they are very different from the cuprates and that they may help us to construct a theory for non-BCS superconductivity.

1.2 Theories of superconductivity

Superconductivity is usually discussed by using the following three theories, i.e. the phenomenological London equations, the phenomenological

Ginzburg-Landau (GL) theory and the microscopic BCS theory, depending on the specific situation. The London equations are usually used to discuss the magnetic response of a superconductor. By treating vortices as point-like "particles", the large-scale vortex static patterns and flux dynamics can be described [29, 30]. The GL theory has been very successful in describing mesoscopic superconductors (sample sizes comparable to the coherence length) and the behavior and structure of vortices [31–33]. Since the numerical approach of GL theory is fully developed and the obtained spatial Cooper-pair density is critical in experiments, the GL theory has become a powerful tool for studying superconductors. However, it is not applicable for nanoscale superconductors with size smaller than the coherence length.

In this thesis, nanoscale superconductors are studied within the framework of the real-space mean-field microscopic BCS theory (Bogoliubov-de Gennes equations), which is the most widely used theory nowadays for such situations. It involves the electronic structure and the energy spectrum. As a result, its applicability is the widest, e.g. available for temperature $T = 0$ K, but it has the largest complexity.

In this section, we introduce these theories for superconductivity. First, we briefly introduce the GL theory since it provides a simpler understanding on superconductivity including a natural derivation for the coherence length ξ, penetration depth λ and flux quantization. Next we introduce the BCS theory in detail. Then, Josephson effect, Andreev reflection and quasiparticle interference are introduced, which are related to the BCS theory.

1.2.1 Ginzburg-Landau theory

The GL theory is a powerful tool to describe the properties of superconductivity and to introduce the coherence length ξ and the magnetic penetration depth λ. It is based on Landau's theory of second-order phase transitions and the essential part of this theory is to introduce a complex order parameter $\Psi(\mathbf{r})$ as pseudo-wavefunction of the superconducting electrons, where $|\Psi(\mathbf{r})|^2$ indicates the density of superconducting electrons $n_s(\mathbf{r})$. Then, the free energy of a homogeneous superconductor (in the absence of the magnetic field) near the critical temperatue T_c has the form:

$$G_s = G_n + \alpha|\Psi|^2 + \frac{\beta}{2}|\Psi|^4 \tag{1.1}$$

where $|\Psi|(\mathrm{r})^2 = n_s/2$ is the density of Cooper pairs, G_s (G_n) is the free energy of the superconducting (normal) state and α and β are material dependent parameters. $\alpha \propto (T - T_c)$ is temperature-dependent, while β is positive and temperature-independent. The principle is shown in Fig. 1.7. When $T > T_c$,

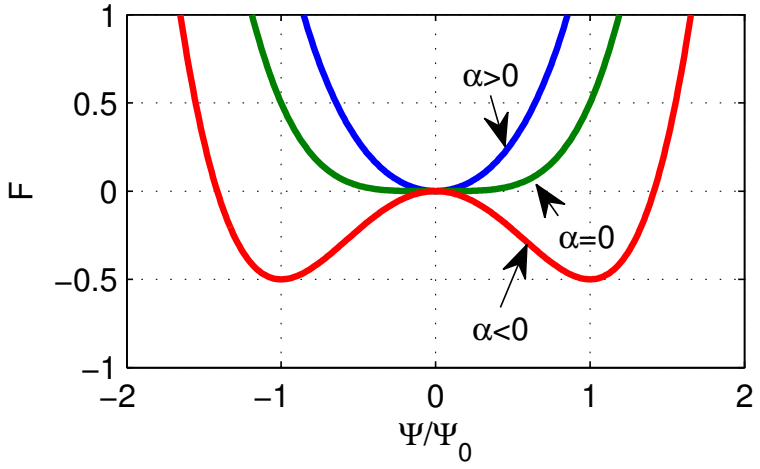

Figure 1.7: Ginzburg-Landau free-energy functions for describing spontaneous symmetry breaking through a second order phase transition.

the energy minimum is formed for $\Psi = 0$ which corresponds to the normal state. When $T < T_c$, the energy minimum occurs for $|\Psi|^2 = -\alpha/\beta$ which is the superconducting state.

In the presence of a magnetic field, the free energy has the form:

$$G_s = \int dV \left[\underbrace{G_n + \alpha|\Psi|^2 + \frac{\beta}{2}|\Psi|^4}_{I} + \underbrace{\frac{1}{2m^*}\left|\frac{\hbar}{i}\nabla\Psi - \frac{e^*}{c}\mathbf{A}\Psi\right|^2}_{II} - \underbrace{\frac{(\mathbf{H}-\mathbf{H_0})^2}{4\pi}}_{III} \right] \tag{1.2}$$

where the term II represents the kinetic energy of Cooper pairs and the term III represents the magnetic energy. The $m^* = 2m_e$ and $e^* = 2e$ are in term II due to the fact that two electrons form a Cooper pair. By minimizing the free energy with respect to the order parameter Ψ^* and the vector potential $\mathbf{A}$, one arrives at the Ginzburg–Landau equations

$$\alpha\Psi + \beta|\Psi|^2\Psi + \frac{1}{2m^*}\left(\frac{\hbar}{i}\nabla - \frac{e^*}{c}\mathbf{A}\right)^2\Psi = 0 \tag{1.3}$$

$$\mathbf{j}_s = -\frac{i\hbar e^*}{2m^*}\left(\Psi^*\nabla\Psi - \Psi\nabla\Psi^*\right) - \frac{e^{*2}}{m^*c}|\Psi|^2\mathbf{A} \tag{1.4}$$

The first equation is similar to the nonlinear Schrödinger's equation and the second equation defines the supercurrent $\mathbf{j}_s$.

Now we derive the coherence length ξ and the penetration depth λ from Eqs. (1.3) and (1.4). In the absence of the magnetic field, Eq. (1.3) in one dimension reads

$$-f + f^3 - \frac{\hbar^2}{2m^*|\alpha|}\frac{\mathrm{d}^2 f}{\mathrm{d}x^2} = 0 \tag{1.5}$$

where $f(x) = \Psi(x)/\Psi_0$ is the normalized wavefunction to its bulk value $\Psi_0 = \sqrt{-\alpha/\beta}$. For the case of a semi-infinite superconductor for $x > 0$ and a normal metal-superconductor boundary at $x = 0$, we have the boundary conditions $f(0) = 0$ and $f(x \to \infty) = 1$. Then, the solution of this equation (1.3) is $f = \tanh(x/\sqrt{2}\xi)$ where

$$\xi^2 = \frac{\hbar^2}{2m^*|\alpha|}. \tag{1.6}$$

The length ξ is the coherence length over which the order parameter heals.

Next we consider a case where a weak magnetic field $\mathbf{H_0}$ is applied, and the order parameter is a constant Ψ_0. Then, Eq. (1.4) reads

$$\mathbf{j}_s = -\frac{4e^{*2}}{mc}|\Psi_0|^2\mathbf{A}. \tag{1.7}$$

Together with Maxwell equation, $\nabla\times\mathbf{H} = 4\pi/c\mathbf{j}_s$, and $\mathbf{H} = \nabla\times\mathbf{A}$, Eq. (1.7) becomes

$$\mathbf{H} + \lambda^2\nabla\times\nabla\times\mathbf{H} = 0, \tag{1.8}$$

where $\mathbf{H}$ is the magnetic field and

$$\lambda^2 = \frac{mc^2}{16|\Psi_0|^2\pi e^{*2}}. \tag{1.9}$$

For the same case of semi-infinite superconductor for $x > 0$ and the interface at $x = 0$, we have the boundary conditions $\mathbf{H}(0) = \mathbf{H_0}$ and $\mathbf{H}(x \to \infty) = 0$. Then, the solution of Eq. (1.8) is $\mathbf{H} = \mathbf{H_0}e^{-x/\lambda}$. It means that the magnetic field penetrates into the superconductor but decreases exponentially in the superconductor. The decay length λ is the penetration length. The meaning of ξ and λ is illustrated in Fig. 1.5.

The ratio $\kappa = \lambda/\xi$ is the Ginzburg–Landau parameter. When $0 < \kappa < 1/\sqrt{2}$, the superconductor is of Type-I with positive surface energy. When $\kappa > 1/\sqrt{2}$, it is of Type-II with negative surface energy leading to the vortex state, where Abrikosov vortices penetrates into the superconductor. Each Abrikosov vortex carries one magnetic flux quantum, ϕ_0. The magnetic flux quantum will be introduced in the next section and the vortex states will be introduced in Sec. 1.3.

1.2.2 Flux quantization

Realizing that superconductivity is fundamentally a quantum phenomenon, Fritz London is the first to predict the flux quantization in 1948. He suggested that the trapped magnetic flux in a superconducting ring should be quantized in units of hc/e where h is the Planck constant, c is the speed of light and e is the electron charge. Later, experiments confirmed it but in units of $hc/2e$ due to Cooper pairs. That is

$$\Phi = n\Phi_0, \tag{1.10}$$

where n is an integer and

$$\Phi_0 = \frac{hc}{2e} \approx 2.07 \times 10^{-7}\ \mathrm{G}\cdot\mathrm{cm}^2. \tag{1.11}$$

Here, we derive the flux quantization from the second GL equation (1.4). Considering an order parameter, $\Psi = \psi e^{i\phi}$ (both ψ and ϕ are real.), the supercurrent can be written as:

$$\mathbf{j}_s = \frac{2e\hbar}{m}|\psi|^2\nabla\phi - \frac{4e^2}{mc}|\psi|^2\mathbf{A}. \tag{1.12}$$

From the contour integral of the vector potential along the path C, where $\mathbf{j}_s = 0$, we find that

$$\oint_C \mathbf{A}\cdot d\mathbf{l} = \frac{c\hbar}{2e}\oint_C \nabla\phi\cdot d\mathbf{l}. \tag{1.13}$$

The term on the left side is the magentic flux, $\oint_C \mathbf{A}\cdot d\mathbf{l} = \int \mathbf{B}\cdot d\mathbf{S} = \Phi$. However, on the right side, the phase change along the closed contour C is $\oint_C \nabla\phi\cdot d\mathbf{l} = 2\pi n$ since the wave function Ψ is single valued. Thus, we obtain flux quantization as expressed by Eq. (1.11).

1.2.3 BCS theory

The BCS theory is the first truly microscopic theory of superconductivity as it explains the origin of conventional superconductivity and its predictions are amazingly close to real experiments. The theory is based on the Landau-Fermi liquid theory. Starting from the assumption that there is some effective attraction between electrons, which can overcome the Coulomb repulsion, electrons are to form a bound state, called a **Cooper pair**. In conventional superconductors, an attraction is generally attributed to an electron-lattice interaction (phonons). The Cooper pairs act like bosons and they all occupy the same energy state, the ground state, at low temperature. Furthermore, in conventional superconductors, the size of a Cooper pair can be very large (e.g., about 10000 Å in Al) in real space so that there is a strong overlap of Cooper pair wavefunctions and a large scale phase coherence is established. They are not easily scattered by the lattice and by defects. It is the reason for the vanishing resistivity. Also, the phase rigidity of the Cooper pairs against magnetic field results in the Meissner effect [6].

The Cooper Problem

The ground state of a free electron gas is a filled Fermi sea. Cooper assumed two electrons with attractive interactions slightly above the Fermi sea. He found that an arbitrarily small attraction between electrons could result in a paired state of electrons with a lower energy than the Fermi energy, which implies that the pair is bound. It captured the essence of superconductivity and leads to the successful BCS theory.

Originally, Cooper considered to add a pair of electrons with momenta $\mathbf{k}$ and $-\mathbf{k}$ and their energies $E_{\mathbf{k}}$ slightly beyond the Fermi surface of the system. Their wave functions are $u_{\mathbf{k}} = e^{i\mathbf{k}\cdot\mathbf{r}}U_{\mathbf{k}}$ and $u_{-\mathbf{k}} = e^{-i\mathbf{k}\cdot\mathbf{r}}U_{-\mathbf{k}}$, respectively. Adding an electron with momentum $-\mathbf{k}$ is equivalent to annihilating a hole with $-\mathbf{k}$ and wavefunction $v^*_{\mathbf{k}} = u_{-\mathbf{k}}$. Here, we write $v^*_{\mathbf{k}} = e^{-i\mathbf{k}\cdot\mathbf{r}}V^*_{\mathbf{k}}$ and we see that $V^*_{\mathbf{k}} = U_{-\mathbf{k}}$. Then, the pair state $\Psi_{\mathbf{k}}$ for momentum $\mathbf{k}$ can be expressed as

$$\Psi_{\mathbf{k}}(\mathbf{r_1}, \mathbf{r_2}) = u_{\mathbf{k}}(\mathbf{r_1})u_{-\mathbf{k}}(\mathbf{r_2}) = U_{\mathbf{k}}V^*_{\mathbf{k}}e^{i\mathbf{k}\cdot(\mathbf{r_1}-\mathbf{r_2})}. \tag{1.14}$$

The linear combination of different $\mathbf{k}$ states gives the real space wave function

$$\Psi(\mathbf{r_1}, \mathbf{r_2}) = \sum_{\mathbf{k}} g(\mathbf{k})e^{i\mathbf{k}\cdot(\mathbf{r_1}-\mathbf{r_2})}, \tag{1.15}$$

where $g(\mathbf{k}) = U_{\mathbf{k}} V_{\mathbf{k}}^*$. Note that $g(\mathbf{k}) = 0$ for $|\mathbf{k}| < k_F$ due to the Pauli exclusion principle.

The Schrödinger equation for the paired electrons has the form

$$\Big[-\frac{\hbar^2}{2m}(\nabla_1^2 + \nabla_2^2) + V(\mathbf{r_1} - \mathbf{r_2}) \Big] \Psi(\mathbf{r_1}, \mathbf{r_2}) = (E + 2E_F)\Psi(\mathbf{r_1}, \mathbf{r_2}) \tag{1.16}$$

where $V(\mathbf{r_1} - \mathbf{r_2})$ is the interacting potential between the paired electrons and E is the energy of the pair relative to the state when the two electrons are at the Fermi level. Inserting Eq. (1.15) into Eq. (1.16), we obtain the Schrödinger equation in momentum space,

$$[2(E_{\mathbf{k}} - E_F) - E] g(\mathbf{k}) = -\sum_{\mathbf{k}'} V_{\mathbf{k},\mathbf{k}'} g(\mathbf{k}'), \tag{1.17}$$

with

$$E_{\mathbf{k}} = \frac{\hbar^2 \mathbf{k}^2}{2m}, \tag{1.18}$$

$$V_{\mathbf{k},\mathbf{k}'} = \Omega^{-1} \int e^{i(\mathbf{k}-\mathbf{k}')\cdot\mathbf{r}} V(\mathbf{r}) d\mathbf{r}, \tag{1.19}$$

where Ω is the volume of the system. For simplicity, he assumed that the interaction is constant near the Fermi level, within the Debye window $\hbar\omega_D$,

$$V_{\mathbf{k},\mathbf{k}'} = \begin{cases} V/\Omega, & |E_{\mathbf{k}} - E_F| \text{ and } |E_{\mathbf{k}'} - E_F| < \hbar\omega_D \\ 0, & \text{otherwise} \end{cases}. \tag{1.20}$$

Then, Eq. (1.17) becomes

$$g(\mathbf{k}) = -\frac{VC/\Omega}{E - 2(E_{\mathbf{k}} - E_F)}, \tag{1.21}$$

where

$$C = \sum_{|\mathbf{k}'-E_F|<\hbar\omega_D} g(\mathbf{k}'). \tag{1.22}$$

is a constant. Eqs. (1.21) and (1.22) form a set of self-consistent equations.

After using the density of states $N(E)$ to replace the summation with an integral, the solution of the eigenvalue can be found:

$$E = -\frac{2\hbar\omega_D}{e^{2/VN(E_F)} - 1}, \tag{1.23}$$

where $N(E_F)$ is the density of states at the Fermi level. This is the binding energy of a Cooper pair and it is always lower than the energy of the normal state no matter how small the interaction V.

The BCS Hamiltonian

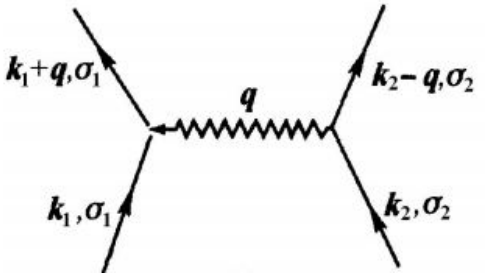

Figure 1.8: Phonon mediated electron-electron interaction. The electron $(\mathbf{k_2}, \sigma_2)$ emits a phonon of momentum $\mathbf{q}$, absorbed by the electron $(\mathbf{k_1}, \sigma_1)$.

The previous section showed that the Fermi see becomes unstable when attractive interactions exist between electrons. The BCS theory suggested that the attractive interactions are a consequence of electron-electron interactions mediated by electron-lattice interactions (electron-phonon). The motivation is the isotope effect $T_c \propto M^{-\alpha}$ where M is the isotope mass of the ion and $\alpha \sim 0.5$. The nature of this electron-phonon interaction is shown in Fig. 1.8 and the Hamiltonian is

$$\hat{H}_I = \frac{1}{2} \sum_{\mathbf{q},\mathbf{k},\mathbf{k'},\sigma_1,\sigma_2} V_{\mathbf{k_1},\mathbf{q}} c^\dagger_{\mathbf{k_1}+\mathbf{q},\sigma_1} c^\dagger_{\mathbf{k_2}-\mathbf{q},\sigma_2} c_{\mathbf{k_2},\sigma_2} c_{\mathbf{k_1},\sigma_1}, \tag{1.24}$$

where $c^\dagger_{\mathbf{k},\sigma}$ and $c_{\mathbf{k},\sigma}$ are the creation and destruction operators of electrons with momentum $\mathbf{k}$ and spin σ, and $\mathbf{q}$ is the momentum of the phonon. The interaction potential $V_{\mathbf{k},\mathbf{q}}$ is

$$V_{\mathbf{k},\mathbf{q}} = 2|M_\mathbf{q}|^2 \frac{\hbar\omega_\mathbf{q}}{(\varepsilon_{\mathbf{k}+\mathbf{q}} - \varepsilon_\mathbf{k}) - (\hbar\omega_\mathbf{q})^2}, \tag{1.25}$$

where $M_\mathbf{q}$ is the ion-electron interaction, ε and $\hbar\omega_\mathbf{q}$ are the energy of electrons and phonon, respectively.

Next, the BCS theory considered a reduced case. First, only those electrons within the Debye energy $\hbar\omega_D$ around the Fermi energy E_F are considered, i.e. $|\varepsilon_{\mathbf{k}+\mathbf{q}} - \varepsilon_\mathbf{k}| < \hbar\omega_D$. The interaction potential $V_{\mathbf{k},\mathbf{q}}$ is assumed to be a constant V. Second, only those pairs with $\mathbf{k_1} + \mathbf{k_2} = 0$ are considered. As shown in Fig. 1.9, for the pairs with total momentum $\mathbf{k_1}+\mathbf{k_2} = \mathbf{K}$, only those

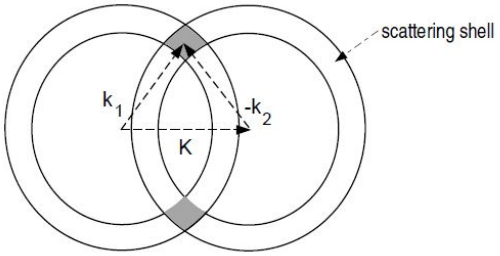

Figure 1.9: If the Cooper pair consists of two electrons having a momentum with sum $\mathbf{k_1} + \mathbf{k_2} = \mathbf{K}$, then the total number of such pairs is proportional to the dashed area.

electrons in the dashed area can participate. When $\mathbf{K} = 0$, the dashed area is maximum and gives the most important contribution. In addition, to insure the antisymmetry of the wavefunction, it is desirable to take pairs of opposite spin. Thus, the best choice for the ground state pairing is $(\mathbf{k}\uparrow, -\mathbf{k}\downarrow)$ and the BCS reduced Hamiltonian is written as

$$\hat{H}_{red} = \sum_{\mathbf{k},\sigma} \varepsilon_{\mathbf{k}} c^{\dagger}_{\mathbf{k},\sigma} c_{\mathbf{k},\sigma} - \sum_{\mathbf{k},\mathbf{k}'} V_{\mathbf{k},\mathbf{k}'} c^{\dagger}_{\mathbf{k}',\uparrow} c^{\dagger}_{-\mathbf{k},\downarrow} c_{-\mathbf{k},\downarrow} c_{\mathbf{k},\uparrow}. \tag{1.26}$$

The first term represents a sum of kinetic energies of all electrons. The second term represents the interaction among electrons. Here, $V_{\mathbf{k},\mathbf{k}'} > 0$ represents the attractive interaction.

The BCS ground state

At $T = 0$ K, the BCS theory proposes that all electrons near the Fermi energy E_F are in the form of Cooper pairs. This is the so-called BCS ground state. The proposed trial wave function for the many-body ground state $|\Psi_{BCS}\rangle$ is:

$$|\Psi_{BCS}\rangle = \prod_{\mathbf{k}} (u_{\mathbf{k}} + v_{\mathbf{k}} c^{\dagger}_{\mathbf{k},\uparrow} c^{\dagger}_{-\mathbf{k},\downarrow}) |\text{vac}\rangle. \tag{1.27}$$

Here $u_{\mathbf{k}}$ and $v_{\mathbf{k}}$ are the probability amplitude of the unoccupied and occupied pair state, respectively. They are variational parameters. The normalization condition reads $|u_{\mathbf{k}}|^2 + |v_{\mathbf{k}}|^2 = 1$. As seen from Eq. (1.27), the number of particles in the system is not conserved. The BCS theory is based on the

grand canonical ensemble. Therefore we have to impose a constraint on the number of electrons N:

$$\langle \Psi_{BCS}|\hat{N}|\Psi_{BCS}\rangle = \langle \Psi_{BCS}| \sum_{\mathbf{k}\sigma} c^{\dagger}_{\mathbf{k}\sigma} c_{\mathbf{k}\sigma} |\Psi_{BCS}\rangle = N. \tag{1.28}$$

Using a Lagrange multiplier, i.e. the Fermi energy E_F, one can minimize the ground-state energy E_S with constant N:

$$\delta E_S = \delta \langle \Psi_{BCS}|\hat{H}_{red} - E_F \hat{N}|\Psi_{BCS}\rangle = 0. \tag{1.29}$$

Substituting the Hamiltonian Eq. (1.26) and the wavefunction Eq. (1.27) into this equation, we obtain

$$E_S = \sum_{\mathbf{k}} 2\xi_{\mathbf{k}} v^2_{\mathbf{k}} + \sum_{\mathbf{k}\mathbf{k}'} V_{\mathbf{k}\mathbf{k}'} u_{\mathbf{k}} v_{\mathbf{k}} u_{\mathbf{k}'} v_{\mathbf{k}'}, \tag{1.30}$$

where $\xi_{\mathbf{k}} = \varepsilon_{\mathbf{k}} - E_F$. By minimizing this energy with respect to $u_{\mathbf{k}}$ and $v_{\mathbf{k}}$ and making use of the normalization condition, one obtains:

$$\begin{aligned} |u_{\mathbf{k}}|^2 &= \frac{1}{2}\Big(1 + \frac{\xi_{\mathbf{k}}}{E_{\mathbf{k}}}\Big), \\ |v_{\mathbf{k}}|^2 &= \frac{1}{2}\Big(1 - \frac{\xi_{\mathbf{k}}}{E_{\mathbf{k}}}\Big), \end{aligned} \tag{1.31}$$

where $E_{\mathbf{k}}$ is

$$E_{\mathbf{k}} = (\xi^2_{\mathbf{k}} + \Delta^2_{\mathbf{k}})^{\frac{1}{2}}, \tag{1.32}$$

and $\Delta_{\mathbf{k}}$ satisfies the relation:

$$\Delta_{\mathbf{k}} = -\sum_{\mathbf{k}'} V_{\mathbf{k}\mathbf{k}'} u_{\mathbf{k}'} v^*_{\mathbf{k}'} = -\frac{1}{2} \sum_{\mathbf{k}'} V_{\mathbf{k}\mathbf{k}'} \frac{\Delta_{\mathbf{k}'}}{E_{\mathbf{k}'}}. \tag{1.33}$$

$\Delta_{\mathbf{k}}$ is called the **pairing potential** or the **order parameter**. Eq. (1.33), the so-called gap equation, must be solved self-consistently.

The total energy of the superconducting ground state ($V_{\mathbf{k}\mathbf{k}'} \equiv V$ in the BCS theory) is given by

$$E_S = \sum_{\mathbf{k}} \Big(\xi_{\mathbf{k}} - \frac{\xi^2_{\mathbf{k}}}{E_{\mathbf{k}}}\Big) - \frac{\Delta^2}{V}. \tag{1.34}$$

The condensation energy is the energy difference between the superconducting state and the normal state:

$$E_{cond} = E_S - E_N \approx \sum_{\mathbf{k}} [\xi_{\mathbf{k}} - E_{\mathbf{k}}] = -\frac{1}{2} N(0) |\Delta|^2, \tag{1.35}$$

where $N(0)$ is the density of states at the Fermi energy. It also shows that the energy of the superconducting ground state is lower than the energy of the normal state.

Elementary Excitations

From the superconducting ground state, the total energy of the system will be increased when the pair state $(\mathbf{k}\uparrow, -\mathbf{k}\downarrow)$ is broken. Due to the Pauli exclusion principle, this can be done by adding an electron in state $\mathbf{k}\uparrow$ or removing an electron from state $-\mathbf{k}\downarrow$. The total energy change must be accounted for (1) energy for removing a pair state from the system and (2) energy for adding the single electron in the system.

According to Eq. (1.30), breaking a pair state with $\mathbf{k}$ increases the energy of the system by an amount

$$\delta F = -2\xi_{\mathbf{k}} v_{\mathbf{k}}^2 - 2 \sum_{\mathbf{k}'} V_{\mathbf{k}\mathbf{k}'} u_{\mathbf{k}} v_{\mathbf{k}} u_{\mathbf{k}'} v_{\mathbf{k}'}. \tag{1.36}$$

With Eq. (1.33), it may be written as

$$\delta F = -2\xi_{\mathbf{k}} v_{\mathbf{k}}^2 + 2\Delta_{\mathbf{k}} u_{\mathbf{k}} v_{\mathbf{k}}. \tag{1.37}$$

After including the kinetic energy of the added electron, the total energy changes by an amount:

$$\begin{aligned} \delta E &= \xi_{\mathbf{k}}(1 - 2v_{\mathbf{k}}^2) + 2\Delta_{\mathbf{k}} u_{\mathbf{k}} v_{\mathbf{k}} \\ &= \xi_{\mathbf{k}} \Big[1 - \big(1 - \frac{\xi_{\mathbf{k}}}{E_{\mathbf{k}}}\big) \Big] + \frac{\Delta_{\mathbf{k}}^2}{E_{\mathbf{k}}} \\ &= E_{\mathbf{k}}. \end{aligned} \tag{1.38}$$

Thus, $E_{\mathbf{k}}$ is the minimum energy required to break a Cooper pair and to create an excitation. $\Delta_{\mathbf{k}}$ is also called the **energy gap** because it is the smallest energy that can be added ($E_{\mathbf{k}} = \Delta_{\mathbf{k}}$ if $\xi_{\mathbf{k}} = 0$).

A single-particle excitation is a superposition of an electron and a hole. This is referred to as a **quasiparticle** and the $E_{\mathbf{k}}$ is the energy of the quasiparticle excitation.

Excited states of the reduced Hamiltonian can be obtained through a canonical transformation (Bogoliubov-Valatin transformation), which diagonalizes the Hamiltonian. These transformations are given by [34]

$$\begin{aligned} \gamma^{\dagger}_{\mathbf{k}\uparrow} &= u_{\mathbf{k}} c^{\dagger}_{\mathbf{k}\uparrow} - v_{\mathbf{k}} c_{-\mathbf{k}\downarrow}, \\ \gamma_{-\mathbf{k}\downarrow} &= u^{*}_{\mathbf{k}} c_{-\mathbf{k}\downarrow} + v^{*}_{\mathbf{k}} c^{\dagger}_{\mathbf{k}\uparrow}, \\ \gamma_{\mathbf{k}\uparrow} &= u^{*}_{\mathbf{k}} c_{\mathbf{k}\uparrow} - v^{*}_{\mathbf{k}} c^{\dagger}_{-\mathbf{k}\downarrow}, \\ \gamma^{\dagger}_{-\mathbf{k}\downarrow} &= u_{\mathbf{k}} c^{\dagger}_{-\mathbf{k}\downarrow} + v_{\mathbf{k}} c_{\mathbf{k}\uparrow}. \end{aligned} \tag{1.39}$$

Acting on the BCS ground state $|\Psi_0\rangle$, one finds

$$\begin{aligned} \gamma^{\dagger}_{\mathbf{k}\uparrow}|\Psi_0\rangle &= |\Psi_{\mathbf{k}\uparrow}\rangle, \\ \gamma^{\dagger}_{-\mathbf{k}\downarrow}|\Psi_0\rangle &= |\Psi_{-\mathbf{k}\downarrow}\rangle, \\ \gamma_{\mathbf{k}\uparrow}|\Psi_0\rangle &= 0, \\ \gamma_{-\mathbf{k}\downarrow}|\Psi_0\rangle &= 0. \end{aligned} \tag{1.40}$$

The quasiparticles operator $\gamma^{\dagger}_{\mathbf{k}\uparrow}$ creates a quasiparticle with $\mathbf{k}\uparrow$ and $\gamma_{-\mathbf{k}\downarrow}$ destroys a quasiparticle with $-\mathbf{k}\downarrow$. These elementary excitations are sometimes called **Bogoliubov quasiparticles**. They are fermions because these operators satisfy the anti-commutation relation:

$$\begin{aligned} \left[\gamma_{\mathbf{k}\sigma}, \gamma^{\dagger}_{\mathbf{k}'\sigma'}\right]_{+} &= \delta_{\mathbf{k}\mathbf{k}'}\delta_{\sigma\sigma'}, \\ \left[\gamma_{\mathbf{k}\sigma}, \gamma_{\mathbf{k}'\sigma'}\right]_{+} &= \left[\gamma^{\dagger}_{\mathbf{k}\sigma}\gamma^{\dagger}_{\mathbf{k}'\sigma'}\right]_{+} = 0. \end{aligned} \tag{1.41}$$

The consequences of the BCS theory

The BCS theory gives the superconducting transition temperature T_c in terms of the electron-phonon coupling potential V and the Debye energy $\hbar\omega_D$:

$$k_B T_c = 1.13\hbar\omega_D e^{-1/N(0)V}, \tag{1.42}$$

where $N(0)$ is the electronic density of states at the Fermi level. Also, the energy gap at zero temperature $\Delta(0)$ is written as

$$\Delta(0) = 2\hbar\omega_D e^{-1/N(0)V}. \tag{1.43}$$

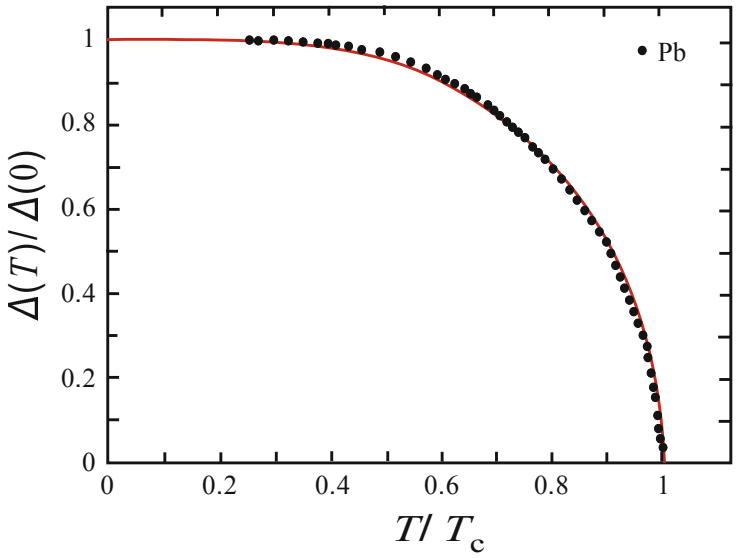

Figure 1.10: Temperature dependence of the gap energy for lead, measured by tunneling. These results agree well with the prediction of the BCS theory (continuous curve). Taken from [35].

The ratio between the $\Delta(0)$ and the $k_B T_c$ is the *universal* BCS value, i.e.

$$\frac{\Delta(0)}{k_B T_c} = 1.76. \tag{1.44}$$

Near the critical temperature, the temperature dependence of the superconducting gap $\Delta(T)$ can be written as [6]

$$\Delta(T \to T_c) \approx 1.74\Delta(0)\sqrt{1-(T/T_c)}. \tag{1.45}$$

The temperature-dependent critical field $\Delta(H)$ is

$$\frac{H_c(T)}{H_c(0)} \approx 1 - \left(\frac{T}{T_c}\right)^2. \tag{1.46}$$

The BCS coherence length at zero temperature is

$$\xi(0) = \frac{\hbar v_F}{\pi\Delta(0)}, \tag{1.47}$$

where v_F is the Fermi velocity.

Due to the energy gap, the specific heat of the superconductor shows the exponential law according to the BCS theory,

$$c_s/\gamma T_c = 1.34\Big(\frac{\Delta(0)}{T}\Big)^{3/2} e^{-\Delta(0)/T}, \tag{1.48}$$

where γ is the coefficient of the linear term of the normal state. The specific heat is suppressed strongly at low temperatures but it increases massively with the exponential law as temperature increase. Near the critical temperature T_c, it is higher than that of the normal conductor and exhibits a jump at T_c.

In this thesis, we use Bogoliubov-de Gennes equations, which are the real space generalization of the BCS theory. We will introduce it in Chapter. 2.

1.2.4 Josephson effect

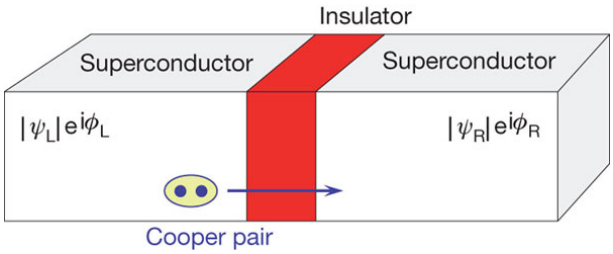

Figure 1.11: The sketch of a Josephson junction. Taken from [36].

The Josephson effect depicts the quantum tunneling of superconducting Cooper pairs. Before Josephson's prediction, it was only known that normal electrons can flow through a potential barrier. In 1962, B.D. Josephson predicted quantum tunneling of Cooper pairs through an insulating barrier between two superconductors. The device is shown in Fig. 1.11. If the insulating barrier is thick, the Cooper pairs can not pass through, but if the barrier is thin enough ($\approx$ 10 nm) there is a non-zero probability for Cooper pairs to tunnel. This is called the **Josephson Effect**. The original derivation is based on the BCS theory. Here we introduce the simplified derivation proposed by Feynman.

Quantum mechanics shows that the superconducting order parameter Ψ satisfies the following Schrödinger equations on each side of the insulating

barrier:

$$\begin{aligned} i\hbar\frac{\partial\Psi_1}{\partial t} &= U_1\Psi_1 + K\Psi_2 \\ i\hbar\frac{\partial\Psi_2}{\partial t} &= U_2\Psi_2 + K\Psi_1 \end{aligned} \tag{1.49}$$

where U is the potential energy, and K is a constant describing the coupling through the junction. Ψ can be written as

$$\begin{aligned} \Psi_1(\mathbf{r}) &= \sqrt{\rho_1}e^{i\theta_1}, \\ \Psi_2(\mathbf{r}) &= \sqrt{\rho_2}e^{i\theta_2}, \end{aligned} \tag{1.50}$$

where ρ is the density of Cooper pairs and θ is the phase. Substituting Eq. (1.50) into Eq. (1.49), one gets

$$\hbar\frac{\partial\rho_1}{\partial t} = -\hbar\frac{\partial\rho_2}{\partial t} = 2K\sqrt{\rho_1\rho_2}sin(\theta_2 - \theta_1) \tag{1.51}$$

$$-\hbar\frac{\partial}{\partial t}(\theta_2 - \theta_1) = U_2 - U_1. \tag{1.52}$$

These are the main equations describing the Josephson effect. The tunneling current through the junction is

$$I = \frac{\partial\rho_1}{\partial t} = I_0\sin\delta, \tag{1.53}$$

where $I_0 = 2K\sqrt{\rho_1\rho_2}/\hbar$ and $\delta = \theta_2 - \theta_1$. When $U_2 - U_1 = 0$ in Eq. (1.52), a constant current passes through the junction, and has a maximum value, I_0. This is the **DC Josephson effect**. When we apply a constant voltage V_0, i.e. $U_1 - U_2 = 2eV$ in Eq. (1.52), $I = I_0\sin(\frac{2eV_0}{\hbar}t)$. Therefore, the Josephson current will oscillate at a frequency $f = \frac{2eV_0}{\hbar}$. This is the **AC Josephson effect**.

1.2.5 Andreev reflection and quasiparticle interference

In this subsection we consider that a single electron is transmitted from a normal metal (N) to a superconductor (S) and we suppose that its energy is lower than the superconducting energy gap, i.e. $\epsilon < |\Delta|$. This process should be blocked at the interface by the superconducting gap $|\Delta|$. However, this single electron can be converted into a Cooper pair by reflecting a hole. This process is called **Andreev reflection**, named after the Russian physicist Alexander F. Andreev.

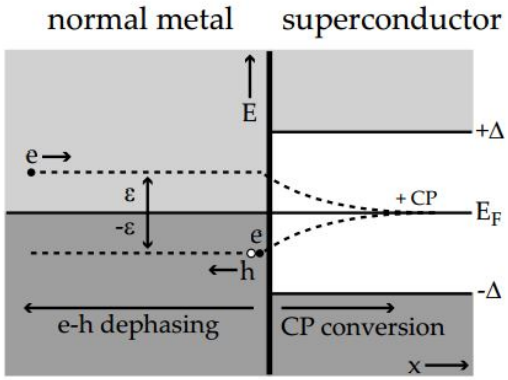

Figure 1.12: Andreev reflection at a normal metal - superconductor interface. Upon reaching the interface, the incoming electron at energy ϵ causes a hole reflection with energy $-\epsilon$ (together they form the correlated electron-hole pair). The incoming electron itself and the missing electron in the valence band have entered the superconductor where they are converted into a Cooper pair.

The Andreev process is shown in Fig. 1.12. An incident electron reaches the S/N interface. It couples with an electron of energy $-\epsilon$ and opposite direction of momentum and spin to form a Cooper pair. Then, the Cooper pair enters the superconductor and leaves a hole behind in the valence band. This hole travels back along the path of the original incident electron due to the opposite direction of the momentum.

The reversed mechanism happens as well. An incident hole with energy $-\epsilon$ in the valence band reaches the S/N interface and pulls a Cooper pair out of the superconductor. One of the electrons occupies the hole, while the other electron occupies the state with energy ϵ in the conduction band. The second electron has opposite direction of momentum and spin compared to the incoming hole. Thus, it travels back along the path of the original incident hole. As a result, each Andreev reflection transfers a charge of $2e$ across the interface, preventing the forbidden single-particle transmission within the energy gap.

We next introduce two kinds of quasiparticle interference effects in S/N systems, both being related to Andreev reflection. They are the **Tomasch effect** occurring in the S side [38–40] and the **McMillan–Rowell effect** occurring in the N side [41, 42]. Their procedures are shown in Fig. 1.13(a). These

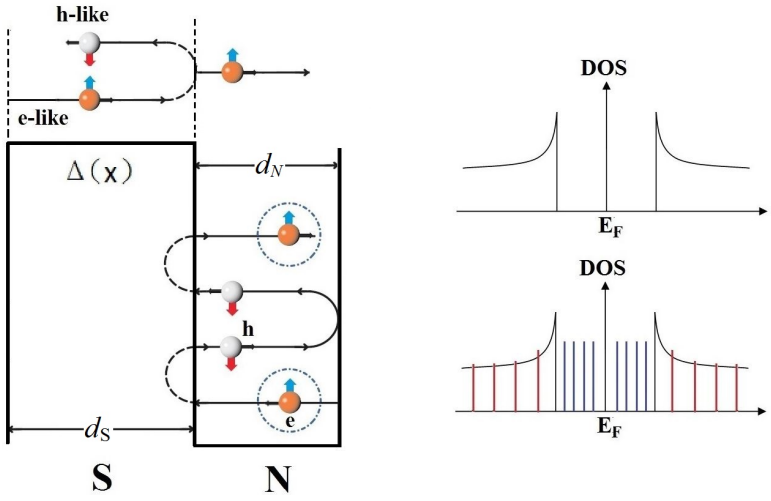

Figure 1.13: Schematic representation of the Tomasch and McMillan–Rowell resonances at a S/N interface. The interfering particles are enclosed in the dashed and dot–dashed circles. Both Tomasch and McMillan–Rowell resonances require Andreev reflection of the incident quasiparticle/electron. They result in oscillations in the DOS shown in the right panel. Taken from [37].

effects result in oscillations in the tunneling conductance [see Fig. 1.13(b)] and vary with the thickness of the S and N layers, respectively. They are geometric resonances and are generally referred to as Tomasch and McMillan–Rowell oscillations.

The Tomasch effect is caused by quasiparticle interferences in the Superconducting (S) side of the interface. The interference is between an incident electron-like quasiparticle (a mixture of a hole and an electron, in which the latter is dominant [43]) and its hole-like counterpart, which is Andreev-reflected back from the interface owing to the local perturbation of the energy gap [40]. The interference occurs for quasiparticle energies

$$V_n = \sqrt{\Delta^2 + (nhv_F^S/2d_S)^2} \quad \text{with} \quad n = 0, 1, 2, \ldots , \tag{1.54}$$

where Δ is the energy gap, h is the Planck constant, v_F^S is the Fermi velocity in the superconductor and d_S its thickness, and therefore shows in the conductance versus bias as a nearly periodic series of oscillations [40]. On

the contrary, the McMillan–Rowell oscillations is caused by single-particle interferences in the non-superconducting (N) side of the interface. In this case, the incident electron is Andreev-reflected as a hole at the interface. However, unlike in the S, in a non-superconducting material an electron and a hole cannot interfere [41]. Therefore, for the interference to occur in the N, the Andreev-reflected hole must subsequently travel to the opposite interface and, after being normal-reflected, propagate back to the S/N interface to undergo a second Andreev reflection[37]. This returns the hole to its original electron state. Here it will interfere with the first incident electron, which gives rise to conductance oscillations with peaks at bias

$$V_m = V_0 + mhv_F^N/4d_N \quad \text{with} \quad m = 0, 1, 2, ... \tag{1.55}$$

where v_F^N is the Fermi velocity in the N and d_N its thickness [41].

In fact, the quasiparticle interference of the Tomasch effect can not only occur in N/S systems, but also in any system with a spatial inhomogeneous superconducting gap, i.e. $\Delta = \Delta(\mathrm{r})$. In nanoscale superconductors, the inhomogeneous superconductivity results from the quantum confinement effect. This effect is exemplified in nanoscale superconductors in Chapter. 5.

1.3 Vortex states

1.3.1 Quantum vortex in superconductors

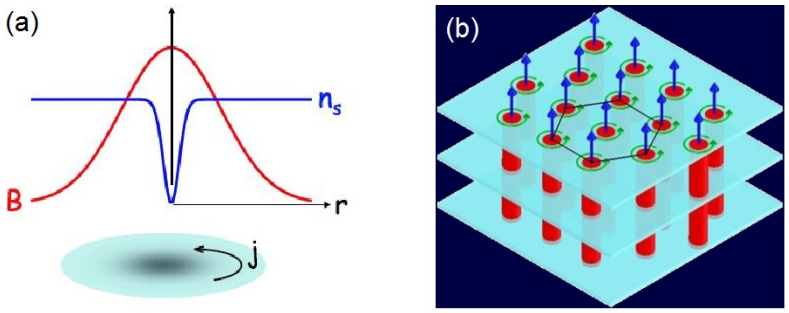

Figure 1.14: (a) Isolated Abrikosov-vortex: sketch of Cooper-pair density $n_s(r)$, magnetic field $B(r)$ and supercurrent $\mathbf{j}$. (b) sketch of Abrikosov triangular lattice.

Abrikosov predicted the vortex state in type-II superconductors in 1957 [44]. Nowadays, it has been realized that the properties of the vortices in superconductors determine the current-carrying performance in most applications.

The vortex has a core with order parameter $\psi = 0$ at the center. It indicates zero superconducting electron density, i.e. $n_s = 0$ at the core, so that it is often called the core of normal state. The supercurrent circulates around this core is such that a single flux quantum Φ_0 is penetrating the sample. The spatial profile of the superconducting electron density n_s, current j_s and the magnetic field B for an isolated vortex are shown in Fig. 1.14(a). The magnetic field distribution far from its core can be described by

$$B(r) = \frac{\Phi_0}{2\pi\lambda^2} K_0\Big(\frac{r}{\lambda}\Big) \approx \sqrt{\frac{\lambda}{r}} exp\Big(-\frac{r}{\lambda}\Big). \tag{1.56}$$

where r is the distance from the vortex core and K_0 is the zeroth-order modified Bessel function of the second kind. At $r \to 0$, the field is simply given by

$$B(0) \approx \frac{\Phi_0}{2\pi\lambda^2} \ln\kappa \tag{1.57}$$

where κ is the GL parameter.

When the vortex moves, it can create a pseudo-resistance and suppresses both the critical current density and the critical field. How to pin a vortex is an important topic for applications.

1.3.2 Vortex interactions

In a clean bulk type-II superconductor, the vortices form an Abrikosov triangular vortex lattice, as shown in Fig. 1.14(b). This is due to the repulsive **vortex-vortex interaction**. This interaction has been studied within the GL theory by Kramer [47], Brandt [48], Chaves [49] and others. They showed that the interaction energy, U_{vv}, in bulk can be expressed as:

$$U_{vv} = \frac{\Phi^2}{8\pi^2\lambda^2}\Big[K_0\Big(\frac{r}{\lambda}\Big) - K_0\Big(\frac{r}{\xi/\sqrt{2}}\Big)\Big], \tag{1.58}$$

where r is the separation of the vortices and K_0 is the zeroth-order modified Bessel function. When the GL parameter $\kappa < 1/\sqrt{2}$, namely in the type-I regime, vortices attract each other. When $\kappa > 1/\sqrt{2}$, in the type-II regime,

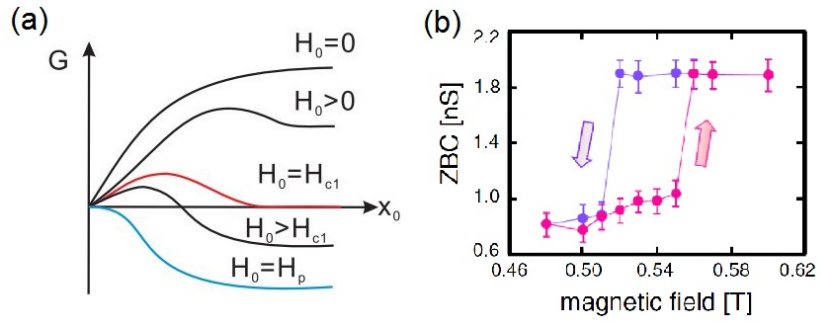

Figure 1.15: (a) Gibbs free energy of an isolated vortex as a function of its distance from the surface for different values of applied field H_0. Taken from [45] (b) The STM zero-bias conductance (ZBC) plot under various magnetic fields measured at the center of an superconducting Pb island. The low and high ZBC refer to the Meissner state and the vortex state, respectively. The ZBC jump indicates the phase transition between the Meissner state and the vortex state. The ZBC jump up corresponds to the entrance of a vortex and the jump down corresponds to the exist of a vortex. This hysteresis-like behavior results from the presence of a surface barrier. Taken from [46].

vortices repel each other. When $\kappa = 1/\sqrt{2}$, vortices do not interact according to this model.

The interaction between a vortex and an antivortex, is always attractive, for both type-I and type-II superconductors. This can be understood in the following way: when a vortex and an antivortex are far from each other the energy of the system is non-zero, as it is the sum of the energy of the vortex and the antivortex; when they are close to each other they will annihilate resulting in zero energy. Hence the interaction is always attractive[49].

There also exists an interaction between the vortex and the surface of a superconductor. When a vortex enters/leaves the superconductor, it has to overcome an energy barrier at the surface, called the **Bean-Livingston barrier**[50]. This barrier can be understood by assuming an antivortex outside the superconductor at the image position with respect to the vortex. The vortex and the image antivortex attract each other, while the surface currents arising from the applied field repel the vortex. The net effect of this potential barrier is shown in Fig. 1.15(a) as a function of applied field H_0. One can see that at $H_0 > H_{c1}$ the presence of a vortex in the superconductor is favoured thermodynamically. However, the vortex is unable to penetrate the super-

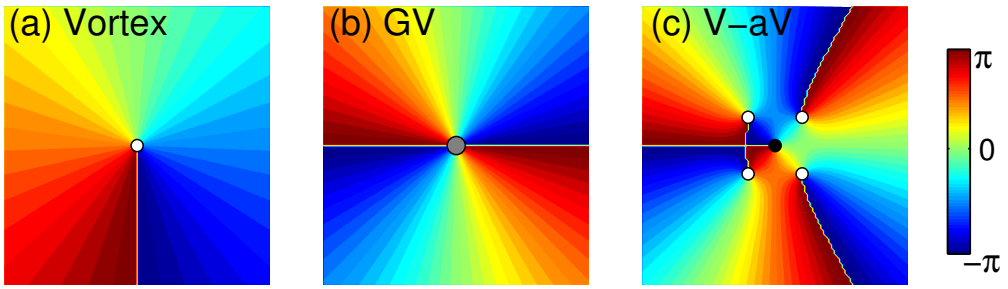

Figure 1.16: The phase plot for the single-vortex (a), a giant vortex with vorticity $L = 2$ (b) and the $L = 4 - 1$ vortex-antivortex structure with total vorticity $L = 3$ (c).

conductor until $H_0 = H_p$ at which the Bean-Livingston barrier vanishes. At $H_0 < H_{c1}$, the presence of a vortex in the superconductor is not favoured thermodynamically. However, the energy barrier prevents the vortex from leaving the superconductor until a lower H_0 for which the barrier vanishes. Therefore, the existence of the barrier results in a hysteresis-like behavior in the magnetization curve and the STM tunneling spectra [see Fig. 1.15(b)].

1.3.3 Vortex states in mesoscopic superconductors

Mesoscopic superconductors are those with dimensions comparable to the penetration depth λ or the coherence length ξ. Vortex states in mesoscopic superconductors strongly depend on the size and geometry of the sample because the vortex-surface interaction dominates. Consequently, these are very different from the Abrikosov triangular lattice in bulk, where only the vortex–vortex interaction plays a role.

During the last two decades, numerous works have been done in this field. Some peculiar vortices such as the giant vortex and the anti-vortex states were unveiled.

In order to distinguish different vortex configurations consisting of vortices, giant vortices and antivortices and also to determine the total number of vortices in the sample more conveniently, we introduce a single quantity, the *vorticity* (or *winding number*) L. By going around a closed path in the plane around a given point anticlockwise, the phase of the order parameter will change L times 2π. The anticlockwise direction is just to make sure that

L for a vortex is always positive. Fig. 1.16(a) shows the phase plot for a single-vortex. The vortex is at the center of the sample. Along a closed path around this vortex, the phase of the order parameter changes with 2π and therefore $L = 1$. Fig. 1.16(b) shows the same phase plot for a giant vortex. The vortex is also at the center of the sample. The phase around the vortex center changes 2 times with 2π indicating that this giant vortex has vorticity $L = 2$. Fig. 1.16(c) shows the vortex-antivortex structure. The antivortex is at the canter and the four vortices surround it. This antivortex has vorticity $L = -1$ so that the total vorticity of this sample is $L = 4 - 1 = 3$. A simpler way to determine the total vorticity L of a sample is to count the number of times that the phase of the order parameters changes by 2π at the sample boundary. This way, we can determine that the total vorticity of the sample $L = 1$, 2 and 3 in Fig. 1.16(a)-(c), respectively.

Next, we show the phase diagram of vortex states for mesoscopic disks in Fig. 1.17(a). When the disk is relatively large, circular shell structures of vortices are observed [51]. As the size of the disk becomes smaller, the boundary imposes a stronger confinement on these vortices. Finally, they are merged to a **giant vortex**, which contains multiquanta vorticity with a single vortex core [31]. The giant vortex is supposed to be unstable in bulk due to the strong vortex-vortex repulsive interaction. However, it can be the ground state in mesoscopic superconductors. Experimentally, this has been observed in various measurements [52, 53].

Fig. 1.17(b) shows the phase diagram of vortex states for mesoscopic superconducting squares. The vortex configurations look more complex than those found in disks. When the square is relatively large, a square arrangement of vortices is observed[30]. As the sample becomes smaller, the boundary confinement imposes the sample's symmetry on the vortex configurations. For the winding number $L = 2$ and 6, a giant vortex is formed at the center of the sample so that the symmetry of the vortex configuration is the same as the sample. For $L = 3$ and 7, where the vorticity is not consistent with the symmetry of the sample, an additional vortex-antivortex (V-aV) pair is formed in order to keep the symmetry. This is called the **symmetry-induced antivortex**. This was also predicted to exist in mesoscopic samples with a discrete symmetry such as triangles [54] and regular polygons. The observation of such as antivortex is challenging. The reasons are: 1) the formation of the V-aV pair is sensitive to the presence of defects in the sample; 2) the distance between the vortex and the antivortex is shorter than ξ. Artificial pinning was proposed in order to enhance the stability region of

such a V-aV molecule[33]. In Chapter 3 and 4 of this thesis, we show that quantum confinement can further stabilize the V-aV states.

1.4 Nanoscale superconductivity

Materials reduced to the nanoscale (usually in the range $1-100$ nanometers) show different physical (mechanical, electrical, optical, etc.) properties as compared to what they exhibit in a bulk. For example, aluminium is a stable material but nanoscale aluminium becomes combustible, copper is an opaque material but nanoscale copper becomes transparent, and gold is an insoluble material but nanoscale gold becomes soluble. These phenomena are attributed to **quantum mechanical** and **surface effects**. Quantum mechanical effects due to discrete energy levels lead to modifications in the electronic structures and the DOS. As an example, the DOS of a free electron system from 3D to 0D is shown in Fig. 1.18. The DOS in lower dimensional systems is quite different from the bulk resulting in a dramatic change in the electronic properties. The Fermi wavelength λ_F is a characteristic length scale for nanoscale systems. When the system dimensions are of the order of λ_F, the changes in the properties are more significant. The increase of the importance of surface effects is due to the increase in surface area to volume ratio in nanoscale systems.

Superconductivity is no exception to this trend. Due to the multiple characteristic length scales in a superconductor, i.e. coherence length ξ, magnetic penetration depth λ and Fermi wavelength λ_F, nanoscale superconductivity shows much richer phenomena.

The study of nanoscale superconductivity started in 1960s, shortly after the formulation of the BCS theory. It was found that the superconducting properties change from bulk ones when the system dimensions are reduced below the coherence length ξ and the magnetic penetration depth λ. The former one destroys the macroscopic phase coherence of Cooper pairs and the latter one decreases the Meissner signal. When the system dimensions are further reduced to the order of the Fermi wavelength λ_F, quantum confinement plays an important role and results in novel phenomena called the **quantum size effect**. These phenomena provide a new approach to investigate the mechanism of superconductivity and, also, provide greater potential for applications in ultrafast, power-saving electronic devices such as superconductive transistors and single-photon detectors.

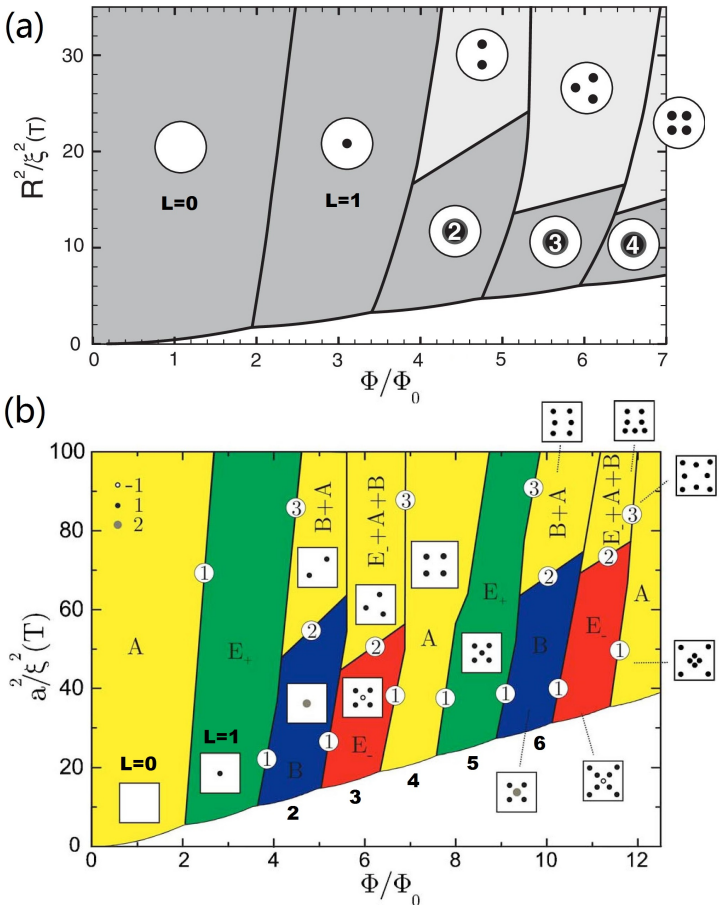

Figure 1.17: (a) Ground state size-flux phase diagram for a mesoscopic superconducting disk. For each phase, the vortex configuration is shown schematically. The numbers inside the circles indicate the vorticities of the giant vortex phases. Vertical lines separate phases with different total vorticity L. Horizontal lines correspond to broken-symmetry phase transitions, which are of giant vortex - multivortex type for $L > 1$. Taken from [55]. (b) Ground state size-flux phase diagram for a mesoscopic superconducting square. The vortex configuration is also shown schematically for each phase. Note the giant vortex states for $L = 2$ and 6, and the vortex-antivortex structures for $L = 3$ and 7. Taken from [56].

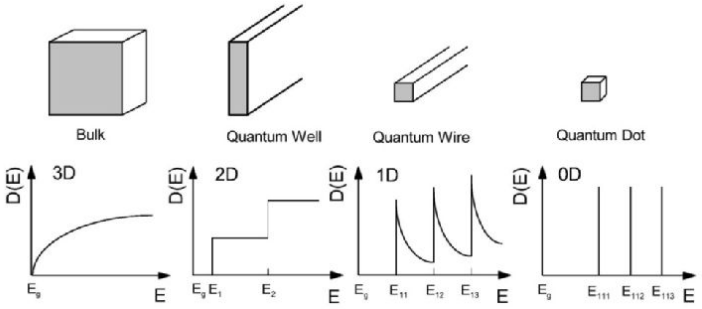

Figure 1.18: Schematic diagram illustrating the electronic density of states and its dependence on the dimensionality.

A superconductor with one, two or three dimensions smaller than ξ and λ are quasi-two-dimensional (2D), quasi-one-dimensional (1D) or quasi-zero-dimensional (0D) superconductors, respectively. In this section, we briefly introduce the theoretical and experimental progress in nanoscale superconductivity regarding the following aspects: 1) Size dependent properties; 2) Quantum size effects; 3) Surface effects and 4) Fluctuation effects.

1.4.1 Size dependence of superconducting properties

In nanoscale superconductivity, the superconducting characteristic lengths, the penetration depth λ and the coherence length ξ, change with the system size. Tinkham [61] showed that their changes were related with the mean free path l in the reduced system. In the dirty limit ($l \ll \xi$), the coherence length ξ is given by:

$$\xi \approx 0.85\sqrt{\xi_0 l}, \tag{1.59}$$

where the intrinsic coherence length $\xi_0 = \hbar v_F/\pi\Delta_0$, with v_F the Fermi velocity. The effective penetration depth λ_{eff} changes to:

$$\lambda_{eff} = \lambda_0(\frac{\xi_0}{1.33l})^{1/2}, \tag{1.60}$$

where λ_0 is the intrinsic penetration depth. From Eqs. (1.59) and (1.60), ξ decreases with decreasing particle size while λ_{eff} increases. Consequently, **a type-I superconductor tends to behave like a type-II superconductor at small sizes**. This has been confirmed in dirty granular Al films [62]. The Al films show type-II behavior but bulk Al is a type-I superconductor.

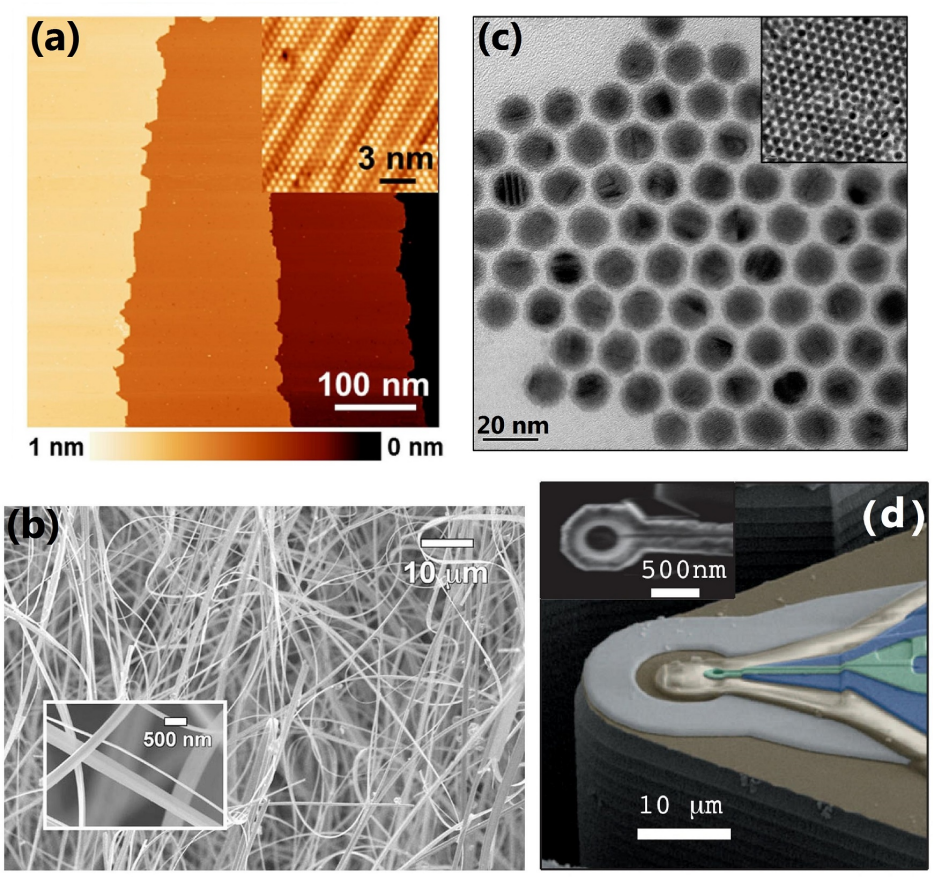

Figure 1.19: (a) STM topographic image of a Pb-SIC film with a few monolayer-thick. The inset shows the high resolution image. Taken from [57]. (b) SEM micrographs of $NbSe_2$ nanowires. The high magnification image given in the inset shows the variation in size and shape of the nanowires. Taken from [58]. (c) TEM images of Pb nanoparticles with core diameters 11.4 ± 0.6 nm. The shell thickness is in the range of $1.5 - 2$ nm. The inset shows an example of self-assembly into a superlattice. Taken from [59]. (d) SEM image of a SQUID. Its pick-up loop diameter is 200 nm. Taken from [60].

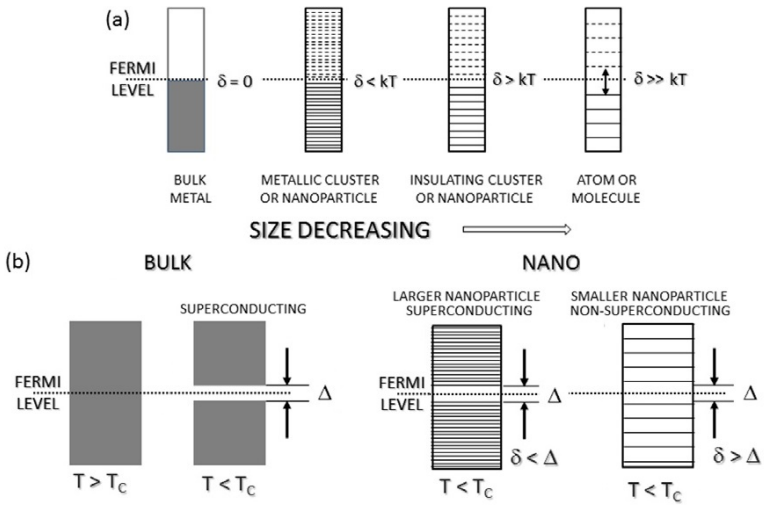

Figure 1.20: Schematic representation of QSEs in metal nanoparticles. The Kubo gap δ is a measure of the discretization of the bands and is inversely proportional to the size. (b) In superconducting nanoparticles, QSE is manifested as the Anderson criterion, according to which superconductivity is destabilized when the size is small enough for the Kubo gap to exceed the superconducting energy gap Δ. Taken from [63]

1.4.2 Quantum size effect (QSE)

According to the BCS theory, superconductivity results from the electronic pairing mainly occurring in a Debye window $\hbar\omega_D$ near the Fermi level E_F. In nanoscale superconductors, the electronic structure changes due to quantum effects leading to new properties. Fig. 1.20 shows that the quantum confinement effect on the electronic wave vector $\mathbf{k}$ in nano-particles results in a Kubo gap δ, which is the inter-level spacing of the discretized electronic energy levels. The Kubo gap $\delta \approx \epsilon_F/N$, where N is the number of electrons in the particle [64], varies with the size and shape of the particles leading to the variation of the DOS near the Fermi level E_F. Therefore the the number of Cooper pairs and the superconducting energy gap Δ become dependent on the size and the shape of the specimen. This is the **quantum size effect**. Usually, the critical temperature T_c and the superconducting energy gap Δ show oscillations when compared to their bulk values as the size changes. When superconductivity is enhanced, i.e. an increase in T_c, it is called the

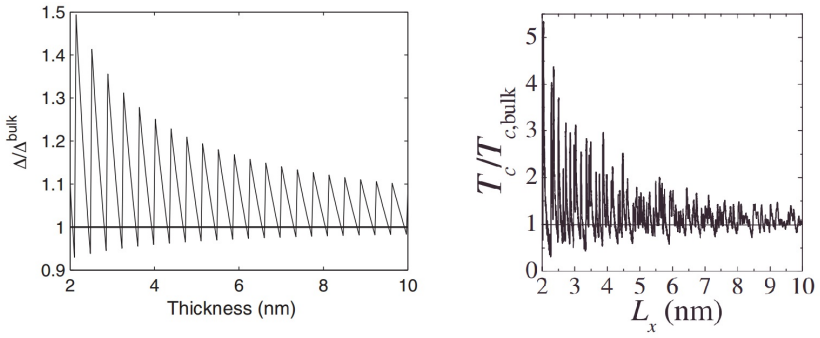

Figure 1.21: Regular and irregular shape resonances induced by QSE in nanofilms and in nanowires, respectively. (Left) the thickness-depedent relative superconducting order parameter Δ/Δ^{bulk} for a nanofilm. This panel is taken from Ref. [66]. (Right) the L_x-dependent relative critical temperature $T_c/T_{c,bulk}$ for a nanowire with square-cross-section. This panel is taken from [67].

shell effect. Anderson argued that the superconducting order parameter cannot, in principle, exist in nanoparticles when their size d is too small so that the Kubo gap δ exceeds the superconducting energy gap Δ. This is known as the **Anderson argument** [65]. For conventional superconductors, d is usually in the range between 4 to 6 nm.

For thin films with thickness down to the nanoscale, Blatt and Thompson, in 1963, suggested oscillations of the energy gap Δ and the critical temperature T_c with peaks that greatly exceeded the bulk limit [68]. This non-monotonic size dependence, usually referred to as **shape resonances**, is a consequence of the quantum size effect. In this case, the electronic spectrum forms subbands due to the quantization of the motion in the perpendicular direction. Each time the bottom of one subband crosses the Fermi level T_c is enhanced above its bulk value. Fig. 1.21 presents the regular shape resonance effect for nanofilms in the left panel and the irregular one predicted for nanowires in the right panel. Similar quantum-size oscillations were theoretically investigated in quantum striped superconductors [69–71]

Initially, the purpose of experiments on superconducting thin films was to verify the prediction of shape resonances and the enhancement in T_c. However, the properties observed often depend on the material and the film morphology. For example, Al [72] and Sn films show a non-monotonic variation of T_c with decreasing film thickness whereas Pb [73], Nb [74, 75] and

In[76] films show a monotonic decrease in T_c. The suppression of T_c has been attributed to either **localization effects** or **inverse proximity effects**. The localization effect is due to the disorder level in granular thin films. The inverse proximity effect is due to the Cooper pairs penetrating into the substrate and the protecting cap layer.

Recent technological advancements in both growth and measurement of nanostructures led to many experiments on low dimensional systems and tests of the quantum size effect of superconductivity. Experiments on crystalline films allows one to address intrinsic thickness-dependent properties. The evolution of superconductivity in ultrathin films of Sn, Pb, Ga, Al, and In was examined as a function of thickness and temperature [84]. They show oscillations of T_c due to the QSE, but no enhancement of T_c has been observed yet. Here we collect some data of ultrathin Pb films with thickness under 30 monolayers and show them in Fig. 1.22. *Ex situ* resistivity [77] and magnetic susceptibility measurements [78] reported oscillations in the value of T_c with each atomic layer of Pb films. It was attributed to quantum size effects. When the film thickness was further decreased, a decrease of T_c was observed. In contrast, *in situ* scanning tunneling spectroscopy (STS) investigations on Pb/Si(111) islands reported no significant change in T_c upon thickness reduction to 5 monolayers. [79, 80]. When the thickness of the Pb film is less than 5 ML, quantum-size oscillations of T_c were observed[57, 81, 82]. The T_c for the 3 ML film is very close to its bulk value. However, T_c is much lower when going down to a monolayer [82]. This suppression of T_c was attributed to localization effects resulting from disorder and film defects and the inverse proximity effects to the substrate. Theoretically, a more realistic model for uniform ultra-thin films was developed [85]. It considers the effect of the substrate, imposes the charge neutrality at the interface and uses a finite quasiparticle lifetime to simulate disorder. The results confirm the shape resonance for such ultra-thin films but the enhancement of T_c above its bulk value is suppressed.

QSE is also predicted to play an important role in superconducting nanowires. As shown in the right panel in Fig. 1.21, the oscillations in T_c show complex and irregular patterns. These patterns are related to the geometry and size of the cross-section [67]. Experimentally, the T_c in most of the elemental superconducting nanowires does not change as the wire diameter is reduced from 100 to 20 nm. Below a wire diameter of 20 nm, phase slips often play an important role. It results in the presence of resistive tails and finite resistances below T_c in transport measurements.

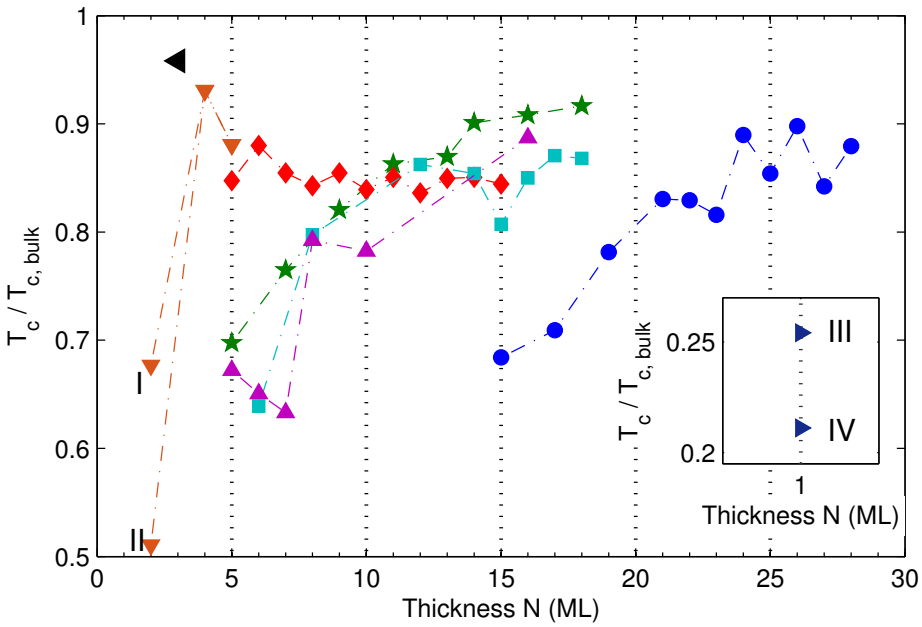

Figure 1.22: Experimental data on the thickness dependence of the critical temperature T_c of Pb nanofilms on Si(111) from different experiments: • is the *Ex situ* data from Ref. [77], ★ is the *Ex situ* magnetic susceptibility data from Ref. [78], ♦ is the *In situ* STS data from Ref. [79], ■ is the *In situ* STS data on Pb/Si(7 × 7) from Ref. [80], ▲ is the *In situ* STS data on Pb/Si($\sqrt{3} \times \sqrt{3}$) from Ref. [80], and ▼ is the *In situ* STS data from Ref. [81]. Note that two different kinds of films result in two different T_c values at $N = 2$ ML. The type I has an 1×1 atomic structure and the type II has an $\sqrt{3} \times \sqrt{3}$ atomic structure. ◀ is the *In situ* STS data from Ref. [57], and ▶ is the *In situ* STS data from Ref. [82]. Note that two different kinds of films result in two different T_c values. The type III is the striped incommensurate (SIC) phase and the type IV is $\sqrt{7} \times \sqrt{3}$-Pb phase. T_c for bulk is $T_{c,bulk} = 7.2$ K. The original figure was made by *Chen et al* [83]

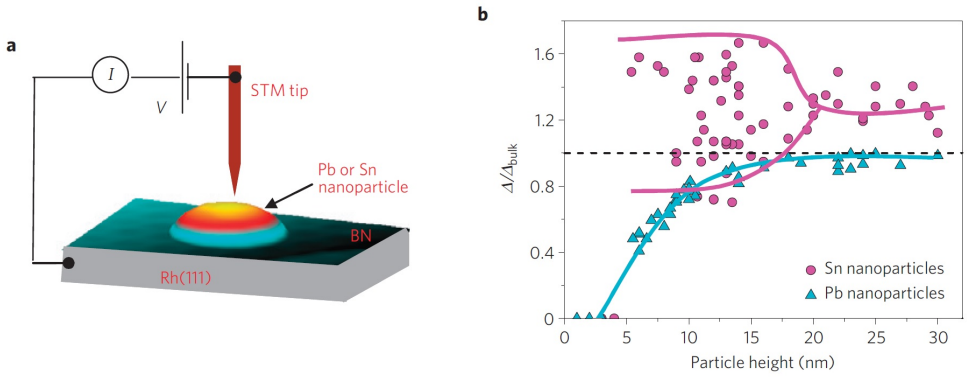

Figure 1.23: Experimental configuration and low-temperature superconducting properties of single, isolated Pb and Sn nanoparticles: observation of shell effects. Taken from [86]

The QSE and the shell effect have been observed in many 0D superconducting nano-particles [87]. For example, elemental superconducting nanoparticles such as Al, Sn, In, Ga showed an increase in T_c with reduction in the particle size[88, 89]. However, Pb showed no change in T_c even down to a particle size of 10 nm[90]. At the same time, there was a substantial drop in the Meissner signal [90]. Later, Li et al showed that In nano-particles exhibit a non-monotonic variation in T_c as a function of particle size while Pb showed a sharp decrease in T_c below 10 nm [87, 91]. Recently, Scanning tunneling spectroscopy (STS) measurements were performed on *in situ* grown single, isolated hemispherical Sn and Pb nanoparticles [86]. The observed oscillations in the superconducting energy gap with particle size confirmed the presence of shell effects in small particles. Moreover, in these experiments an accurate determination of the size and shape of the nanoparticle is possible so that the quantitative comparison of the theoretical results of the superconducting properties with particle size is also possible. As a result, it was found that the variation of T_c with particle size does not appear to follow a general rule. Many factors have been discussed in the literature to understand the mechanisms influencing the evolution of T_c with particle size. They are mostly due to phonon softening, substrate effects and inverse proximity effects.

With the numerous experiments performed on nanoscale superconduc-

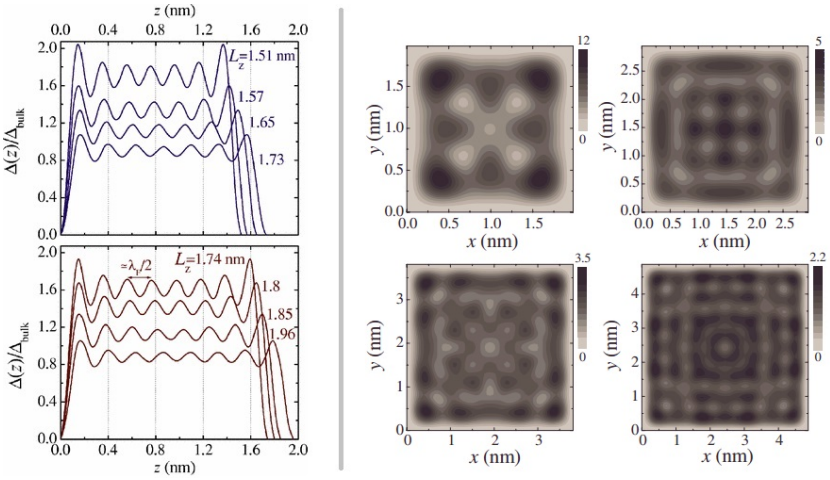

Figure 1.24: Inhomogeneous spatial superconducting order parameter due to the quantum confinement effect. (left) spatial distribution of the superconducting order parameter $\Delta(z)$ in a film of various thicknesses L_z. Taken from [92]. (right) contour plots of $\Delta(x, y)$ (meV) in a nanowire with square cross section of various length $L_x = 1.98$, 2.95, 3.81, and 4.87 nm. Taken from [67].

tors, many theoretical works were also performed to investigate the QSE on low dimensional superconductivity. By numerically solving the Bogoliubov-de Gennes equations, Shanenko et al predicted interesting shape resonance effects in nanowires (see Fig. 1.21), which postulate huge oscillations in the T_c with small changes in the nano-wire diameter. In addition, multiband-like electronic structures were predicted in nanoscale films and nanowires due to quantum confinement effects [93], which further induces strip-like inhomogeneous spatial superconducting order parameter [67, 92], the new Andreev-type states [94] and a cascade structure of the superconductor-to-normal transition driven by a magnetic field or supercurrent [95]. Shell effects, which are the analogue of shape resonance effects in superconducting nanoparticles, were predicted with the use of the Richardson formalism[96, 97] and a semi-classical analytical description [98]. A similar description was later employed in [99] to estimate finite size effects on the energy gap as a function of the particle geometry.

1.4.3 Surface effect

The surface effect is important for small particles due to the increase in the ratio of the surface to volume. The surface atoms have a lower coordination number than the atoms in the bulk of the particle. This makes the frequency of the surface phonons lower than those of the bulk phonons. This phenomenon is called **phonon softening**. It has been theoretically studied by Dickey and Paskin using molecular dynamic simulations [100] and predicts a stronger electron-phonon coupling constant g with decreasing particle size [89].

Experimentally, an increase in T_c has been reported for weak coupling superconductors such as Al, Sn, Ga and In. Abeles et al[88] observed an increase in g with decreasing particle size for Al particles. Hence, the increase in T_c in these Al particles is believed to be due to phonon softening. However, in strong coupling superconductors such as Pb, this effect can be offset by an increase in the phonon frequency cut off resulting from a quantization of the phonon wave vector. Fenton and Leavens[101] worked out the Eliashberg theory for Pb nano-particles with diameter around 5 nm. They showed that there is a significant increase in Δ but T_c does not change appreciably so that the factor $2\Delta/k_BT_c$ increases. Hence, it should be noted that whenever surface effects dominate in small superconducting particles, any change in T_c will be accompanied by a similar changes in the ratio $2\Delta/k_BT_c$ [63].

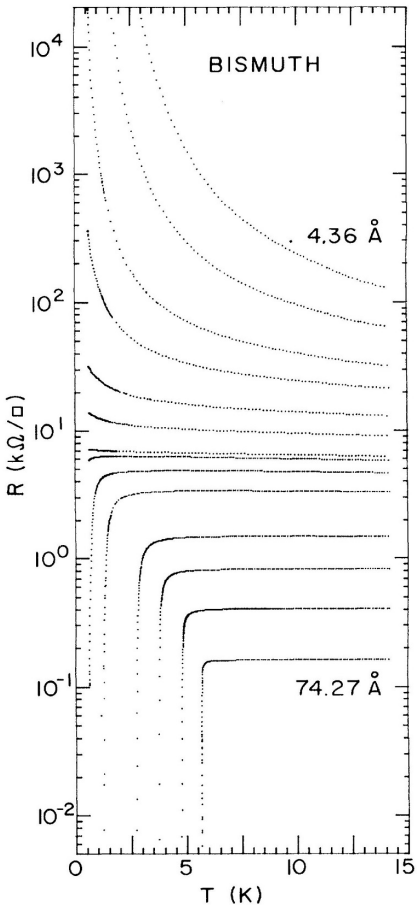

Figure 1.25: Evolution of the temperature dependence of the sheet resistance $R(T)$ with thickness for a Bi film. Film thicknesses are shown for a range from 4.36 to 74.27 nm. Taken from [102]

1.4.4 Fluctuations in low-dimensional superconductivity

Superconducting fluctuations often play an important role in experiments on low-dimensional superconductors. Near absolute zero, quantum fluctuations appear and usually depend on the disorder level of the sample. As the temperature increases, thermal fluctuations becomes more important. In the following we briefly introduce the fluctuations effect in nanofilms (2D superconductivity), nanowires (1D) and nanoparticles (0D).

In a disordered nanofilm, resistance strongly depends on the film thickness. As shown in Fig. 1.25, there exits a critical thickness below which systems show finite resistances even near absolute zero. This is the **superconductor-insulator transition**, which is also known to be a quantum

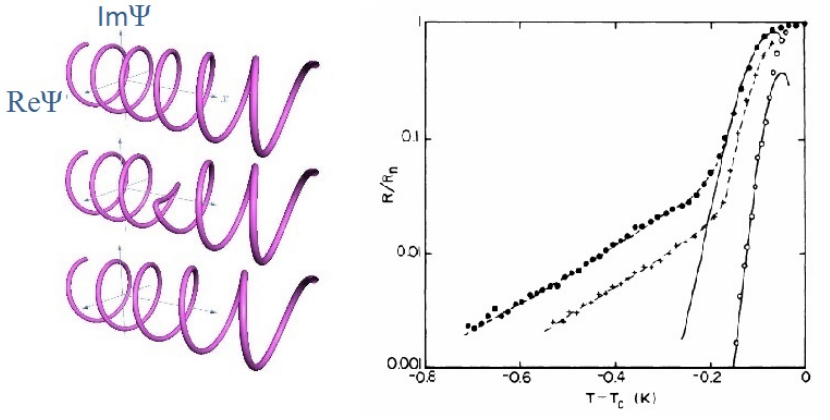

Figure 1.26: (a) The chronology of a phase slip event in a nanowire. During the phase slip event, the total phase difference between the two ends changes from 12π in the top panel to 10π in the bottom panel as a result of a single phase slip event shown in the middle curve. Taken from [103]. (b) Resistance vs temperature for three In nanowires. The sample diameters were 410 Å (•), 505 Å (+) and 720 Å (o). Taken from [104]

phase transition. In 2D superconductivity such as for nanofilms, the existence of true long-range order of Cooper pairs is not possible due to phase fluctuations. As a result, a 2D nanofilm goes through a phase transition (Kosterlitz-Thouless transition) from a superconducting state to an insulating state at low temperatures.

In a 1D superconducting nanowire with wire diameter smaller than the superconducting coherence length, fluctuation effects often result in phase slips leading to a loss of superconductivity. The mechanism of the phase slip is shown in Fig. 1.26(a). Before the phase slip event, there are 6 helical turns along the length of a wire such that the total phase difference is $\Delta\phi = 12\pi$. During the phase slip, the order parameter Ψ goes to zero at some point causing the phase to slip by 2π. After the phase slip event, one helical turn is subtracted so that the total phase difference is $\Delta\phi = 10\pi$. So, in a phase slip event, the system essentially goes from a superconducting state with some value of $\Delta\phi$ to a superconducting state with a value of $\Delta\phi$ different from the previous value by 2π [105]. Mathematically, this can be understood using the Josephson effect where the voltage across the system is given by $V = d(\Delta\phi)/dt$. Fig. 1.26(b) shows the resistance of In nanowires as a function

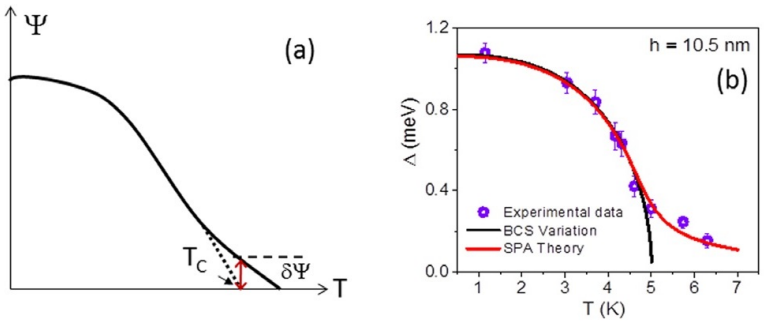

Figure 1.27: (a) Schematic representation of the fluctuation in the superconducting order parameter close to T_c. (b) Effect of thermal fluctuations on the superconducting energy gap in nanoparticles of Pb as measured by STM. Taken from [63]

of temperature T. When $T < T_c$, it shows a tail of finite resistance. The influence is enhanced with decreasing wire diameter. For typical materials with diameter $5 - 10$ nm, phase slips result in a finite resistance in the superconducting normal state even at $T = 0$.

In a 0D superconducting nanoparticle, thermal fluctuations tend to smear out the superconducting phase transition in the zero magnetic field, leading to a fluctuation-induced 'critical region' near T_c [6, 63]. Fig. 1.27(a) shows the schematic 'critical region' of the superconducting order parameter near T_c. Experimentally, the 'critical' region can be measured by using STS. As shown in Figs. 1.27(b), isolated Pb nanoparticles smaller than 13 nm were found to exhibit a 'critical' region well beyond the mean field T_c, in which thermodynamic fluctuations lead to a finite energy gap [106]. The fluctuation dominated region extends to as high as $1.4T_c$. The mean-field BCS theory fails to describe the 'critical' region but the static path approximation (SPA) can fit it well.

In conclusion, fluctuation effects often change the superconducting properties of low-dimensional systems and make the mean-field BCS theory invalid. However, throughout the thesis we study nanoscale superconductivity by using the mean-field theory. Therefore, our results are only valid when fluctuations are not significant. For example, fluctuations are mostly suppressed at near absolute zero, for samples in the clean limit and for small ξ (of the order of λ_F).

1.5 Scanning tunneling microscope (STM)

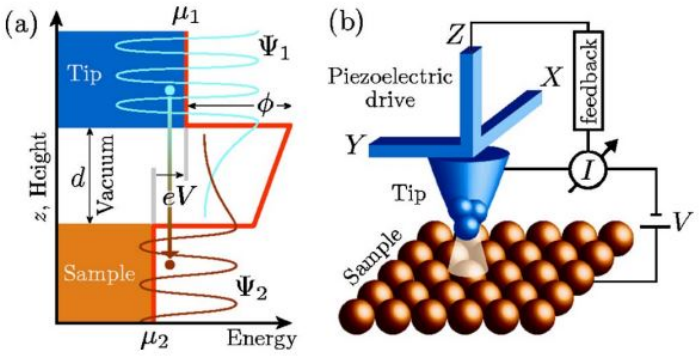

Figure 1.28: Principle of STM. (a) Tunneling process between the tip and the sample across a vacuum barrier of width d. The electron wave function Ψ decays exponentially into vacuum with a small overlap, allowing electrons to tunnel from one electrode to the other. With a positive bias voltage V applied to the sample, electrons tunnel preferentially from the tip into unoccupied sample states. (b) Schematic view of the scanning tunneling microscope. Taken from [107].

A STM is an instrument for imaging surfaces and their electronic properties at the atomic scale. It was developed in 1981 by Gerd Binnig and Heinrich Rohrer (at IBM Zürich). Since the resolution can be down to 0.1 nm, it is one of the most powerful experimental techniques for the investigation of nanoscale materials.

The principle of the STM is shown in Fig. 1.28. It is based on the quantum tunneling effect. When a tip is very close to the surface and a bias voltage is applied between them, a tunneling current is caused to flow. The tunneling current is a function of the distance between the tip and the sample, bias voltage, and the local density of states (LDOS) of the sample and the tip [108]. Using Bardeen's transfer Hamiltonian formalism, the tunneling current I under the bias voltage V is found to be [109, 110]

$$I(V) = \frac{4\pi e}{\hbar} \int_0^{eV} [f(E-eV) - f(E)] N_T(E-eV) N_S(E) T(E, eV) dE, \quad (1.61)$$

where $f(E)$ is the Fermi distribution function, N_T and N_S are the DOS in the tip and sample, respectively, and T is the tunneling matrix element. $N_T(E)$

is a *constant* in many surfaces of simple metals near the Fermi energy E_F. For low temperatures and a constant tunneling matrix element, the tunneling current reduces to

$$I \propto \int_0^{eV} N_S(E - eV)dE. \tag{1.62}$$

Thus, the tunneling conductance dI/dV determines the energy dependence of DOS at the tip's position:

$$dI/dV \propto N_S(-eV) \quad \text{or} \quad dI/dV \propto N_S(E_F - eV), \tag{1.63}$$

since the zero-bias voltage corresponds to the Fermi level.

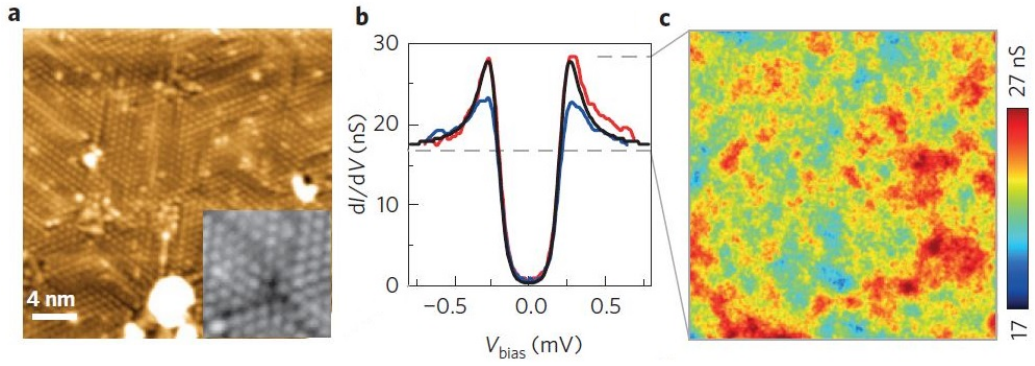

Figure 1.29: (a) STM topographic images of one-atomic-layer films of Pb on Si(111). Insets show the atomic resolution. (b) local tunnelling conductance spectra at $T = 320$ mK for various positions. (c) Corresponding conductance maps at bias energy of the quasiparticle peaks in the tunnelling spectra (b). Taken from [111].

When the tip is scanned over the sample surface while the tunneling current is kept as a constant, the tip height follows a contour of constant local density of states and provides information on the topography of the sample surface. For example, a STM topographic images of one-atomic-layer films of Pb on Si(111) is shown in Fig. 1.29(a). When voltage is swept at a given location, information on the electronic structure can be obtained [108]. This type of measurement is called scanning tunneling spectroscopy (STS). It results in the LDOS as a function of the bias energy. For example, local tunnelling conductance spectra for various positions and a conductance map at a certain bias voltage are shown in Fig. 1.29(b) and (c), respectively. The

advantage of STM make the measurements extremely local. For example, the density of states at an impurity site can be compared to the density of states far from impurities [112].

In conclusion, STM is one of the most powerful experimental instruments for studying nanoscale superconductivity and it is widely used to obtain topographic images and measure the LDOS. Throughout the thesis, the theoretically obtained LDOS can be directly measured on nanoscale samples by using the STM.

1.6 Organization and contribution of the thesis

As mentioned previously, nanoscale superconductivity exhibits richer phenomena than bulk superconductivity. In nanoscale superconductors, the quantum confinement effect plays an important role. This will allow us to artificially design the electronic properties by changing its size, geometry and structure of the superconductor, leading to the control and enhancement of superconductivity. It provides us with a great potential for applications in ultrafast, power-saving electronic devices such as superconducting transistors and single-photon detectors. However, the interplay between superconductivity and quantum confinement has not been fully understood yet. The recent experimental realization of high-quality metallic superconducting nanofilms and nanowires confirmed the quantum size effect, which makes this theoretical study very timely.

In this thesis, we study several aspects of nanoscale superconductivity. The topics that are covered range from vortex states under the influence of quantum confinement effect to the electronic structure in different nanostructures. The density of states obtained in this thesis can be compared with results from STM/STS experiments, which is one of the most powerful tools for studying nanoscale superconductors nowadays. The approach used in this thesis is the Bogoliubov de-Gennes (BdG) formalism and it is solved numerically and totally self-consistent. Since the BdG formalism is a generalization of the BCS theory, the properties presented in this thesis are reliable for conventional superconductors. However, the BCS theory is a mean-field theory, which neglects fluctuation effects. Thus, our results can not directly be applied to the cases where fluctuations are important. In

such cases, our results can be considered as the first-order approximation and further improvements have to be made. In summary, our results are valid for clean metallic superconductors near absolute zero where fluctuations are suppressed.

Next we show the organization of this thesis.

In **Chapter 1**, we first present the background of superconductivity including historical aspects, fundamental properties and theories (the microscopic BCS theory and the phenomenological GL theory). Next, the vortex states in mesoscopic superconductors and the recent progresses on nanoscale superconductivity are introduced. The most important experimental tools, STM/STS are been described.

In **Chapter 2**, we give a brief introduction of the Bogoliubov de-Gennes formalism, which is used throughout the thesis. Then, two examples are presented in order to show the numerical approach in detail. The first one is the simplest and the well-known homogeneous system. The second one is the electronic structure around an isolated vortex. These results are helpful for the understanding of the results presented in the following chapters.

In **Chapter 3**, we study vortex states under the influence of quantum confinement effect in nanoscale superconductors. Previous works have shown already that vortex matter in mesoscopic superconductors is strongly affected by the geometry of the sample. Here, we show that nanoscale superconductors with coherence length comparable to the Fermi wavelength the shape resonances of the order parameter results in an additional contribution to quantum topological confinement - leading to **unconventional vortex configurations**. Our results for a square geometry reveal a plethora of asymmetric, giant multi-vortex, and vortex-antivortex structures, stable over a wide range of parameters and which are very different from those predicted by the Ginzburg-Landau theory. These unconventional states are relevant for high-T_c nanograins, confined Bose-Einstein condensates, and graphene flakes with proximity-induced superconductivity.

In **Chapter 4**, we expand the previous study from Chapter 3, systematically to larger systems, larger Fermi wavelengths and finite temperatures. The parameter space is scanned in order to study the emergence of exotic vortex states due to oscillations of the order parameter. In this chapter, we show that several unconventional vortex states, including asymmetric ones, giant multi-vortex combinations, and states comprising a giant antivortex, were found as ground states and their stability was found to be very sensitive on the value of $k_F\xi_0$, the size of the sample W, and the magnetic

flux Φ. By increasing the temperature and/or enlarging the size of the sample, quantum confinement is suppressed and conventional mesoscopic vortex states as predicted by the Ginzburg-Laudau theory are recovered. However, contrary to the GL results we found that the states containing symmetry-induced vortex-antivortex pairs are stable over the whole temperature range. It turns out that the inhomogeneous order parameter induced by quantum confinement favors vortex-antivortex molecules, as well as giant vortices with a rich structure in the vortex core.

In **Chapter 5**, we study the effect of non-magnetic impurities on the local density of states and the transport properties in superconducting nanowires. Such impurities have very little effect on the bulk properties of conventional superconductors. However, as the dimensionality is reduced, the effect of impurities becomes more significant. In this chapter, we investigate superconducting nanowires with diameter comparable to the Fermi wavelength λ_F (which is less than the superconducting coherence length). We find that: 1) impurities strongly affect the superconducting properties, 2) the effect is impurity position-dependent, and 3) it exhibits opposite behavior for resonant and off-resonant wire widths. We show that this is due to the interplay between the shape resonances of the order parameter and the sub-band energy spectrum induced by lateral quantum confinement. These effects can be used to manipulate the Josephson current, filter electrons by subband and investigate the symmetries of the superconducting subband gaps.

In **Chapter 6**, we study the Tomasch effect (TE) in nanoscale superconductors. The Tomasch effect (TE) is due to quasiparticle interference (QPI) as induced by a nonuniform superconducting order parameter, which results in oscillations in the density of states (DOS) at energies above the superconducting gap. Quantum confinement in nanoscale superconductors leads to an inhomogeneous distribution of the Cooper-pair condensate, which, as we found, triggers the manifestation of a new TE. We investigate the electronic structure of nanoscale superconductors and describe the TE determined by two types of processes, involving two- or three- subband QPIs. Both types of QPIs result in additional BCS-like Bogoliubov-quasiparticles and BCS-like energy gaps leading to oscillations in the DOS and modulated wave patterns in the local density of states. These effects are strongly related to the symmetries of the system. A reduced 4×4 inter-subband BdG Hamiltonian is established in order to describe analytically the TE of two-subband QPIs.

Finally we conclude the thesis in **Chapter 7** and present an outlook for future studies.

Chapter 2

Theoretical approach

2.1 The Bogoliubov-de Gennes (BdG) equations

2.1.1 The derivation

In this section, we show how to obtain the BdG equations from the BCS theory. The starting point of the derivation is to define the creation and annihilation operators Ψ and $\Psi^\dagger$, respectively, in real space:

$$\begin{array}{r} \Psi(\mathbf{r}\sigma) = \sum_{\mathbf{k}} e^{i\mathbf{k}\cdot\mathbf{r}} c_{\mathbf{k}\sigma} \\ \Psi^\dagger(\mathbf{r}\sigma) = \sum_{\mathbf{k}} e^{-i\mathbf{k}\cdot\mathbf{r}} c^\dagger_{\mathbf{k}\sigma} \end{array} . \tag{2.1}$$

Here $c_{\mathbf{k}\sigma}$ and $c^\dagger_{\mathbf{k}\sigma}$ are the creation and annihilation operators defined in momentum space in the BCS theory where $\sigma =\uparrow$ or $\downarrow$ is the spin index. $\Psi(\mathbf{r}\sigma)$ ($\Psi^\dagger(\mathbf{r}\sigma)$) creates (removes) an electrons with spin σ from position $\mathbf{r}$. Assuming a point-like attractive interaction in real space (s-wave coupling) with strength $V > 0$, the Hamiltonian $\hat{H}$ can be written as

$$\begin{aligned} \hat{H} &= \hat{H}_0 + \hat{H}_1 \\ \hat{H}_0 &= \int d\mathbf{r} \sum_\sigma \Psi^\dagger(\mathbf{r}\sigma) \Big[\frac{\hat{\mathbf{p}}^2}{2m_e} + U_0(\mathbf{r}) \Big] \Psi(\mathbf{r}\sigma), \\ \hat{H}_1 &= -\frac{1}{2} V \int d\mathbf{r} \sum_{\sigma\sigma'} \Psi^\dagger(\mathbf{r}\sigma) \Psi^\dagger(\mathbf{r}\sigma') \Psi(\mathbf{r}\sigma') \Psi(\mathbf{r}\sigma), \end{aligned} \tag{2.2}$$

where $\hat{\mathbf{p}}$ is the momentum operator. $\hat{H}_0$ above represents a sum of the single-particle kinetic and potential energies. $U_0(\mathbf{r})$ incorporates crystal potentials and external potentials such as impurities and disorder. $\hat{H}_1$ presents the effective electron-electron interaction between Cooper pairs.

To simplify the theory, an effective *mean-field* Hamiltonian is introduced [34]:

$$\hat{H}_{eff} = \int d\mathbf{r}\Big[\Psi^\dagger(\mathbf{r}\sigma)\hat{H}_e\Psi(\mathbf{r}\sigma) + U(\mathbf{r})\Psi^\dagger(\mathbf{r}\sigma)\Psi(\mathbf{r}\sigma) + \Delta(\mathbf{r})\Psi^\dagger(\mathbf{r}\uparrow)\Psi^\dagger(\mathbf{r}\downarrow) + \Delta^*(\mathbf{r})\Psi(\mathbf{r}\downarrow)\Psi(\mathbf{r}\uparrow) + W(\mathbf{r})\Big], \quad (2.3)$$

with

$$\hat{H}_e = \frac{\hat{\mathbf{p}}^2}{2m_e} + U_0(\mathbf{r}) - E_F, \quad (2.4)$$

where E_F is the Fermi energy as in the BCS theory. $U(\mathbf{r})$ is the Hartree-Fock potential resulting from the pairing interaction. The two terms containing $\Delta(\mathbf{r})$ in Eq. (2.3) represents Cooper-pair scattering. It is worth noting that both of these terms change the number of particles by two. $\Delta(\mathbf{r})$ is the superconducting order parameter which depends on the position $\mathbf{r}$. The last term, $W(\mathbf{r})$, does not depend on the fields Ψ and $\Psi^\dagger$.

Since the effective Hamiltonian $\hat{H}_{eff}$ is quadratic in Ψ and $\Psi^\dagger$, we can diagonalize it into

$$\hat{H}_{eff} = E_g + \sum_{n,\sigma} E_n \gamma^\dagger_{n\sigma}\gamma_{n\sigma}, \quad (2.5)$$

where E_g is the ground state energy, $\gamma^\dagger_{n\sigma}$ and $\gamma_{n\sigma}$ are the creation and annihilation operators of quasiparticles with quantum number n and spin σ, and E_n is the energy eigenvalue of the quasiparticle excitation. The diagonalization is achieved by performing a unitary transformation,

$$\begin{aligned}\Psi^\dagger(\mathbf{r}\uparrow) &= \sum_n \Big(u^*_n\gamma^\dagger_{n\uparrow} - v_n\gamma_{n\downarrow}\Big),\\ \Psi(\mathbf{r}\downarrow) &= \sum_n \Big(v^*_n\gamma^\dagger_{n\uparrow} + u_n\gamma_{n\downarrow}\Big),\end{aligned} \quad (2.6)$$

where u_n and v_n, in analogy to Eq. (1.39), are the amplitudes of the electron and hole parts of the quasiparticle with quantum number n, respectively. The $\gamma_{n\sigma}$ and $\gamma^\dagger_{n\sigma}$ here still satisfy the fermion anti-commutation relations,

similarly to Eq. (1.41). Using Eq. (2.5) and the anti-commutation relations for $\gamma_{n\sigma}$ and $\gamma^{\dagger}_{n\sigma}$, we can write:

$$\begin{aligned}[\hat{H}_{eff}, \gamma_{n\sigma}] &= -E_n \gamma_{n\sigma}, \\ [\hat{H}_{eff}, \gamma^{\dagger}_{n\sigma}] &= E_n \gamma^{\dagger}_{n\sigma},\end{aligned} \tag{2.7}$$

and

$$\begin{aligned}[\Psi(\mathbf{r}\uparrow), \hat{H}_{eff}] &= [\hat{H}_e + U(\mathbf{r})]\Psi(\mathbf{r}\uparrow) + \Delta(\mathbf{r})\Psi^{\dagger}(\mathbf{r}\downarrow), \\ [\Psi(\mathbf{r}\downarrow), \hat{H}_{eff}] &= [\hat{H}_e + U(\mathbf{r})]\Psi(\mathbf{r}\downarrow) - \Delta^{*}(\mathbf{r})\Psi^{\dagger}(\mathbf{r}\uparrow).\end{aligned} \tag{2.8}$$

From Eqs. (2.6-2.8), we obtain the BdG equations:

$$\begin{bmatrix} \hat{H}_e + U(\mathbf{r}) & \Delta(\mathbf{r}) \\ \Delta^{*}(\mathbf{r}) & -[\hat{H}^{*}_e + U(\mathbf{r})] \end{bmatrix} \begin{bmatrix} u_n(\mathbf{r}) \\ v_n(\mathbf{r}) \end{bmatrix} = E_n \begin{bmatrix} u_n(\mathbf{r}) \\ v_n(\mathbf{r}) \end{bmatrix}. \tag{2.9}$$

Note that they are Schrödinger-like equations for the electron and hole amplitudes, u and v of a quasiparticle which are coupled by the pairing potential $\Delta(\mathbf{r})$. It is important to know that $\Delta(\mathbf{k})$ in the BCS theory is different from the $\Delta(\mathbf{r})$ in the BdG equations. $\Delta(\mathbf{k})$ is the energy gap to create a quasiparticle excitation in state $\mathbf{k}$ but $\Delta(\mathbf{r})$ is the spatial dependent superconducting order parameter.

The BdG equations (2.9) have a very important property: if $(u_n,\ v_n)^T$ is the solution for the eigen-energy E_n, $(-v^{*}_n,\ u_n)^T$ is the solution for the eigen-energy $-E_n$. By taking this property, the calculation time cost can be cut almost by half in most of the situations.

2.1.2 The self-consistency condition

We now determine the Hartree-Fock potential $U(\mathbf{r})$ and the pairing potential $\Delta(\mathbf{r})$ in Eq. (2.9). The idea is to choose $U(\mathbf{r})$ and $\Delta(\mathbf{r})$ so that the average $\langle H_{eff}\rangle$ of the effective Hamiltonian has a local minimum for the same states as the average of the true Hamiltonian $\langle H\rangle$.

First we write

$$\begin{aligned}\langle H\rangle = &\int d\mathbf{r} \sum_{\sigma} \left\langle \Psi^{\dagger}(\mathbf{r}\sigma)\hat{H}_e\Psi(\mathbf{r}\sigma)\right\rangle \\ &- \frac{V}{2}\int d\mathbf{r} \sum_{\sigma\sigma'} \left\langle \Psi^{\dagger}(\mathbf{r}\sigma)\Psi^{\dagger}(\mathbf{r}\sigma')\Psi(\mathbf{r}\sigma')\Psi(\mathbf{r}\sigma)\right\rangle.\end{aligned} \tag{2.10}$$

By making use of Wick's theorem

$$\begin{aligned}\langle \Psi_1^\dagger \Psi_2^\dagger \Psi_3 \Psi_4 \rangle = \langle \Psi_1^\dagger \Psi_2^\dagger \rangle \langle \Psi_3 \Psi_4 \rangle \\ + \langle \Psi_1^\dagger \Psi_4 \rangle \langle \Psi_2^\dagger \Psi_3 \rangle - \langle \Psi_1^\dagger \Psi_3 \rangle \langle \Psi_2^\dagger \Psi_4 \rangle,\end{aligned} \tag{2.11}$$

the product $\langle \Psi^\dagger \Psi^\dagger \Psi \Psi \rangle$ from Eq. (2.10) can be simplified into

$$\begin{aligned}\sum_{\sigma\sigma'} \big\langle \Psi^\dagger(\mathbf{r}\sigma)\Psi^\dagger(\mathbf{r}\sigma')\Psi(\mathbf{r}\sigma')\Psi(\mathbf{r}\sigma)\big\rangle &= \big\langle \Psi^\dagger(\mathbf{r}\uparrow)\Psi^\dagger(\mathbf{r}\downarrow)\big\rangle\big\langle \Psi(\mathbf{r}\downarrow)\Psi(\mathbf{r}\uparrow)\big\rangle \\ &+ \big\langle \Psi^\dagger(\mathbf{r}\downarrow)\Psi^\dagger(\mathbf{r}\uparrow)\big\rangle\big\langle \Psi(\mathbf{r}\uparrow)\Psi(\mathbf{r}\downarrow)\big\rangle \\ &+ \sum_{\sigma\sigma'} \big\langle \Psi^\dagger(\mathbf{r}\sigma)\Psi(\mathbf{r}\sigma)\big\rangle\big\langle \Psi^\dagger(\mathbf{r}\sigma')\Psi(\mathbf{r}\sigma')\big\rangle \\ &- \sum_{\sigma\sigma'} \big\langle \Psi^\dagger(\mathbf{r}\sigma)\Psi(\mathbf{r}\sigma')\big\rangle\big\langle \Psi^\dagger(\mathbf{r}\sigma')\Psi(\mathbf{r}\sigma)\big\rangle.\end{aligned} \tag{2.12}$$

Considering Cooper pairing, we have

$$\big\langle \Psi^\dagger(\mathbf{r}\uparrow)\Psi^\dagger(\mathbf{r}\downarrow)\big\rangle \neq 0 \text{ and } \big\langle \Psi(\mathbf{r}\downarrow)\Psi(\mathbf{r}\uparrow)\big\rangle \neq 0.$$

In the singlet state pairing only occurs for particles with opposite spins, and thus we have

$$\big\langle \Psi^\dagger(\mathbf{r}\uparrow)\Psi^\dagger(\mathbf{r}\uparrow)\big\rangle = 0 \text{ and } \big\langle \Psi(\mathbf{r}\downarrow)\Psi(\mathbf{r}\downarrow)\big\rangle = 0.$$

Assuming that there is no magnetic interaction, we have

$$\big\langle \Psi^\dagger(\mathbf{r}\uparrow)\Psi(\mathbf{r}\downarrow)\big\rangle = 0 \text{ and } \big\langle \Psi^\dagger(\mathbf{r}\downarrow)\Psi(\mathbf{r}\uparrow)\big\rangle = 0.$$

Finally, we obtain

$$\begin{aligned}\sum_{\sigma\sigma'} \big\langle \Psi^\dagger(\mathbf{r}\sigma)\Psi^\dagger(\mathbf{r}\sigma')\Psi(\mathbf{r}\sigma')\Psi(\mathbf{r}\sigma)\big\rangle &= 2\big\langle \Psi^\dagger(\mathbf{r}\uparrow)\Psi^\dagger(\mathbf{r}\downarrow)\big\rangle\big\langle \Psi(\mathbf{r}\downarrow)\Psi(\mathbf{r}\uparrow)\big\rangle \\ &+ 2\big\langle \Psi^\dagger(\mathbf{r}\uparrow)\Psi(\mathbf{r}\uparrow)\big\rangle\big\langle \Psi^\dagger(\mathbf{r}\downarrow)\Psi(\mathbf{r}\downarrow)\big\rangle.\end{aligned} \tag{2.13}$$

The variation of the true energy becomes

$$\begin{aligned}\delta\langle H\rangle = &\int d\mathbf{r}\sum_{\sigma}\delta\Big\langle\Psi^{\dagger}(\mathbf{r}\sigma)\hat{H}_e\Psi(\mathbf{r}\sigma)\Big\rangle\\ &- V\int d\mathbf{r}\Big[\big(\delta\langle\Psi^{\dagger}(\mathbf{r}\uparrow)\Psi^{\dagger}(\mathbf{r}\downarrow)\rangle\big)\big\langle\Psi(\mathbf{r}\downarrow)\Psi(\mathbf{r}\uparrow)\big\rangle\\ &+\big\langle\Psi^{\dagger}(\mathbf{r}\uparrow)\Psi^{\dagger}(\mathbf{r}\downarrow)\big\rangle\big(\delta\langle\Psi(\mathbf{r}\downarrow)\Psi(\mathbf{r}\uparrow)\rangle\big)\Big]\\ &- V\int d\mathbf{r}\Big[\big(\delta\langle\Psi^{\dagger}(\mathbf{r}\uparrow)\Psi(\mathbf{r}\uparrow)\rangle\big)\big\langle\Psi^{\dagger}(\mathbf{r}\downarrow)\Psi(\mathbf{r}\downarrow)\big\rangle\\ &+\big\langle\Psi^{\dagger}(\mathbf{r}\uparrow)\Psi(\mathbf{r}\uparrow)\big\rangle\big(\delta\langle\Psi^{\dagger}(\mathbf{r}\downarrow)\Psi(\mathbf{r}\downarrow).\end{aligned} \tag{2.14}$$

The variation of the effective energy with respect to variations of Ψ:

$$\begin{aligned}\delta\langle H_{eff}\rangle = &\int d\mathbf{r}\sum_{\sigma}\delta\Big\langle\Psi^{\dagger}(\mathbf{r}\sigma)[\hat{H}_e+U(\mathbf{r})]\Psi(\mathbf{r}\sigma)\Big\rangle\\ &+\int d\mathbf{r}\Big[\Delta(\mathbf{r})\delta\langle\Psi^{\dagger}(\mathbf{r}\uparrow)\Psi^{\dagger}(\mathbf{r}\downarrow)\rangle+\Delta^{*}(\mathbf{r})\delta\langle\Psi(\mathbf{r}\downarrow)\Psi(\mathbf{r}\uparrow)\rangle\Big].\end{aligned} \tag{2.15}$$

Comparing Eqs. (2.14) and (2.15), we find that

$$U(\mathbf{r}) = -V\langle\Psi^{\dagger}(\mathbf{r}\uparrow)\Psi(\mathbf{r}\uparrow)\rangle = -V\langle\Psi^{\dagger}(\mathbf{r}\downarrow)\Psi(\mathbf{r}\downarrow)\rangle \tag{2.16}$$

and

$$\begin{aligned}\Delta(\mathbf{r}) &= -V\langle\Psi(\mathbf{r}\downarrow)\Psi(\mathbf{r}\uparrow)\rangle = V\langle\Psi(\mathbf{r}\uparrow)\Psi(\mathbf{r}\downarrow)\rangle,\\ \Delta^{*}(\mathbf{r}) &= -V\langle\Psi^{\dagger}(\mathbf{r}\uparrow)\Psi^{\dagger}(\mathbf{r}\downarrow)\rangle = V\langle\Psi^{\dagger}(\mathbf{r}\downarrow)\Psi^{\dagger}(\mathbf{r}\uparrow)\rangle.\end{aligned} \tag{2.17}$$

By using the averages of the fermion quasiparticles:

$$\begin{aligned}\langle\gamma^{\dagger}_{n\sigma}\gamma_{n'\sigma'}\rangle &= \delta_{nn'}\delta_{\sigma\sigma'}f_n,\\ \langle\gamma_{n\sigma}\gamma^{\dagger}_{n'\sigma'}\rangle &= \delta_{nn'}\delta_{\sigma\sigma'}(1-f_n),\\ \langle\gamma_{n\sigma}\gamma_{n'\sigma'}\rangle &= \langle\gamma^{\dagger}_{n\sigma}\gamma^{\dagger}_{n'\sigma'}\rangle = 0,\end{aligned} \tag{2.18}$$

with Fermi-Dirac distribution function $f_n = f(E_n) = [1+\exp(E_n/k_BT)]^{-1}$, and replace Ψ with γ, using Eq. (2.6) we can write the Hartree-Fock potential $U(\mathbf{r})$ and the pairing potential $\Delta(\mathbf{r})$ explicitly, i.e.

$$U(\mathbf{r}) = -V\sum_{n}\Big[|u_n(\mathbf{r})|^2 f(E_n)+|v_n(\mathbf{r})|^2(1-f(E_n))\Big], \tag{2.19}$$

$$\Delta(\mathbf{r}) = +V\sum_{0\leqslant E_n\leqslant\hbar\omega_D} u_n(\mathbf{r})v_n^{*}(\mathbf{r})(1-2f(E_n)). \tag{2.20}$$

These two are the self-consistency conditions.

The Hartree-Fock potential U has almost no effect on the properties of superconductivity [113], and therefore we drop this item in the remainder of the thesis. Eq. (2.20) is called the gap equation. The summation in Eq. (2.20) is restricted to states with energy around the Fermi surface E_F within the Debye energy window $\hbar\omega_D$, as in the BCS theory.

Other important quantities are calculated as follows:

- The currrent:

$$\begin{aligned}\mathbf{J}(\mathbf{r}) = \frac{e\hbar}{2mi}\sum_n \Big\{ & u_n^*(\mathbf{r})\big[\nabla - \frac{ie}{\hbar c}\mathbf{A}\big]u_n(\mathbf{r})f_n \\ & + v_n(\mathbf{r})\big[\nabla - \frac{ie}{\hbar c}\mathbf{A}\big]v_n^*(\mathbf{r})(1-f_n) - \text{H.c.}\Big\}.\end{aligned} \tag{2.21}$$

- The electron density:

$$n_e = \frac{2}{\Omega}\int d\mathbf{r}\sum_n [|u_n(\mathbf{r})|^2 f_n + |v_n(\mathbf{r})|^2(1-f_n)], \tag{2.22}$$

  where Ω is the volume of the system.

- The local density of states (LDOS)

$$N(\mathbf{r}, E) = \sum_n [|u_n(\mathbf{r})|^2\delta(E-E_n) + |v_n(\mathbf{r})|^2\delta(E+E_n)], \tag{2.23}$$

  where E is the bias energy and δ is the Dirac delta function.

- The Gibbs free energy:

$$\begin{aligned} G &= \langle H_{eff}\rangle - TS + F_H \\ &= 2\sum_n \big(E_n f_n - E_n\int d\mathbf{r}|v_n|^2\big) + \int d\mathbf{r}\Big[2\Delta(\mathbf{r})\big(\sum_n u_n^* v_n[1-2f_n]\big) \\ &\quad - \big(V\sum_n u_n^* v_n[1-2f_n]\big)\big(\sum_{n'} u_{n'} v_{n'}^*[1-2f_{n'}]\big)\Big] - TS + F_H, \end{aligned} \tag{2.24}$$

  where $S = -2k_B[f_n \ln f_n + (1-f_n)\ln(1-f_n)]$ is the entropy and $F_H = \int d\mathbf{r}[\mathbf{H}(\mathbf{r}) - \mathbf{H}_0(\mathbf{r})]^2/8\pi$ is the magnetic field exclusion energy in the

presence of the applied field $\mathbf{H}_0(\mathbf{r})$. Note that this equation is not only valid for a converged result but is also valid for a result which has not converged yet. The detailed derivation will be shown in the next section.

The procedure of solving the BdG equations consists of three steps: (i) Solve the BdG equation (2.9) with an initial guess for the pairing potential $\Delta(\mathbf{r})$ and obtain the quasi-particle energy E_n, and the wave functions u_n and v_n. (ii) Calculate a new $\Delta(\mathbf{r})$ by inserting the u_n and v_n into the self-consistency condition Eq. (2.20). (iii) Repeat the previous two steps until $\Delta(\mathbf{r})$ converges. After we obtain a converged solution, all other information such as the electronic structure, energy spectrum and the LDOS can be extracted from E_n, u_n and v_n.

2.1.3 The free energy

In this section we show how to obtain the Gibbs free energy shown in Eq. (2.24). We focus on the average effective Hamiltonian $\langle H_{eff}\rangle$. The idea is to set both average Hamiltonians (the effective one and the true one) to be the same, i.e. $\langle H\rangle = \langle H_{eff}\rangle$, after convergence for Δ is reached. First, the average of the true Hamiltonian (2.10), given the pairing potential Δ is:

$$\begin{aligned}\langle H\rangle_\Delta = &\int d\mathbf{r}\sum_\sigma \Big\langle \Psi^\dagger(\mathbf{r}\sigma)\hat{H}_e\Psi(\mathbf{r}\sigma)\Big\rangle_\Delta \\ &- V\int d\mathbf{r}\Big[\big\langle\Psi^\dagger(\mathbf{r}\uparrow)\Psi^\dagger(\mathbf{r}\downarrow)\big\rangle\big\langle\Psi(\mathbf{r}\downarrow)\Psi(\mathbf{r}\uparrow)\big\rangle \\ &+ \big\langle\Psi^\dagger(\mathbf{r}\uparrow)\Psi(\mathbf{r}\uparrow)\big\rangle\big\langle\Psi^\dagger(\mathbf{r}\downarrow)\Psi(\mathbf{r}\downarrow)\big\rangle\Big]_\Delta .\end{aligned} \tag{2.25}$$

Note that Eq. (2.13) has been used in $\langle H\rangle_\Delta$. The last term representing the Hatree-Fock potential $U(\mathbf{r})$ can be incorporated in the single-particle potential in $\langle\Psi^\dagger\hat{H}_e\Psi\rangle$. In what follows we omit it and Eq. (2.25) becomes

$$\begin{aligned}\langle H\rangle_\Delta = &\int d\mathbf{r}\sum_\sigma \Big\langle \Psi^\dagger(\mathbf{r}\sigma)\hat{H}_e\Psi(\mathbf{r}\sigma)\Big\rangle_\Delta \\ &- V\int d\mathbf{r}\Big[\big\langle\Psi^\dagger(\mathbf{r}\uparrow)\Psi^\dagger(\mathbf{r}\downarrow)\big\rangle\big\langle\Psi(\mathbf{r}\downarrow)\Psi(\mathbf{r}\uparrow)\big\rangle\Big]_\Delta .\end{aligned} \tag{2.26}$$

We now estimate the effective one $\langle H_{eff}\rangle$. From Eq. (2.3), we have

$$\begin{aligned}\langle H_{eff}\rangle &= \int d\mathbf{r}\sum_{\sigma}\Big\langle\Psi^{\dagger}(\mathbf{r}\sigma)\hat{H}_{e}\Psi(\mathbf{r}\sigma)\Big\rangle_{\Delta}\\ &+\int d\mathbf{r}\Big[\Delta(\mathbf{r})\langle\Psi^{\dagger}(\mathbf{r}\uparrow)\Psi^{\dagger}(\mathbf{r}\downarrow)\rangle+\Delta^{*}(\mathbf{r})\langle\Psi(\mathbf{r}\downarrow)\Psi(\mathbf{r}\uparrow)\rangle+W(\mathbf{r})\Big]\\ &=\int d\mathbf{r}\sum_{\sigma}\Big\langle\Psi^{\dagger}(\mathbf{r}\sigma)\hat{H}_{e}\Psi(\mathbf{r}\sigma)\Big\rangle_{\Delta}\\ &-2V\int d\mathbf{r}\Big[\big\langle\Psi^{\dagger}(\mathbf{r}\uparrow)\Psi^{\dagger}(\mathbf{r}\downarrow)\big\rangle\big\langle\Psi(\mathbf{r}\downarrow)\Psi(\mathbf{r}\uparrow)\big\rangle\Big]_{\Delta}+\int d\mathbf{r}W(\mathbf{r}).\end{aligned}\tag{2.27}$$

Therefore, $\langle H\rangle=\langle H_{eff}\rangle$ when

$$W(\mathbf{r})=V\big\langle\Psi^{\dagger}(\mathbf{r}\uparrow)\Psi^{\dagger}(\mathbf{r}\downarrow)\big\rangle\big\langle\Psi(\mathbf{r}\downarrow)\Psi(\mathbf{r}\uparrow)\big\rangle.\tag{2.28}$$

The complete expression for H_{eff} is

$$\begin{aligned}\hat{H}_{eff} &= \int d\mathbf{r}\sum_{\sigma}\big[\Psi^{\dagger}(\mathbf{r}\sigma)\hat{H}_{e}\Psi(\mathbf{r}\sigma)\big]\\ &+\int d\mathbf{r}\big[\Delta(\mathbf{r})\Psi^{\dagger}(\mathbf{r}\uparrow)\Psi^{\dagger}(\mathbf{r}\downarrow)+\Delta^{*}(\mathbf{r})\Psi(\mathbf{r}\downarrow)\Psi(\mathbf{r}\uparrow)\big]\\ &+V\int d\mathbf{r}\big\langle\Psi^{\dagger}(\mathbf{r}\uparrow)\Psi^{\dagger}(\mathbf{r}\downarrow)\big\rangle\big\langle\Psi(\mathbf{r}\downarrow)\Psi(\mathbf{r}\uparrow)\big\rangle.\end{aligned}\tag{2.29}$$

Inserting Eq. (2.17) into Eq. (2.29), we have

$$\begin{aligned}\hat{H}_{eff} &= \int d\mathbf{r}\sum_{\sigma}\big[\Psi^{\dagger}(\mathbf{r}\sigma)\hat{H}_{e}\Psi(\mathbf{r}\sigma)\big]\\ &-V\int d\mathbf{r}\big[\big\langle\Psi(\mathbf{r}\downarrow)\Psi(\mathbf{r}\uparrow)\big\rangle\Psi^{\dagger}(\mathbf{r}\uparrow)\Psi^{\dagger}(\mathbf{r}\downarrow)\\ &+\big\langle\Psi^{\dagger}(\mathbf{r}\uparrow)\Psi^{\dagger}(\mathbf{r}\downarrow)\big\rangle\Psi(\mathbf{r}\downarrow)\Psi(\mathbf{r}\uparrow)\big]\\ &+V\int d\mathbf{r}\big\langle\Psi^{\dagger}(\mathbf{r}\uparrow)\Psi^{\dagger}(\mathbf{r}\downarrow)\big\rangle\big\langle\Psi(\mathbf{r}\downarrow)\Psi(\mathbf{r}\uparrow)\big\rangle.\end{aligned}\tag{2.30}$$

Next, we calculate $\langle H_{eff}\rangle$ from Eq. (2.30). By using Eq. (2.6) and the mean value rules Eq. (2.18), we have

$$\begin{aligned}\langle H_{eff}\rangle = \int d\mathbf{r} \sum_n \Big\{ &\big[2u_n^* \hat{H}_e u_n f_n + 2v_n \hat{H}_e v_n^* (1-f_n)\big] \\ &- \big(V \sum_{n'} u_{n'} v_{n'}^* [1-2f_{n'}]\big)\big(u_n^* v_n [1-2f_n]\big)\Big\}.\end{aligned} \tag{2.31}$$

By using the BdG equations (2.9), we obtain

$$\begin{aligned}\langle H_{eff}\rangle &= \int d\mathbf{r} \sum_n \Big\{2u_n^*(E_n u_n - \Delta v_n) f_n + 2v_n(\Delta u_n^* - E_n v_n^*)(1-f_n) \\ &- \big(V \sum_{n'} u_{n'} v_{n'}^* [1-2f_{n'}]\big)\big(u_n^* v_n [1-2f_n]\big)\Big\} \\ &= \int d\mathbf{r} \sum_n \Big\{2E_n |u_n|^2 f_n - 2E_n |v_n|^2 (1-f_n) \\ &+ 2\Delta u_n^* v_n (1-2f_n) - \big(V \sum_{n'} u_{n'} v_{n'}^* [1-2f_{n'}]\big)\big(u_n^* v_n [1-2f_n]\big)\Big\}.\end{aligned} \tag{2.32}$$

Finally, we get

$$\begin{aligned}\langle H_{eff}\rangle = 2\sum_n E_n f_n - 2\sum_n E_n \int d\mathbf{r} |v_n|^2 + \int d\mathbf{r} \Big[2\Delta(\mathbf{r})\big(\sum_n u_n^* v_n [1-2f_n]\big) \\ - \big(V \sum_n u_n^* v_n [1-2f_n]\big)\big(\sum_{n'} u_{n'} v_{n'}^* [1-2f_{n'}]\big)\Big],\end{aligned} \tag{2.33}$$

which is the same as the term in Eq. (2.24)

We have to mention that if the summation n in the gap equation (2.20) is over the *whole spectrum*, the $\langle H_{eff}\rangle$ can be reduced to

$$\begin{aligned}\langle H_{eff}\rangle = 2\sum_n E_n f_n - 2\sum_n E_n \int d\mathbf{r} |v_n|^2 \\ + \frac{1}{V}\int d\mathbf{r} \Big[2\Delta(\mathbf{r})\Delta_{new}^*(\mathbf{r}) - |\Delta_{new}(\mathbf{r})|^2\Big],\end{aligned} \tag{2.34}$$

where Δ is the initial input for the BdG equation (2.9) and Δ_{new} is the one obtained from the gap equation. For the energy $\langle H_{eff}\rangle$ with a converged Δ, which means $\Delta = \Delta_{new}$, it can be further reduced to

$$\langle H_{eff}\rangle = 2\sum_n E_n f_n - 2\sum_n E_n \int d\mathbf{r}|v_n|^2 + \frac{1}{V}\int d\mathbf{r}|\Delta(\mathbf{r})|^2. \tag{2.35}$$

In this thesis, we always calculate the free energy of the system by using Eq. (2.24).

2.2 Homogeneous system

2.2.1 Formulation

In this section, we present a simple case, the homogeneous two-dimensional superconducting film, and show how to use the BdG equations in detail. In this homogeneous system, the order parameter $\Delta(\mathbf{r})$ is a constant $\Delta(\mathbf{r}) = \Delta$. Thus the BdG equations in the absence of a magnetic field can be written as

$$\begin{bmatrix} \hat{H}_e & \Delta \\ \Delta & -\hat{H}_e \end{bmatrix} \begin{bmatrix} u_n(\mathbf{r}) \\ v_n(\mathbf{r}) \end{bmatrix} = E_n \begin{bmatrix} u_n(\mathbf{r}) \\ v_n(\mathbf{r}) \end{bmatrix}, \tag{2.36}$$

where $\hat{H}_e = -(\hbar\nabla)^2/2m - E_F$ is the single-electron Hamiltonian with E_F the Fermi energy, $u_n(v_n)$ are electron(hole)-like quasiparticle eigen-wavefunctions and E_n are the quasiparticle eigen-energies. The $u_n(v_n)$ obey the normalization condition

$$\int (|u_n(\mathbf{r})|^2 + |v_n(\mathbf{r})|^2)d\mathbf{r} = 1. \tag{2.37}$$

Here we consider a square unit cell with length W to perform the calculation. The value for W has to be taken large enough so that the results are W-independent. Periodic boundary conditions are used for the wavefunctions u_n and v_n. For this case, we have $\hat{H}_e\phi_{\mathbf{k}} = \epsilon_{\mathbf{k}}\phi_{\mathbf{k}}$ where $\epsilon_{\mathbf{k}} = \frac{\hbar^2\mathbf{k}^2}{2m} - E_F$ is the eigen-energy of the single-electron Hamiltonian H_e and the corresponding eigen-wavefunctions $\phi_{\mathbf{k}} = e^{i\mathbf{k}\cdot\mathbf{r}}/W$ are plane waves with wave vector $\mathbf{k}$. Note that $\mathbf{k} = (k_x, k_y) = (\frac{2\pi m}{W}, \frac{2\pi m'}{W})$ with $m, m' \in \mathbb{Z}$.

The wave functions $\phi_{\mathbf{k}}$ form a complete orthonormal basis set and therefore the wave functions u_n and v_n can be expanded in terms of $\phi_{\mathbf{k}}$:

$$u_n(\mathbf{r}) = \textstyle\sum_{\mathbf{k}} u_{\mathbf{k}}^n \frac{e^{i\mathbf{k}\cdot\mathbf{r}}}{W}, \qquad v_n(\mathbf{r}) = \textstyle\sum_{\mathbf{k}} v_{\mathbf{k}}^n \frac{e^{i\mathbf{k}\cdot\mathbf{r}}}{W}, \tag{2.38}$$

with the normalization condition:

$$\sum_{\mathbf{k}} |u_{\mathbf{k}}^n|^2 + |v_{\mathbf{k}}^n|^2 = 1. \tag{2.39}$$

Since the number of basis functions can not be infinite in our numerical calculations, we have to consider which basis functions are important for this case. Based on the fact that only those states close to the Fermi energy E_F (within the Debye energy $\hbar\omega_D$) are needed in the gap equation, we only take basis functions $\phi_{\mathbf{k}}$ with eigen-energies around the Fermi energy E_F, i.e. $|\epsilon_{\mathbf{k}}| < \chi(\hbar\omega_D)$. Because $\mathbf{k}$ is a good quantum number in this case (as shown later in this section), it is sufficient to take $\chi > 1$. Here, we take $\chi = 2$, which can definitely give accurate results.

Supposing that there are N states $\phi_{\mathbf{k}}$ used to expand u_n and v_n, the BdG equations (2.36) will be reduced to a $2N \times 2N$ matrix equation after we substitute Eq. (2.38):

$$\begin{bmatrix} T & \widetilde{\Delta} \\ \widetilde{\Delta} & -T \end{bmatrix} \psi_n = E_n \psi_n \tag{2.40}$$

where $\psi_n^T = (u_{\mathbf{k}_1}^n, \cdots, u_{\mathbf{k}_N}^n, v_{\mathbf{k}_1}^n, \cdots, v_{\mathbf{k}_N}^n)$. Due to the orthonormality of the plane wave functions $\phi_{\mathbf{k}}$, the matrix elements are given by

$$T_{\mathbf{k},\mathbf{k}'} = \epsilon_{\mathbf{k}} \delta_{\mathbf{k},\mathbf{k}'} \qquad \widetilde{\Delta}_{\mathbf{k},\mathbf{k}'} = \Delta \delta_{\mathbf{k},\mathbf{k}'}. \tag{2.41}$$

From this matrix equation, we find that only the diagonal matrix elements of T and $\widetilde{\Delta}$ are non-zero, as shown in Fig. 2.1. Such matrix can be converted into N independent 2×2 matrices equations. Each of the 2×2 matrix reads

$$\begin{bmatrix} T_{\mathbf{k}} & \Delta \\ \Delta & -T_{\mathbf{k}} \end{bmatrix} \begin{bmatrix} u_{\mathbf{k}}^n \\ v_{\mathbf{k}}^n \end{bmatrix} = E_{\mathbf{k}}^n \begin{bmatrix} u_{\mathbf{k}}^n \\ v_{\mathbf{k}}^n \end{bmatrix}. \tag{2.42}$$

It means that the quasiparticle amplitudes $(u_{\mathbf{k}}^n,\ v_{\mathbf{k}}^n)^T$ are $\mathbf{k}$-separated and $\mathbf{k}$ is a good quantum number. Then, the positive eigen-energies and the corresponding quasiparticle amplitudes for each $\mathbf{k}$ are

$$\begin{aligned} E_{\mathbf{k}} &= (\epsilon_{\mathbf{k}}^2 + \Delta^2)^{\frac{1}{2}}, \\ u_{\mathbf{k}} &= \frac{1}{\sqrt{2}} \Big(1 + \frac{\epsilon_{\mathbf{k}}}{E_{\mathbf{k}}}\Big)^{\frac{1}{2}}, \\ v_{\mathbf{k}} &= \frac{1}{\sqrt{2}} \Big(1 - \frac{\epsilon_{\mathbf{k}}}{E_{\mathbf{k}}}\Big)^{\frac{1}{2}}. \end{aligned} \tag{2.43}$$

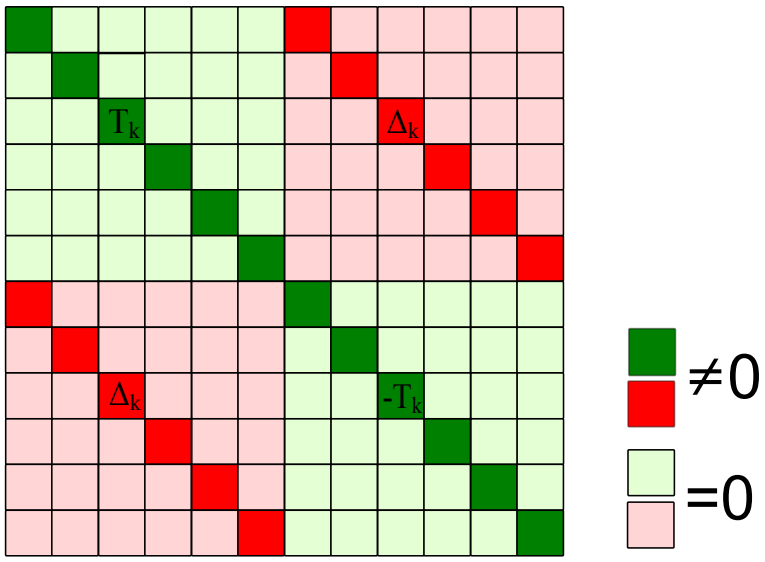

Figure 2.1: Schematic $2N \times 2N$ BdG matrix components. Only the diagonal elements of T (green) and Δ (red) are non-zero (presented by dark blocks). Other light blocks indicate the zero elements. Note that the blocks labeled by $\pm T_{\mathbf{k}}$ and $\Delta_{\mathbf{k}}$ can form a 2×2 matrix due to the independence with other non-zero matrix elements. Thus, the $2N \times 2N$ BdG matrix can be converted to N 2×2 matrices.

Their contribution to Δ is independent from the other values of $\mathbf{k}$. From these eigen-wavefunctions and eigen-energies, the superconducting order parameter is calculated according to the gap equation:

$$\Delta = g \sum_{E_n < \hbar\omega_D} u_n v_n^* [1 - 2f(E_n)], \tag{2.44}$$

where g is the coupling constant and $f(E_n) = [1 + \exp(E_n/k_B T)]^{-1}$ is the Fermi distribution function, where T is the temperature.

Δ has to be obtained self-consistently. So we have to start with an initial guess of Δ and take the procedure which has been shown in the previous section (2.1.2). When the difference between the Δ of the last two iterative steps is $\delta < 10^{-5}$ meV, the Δ is considered to be converged and taken as the final result.

The free energy F_S and the DOS can be calculated from Eqs. (2.24) and (2.23), respectively. The free energy of the normal state can be obtained by

putting $\Delta = 0$.

2.2.2 Results

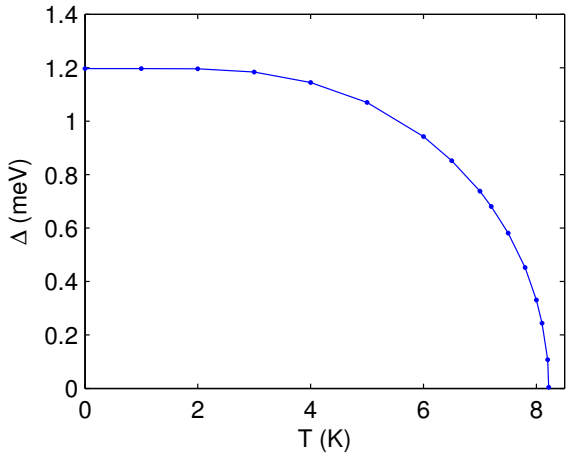

Figure 2.2: Order parameter Δ as a function of temperature T.

Here we show the results for the homogeneous case with the following microscopic parameters: effective mass $m = 2m_e$, $E_F = 40$ meV, $\hbar\omega_D = 3$ meV and the coupling constant g is set so that the bulk gap at zero temperature is $\Delta_0 = 1.2$ meV, which yields $T_c \approx 8.22$ K. The coherence length at zero temperature is $\xi_0 = \hbar v_F/(\pi\Delta_0) = 14.7$ nm with Fermi velocity v_F, which yields $k_F\xi_0 = 21.23$. The prototype material for these parameters can be $NbSe_2$[114]. The bulk gap should be obtained for a very large computational unit cell, i.e. the length of the unit cell $W \to \infty$. Here, we set $W = 3$ μm so that it is large enough to obtain the properties of bulk superconductivity.

Fig. 2.2 shows the order parameter $\Delta(T)$ as a function of temperature T. $\Delta(T)$ decreases with increasing temperature. This behavior is consistent with the BCS theory shown in Fig. 1.10. Fig. 2.3 shows the free energy of the superconducting state F_S and the normal state F_N as a function of temperature T. The F_S is always lower than the F_N indicating that the superconducting state is a more stable state than the normal state. From the energy difference $F_S - F_N$, we find that the phase transition at T_c is of second-order. Fig. 2.4 shows the DOS as a function of bias energy E at temperature $T = 0$ K, 6 K and 8 K. The coherence peaks at the energy of

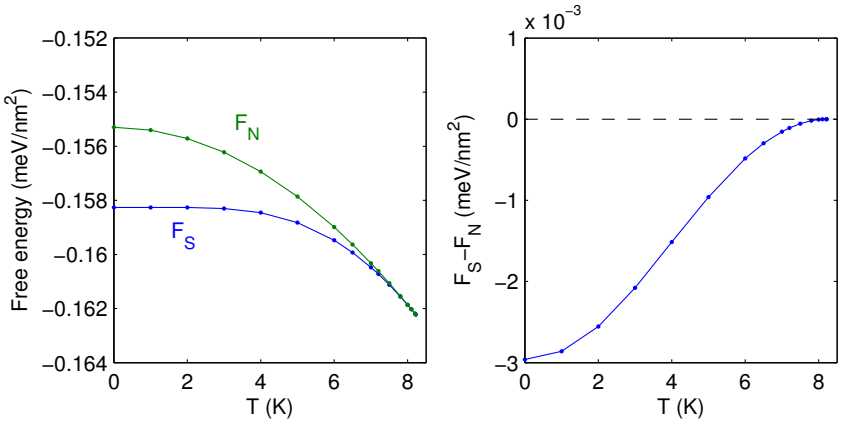

Figure 2.3: (Left) Free energy per unit area of the superconducting state F_S and the normal state F_N as a function of temperature T. (Right) Energy difference $F_S - F_N$ per unit area as a function of temperature T.

the gap are clearly visible. As temperature is increased, the energy gap and the coherence peak height decrease.

2.3 Isolated vortex

2.3.1 Formulation

In this subsection, we present the well-known case of single vortex with winding number $L = 1$ and 2 at the center of a superconducting disk (with radius R). $L = 1$ corresponds to the single vortex carrying one flux quantum and $L = 2$ corresponds to the giant vortex carrying two flux quanta. Due to the cylindrical symmetry, we take circular cylindrical coordinates $\mathbf{r} = (r, \theta)$. We start from the BdG equations:

$$\begin{bmatrix} \hat{H}_e & \Delta(\mathbf{r}) \\ \Delta^*(\mathbf{r}) & -\hat{H}_e^* \end{bmatrix} \begin{bmatrix} u_n(\mathbf{r}) \\ v_n(\mathbf{r}) \end{bmatrix} = E_n \begin{bmatrix} u_n(\mathbf{r}) \\ v_n(\mathbf{r}) \end{bmatrix}, \tag{2.45}$$

where the single-electron Hamiltonian in the presence of a magnetic field is

$$\hat{H}_e = \frac{1}{2m}\left(\frac{\hbar}{i}\nabla - \frac{e}{c}\mathbf{A}(\mathbf{r})\right)^2 - E_F, \tag{2.46}$$

where $\mathbf{A}(\mathbf{r})$ is the magnetic vector potential and the gauge $\nabla \cdot \mathbf{A} = 0$ is taken. $u_n(v_n)$ are the electron(hole)-like quasiparticle eigen-wavefunctions.

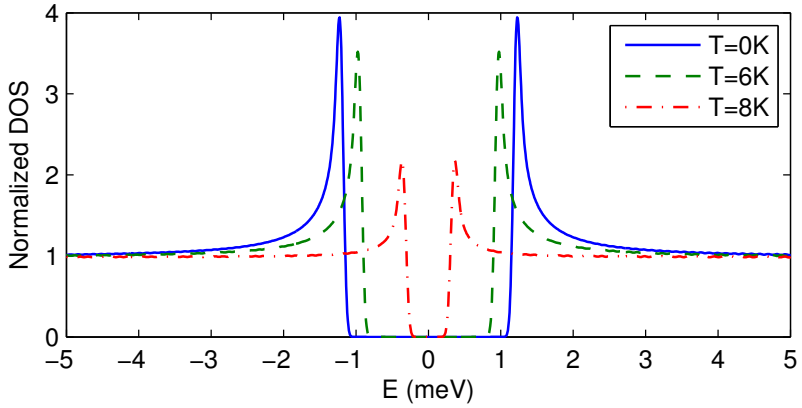

Figure 2.4: Normalized density of states (DOS) as a function of bias energy E at temperature $T = 0$ K, 6 K and 8 K.

Due to elastic-scattering for wavefunctions at the boundary $r = R$, Dirichlet boundary conditions are used, i.e.

$$u_n(R) = v_n(R) = 0. \tag{2.47}$$

In the absence of a magnetic field, $\mathbf{A}(\mathbf{r}) = 0$, we have $\hat{H}_e\phi_{k,l}(\mathbf{r}) = \epsilon_{k,l}\phi_{k,l}(\mathbf{r})$ where $\epsilon_{k,l}$ and $\phi_{k,l}(\mathbf{r})$ are the eigen-energy and eigen-states of the single-electron Hamiltonian $\hat{H}_e$. The quantum numbers k and l represent the radial and angular momentum, respectively. The eigen-energy $\epsilon_{k,l}$ reads

$$\epsilon_{k,l} = \frac{\hbar^2\alpha_{k,l}^2}{2mR^2} - E_F \tag{2.48}$$

and $\phi_{k,l}(\mathbf{r})$ is normalized and reads

$$\phi_{k,l}(\mathbf{r}) = \varphi_{k,l}(r)\frac{e^{il\theta}}{\sqrt{2\pi}} \tag{2.49}$$

with

$$\varphi_{k,l}(r) = \frac{\sqrt{2}}{R}J_l(\alpha_{k,l}\frac{r}{R})/J_{l+1}(\alpha_{k,l}). \tag{2.50}$$

$\alpha_{k,l}$ in Eqs. (2.48) and (2.50) is the $k-$th zero of the Bessel function (first kind) of order l, J_l. $k \in \mathbb{N}$ and $l \in \mathbb{Z}$ are quantum numbers.

The set $\phi_{k,l}(\mathbf{r})$ is a complete orthonormal basis set and the quasiparticle amplitudes, $u_n(\mathbf{r})$ and $v_n(\mathbf{r})$, can be expanded in terms of $\phi_{k,l}(\mathbf{r})$, i.e.

$$u_n(\mathbf{r}) = \textstyle\sum_{k,l} c_{k,l}\phi_{k,l}(\mathbf{r}), \qquad v_n(\mathbf{r}) = \sum_{k,l} d_{k,l}\phi_{k,l}(\mathbf{r}). \tag{2.51}$$

Following the previous section for the homogeneous system, we only include basis functions $\phi_{k,l}$ with eigen-energy $\epsilon_{k,l}$ around the Fermi level E_F in our calculations, i.e. $|\epsilon_{k,l}| < \varepsilon$, where ε is usually of the order of the Debye energy $\hbar\omega_D$. Suppose that s angular momenta are included, i.e. $l = \{l_1,\ l_2, \cdots,\ l_s\}$ and N_l basis functions for the angular momentum l. Thus, the total number of basis functions included in the calculation is

$$N = N_{l_1} + N_{l_2} + \cdots + N_{l_s}. \tag{2.52}$$

Then, the BdG equations (2.45) will be reduced to a $2N \times 2N$ matrix equation,

$$\begin{bmatrix} T & \widetilde{\Delta} \\ \widetilde{\Delta}^\dagger & -T^* \end{bmatrix} \psi_n = E_n \psi_n, \tag{2.53}$$

where $\widetilde{\Delta}^\dagger$ is the conjugate transpose of $\widetilde{\Delta}$ and ψ_n is a column vector with $2N$ elements

$$\begin{aligned} \psi_n^T = (&c^n_{1,l_1}, \cdots, c^n_{N_{l_1},l_1}, c^n_{1,l_2}, \cdots, c^n_{N_{l_2},l_2}, \cdots, c^n_{1,l_s}, \cdots, c^n_{N_{l_s},l_s}, \\ &d^n_{1,l_1}, \cdots, d^n_{N_{l_1},l_1}, d^n_{1,l_2}, \cdots, d^n_{N_{l_2},l_2}, \cdots, d^n_{1,l_s}, \cdots, d^n_{N_{l_s},l_s}). \end{aligned} \tag{2.54}$$

The matrix elements $T_{kl,k'l'}$, $-T_{kl,k'l'}$ and $\widetilde{\Delta}_{kl,k'l'}$ are

$$\begin{aligned} T_{kl,k'l'} &= \langle k,l|\hat{H}_e|k',l'\rangle \\ &= \left\langle k,l\middle|\frac{1}{2m}\Big[-\hbar^2\nabla^2 - 2\frac{e\hbar}{ic}\mathbf{A}\cdot\nabla + \big(\frac{e}{c}\big)^2\mathbf{A}^2\Big] - E_F\middle|k',l'\right\rangle \\ &= \Big(\frac{\hbar^2\alpha^2_{k,l}}{2m} - E_F\Big)\delta_{kk'}\delta_{ll'} - \frac{e\hbar}{imc}\left\langle k,l\middle|\mathbf{A}\cdot\nabla\middle|k',l'\right\rangle \\ &\quad + \frac{1}{2m}\Big(\frac{e}{c}\Big)^2\left\langle k,l\middle|\mathbf{A}^2\middle|k',l'\right\rangle, \end{aligned} \tag{2.55}$$

$$\begin{aligned} -T^*_{kl,k'l'} &= \langle k,l| - \hat{H}^*_e|k',l'\rangle \\ &= -\Big(\frac{\hbar^2\alpha^2_{k,l}}{2m} - E_F\Big)\delta_{kk'}\delta_{ll'} - \frac{e\hbar}{imc}\left\langle k,l\middle|\mathbf{A}\cdot\nabla\middle|k',l'\right\rangle \\ &\quad - \frac{1}{2m}\Big(\frac{e}{c}\Big)^2\left\langle k,l\middle|\mathbf{A}^2\middle|k',l'\right\rangle \end{aligned} \tag{2.56}$$

and

$$\widetilde{\Delta}_{kl,k'l'} = \langle k, l|\Delta(\mathbf{r})|k', l'\rangle. \tag{2.57}$$

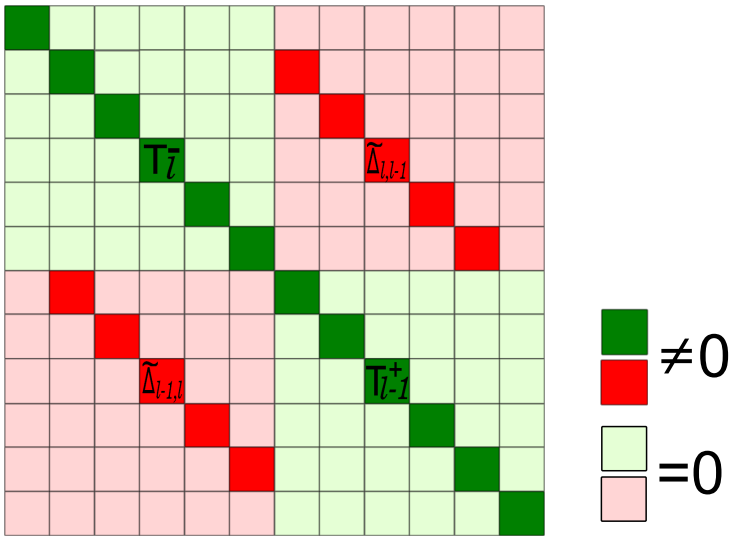

Figure 2.5: Schematic $2N \times 2N$ BdG matrix components for the case of $L = 1$. Light blocks only contain the elements with zero value. Only the diagonal blocks of the T_l^- and $-T_l^+$ (green) and the first diagonal blocks of $\widetilde{\Delta}_{l,l-1}$ ($\widetilde{\Delta}_{l-1,l}$) below (above) the main diagonal are non-zero (presented by dark blocks). Note that the blocks labeled by T_l^-, $-T_l^+$, $\widetilde{\Delta}_{l,l-1}$ and $\widetilde{\Delta}_{l-1,l}$ can form a $2N_l \times 2N_l$ matrix due to the independence with other non-zero blocks. Finally, this $2N \times 2N$ BdG matrices can be converted to $s-1$ number of $2N_l \times 2N_l$ matrix where s is the number of different angular momentum l. Their contribution to Δ can be calculated independently.

In this case, the calculation can be simplified by taking advantage of the cylindrical symmetry. Due to the fact that the vortex is imposed at the center of the disk, the order parameter $\Delta(\mathbf{r})$ can be written as

$$\Delta(\mathbf{r}) = \Delta(r)e^{iL\theta}, \tag{2.58}$$

and the vector potential $\mathbf{A}(\mathbf{r})$ can also be written as

$$\mathbf{A}(\mathbf{r}) = A_\theta(r)\hat{\mathbf{e}}_\theta \tag{2.59}$$

where $\hat{\mathbf{e}}_\theta$ is the azimuthal unit vector. Then, the terms $\langle k,l|\mathbf{A}\cdot\nabla|k',l'\rangle$ and $\langle k,l|\mathbf{A}^2|k',l'\rangle$ in Eqs. (2.55) and (2.56) can be written as

$$\begin{aligned}\left\langle k,l\middle|\mathbf{A}\cdot\nabla\middle|k',l'\right\rangle &= \int \phi^*_{k,l}\mathbf{A}\cdot(\nabla\phi_{k',l'})dS \\ &= \int_0^{2\pi}\int_0^R \varphi_{k,l}\frac{e^{-il\theta}}{\sqrt{2\pi}}A_\theta\frac{1}{r}\frac{\partial}{\partial\theta}(\varphi_{k',l'}\frac{e^{il'\theta}}{\sqrt{2\pi}})rdrd\theta \\ &= \Big(il\int_0^R \varphi_{k,l}(r)A_\theta(r)\varphi_{k',l'}(r)dr\Big)\delta_{ll'}\end{aligned} \tag{2.60}$$

and

$$\begin{aligned}\left\langle k,l\middle|\mathbf{A}^2\middle|k',l'\right\rangle &= \int \phi^*_{k,l}\mathbf{A}^2\nabla\phi_{k',l'}dS \\ &= \Big(\int_0^R \varphi_{k,l}(r)A^2_\theta(r)\varphi_{k',l'}(r)rdr\Big)\delta_{ll'}.\end{aligned} \tag{2.61}$$

Now the matrix elements $T_{kl,k'l'}$, $-T_{kl,k'l'}$ and $\widetilde{\Delta}_{kl,k'l'}$ are

$$\begin{aligned}T_{kl,k'l'} = \Bigg[&\Big(\frac{\hbar^2\alpha^2_{k,l}}{2m}-E_F\Big)\delta_{kk'} - l\frac{e\hbar}{mc}\int_0^R \varphi_{k,l}(r)A_\theta(r)\varphi_{k',l'}(r)dr \\ &+\frac{e^2}{2mc^2}\int_0^R \varphi_{k,l}(r)A^2_\theta(r)\varphi_{k',l'}(r)rdr\Bigg]\delta_{ll'}\end{aligned} \tag{2.62}$$

$$\begin{aligned}-T^*_{kl,k'l'} = -\Bigg[&\Big(\frac{\hbar^2\alpha^2_{k,l}}{2m}-E_F\Big)\delta_{kk'} + l\frac{e\hbar}{mc}\int_0^R \varphi_{k,l}(r)A_\theta(r)\varphi_{k',l'}(r)dr \\ &+\frac{e^2}{2mc^2}\int_0^R \varphi_{k,l}(r)A^2_\theta(r)\varphi_{k',l'}(r)rdr\Bigg]\delta_{ll'}\end{aligned} \tag{2.63}$$

and

$$\begin{aligned}\widetilde{\Delta}_{kl,k'l'} &= \langle k,l|\Delta(\mathbf{r})|k',l'\rangle \\ &= \int_0^{2\pi}\int_0^R \varphi_{k,l}\frac{e^{-il\theta}}{\sqrt{2\pi}}\Delta(r)e^{iL\theta}\varphi_{k',l'}\frac{e^{il'\theta}}{\sqrt{2\pi}}rdrd\theta \\ &= \Bigg[\int_0^R \varphi_{k,l}\Delta(r)\varphi_{k',l'}rdr\Bigg]\delta_{l,l'+L}\end{aligned} \tag{2.64}$$

It is worth noting that $T_{kl,k'l'}$, $-T^*_{kl,k'l'}$ and $\widetilde{\Delta}_{kl,k'l'}$ are filled by real numbers and that $T_{kl,k'l'}$ is different from $-T^*_{kl,k'l'}$. Therefore we label T as T^- and $-T^*$ as $-T^+$ and the matrix equations (2.53) read

$$\begin{bmatrix} T^- & \widetilde{\Delta} \\ \widetilde{\Delta}^T & -T^+ \end{bmatrix} \psi_n = E_n \psi_n, \tag{2.65}$$

where $\widetilde{\Delta}^T$ is the transpose of $\widetilde{\Delta}$. From this matrix equation we find that only the diagonal blocks of the T_l^- and $-T_l^+$ and the $L-$th diagonal blocks of $\widetilde{\Delta}_{l,l-L}$ ($\widetilde{\Delta}_{l-L,l}$) below (above) the main diagonal are non-zero. For the case of $L = 1$, the schematic diagram for the matrix components are shown in Fig. 2.5. Such a matrix can be converted into $s - L$ $2N_l \times 2N_l$ smaller matrices. Each of the $2N_l \times 2N_l$ matrices reads

$$\begin{bmatrix} T_l^- & \widetilde{\Delta}_{l,l-L} \\ \widetilde{\Delta}_{l-L,l} & -T_{l-L}^+ \end{bmatrix} \psi_{\nu,l} = E_{\nu,l} \psi_{\nu,l}. \tag{2.66}$$

These represent the quasiparticle coupling between the electron amplitude u_n with angular momentum l and the hole amplitude v_n with angular momentum $l - L$.

In principle, we have to include all the states with positive energy $E_n > 0$ over all the angular momentum l. However, the calculation can be further reduced by using the properties of the BdG equations which are invariant under the transformations:

$$\begin{aligned} u_{\nu,l}(\mathbf{r}) &\to v^*_{\nu,-l}(\mathbf{r}) \\ v_{\nu,l}(\mathbf{r}) &\to -u^*_{\nu,-l}(\mathbf{r}) \\ E_{\nu,l} &\to -E_{\nu,-l}. \end{aligned} \tag{2.67}$$

Therefore, the computational time can be cut almost in half by obtaining positive- and negative-energy solutions for positive l only.

As in the homogeneous case, the superconducting order parameter is calculated according to the gap equation:

$$\Delta = g \sum_{E_n < \hbar\omega_D} u_n v_n^* [1 - 2f(E_n)], \tag{2.68}$$

where g is the coupling constant and $f(E_n) = [1 + \exp(E_n/k_B T)]^{-1}$ is the Fermi distribution function, where T is the temperature. The supercurrent

is calculated from Eq. (2.21) and the field included by the supercurrent is calculated by Maxwell's equation

$$\nabla \times \nabla \times \mathbf{A}(\mathbf{r}) = \mathbf{j} \tag{2.69}$$

with $\mathbf{B} = \nabla \times \mathbf{A}$. Again, Δ and $\mathbf{A}$ have to be obtained self-consistently. The LDOS is calculated by using Eq. (2.23).

2.3.2 Results

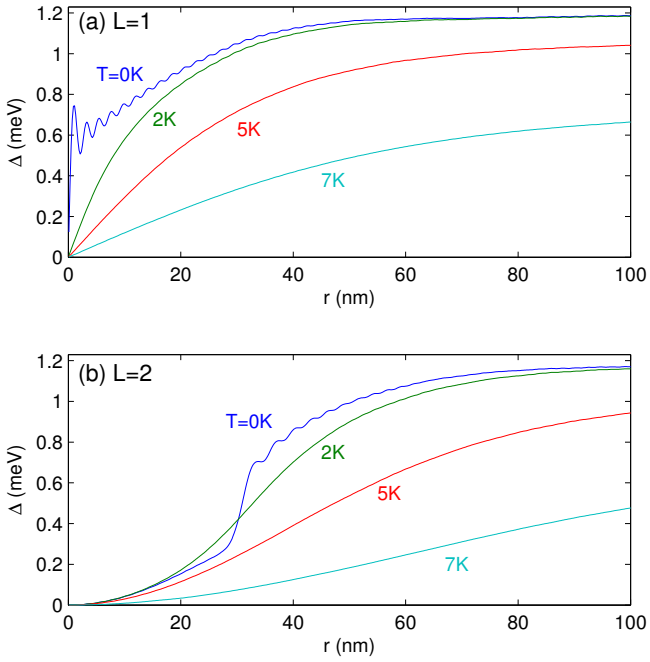

Figure 2.6: Order parameter $\Delta(r)$ around a vortex core at temperatures $T = 0$ K, 2 K, 5 K and 7 K. Panels (a) and (b) correspond to the winding number $L = 1$ and $L = 2$, respectively.

We present results for the same microscopic parameters as introduced in the homogeneous case. The applied magnetic field is taken $\mathbf{H} = 0$. The radius $R = 700$ nm is large enough so that the properties of the vortex are not affected by surface effects.

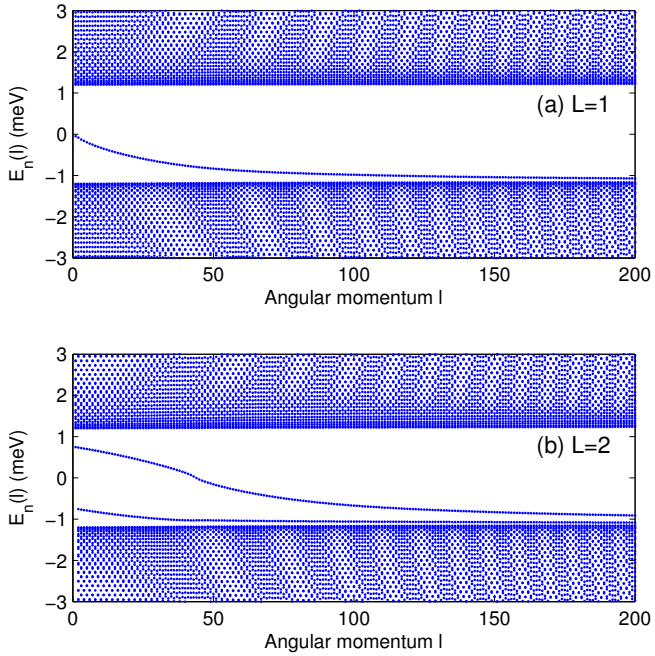

Figure 2.7: Quasiparticle excitation spectrum as a function of positive angular momentum l at temperature $T = 0$ K. Panels (a) and (b) correspond to the winding number $L = 1$ and $L = 2$, respectively.

Fig. 2.6 shows the order parameter $\Delta(r)$ as a function of the radial coordinate r for various temperatures T. Panels (a) and (b) correspond to the winding number $L = 1$ and 2, respectively. It is seen that the order parameter $\Delta(r)$ is suppressed to zero at the center for both cases due to the existence of the vortex core. With r increasing, the order parameter $\Delta(r)$ gradually recovers the bulk value. For $L = 1$, the length scale over which the order parameter recovers the bulk value is a few times the coherence length. The vortex core size is defined by $\xi_c^{-1} = \lim_{r\to 0}\Delta(r)/[r\Delta(r \to \infty)]$. It indicates that the core size decreases with decreasing temperature. This is the Kramer-Pesch effect [115]. Friedel-like oscillations in $\Delta(r)$ at $T = 0$ are clearly visible. The reason is that the lowest bound states dominate the physical quantities at low temperature, and these states have a large oscillation amplitude near the core [116]. For $L = 2$, the vortex core size is much larger than the $L = 1$ core. Also, the Kramer-Pesch effect and the Friedel-

like oscillations at $T = 0$ are clearly seen. These effects are different from the $L = 1$ case and they have been discussed in Refs. [117, 118].

Fig. 2.7 shows the quasiparticle excitation spectrum as a function of angular momentum l at $T = 0$ K. Panels (a) and (b) correspond to the winding number $L = 1$ and 2, respectively. For $L = 1$, it can be seen that a bound state branch exists inside the energy gap. The lowest bound state energy is very close to zero for the angular momentum $l = 1$. This was initially thought to be exactly zero but was later proven not to be [116]. With l increases, the bound state energy increases towards the gap edge. The quantization of the energy levels in the scattering states (above the gap) is due to the finite radius R. For $L = 2$, it has two bound-state branches. Based on the WKBJ approximation [119], these two bound-state branches cross the Fermi level and are given approximately as:

$$l \approx k_F r_\Delta \cos\Big[\big(\frac{1}{2} + q\big)\frac{\pi}{2}\Big]; \quad q = 0 \text{ and } \frac{1}{2}, \tag{2.70}$$

where r_Δ is the half depth radius of the pairing potential well at the core. It is worth noting that both vortex cores exhibit the Tomasch effect, which is a quasiparticle interference above the energy gap due to the spatial inhomogeneous $\Delta(r)$. For more details about Tomasch effect, please see Ref. [114] and Chapter 6 in this thesis.

Fig. 2.8 shows the LDOS as a function of energy E and radial coordinate r for $T = 0$ K. Panels (a) and (b) correspond to the winding number $L = 1$ and 2, respectively. For $L = 1$, the bound state peak around zero energy at $r = 0$ corresponds to the lowest angular momentum $l = 1$. With r increasing, the bound state branches of both positive and negative bias increase in energy and finally merge with the gap edge far away from the vortex core, where the BCS DOS is recovered. For $L = 2$, there are two bound state peaks at $r = 0$ but they symmetrically sit on the positive and negative bias energy. There is a zero energy peak at $r \neq 0$ corresponding to the states resulting from bound-state branches crossing the Fermi level. With r increasing, the behavior is similar to the $L = 1$ vortex case. Note that the coherence peaks do not develop near the vortex core. These results are consistent with previous works [114, 120–122].

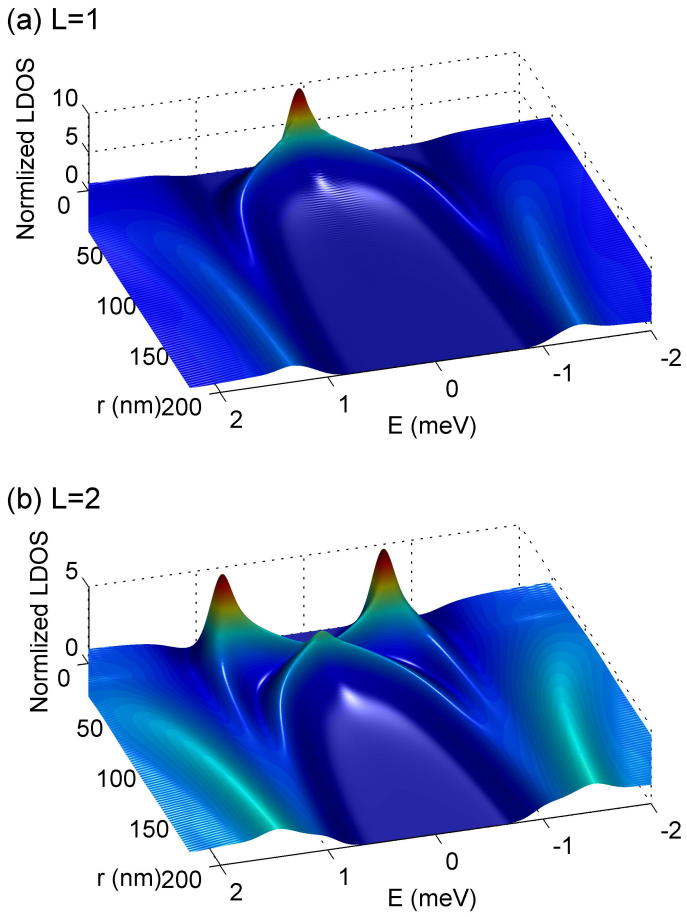

Figure 2.8: LDOS as a function of bias energy E and radial coordinate r for $T = 0$ K. Panels (a) and (b) correspond to the winding number $L = 1$ and $L = 2$, respectively.

Chapter 3

Unconventional vortex states in nanoscale superconductors due to shape-resonated inhomogeneity of the Cooper-pair condensate

Vortex matter in mesoscopic superconductors is known to be strongly affected by the geometry of the sample. Here we show that in nanoscale superconductors with coherence length comparable to the Fermi wavelength the shape resonances of the order parameter results in an additional contribution to the quantum topological confinement - leading to unconventional vortex configurations. Our Bogoliubov-de Gennes calculations in a square geometry reveal a plethora of asymmetric, giant multi-vortex, and vortex-antivortex structures, stable over a wide range of parameters and which are very different from those predicted by the Ginzburg-Landau theory. These unconventional states are relevant for high-T_c nanograins, confined Bose-Einstein condensates, and graphene flakes with proximity-induced superconductivity.

The results of this chapter were published as: L.-F. Zhang, L. Covaci, M. V. Milošević, G. R. Berdiyorov, and F. M. Peeters, Phys. Rev. Lett. **109**, 107001 (2012).

3.1 Introduction

In the last decades, the effect of the boundary on mesoscopic superconductors with dimensions comparable to the penetration depth λ or the coherence length ξ has been intensively studied [31, 123–129]. In applied magnetic field, it was found that the vortex states strongly depend on the size and geometry of the sample and are generally different from the Abrikosov triangular lattice observed in bulk type-II conventional superconductors (where only the vortex-vortex interaction plays a role). For example, a giant vortex induced by strong boundary confinement was predicted [31] as the ground state in disks which was subsequently observed experimentally [52, 53]. In square samples, a peculiar state with an anti-vortex at the center surrounded by four vortices was predicted theoretically [32, 33, 130], but never observed experimentally up to now.

All of the above theoretical works are based on the Ginzburg-Landau (GL) theory. When the superconductor is downscaled to nano-meter sizes, quantum confinement [65] leads to unique phenomena, especially in samples with dimensions of the order of the Fermi wave length λ_F. The GL theory is no longer applicable in this regime and the microscopic Bogoliubov-de Gennes formalism is required. The discretization of the energy levels around the Fermi level E_F was shown to induce quantum-size effect [67, 92], quantum-size cascades [95] and the shell effect [86]. As one of the important results, Ref. [67] reported the wave-like inhomogeneous spatial distribution of the order parameter, further enhanced at the boundary due to quantum confinement. The latter is important since it is well known that vortices tend to migrate and be pinned in areas where superconductivity is suppressed [131], i.e. it is energetically favorable for a vortex to suppress the superconducting order parameter in the region where it is already weak. In reality the behavior is much more complex and in some instances the vortex can be pinned where the gap is large [132]. The appearance of oscillations in the order parameter profile due to quantum confinement is thus expected to influence the vortex states. For conventional superconductors, $k_F\xi_0 \approx 10^3$ (k_F is the Fermi wave vector and ξ_0 is the BCS coherence length), systems of size comparable to λ_F will not be large enough to host a vortex (being much smaller than the coherence length). However, materials with small coherence lengths, e.g. *high-T_c cuprate superconductors*, will have $k_F\xi_0 \approx 1-4$ and therefore in such systems it is possible to obtain vortex states in the quantum confinement regime. Another such system is a *graphene flake* deposited on

top of a superconductor. Because of the proximity effect, superconducting correlations will diffuse in graphene[133–136]. Such a system is in the clean limit since the scattering length in graphene is large. More importantly, in graphene, near the Dirac point, the Fermi wavelength is very large and can be easily manipulated by doping. In other words, $k_F\xi_0$ can be tuned, which will allow for different vortex patterns to be realized in the graphene flake in the quantum confinement regime, but for more accessible sample sizes (above 100 nm).

In order to experimentally detect vortex states in nano-sized superconductors, one can extract information about the local density of states (LDOS) from measurements of the differential conductance with scanning tunneling microscopy (STM) [46, 53, 137]. An extensive analysis of the LDOS profile of the vortex states has been performed in the past [116, 120, 122, 138, 139]. It is generally known that the bound states in the vortex core lead to peaks in the LDOS at energies below the superconducting gap, though the exact formation of peaks in the spectrum of a multiple flux line (giant vortex) will depend on the vorticity [140]. Also, when $k_F\xi_0$ is small, the spectrum becomes particle-hole asymmetric and the lowest vortex bound state has a finite energy [116]. In the quantum confinement regime, there exist strong vortex-vortex and vortex-boundary interactions and the quasiparticle spectrum becomes much more complicated. In this case the lowest bound state peak position does not generally coincide with the vortex core [141]. Furthermore, in case of strong interactions, vortex and surface bound states may combine to form a complex state where LDOS contributions of individual constituents are not clearly visible.

In this chapter we present novel vortex states that appear from the interplay between quantum confinement, inhomogeneous superconductivity, an external magnetic field, and the sample geometry, in a nano-sized superconducting square. We performed calculations for a sample in the quantum limit by solving Bogoliubov-de Gennes (BdG) equations self-consistently. In what follows, we keep constant the size of the sample and the bulk coherence length $\xi_0 = \hbar v_F/\pi\Delta_0$ (where v_F is the Fermi velocity and Δ_0 is the order parameter at zero temperature), while we change the parameter $k_F\xi_0$ and thereby tune the influence of the confinement on the vortex structure.

3.2 Formalism

We start from the well-known BdG equations:

$$[K_0 - E_F]\, u_n(\mathbf{r}) + \Delta(\mathbf{r}) v_n(\mathbf{r}) = E_n u_n(\mathbf{r}), \tag{3.1}$$

$$\Delta(\mathbf{r})^* u_n(\mathbf{r}) - [K_0^* - E_F]\, v_n(\mathbf{r}) = E_n v_n(\mathbf{r}), \tag{3.2}$$

where $K_0 = (i\hbar\nabla + e\mathbf{A}/c)^2/2m$ is the kinetic energy and E_F is the Fermi energy, $u_n(v_n)$ are electron(hole)-like quasi-particle eigen-wave functions, E_n are the quasi-particle eigen-energies, and $\mathbf{A}$ is the vector potential (we use the gauge $\nabla \cdot \mathbf{A} = 0$).

The pair potential is determined self-consistently from the eigen-wave functions and eigen-energies:

$$\Delta(\mathbf{r}) = g \sum_{E_n < E_c} u_n(\mathbf{r}) v_n^*(\mathbf{r})[1 - 2f_n], \tag{3.3}$$

where g is the coupling constant, E_c is the Debye energy, and $f_n = [1 + \exp(E_n/k_B T)]^{-1}$ is the Fermi distribution function, where T is the temperature. We consider the two-dimensional problem and assume a circular Fermi surface. The confinement imposes Dirichlet boundary conditions (i.e. $u_n(\mathbf{r}) = 0,\ v_n(\mathbf{r}) = 0,\ r \in \partial S$) such that the order parameter vanishes at the surface. In an extreme type-II superconductor (and/or very thin sample), it is reasonable to neglect the contribution of the supercurrent to the total magnetic field. For such a case, we discretize Eqs. (3.1-3.3) and by using the finite difference method we solve them self-consistently. A detailed recipe regarding the calculation will be presented in Sec. 4.2.

The free energy [142, 143] of the system is then calculated as:

$$\begin{aligned} F &= \sum_n 2E_n f_n + 2k_B T[f_n \ln f_n + (1 - f_n)\ln(1 - f_n)] \\ &+ \int d\mathbf{r} \left[-2 \sum_n E_n |v_n|^2 + 2\Delta(\mathbf{r}) \sum_n u_n^* v_n [1 - 2f_n] \right. \\ &- \left. g \sum_n u_n^* v_n (1 - 2f_n) \sum_{n'} u_{n'} v_{n'}^* (1 - 2f_{n'}) \right], \end{aligned} \tag{3.4}$$

where the spatial dependence of u_n and v_n is implicit. The local density of states $N(r, E)$ is calculated from

$$N(r, E) = -\sum_n [f'(E_n - E)|u_n|^2 + f'(E_n + E)|v_n|^2]. \tag{3.5}$$

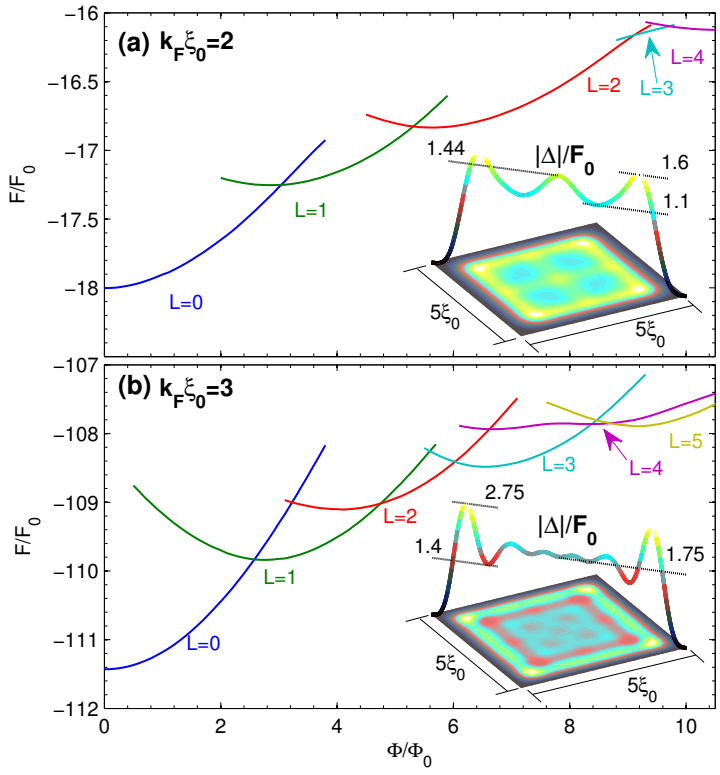

Figure 3.1: Free energy as a function of the magnetic flux through the square sample, for (a) $k_F\xi_0 = 2$, and (b) $k_F\xi_0 = 3$. Here, $F_0 = \hbar^2/2m\xi_0^2$. The insets show the contour plots of the order parameter with the diagonal profiles in the absence of applied magnetic field.

In this chapter, we consider as an example a thin superconducting square with size $5\xi_0 \times 5\xi_0$. The microscopic parameters are set to keep $\Delta_0/E_c = 0.2$. The calculations are done for different parameters $k_F\xi_0$. Since we consider the zero temperature case, the system is always in the quantum limit (where $T/T_c < 1/k_F\xi_0$).

3.3 Results

Fig. 3.1 shows our numerical results for the free energy of the found stable vortex configurations (the states with up to five vortices are shown) for

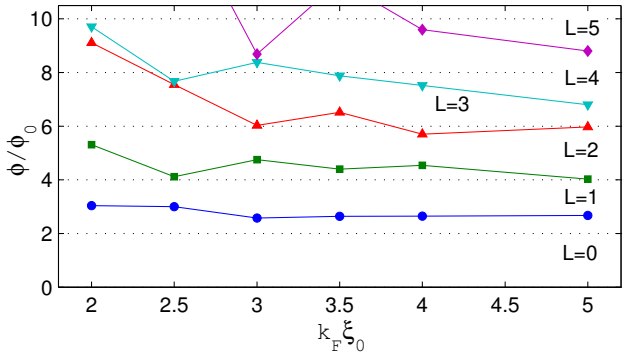

Figure 3.2: Transition fluxes in units of Φ_0 between ground states with consecutive vorticities for different $k_F\xi_0$.

two values of the key parameter, $k_F\xi_0$. The insets show the inhomogeneous profile of the superconducting order parameter *in the absence of an applied magnetic field* which is expected to strongly influence the vortex structure. When comparing with conventional free energy curves obtained from the GL theory [144], many differences can be observed. First, the penetration field for the first vortex is suppressed because the order parameter is not homogeneous, allowing the vortex to penetrate easier at locations where the order parameter is weakened. Second, the stability range in flux for different vortex states (with vorticity L) is not monotonically decreasing towards $1\Phi_0$ as L increases. Moreover, those stability ranges strongly vary when $k_F\xi_0$ is changed! For example, for $k_F\xi_0 = 2$ the vortex structures with even vorticity are stable over a broader magnetic field range while for $k_F\xi_0 = 3$ surprisingly the structures with odd vorticity are the favored ones! The main reason behind this phenomenon is that different confinement-induced oscillations in the order parameter for different $k_F\xi_0$ value will stabilize different symmetries of the vortex pattern. To illustrate this effect better, we plot in Fig. 3.2 the applied magnetic flux at which ground-state transitions between states with consecutive vorticities occur, as a function of $k_F\xi_0$. Notice the varying ranges of stability of different vortex states, which are very sensitive to $k_F\xi_0$. Of course, for large $k_F\xi_0$ the behavior of the system converges to a more conventional picture (with each new vortex entering the system with roughly one flux-quantum added).

To underpin the reasons for this varying stability of vortex states in what is otherwise a rather simple, square system, we show in Fig. 3.3 some of

the typical states for the case of $k_F\xi_0 = 2$ (the order parameter, its phase, and corresponding LDOS). As elaborated above, the quantum confinement of electrons here strongly affects the spatial distribution of the order parameter [see inset in Fig. 3.1(a)], having three oscillations across the square and four distinct minima that enhance the fourfold symmetry. This automatically leads to the improved stability of states with even vorticity, similar to the case of a square with 4 antidots [145]. We also observe that, before ceasing at the boundary, the order parameter is enhanced near the surface, with the highest value found near the corners. Due to the effect of the boundary and the shape resonances, the order parameter is also enhanced at the center of the square. To reiterate a fairly obvious point, vortices are repelled by the peak positions of the superconducting pair amplitude, and the four low amplitude locations (with value only 2/3 of the peaks) will pin vortices rather strongly. Figs. 3.3(a-c), show the $L = 1$ ground state for applied flux $\Phi/\Phi_0 = 4$. Surprisingly, we find that the only vortex in this state is actually sitting in one of the minima of the order parameter and the *fourfold symmetry is broken*. We emphasize that this state is *not possible* within the GL formalism where the single vortex will always sit in the center of the square.

From an experimental point of view, in the absence of any reference energy, the zero-bias LDOS is most relevant. Here instead we will show the LDOS for the lowest energy vortex bound state. As shown in Ref.[116], this energy depends on $k_F\xi_0$ in the following way:

$$E_{low}/\Delta = (2k_F\xi_0)^{-1} \ln(3.33k_F\xi_0). \tag{3.6}$$

Therefore for the $L = 1$ state we plot the LDOS at $E/F_0 = 0.57$ [Fig. 3.3(c)]. Note that this lowest vortex bound state is not localized in the vortex core but is shifted towards the center of the square. We attribute this to the interactions of the quasiparticles not only with the four deepest minima of the inhomogeneous order parameter but also with the edges and the corners - where the order parameter is also suppressed [see inset of Fig. 3.1(a)]. The effect of this interaction can also be inferred from the finite LDOS at the corner of the sample, next to the vortex.

When increasing further the magnetic field, an additional vortex enters the system (forming $L = 2$ state) and another unexpected spatial distribution is stabilized. We illustrate this in Figs. 3.3(d-f) for applied flux $\Phi/\Phi_0 = 6$. The confinement seems to act strongly and vortices are compressed closer to each other. However, the enhancement of the order parameter in the

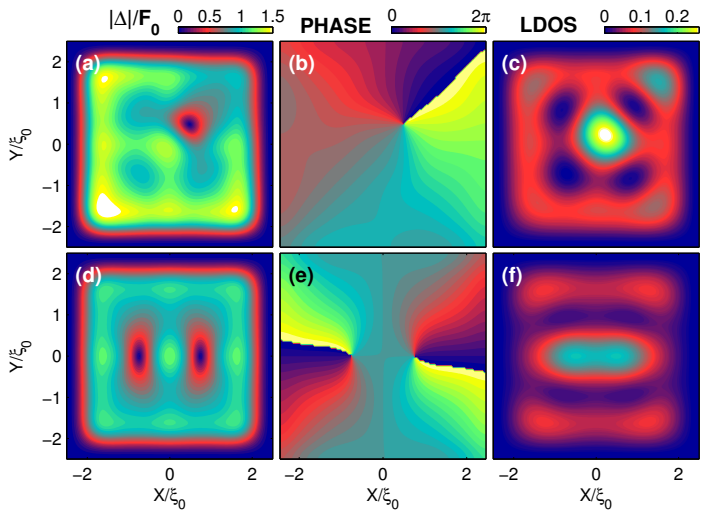

Figure 3.3: Contour plots of the absolute value of the order parameter (left), the phase of the order parameter (center) and the LDOS at $E/F_0 = 0.57$ in (c) and $E/F_0 = 0.48$ in (f) (right) for $k_F\xi_0 = 2$. Panels (a), (b) and (c) are for $\Phi/\Phi_0 = 4$ and $L = 1$ state. Panels (d), (e) and (f) correspond to $\Phi/\Phi_0 = 6$ and $L = 2$ state.

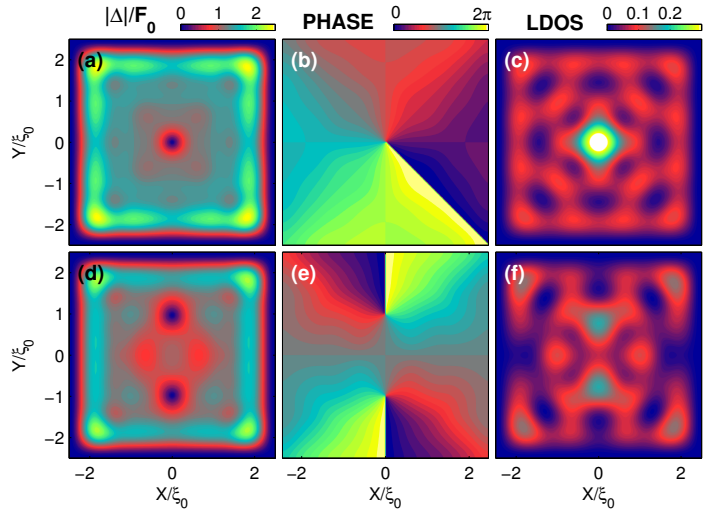

Figure 3.4: Contour plots of the absolute value of the order parameter (left), the phase of the order parameter (center) and the LDOS (right) for $k_F\xi_0 = 3$. Panels (a), (b) and (c) are for $\Phi/\Phi_0 = 3$ and $L = 1$ state [(c) plotted at $E/F_0 = 0.89$]. Panels (d), (e) and (f) correspond to $\Phi/\Phi_0 = 5.8$ and $L = 2$ state [(f) plotted at $E/F_0 = 0.53$].

center of the sample due to quantum resonance prevents the two vortices from merging. As a consequence, vortices are *squeezed into elliptical shapes*, as a pair parallel to one of the sample edges. This vortex configuration is as different as one can be from the known GL results, where the two vortices are *always* found sitting on the diagonal, or merged into a giant vortex, and have always an almost circular core. The LDOS plot [Fig. 3.3(f)] again reveals strong competing interactions, different from those acting on vortices. For example, we see evidence of the interaction of bound states inside the vortex cores, since the maximum in the LDOS is reached between the vortices and not at the center of each vortex. Also, the vortex-surface interaction of the bound states is enhanced, leading to LDOS being clearly appreciable near the surface.

To check further the influence of the length scales in our sample, we also calculated the vortex states for $k_F\xi_0 = 3$. In this case, the inset of Fig. 3.1(b) shows six local maxima along the diagonal, twice as many as in the $k_F\xi_0 = 2$ case. There are also strong oscillations near the corners but relatively flatter away from the boundary. Again, as expected, the four-fold symmetry is

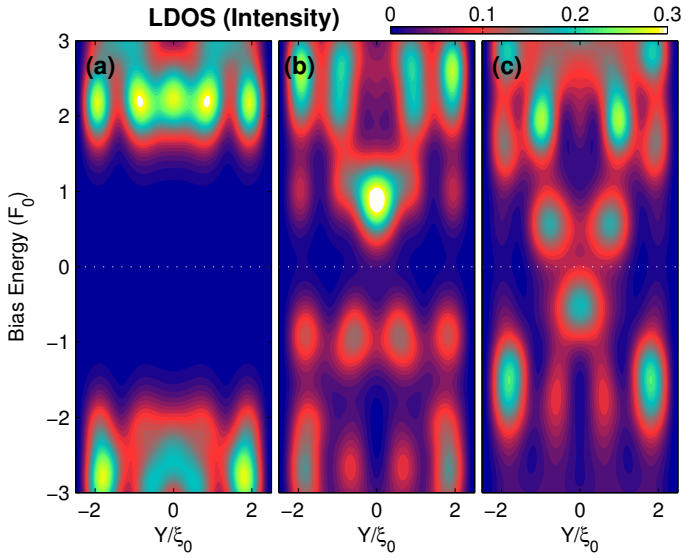

Figure 3.5: LDOS as a function of energy and position along $x = 0$ for $k_F\xi_0 = 3$. Panel (a) is for $\Phi/\Phi_0 = 0$ and $L = 0$ state. Panels (b) and (c) are for the $L = 1$ and $L = 2$ states, respectively, shown in Fig. 3.4.

maintained, but now there are no strong minima in the fourfold arrangement deep inside the sample. For that reason, for $\Phi/\Phi_0 = 3$, the $L = 1$ ground state is conventional and contains one vortex at the center of the square [Fig. 3.4(a-c)]. The LDOS for the lowest bound state energy [see Fig. 3.4(c)] is strongly localized in the vortex core, but additional states extended over the whole sample appear. The lowest energy $E/F_0 = 0.89$ is very close to the value inferred from Eq. (3.6). For $\Phi/\Phi_0 = 5.8$, the $L = 2$ state is the ground state [Fig. 3.4(d-f)] and although it still shows the vortex pair parallel to the side of the square, the shape of the vortices is closer to the conventional picture. The LDOS for the lowest bound state energy [see Fig. 3.4(f)] is also strongly localized near the vortex core. However, due to vortex-vortex interactions, the bound state is split and the lowest energy $E/F_0 = 0.53$ is lower than the value inferred from Eq. (3.6). Fig. 3.5 shows he energy dependence of the LDOS over a line defined by $x = 0$ for $L = 0, 1, 2$ for $k_F\xi_0 = 3$. In the Meissner state the superconducting gap is clearly observed. The $L = 1$ state is strongly particle-hole asymmetric, as expected [116], while the LDOS for the $L = 2$ state shows the splitting of the lowest energy state.

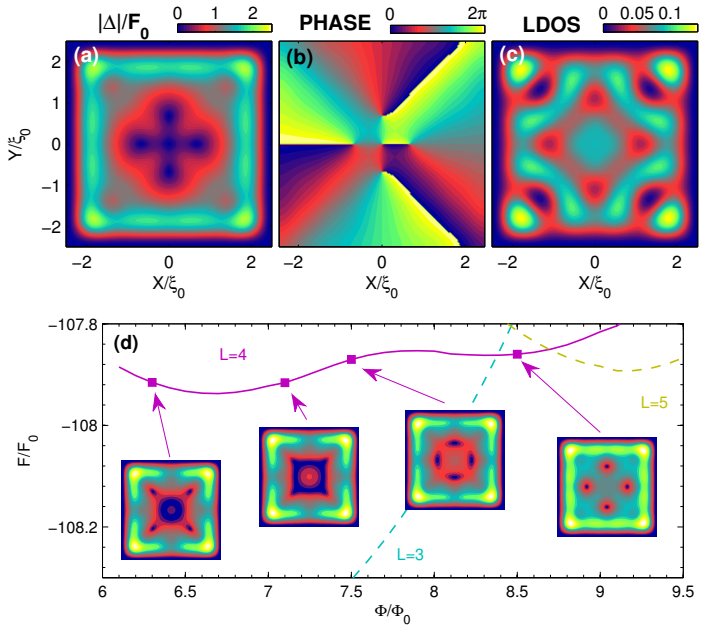

Figure 3.6: Contour plots of the absolute value of the order paramenter (a), the phase of the order parameter (b) and the LDOS at $E/F_0 = 0.57$ in (c) for $k_F\xi_0 = 3$ and $\Phi/\Phi_0 = 7$ ($L = 3$). Panel (d) shows the vortex configurations for the $L = 4$ state and their corresponding energies.

When the flux through the square is increased to $\Phi/\Phi_0 = 7$, as shown in Figs. 3.6(a-c), the ground state has vorticity $L = 3$ and is *not conventional*. We in fact find the vortex-antivortex (v-av) molecule, similar to the symmetry-induced ones predicted by the GL theory [32, 33, 130] (4 vortices with an anti-vortex in between, so that the total vorticity is $L = 4-1$). There the size of the v-av molecule was found to be very small, possibly larger if artificial pinning centers are introduced [130, 146]. In the present case, the vortex-antivortex molecule is *stable over a wide range of fields* because of the symmetry of the oscillatory pattern of the order parameter due to the quantum confinement. The LDOS at $E/F_0 = 0.57$, shown in Fig. 3.6(c), reveals again that since the vortices are located closer together, the bound states are not localized in the cores but are extended over the whole square.

Another found difference from earlier studies is the behavior of the $L = 4$ state for $k_F\xi_0 = 3$. As shown in the free energy curve in Fig. 3.6(d), we revealed a *continuous phase transition* between the configuration with the vortices located on the diagonal (at lower fields) and the configuration with the four vortices sitting near the edges of the square (higher fields), a state never found within GL! The transition between the two four-fold symmetric states is quite peculiar and yet unseen in mesoscopic superconductivity - it involves the appearance of vortex-antivortex pairs near the center of the square. As the field is increased, the diagonal vortices annihilate with the central anti-vortices, and central vortices move to the side location. Moreover, the $L = 4$ configuration with side vortices becomes the ground state for $\Phi/\Phi_0 = 8.5$. Due to the inhomogeneity of the order parameter, these vortices never merge into a giant vortex, contrary to the known GL picture for samples of smaller sizes.

3.4 Conclusion and discussion

In conclusion, we found *novel* vortex states with *unconventional* stability ranges and unconventional transition between them in a superconducting square in the quantum limit, where significant departures from previous works based on the GL theory are found. Experimentally, these states can be accessed through STM measurements. Additionally, we showed that competing interactions in the quantum limit for the bound states are different from those for the vortices, so that the conventional picture of a vortex bound to lowest energy states does not hold. Instead we predict that the maxima

in LDOS of the lowest energy states will be observed between vortices and near surfaces. These peculiar phenomena are made possible by strong quantum confinement, which induces spatial oscillations in the order parameter. Their specific pattern depends on the ratio of ξ_0 and λ_F, which is unfavorable for oscillations in elementary superconductors, but is small enough in high-T_c materials. However, to observe these novel states in the latter case, one should deal with very small samples. As an alternative, we propose the study of a graphene flake in contact to a superconducting film, where the Fermi energy of graphene can be tuned by a gate. In the case of graphene on Pb, our calculations show that one could tune $k_F\xi_0$ in the broad range of $0.1 - 10$ by shifting the Fermi energy in a 400×400 nm flake from 0.01 to 0.1 eV above the Dirac point. Another system where effects of quantum confinement on vortex matter can be probed systematically are the optically trapped cold gases [147], which are nowadays extremely controllable. Further investigations will address the rich physics in the quantum limit, and show the effects of our findings in the 3D-confined case[148–150] and multi-condensate samples[151], but where also barriers for vortex motion across the oscillating landscape can be investigated for, possible use as Q-bits or other vortex devices[152].

Unconventional vortex states in nanoscale superconductors due to shape-resonated inhomogeneity of the Cooper-pair condensate

Chapter 4

Vortex states in nanoscale superconducting squares: the influence of quantum confinement

Bogoliubov-de Gennes theory is used to investigate the effect of the size of a superconducting square on the vortex states in the quantum confinement regime. When the superconducting coherence length is comparable to the Fermi wavelength, the shape resonances of the superconducting order parameter have strong influence on the vortex configuration. Several unconventional vortex states, including asymmetric ones, giant multi-vortex combinations, and states comprising giant antivortex, were found as ground states and their stability was found to be very sensitive on the value of $k_F\xi_0$, the size of the sample W, and the magnetic flux Φ. By increasing the temperature and/or enlarging the size of the sample, quantum confinement is suppressed and the conventional mesoscopic vortex states as predicted by the Ginzburg-Landau (GL) theory are recovered. However, contrary to the GL results we found that the states containing symmetry-induced vortex-antivortex pairs are stable over the whole temperature range. It turns out that the inhomogeneous order parameter induced by quantum confinement favors vortex-antivortex molecules, as well as giant vortices with a rich struc-

The results of this chapter were published as: L.-F. Zhang, L. Covaci, M. V. Milošević, G. R. Berdiyorov, and F. M. Peeters, Phys. Rev. B. **88**, 144501 (2013).

ture in the vortex core - unattainable in the GL domain.

4.1 Introduction

Vortex states in mesoscopic superconductors have been extensively studied in the past two decades, both theoretically and experimentally.[30, 31, 46, 54, 114, 123–126, 128, 137, 144, 151, 153–166] Two main interactions have been found to govern vortex behavior in a mesoscopic system. The first one is the vortex-vortex interaction, which causes vortices to form Abrikosov triangular lattices in bulk type-II superconductors. The second one is the interaction between vortices and sample boundaries, which makes vortex configurations strongly dependent on the size and geometry of mesoscopic samples-whose dimensions are of the order of the penetration depth λ or the coherence length ξ. For example, in square mesoscopic samples, vortex configurations try to best match the C_4 symmetry. When there is only one vortex in the sample ($L = 1$ state where L is the winding number or vorticity), the vortex always sits in the center of the sample in order to balance the boundary effect from all sides. For the $L = 2$ state, two vortices sit on the diagonal such that the vortex-vortex separation is maximal in order to minimize the intervortex interaction. A giant vortex with $L = 2$ can be induced when the boundary confinement pushes two single vortices together, as predicted theoretically[31] and observed experimentally.[52, 53, 157] For $L = 3$ state, because of its incompatability with the four-fold symmetry, the theory predicts that the ground state corresponds to an anti-vortex sitting at the center surrounded by four vortices.[32, 33, 130] In short, the symmetry of the sample largely determines the vortex configurations when the size of the superconductor is reduced.

However, the properties of nanoscale superconductors, whose sizes are of the order of the Fermi wavelength λ_F, are very different from those of mesoscopic superconductors. This is because the distance between electronic levels becomes comparable to the superconducting energy gap due to quantum confinement [65]. As a consequence, the number of Cooper pairs is suppressed which leads to the quantum-size effect (QSE),[67, 92, 167] quantum-size cascades,[95] the shell effect[86] and inhomogeneous spatial distribution of the order parameter.[67] The latter is the most important for the present work because it is expected to strongly influence the vortex states in nanoscale superconductors. A similar behavior was shown for an isolated

vortex core, where oscillations of there order parameter on the order of the Fermi wavelength were predicted. [168]

Inhomogeneous superconductivity has been studied in various systems in the last decades and shows more complex behavior than homogeneous ones. It is known that vortices tend to migrate and get pinned in areas where superconductivity is suppressed.[131] The reason is that it is more favorable energetically for a vortex to suppress the superconducting order parameter in a region where it has already been suppressed, although sometimes vortices can be pinned where the gap is large.[132] Some three-dimensional (3D) samples can also be treated as inhomogeneous systems.[127, 148–150, 169–171] For example for a 3D tip geometry, an asymmetric $L = 1$ vortex state can be the ground state because the thick region prevents the vortex from penetrating it.[169] In multi-layered superconductors, vortices enter first and reside favorably in the weak layers. Then, vortices will penetrate into the strong layers only after weak layers become saturated and various vortex clusters and asymmetric vortex states are induced.[153] Also, the fabrication of anti-dots in superconductors results in a spatially varying superconducting energy gap with a barrier at the interfaces. In these systems, the combination of the giant vortex, multi-vortex and anti-vortex states can be found as ground state, which depends strongly on the detailed geometry of the antidots. [145, 172, 173]

For conventional superconductors, $k_F\xi_0 \approx 10^3$ (k_F is the Fermi wave vector and ξ_0 is the BCS coherence length), systems of size comparable to λ_F will not be large enough to host a vortex (being much smaller than the coherence length). However, materials with small coherence lengths, e.g. high-T_c cuprate superconductors, will have $k_F\xi_0 \approx 1 - 4$ and therefore in such systems it is possible to obtain vortex states in the quantum confinement regime. Another such system is a graphene flake deposited on top of a superconductor. Because of the proximity effect, Cooper pairs will diffuse in graphene[133–136]. In graphene the scattering length is large, therefore such a system is in the clean limit. More importantly, near the Dirac point, the Fermi wavelength is very large and can be easily manipulated by doping. In other words, $k_F\xi_0$ can be tuned, which will allow for different vortex patterns to be realized in the graphene flake in the quantum confinement regime, but for more accessible sample sizes (even above 100nm). A similar configuration was also recently proposed by Knopnin et. al in Ref.[174]. Yet another system where effects of quantum confinement on vortex matter can be probed systematically are the optically trapped cold gases [147], which are nowadays

extremely controllable.

For studying such nanoscale systems, microscopic Bogoliubov-de Gennes (BdG) theory is required. Previous works used the BdG method to focus on isolated single vortex lines[116, 120, 168, 175], giant vortices[122, 139] and to describe the local density of states modifications due to vortex-vortex and vortex-boundary interactions[138, 141, 176, 177] but are in the mesoscopic limit as opposed to the nanoscale limit considered here. Although Refs. [166] and [178] studied the ground vortex states in a mesoscopic-nanoscopic crossover region by solving the BdG equations self-consistently, quantum confinement effects do not play any role. Recently, we investigated [179] the vortex states in nano-scale superconducting squares. We found unconventional vortex states in the quantum limit due to shape-induced resonances in the inhomogeneous Cooper-pair condensate. Vortex-antivortex structures, asymmetric vortex states and vortex clusters were found as ground states over a wide range of parameters. They are distinct from previous results obtained in mesoscopic superconductors using the GL theory. However, there are still several aspects that remained unclear. For example, how does the size of the sample affect the vortex states in nanoscale superconductors? Under which conditions, does one recover the conventional GL results? Why are the antivortex states more stable in the nanoscale limit while giant vortex states are unfavorable? How do the vortex states change if temperature is increased?

In order to answer these questions, in this paper, we study vortex states in nanoscale superconducting squares systematically. Vortex states for different sample sizes, $k_F\xi_0$ parameters and temperatures T are investigated and the stability of the symmetry-induced vortex/anti-vortex molecules is discussed. More unconventional states, very different from the ones obtained within GL theory, are found. This study is therefore fully complementary to what is known for vortex matter in superconductors.

The chapter is organized as follows. In Sec. 4.2, we introduce the theoretical approach, i.e. the BdG approach for a square geometry. In Sec. 4.3, we present the inhomogeneous superconducting state in the absence of the magnetic field in order to better understand the QSE in nano-scale superconductors. In Sec. 4.4, the ground states and metastable states are studied at zero temperature and on the sample size dependence of the vortex states is discussed. In Sec. 4.5, the finite temperature ground states are studied. In Sec. 4.6, we discuss the generation of vortex/anti-vortex molecules and study the structure of the vortex core. Finally, we summarize our findings in

Sec. 4.7.

4.2 Theoretical formalism

In the presence of a magnetic field, the Bogoliubov-de Gennes (BdG) equations read

$$\begin{pmatrix} H_e & \Delta(\mathbf{r}) \\ \Delta(\mathbf{r})^* & -H_e^* \end{pmatrix} \begin{pmatrix} u_n(\mathbf{r}) \\ v_n(\mathbf{r}) \end{pmatrix} = E_n \begin{pmatrix} u_n(\mathbf{r}) \\ v_n(\mathbf{r}) \end{pmatrix}, \tag{4.1}$$

where $u_n(v_n)$ are electron-(hole-)like quasi-particle eigen-wave functions and E_n are the quasi-particle eigen-energies. The single-electron Hamiltonian reads $H_e = \frac{1}{2m}(\frac{\hbar\nabla}{i} - \frac{e\mathbf{A}}{c})^2 - E_F$ with E_F being the Fermi energy and $\mathbf{A}$ the vector potential (we consider a gauge such that $\nabla \cdot \mathbf{A} = 0$). Furthermore, we take the electron band-mass to be isotropic (i.e., $m_x = m_y = m$) and a circular Fermi surface. The pair potential is determined self-consistently from the eigen-wave functions and eigen-energies:

$$\Delta(\mathbf{r}) = g \sum_{E_n < E_c} u_n(\mathbf{r}) v_n^*(\mathbf{r})[1 - 2f_n], \tag{4.2}$$

where g is the coupling constant, E_c is the Debye energy, and $f_n = [1 + \exp(E_n/k_BT)]^{-1}$ is the Fermi distribution function at temperature T.

We consider now a two-dimensional superconducting square with the size W. The confinement imposes Dirichlet boundary conditions (i.e. $u_n(\mathbf{r}) = 0,\ v_n(\mathbf{r}) = 0,\ \mathbf{r} \in \partial S$) such that the order parameter vanishes at the surface. In an extreme type-II superconductor (and/or very thin sample), it is reasonable to neglect the contribution of the supercurrent to the total magnetic field.

In this case, the free energy [142, 143] of the system is given by

$$\begin{aligned} F &= \sum_n 2E_n f_n + 2k_BT[f_n \ln f_n + (1 - f_n)\ln(1 - f_n)] \\ &+ \int dr \left[-2 \sum_n E_n |v_n|^2 + 2\Delta(r) \sum_n u_n^* v_n [1 - 2f_n] \right. \\ &- \left. g \sum_n u_n^* v_n (1 - 2f_n) \sum_{n'} u_{n'} v_{n'}^* (1 - 2f_{n'}) \right], \end{aligned} \tag{4.3}$$

Sample	I	II	III
E_F/F_0	4	9	25
E_c/F_0	$30/\pi$	$30/\pi$	$50/\pi$
Δ_0/F_0	1.245	1.85	3.14
$k_F\xi_0$	2.04	3.09	5.07

Table 4.1: The parameters of the considered sample. Coupling constant $g = 0.4343$ and E_F is measured from the bottom of the quadratic band.

where the spatial dependence of u_n and v_n is implicit.

In order to solve Eqs. (4.1) and (4.2) numerically, we expanded the wave functions u_n and v_n as

$$\begin{pmatrix} u_n(\mathbf{r}) \\ v_n(\mathbf{r}) \end{pmatrix} = \sum_{j_x j_y \epsilon \mathbb{N}^+} \varphi_{j_x,j_y}(x,y) \begin{pmatrix} u^n_{j_x j_y} \\ v^n_{j_x j_y} \end{pmatrix}, \tag{4.4}$$

where the basis set

$$\varphi_{j_x,j_y}(x,y) = \frac{2}{W} \sin\left(\pi j_x \frac{x}{W}\right) \sin\left(\pi j_y \frac{y}{W}\right) \tag{4.5}$$

is the basis eigen-states of the Hamiltonian H_e in the absence of the magnetic field. The corresponding eigen-energies of such states are $T_{j_x j_y} = \frac{\hbar^2}{2m}(\frac{\pi}{W})^2(j_x^2 + j_y^2) - E_F$. Through comparison with results obtained by using the finite difference method, we found that the results are converged when we include the states with energies as large as $\Phi/\Phi_0 + 5$ times the cutoff energy E_c, i.e. $T_{j_x j_y} \in (\Phi/\Phi_0 + 5) \times [-E_c, E_c]$ where Φ_0 is the flux quantum and Φ the flux through our sample.

In our numerical investigations, we restrict ourselves to the three materials (or samples) with parameters given in Table 4.1. For convenience, we measure the distance in units of the bulk coherence length at zero temperature ξ_0 and the energy in units of $F_0 = \hbar^2/2m\xi_0^2$. Here, $\xi_0 = \hbar v_F/\pi\Delta_0$ where v_F is the Fermi velocity and Δ_0 is the bulk value of the order parameter at zero temperature. Note that E_F and Δ_0 are not independent when $F_0 \propto \Delta_0^2/E_F$ up to a constant.

To find the different vortex configurations, which include all stable states, we search for the self-consistent solutions in the following two steps. (1) Global scanning: Starting from any reasonable vortex state (usually, we start from the Meissner state at $\Phi/\Phi_0 = 0$), we slowly sweep up/down the applied

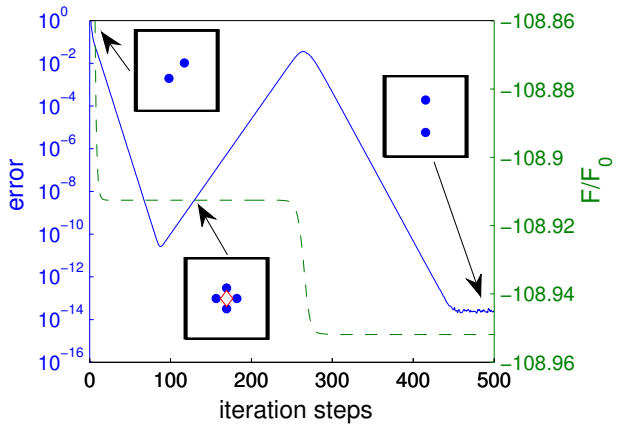

Figure 4.1: Error (solid line) and free energy (dashed line) as a function of iteration steps for sample II for $W/\xi_0 = 5$ at $\Phi/\Phi_0 = 5$ and $T/T_c = 0$. Three insets show the initial, intermediate and final vortex configurations. The solid dots and open diamonds in the insets indicate $L = 1$ vortex and $L = -2$ giant antivortex, respectively.

flux with regular intervals $0.1\Phi_0$ and recalculate the superconducting states each time, until a new state is found. Then, we repeat the sweeping process from the new state until no new vortex configurations appears. (2) Special initial states: Starting from usual states obtained in GL theory[144], we sweep up/down the applied flux. If a new state appears, we repeat the step (1). In such a way, we are able to trace back and forth all found vortex states in the whole region of their stability and make sure that the usual GL states are always considered.

The minimum tolerance in the change of the order parameter between two steps in the self-consistent iteration is

$$max\left\{\left|\Delta^i(x,y) - \Delta^{i-1}(x,y)\right|\right\} < 10^{-13} \tag{4.6}$$

where Δ^i and Δ^{i-1} is the order parameter at the i^{th} and $i-1^{th}$ iteration. We use the absolute tolerance since the relative tolerance can be abnormally high in the vortex core where $|\Delta| \to 0$. This is quite strict when we compared to $|\Delta_0|$ but is necessary in order to ensure the precision in finding the true ground states in the BdG calculation. We show an example the evaluation of the vortex configuration for sample II and $W/\xi_0 = 5$ at flux $\Phi/\Phi_0 = 5$. Based on the GL theory, the ground state of $L = 2$ for such a system should be

giant vortex state or multi vortex state (for larger squares) where two vortices sit on the diagonal of the sample. We start the calculation with such multi vortex state as initial state. As seen from the Fig. 4.1, the vortices merge into a vortex anti-vortex molecule and the result converges quickly. The error between each steps reach as low as 10^{-11}. However, the error increases gradually when we continue the self-consistent procedure. After second-order phase transition, the new state with two vortices sitting parallel to one of the sides has lower energy. Finally, the symmetry of the state does not change and the error is always around 10^{-14} which comes from non-physical factors, i.e. numerical accuracy.

In the calculation, we found some situations where results do not converge and this usually comes from the change in the number of the quasi-states contained in the Debye window. To avoid this, we set the smearing energy E_S for the quasi-states. Then, the self-consistent condition reads

$$\Delta(\mathbf{r}) = g \sum_{E_n>0} u_n(\mathbf{r}) v_n^*(\mathbf{r})[1-2f_n] \times f(E_n - E_c), \tag{4.7}$$

where $f(E_n - E_c) = [1 + \exp(\frac{E_n - E_c}{E_S})]^{-1}$ is the Fermi distribution function. Note that the summation in Eq. (4.7) is over the whole positive spectrum. The choice of E_S is empirical. It should be enough small in order not to affect the results. Meanwhile, it should be enough large to make the result converge through the iteration. Our experience show that $E_S/F_0 = 0.2267$ is suitable for our current work.

4.3 Spontaneous inhomogeneous superconductivity induced by quantum confinement

First, we study the spatial distribution of the order parameter as a function of sample size in the absence of the magnetic field since the vortex configurations will be strongly affected by that distribution once the magnetic field is applied. In Fig. 4.2 contour plots of the order parameter $\Delta(x, y)$ and the corresponding diagonal profiles are shown for sample I-III with different sizes. As expected, all the order parameters are fourfold symmetric and show Friedel-like oscillations in space which result in four well defined peaks

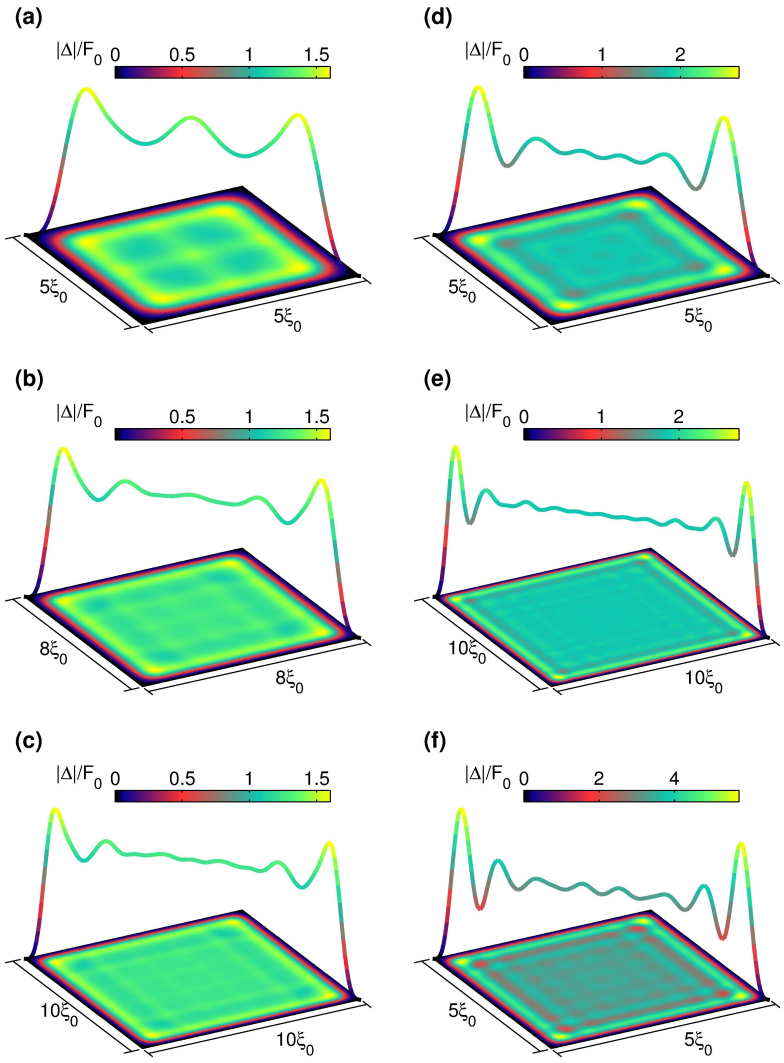

Figure 4.2: Contour plots of the order parameter $\Delta(x, y)$ with the corresponding diagonal profiles in the absence of applied magnetic field. Panels (a)-(c) are for sample I with sizes $W/\xi_0 = 5, 8, 10$, respectively. Panels (d) and (e) are for sample II with sizes $5\xi_0$ and $10\xi_0$, respectively. Panel (f) corresponds to sample III with size $5\xi_0$.

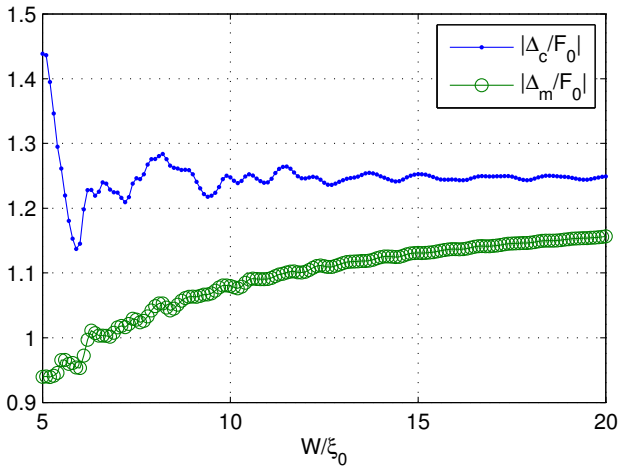

Figure 4.3: Size dependence of the order parameter in the center of the sample $|\Delta_c|$ and the spatially averaged $|\Delta_m|$ for sample I.

at each corner. Hence, the superconductivity is inhomogeneous. For example, Figs. 4.2 (a)-(c) show the results for sample I with size $W/\xi_0 = 5, 8, 10$, respectively. For $W/\xi_0 = 5$, there are three oscillations in the order parameter along the diagonal and the resonant central peak prevents vortex from sitting here. However, the profile of the order parameter can be changed dramatically when the size of the sample changes. For $W/\xi_0 = 8$ [shown in Figs. 4.2(b)], we found that the central peak disappears and a relatively flatter area generates in the center. When W/ξ_0 is increased to 10, the flat area enlarges and the Friedel-like oscillations can be neglected at center when we compared it with oscillations near boundary. It indicates that the oscillations of the order parameter result from the quantum confinement effect (or boundary effect).

In order to study the quantum size effect on the order parameter, we show the amplitude of the order parameter in the center of the sample $|\Delta_c|$ and the spatially averaged value over the whole sample $|\Delta_m|$ for the sample I with sizes $W/\xi_0 = 5-20$ in Fig. 4.3. As seen, $|\Delta_c|$ changes dramatically with W/ξ_0 increasing and converge to $\Delta/F_0 = 1.245$ when $W/\xi_0 > 15$. At the same time, the $|\Delta_m|$ increases gradually with W/ξ_0 increasing. In principle, both of the parameters will converge as $W \to \infty$ where the boundary effect can be totally neglected. Since $|\Delta_c|$ and $|\Delta_m|$ show strong quantum size effect between $W/\xi_0 = 5$ and 10, we limit ourselves in following sections to

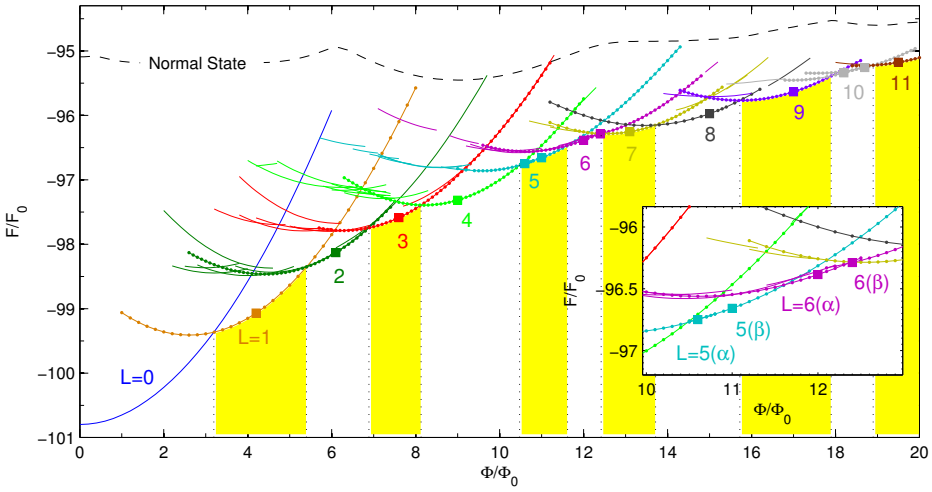

Figure 4.4: Free energy as a function of the magnetic flux through sample I with size $10\xi_0 \times 10\xi_0$. Different colors indicate the different winding numbers L and the shaded area indicates the flux range over which the vortex state with winding number L is the ground state. The vortex configurations of the ground state marked by solid squares are shown separately in Fig. 4.5 and the corresponding free energy curves are marked by dots. The inset zooms in the region where $L = 5$ and 6 are the ground states

study the samples for these particular size .

The profile of Δ is also strongly affected by $k_F\xi_0$. Figs. 4.2(d) and (e) show results for sample II with size $W/\xi_0 = 5$ and 10 and (f) is for sample III with size $W/\xi_0 = 5$. Comparing to the sample I with the same size, we found that the wave number and the amplitude of the oscillations along diagonal are larger. It indicates that the superconducting order parameter shows more inhomogeneous behavior with larger $k_F\xi_0$.

4.4 Vortex configurations at zero temperature

In this section, we consider the zero temperature case for which the system is always in the quantum limit ($T/T_c < 1/k_F\xi_0$). First, we study the sample I with size $10\xi_0 \times 10\xi_0$ and show in Fig. 4.4 the free energy of the stable vortex

states for flux $\Phi/\Phi_0 \in [0, 20]$. Different curves (colors) represent states with different winding number L and the states among them which reached the ground state are marked by dots. Vertical lines and shadows show the flux range for each L state as the ground state. The top dashed line stands for the free energy of the system in the normal state when the coupling constant g is set to zero. When compared with the GL theory[144], one of the differences is that the free energy of the normal state depends on the magnetic field while it is a constant in GL theory. The reason is that the energy levels of the confined electrons are different for different magnetic fields. In our case, the change of the energy is relatively small when compared with the energy gap (energy difference between the normal state and the superconducting state) especially in weak fields. Although the shown energy curves look conventional, there are significant differences with the GL theory.[144]

By sweeping the magnetic field up and down, we can get the full energy spectrum and the corresponding vortex states. For a certain magnetic field, it is common to have more than one converged solution. The lowest energy state is the ground state while the states with higher energy are referred to as metastable states. In Fig. 4.5, we show the contour plot of the absolute value of the order parameter of the corresponding ground states for various winding numbers.

As can be seen from Fig. 4.4, the system favors states with winding numbers $L = 1, 4, 8$ and 9 because they have relatively large ground state flux range (excluding the Meissner state). From Fig. 4.5, we observe that these states have fourfold symmetry which is compatible with the sample geometry. One interesting feature of this system is the richness of metastable states. These states appear for all winding numbers L except $L = 0$ and 1. The number of metastable states reaches a peak for $L = 4$ and equals 11. From the free energy curves, we notice that the energy difference between the ground state and the metastable states can sometimes be very small. This makes the ground state difficult to find in simulations unless we sweep the field up and down many times. We also note that most metastable states are focused at lower magnetic fields from the corresponding ground state flux range. The reason is that vortices get easily stuck at the boundary due to the pronounced oscillations of the order parameter. For the same reason, their stability range is narrower due to asymmetry.

The number of metastable states decreases for higher L. In this case, the shorter distances between vortices cause strong interaction between them. This limits the choice of stable positions for vortices and therefore the number

of metastable states are lower. Due to this reason, metastable states are less favorable for smaller samples because of easy saturation with vortices. For example, no metastable states were found in sample I with size $W/\xi_0 = 5$.

4.4.1 Ground states

Next we discuss the ground states configurations for different vorticities in more detail. For the $L = 1$ state, shown in Fig. 4.5, the vortex sits at the center of the sample which is compatible with the conventional picture. Although such result is observed for different parameters of the sample, the state with diagonal location of the vortex can also be found in some cases.[179] It is clear that the order parameter around the vortex core is suppressed and the profile shows the competition between C_4 symmetry and C_∞. It means that the vortex has long range (longer than ξ_0) interaction with other objects such as the other vortices and/or boundaries.

By increasing the flux to $\Phi/\Phi_0 = 5.24$, the ground state shifts from $L = 1$ to $L = 2$ and two vortices sit along the diagonal. This again coincides with the result from GL theory, and results from the competition between the confinement imposed on vortices by the Meissner currents and the vortex-vortex repulsion. In this case, these effects can be clearly seen from the profile of the order parameter, especially from the suppressed area around the vortices. The vortex-vortex interaction suppresses the order parameter mostly in the area between them. This can not be found in GL theory because the order parameter is always smooth and changes slowly in space. The state with $L = 3$ shown in Fig. 4.5 becomes the ground state when the field applied flux is between $\Phi/\Phi_0 = 6.9$ and 8.12. It resembles the multi-vortex state obtained within GL theory where the three vortices are at the apices of a equilateral triangle. However, the perpendicular bisector of the triangle always coincides with one of the diagonals of the square sample in GL theory while it is parallel to one of the edges in our case. This is because the grid-like pattern in the inhomogeneity of the order parameter imposes preferential positions for the vortices inside the square. The state $L = 4$ has a similar feature but the configuration is compatible with the GL result.

From these states, we conclude that when the GL vortex configuration, which minimizes the vortex-vortex and vortex-boundary interaction, matches the oscillation pattern due to quantum confinement, then the state has a wider flux stability range.

Two ground states, $L = 5(\alpha)$ and $L = 5(\beta)$, are found for $L = 5$ in the

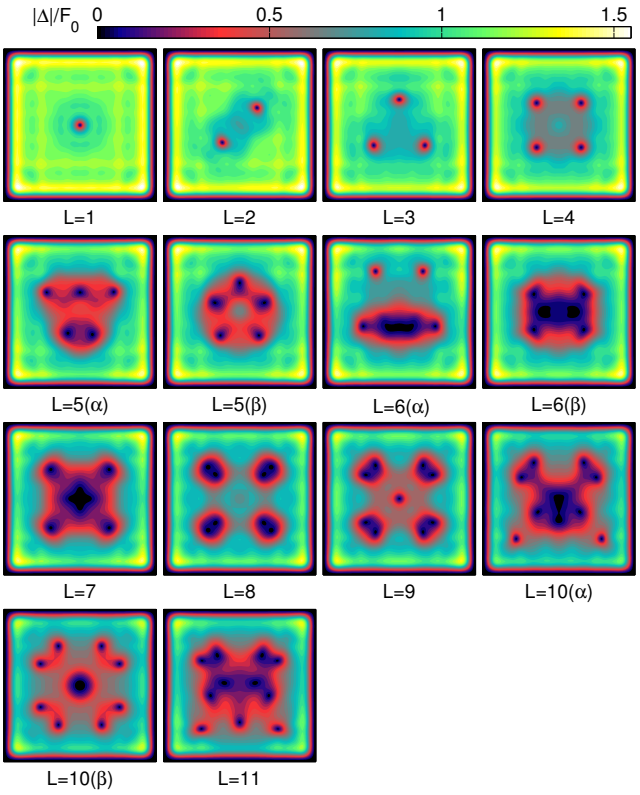

Figure 4.5: Contour plot of the amplitude of the order parameter for the ground states marked by solid squares shown in Fig. 4.4. $L = 10(\alpha)$ and (β) are for flux $\Phi/\Phi_0 = 18.2$ and 18.7, respectively. Darkest areas indicate the positions of vortices. Note that at the center an anti-vortex (for $L = 7$) or a giant vortex [for $L = 10(\beta)$] can spontaneously form. Note also that for some vorticities two different ground states are found (at different magnetic fields).

flux ranges $\Phi/\Phi_0 = 10.48 - 10.78$ and $10.78 - 11.62$, respectively. Both of them have a pentagonal vortex configuration. This is because the particular shape resonance at the considered field causes the order parameter to be peaked at the center. Therefore, it costs energy for vortices to sit in the center of the sample. For the same reason, the ground states $L = 6(\alpha)$ and $L = 6(\beta)$ do not have vortices in the center. Moreover, when $L \geqslant 6$, vortices start to be compressed in the sample. If they do not form giant vortices, they will be very close to each other and form string-like structures [see $L = 6(\alpha)$ state].

States with $L = 7$, $L = 8$, $L = 9$ and $L = 10(\beta)$ shown in the panels of Fig. 4.5 have a common feature, as all of them keep the fourfold symmetry. $L = 7$ contains an antivortex at the center while $L = 9$ and $L = 10(\beta)$ have a single vortex and a giant vortex with $2\Phi_0$ at the center, respectively. The state with $L = 7$ is the only ground state which contains an antivortex. The antivortex is closely surrounded by four vortices and forms the core structure for $L = 7$. The outer shell is formed by the remaining four individual vortices sitting at four corners. States with $L = 8$ and $L = 9$ contain vortex dimers, i.e. two vortices close to each other at each corner. The fourfold symmetry makes both former states have a larger ground state flux range. $L = 10(\beta)$ also keeps the C_4 symmetry but the energy is sometimes even higher than the state $L = 10(\alpha)$, which has only C_2 symmetry. The reason is that the giant vortex costs extra energy.

In order to visualize the changes in the ground states when key parameters change, we plot the phase diagram for samples I-III for $W/\xi_0 = 5 - 10$ and $\Phi/\Phi_0 = 0 - 10$ in Fig. 4.6. Different shadings of blocks in Fig. 4.6 indicate different vortex types. The plain white background represents conventional multi-vortex states as found within the GL theory, while the blue background with square grid represents giant vortices, also compatible with the result obtained from GL theory. Asymmetric vortex states attained only by BdG theory are represented by yellow background with horizontal grid pattern. States containing parallel vortex chains, represented by orange background with vertical grid pattern, and part of the vortex-antivortex molecules represented by pink(grey) background, are new compared to GL theory.

We can conclude from Fig. 4.6 that the quantum size effect is important not only for the transition field and the stability range of the different vortex states, but also for the vortex configurations. The reason is that the oscillation patterns of the order parameter are very sensitive to $k_F\xi_0$ and may cause totally different behaviors even for two samples of identical size.

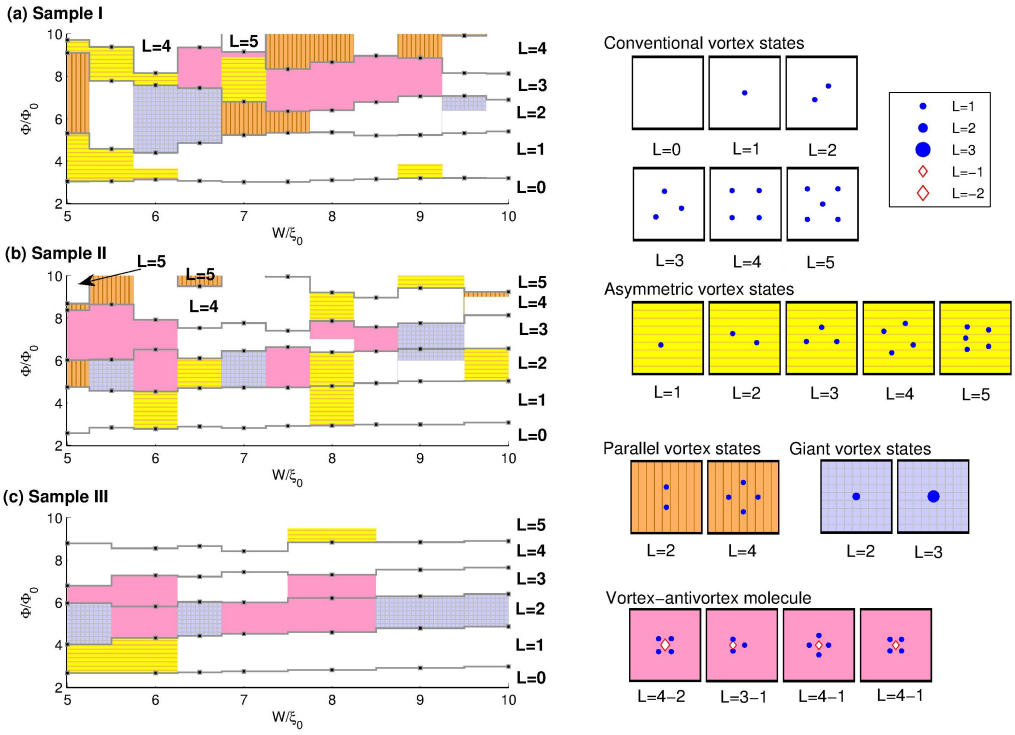

Figure 4.6: Phase diagram for samples I-III. Different shadings of the background indicate different types of vortex states. Black(blue) dots indicate vortices, and diamonds indicate antivortices in the schematic diagrams of vortex configurations (right figures). The symbols are larger when vortices contain multiple flux quanta.

As can be seen from Fig. 4.6(a) and (b), the vortex phase transition fields vary greatly with sample size W except for the phase boundary between $L = 0$ and $L = 1$ state. All the phase boundaries oscillate with W. We find that some samples favor vortex states with even winding number L while other disfavor them. For example, sample I with $W/\xi_0 = 5$ favors $L = 2$ state whereas the one with $W/\xi_0 = 7$ disfavors $L = 4$ to the point of non-existance. When W becomes large, the transition fields start to converge and the flux stability range of each L state will be roughly one flux quantum.

When compared to samples I and II, sample III (with large $k_F\xi_0$) shows a more conventional picture. Moreover, the phase transition field increases only slightly with increasing W. It means that for large $k_F\xi_0$, the quantum size effect on the transition field, at least when winding number L is small, can be neglected. Nevertheless, a plethora of different vortex configurations is found. For example, an asymmetric $L = 1$ state is found in all three samples. Moreover, sample I always shows asymmetric states when $W/\xi_0 < 6$. One other interesting phenomenon is that, for $L = 2$, sample II can host all five types of vortex states with W increasing.

From the phase diagram in Fig. 4.6, we notice that nanoscale superconductors favor anti-vortices and disfavor giant vortices. For example, the giant vortex state appears for $L = 2$ in sample II with $W/\xi_0 = 7$. Based on GL theory, only smaller samples will exhibit a giant vortex configuration. However, when $W/\xi_0 < 7$, the two individual vortices form an asymmetric vortex state. On the other hand, we find that the probability of forming anti-vortices is much higher than in GL theory. In GL case, antivortex states usually appear for $L = 3$ when four vortices are at the four corners and surround a centered antivortex. Usually the distance between vortices and the antivortex is small (less than ξ). In the BdG calculation, at least two more antivortex states can be found. One is still the $L = 3$ state and the antivortex is still at the center but four vortices are at the edges instead of the corners. This configuration was first presented by us in Ref. [179] where we showed that the size of the vortex/anti-vortex(V-aV) molecule is larger than the one obtained with GL theory. The other antivortex state appears for $L = 2$. In this case, the four vortices still sit at four corners but the centered antivortex carries two flux quanta, e.g. it is a giant antivortex! Due to the strong vortex-antivortex interaction, the size of such V-aV molecule is small.

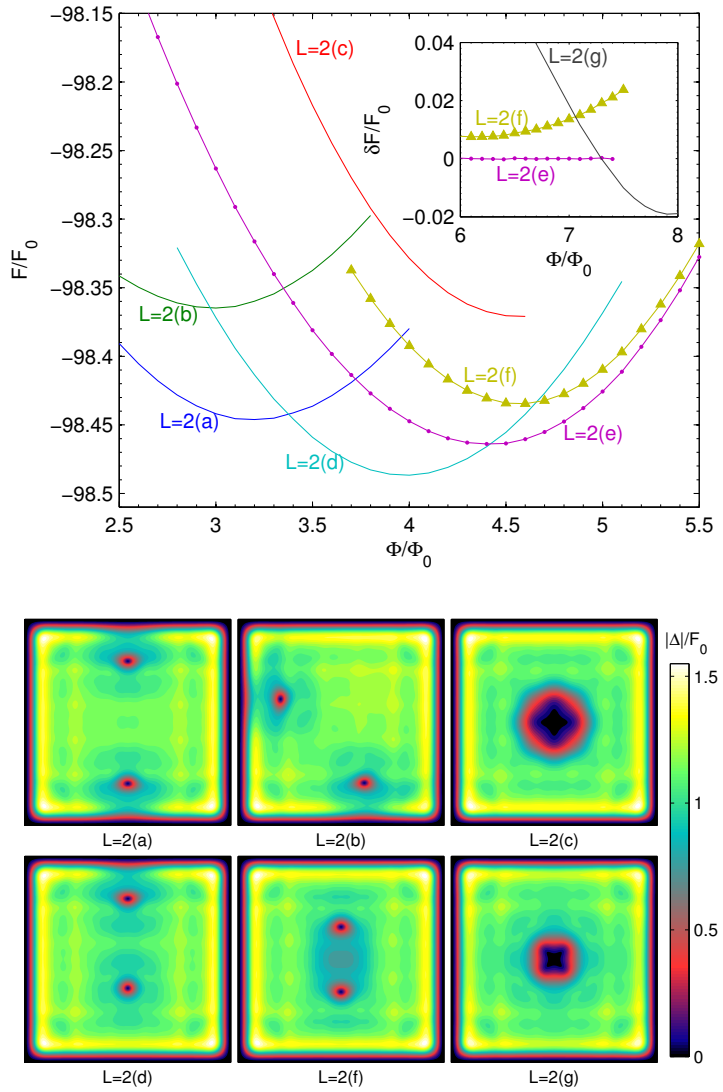

Figure 4.7: Free energy curves of states with $L = 2$ in sample I with size $W/\xi_0 = 10$ (top panel) and the corresponding contour plots of the order parameter (bottom panel). Note that the contour plot of the ground state $L = 2(e)$ is shown in Fig. 4.5. The inset shows the energy difference between the ground state $L = 2(e)$ and the metastable states $L = 2(f)$ and $L = 2(g)$ at higher field.

4.4.2 Metastable states

Next we will briefly discuss the metastable states of this system. To do this, we start from sample I with $W/\xi_0 = 10$. Metastable states are important in the BdG formalism because the energy difference between the ground and the metastable states can be very small. This suggests that these states could be easily found in experiments. Alternatively, some metastable states can become ground states as the parameters are changed.

All six found metastable states for $L = 2$ and their free energy curves are shown in Fig. 4.7. The state $L = 2(f)$ is similar to the ground state $L = 2(e)$, but rotated over 45°, hence their free energies are very close to each other. Actually, the difference in the orientation of the vortex pattern always results in a small difference in energy. State (f) is not obtained within the GL theory. In our case, due to the shape-resonant inhomogeneity of the order parameter, the rotation of the vortex pattern to the ground-state configuration is prevented by the spatial oscillations of the order parameter.

The metastable state $L = 2(g)$ is only stable at higher field and its free energy is very close to the ground state $L = 2(e)$. Therefore we zoomed on the energy difference in the inset of Fig. 4.7. From the figure, one sees that the energy of the $L = 2(g)$ state is lower than the ground state, $L = 2(e)$, when the applied flux is larger than $\Phi/\Phi_0 = 7.3$. In fact, the state can exist even up to $\Phi/\Phi_0 = 10$. From the vortex configuration shown in Fig. 4.7, we find that this state is a giant vortex. Such a state has been predicted by the GL theory because the magnetic field pushes the two vortices towards each other and makes them merge into a giant vortex. Usually, the phase transition between the multi vortex state and the giant vortex state is continuous (second-order). However, the barrier induced by the inhomogeneity of the order parameter leads to a first order phase transition in our case. One more difference between the BdG giant vortex and the one in GL theory is its core structure. Due to the shape resonances, the contour plot of the core shows a diagonal cross shape while the giant vortex core in the GL case is always circular. Furthermore, the giant vortex state in our results has two allotropes: see state $L = 2(c)$, compared to the state $L = 2(g)$. The $L = 2(g)$ state exists up to higher field while $L = 2(c)$ only exists in lower field. Hence, the size of the giant vortex seen in $L = 2(c)$ is larger than the one seen in $L = 2(g)$. Another difference between them is the orientation of the core. $L = 2(g)$ has diagonal cross shape while the state $L = 2(c)$ has edge cross shape.

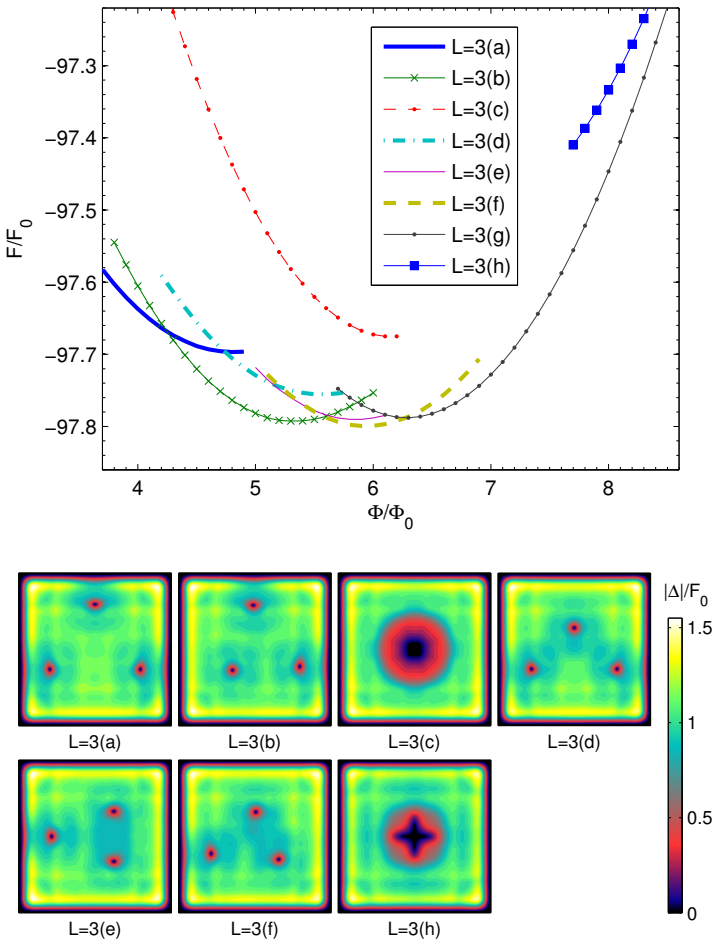

Figure 4.8: Free energy curves of states with $L = 3$ in sample I with size $W/\xi_0 = 10$ and the corresponding contour plots of the order parameter. The contour plot of the ground state $L = 3(g)$ is shown in Fig. 4.5.

Other three metastable states $L = 2(a)$, $L = 2(b)$ and $L = 2(d)$ are observed only in lower field. They have in common the fact that at least one vortex is stuck at the boundary since the Meissner current pushes the vortex outward at low fields. It is obvious that they have lower energy when the applied field is lower. The energy of state $L = 2(a)$ is always lower than the one of state $L = 2(b)$ because of the longer distance between the vortices. As is usual in mesoscopic superconductors, vortices in these states avoid to be located at the very corners of the sample, due to strong local superconductivity there.

For the $L = 3$ metastable states, the results are summarized in Fig. 4.8. The state $L = 3(h)$ is a V-aV state and exists only in higher field while the giant vortex $L = 3(c)$ only exists in lower field. Note again that the energy of the giant vortex states is much higher than the other metastable states with three single vortices. $L = 3(f)$ has lowest energy for $L = 3$ around $\Phi/\Phi_0 = 6$, when there is one vortex located at the boundary. States $L = 3(b)$ and $L = 3(a)$ follow when the field decreases and there are two and three vortices stuck at the boundaries, respectively. States $L = 3(d)$ and $L = 3(e)$ are disfavored and have higher energy due to the close distance between vortices. Note again that no vortex sits at the corners in this states.

States with $L = 4$ show a wide ground state flux range and 11 different metastable states, which is the largest variety of all L vortex states. From Fig. 4.9, we find that the metastable states concentrate around the applied flux $\Phi/\Phi_0 = 6.5$.

For low fields, we conclude again that vortices are close to the surface and these states are always the lowest energy state for a given L state at low fields. States $L = 4(b)$ and $L = 4(c)$ have C_4 symmetry and all of the four vortices are trapped close to the boundary. Please note that in the state $L = 4(a)$ four vortices sit at the corners. This kind of state is rare in the BdG results because corners give the highest potential energy contribution for vortices. From the free energy curve of the state $L = 4(a)$, we can find that the slope of the energy curve is opposite to the other $L = 4$ states [such as $L = 4(b)$] in this field range. This indicates that vortices are repelled by the Meissner current in order to balance the inward force the vortices experience from the corner. When the field is too low, a vortex is expelled from the sample and the state jumps to a $L = 3$ state. The vortex configuration $L = 4(f)$ has been found experimentally in conventional mesoscopic superconductors[30] but was a result of the presence of pinning sites. This state can not be obtained in plane squares within the GL theory . Another state to notice is

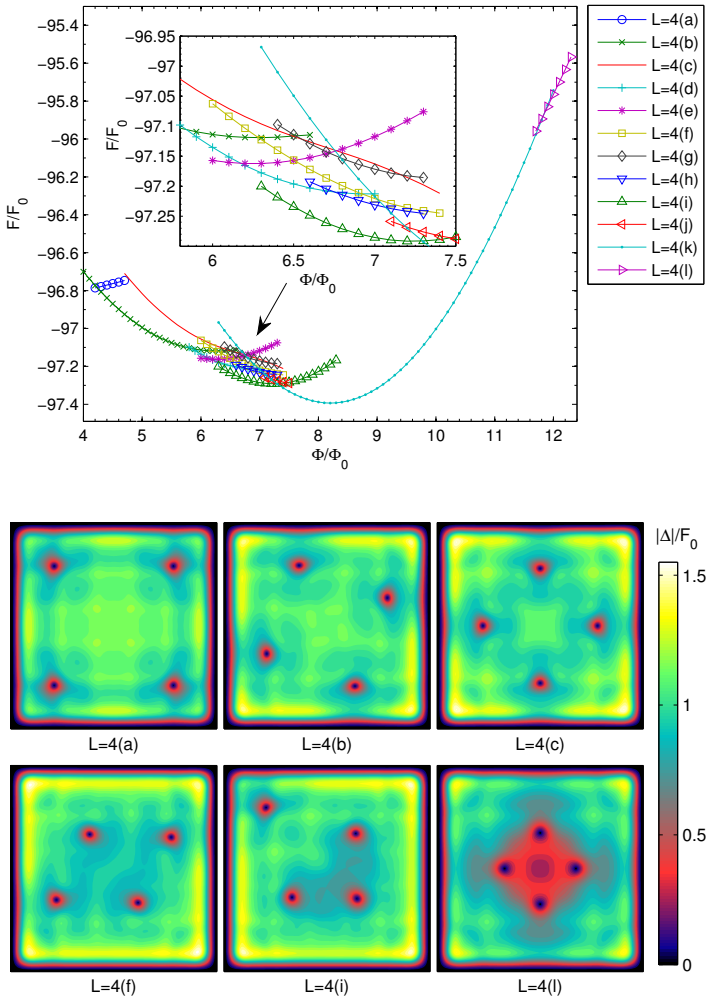

Figure 4.9: Free energy curves of vortex states with $L = 4$ in sample I with size $W/\xi_0 = 10$ and the contour plots of the order parameter of selected vortex states. Inset shows details of the free energy curve around $\Phi/\Phi_0 = 6.5$. The contour plot of ground state $L = 4(k)$ is shown in Fig. 4.5.

$L = 4(i)$ whose energy curve does not cross any other $L = 4$ curve. When the superconductor is in this state and the field is swept down, this state will be the first to jump to the $L = 3$ state. This is understandable from the vortex configuration of $L = 4(i)$ because the vortex at the corner is easily expelled when field is lowered.

At high fields only one metastable state exists $L = 4(l)$. It can be seen as the state obtained after a 90 degrees rotation of the ground state-$L = 4(k)$. This is a consequence of the fact that the inhomogeneous pattern of the order parameter changes with field. At such a high field, the corner vortex position in state $L = 4(k)$ becomes unstable, which forces the vortices to sit at the edges, similar to the $L = 4(l)$ case. At the same time, the strong field pushes vortices closer together so that the distance between vortices in $L = 4(l)$ is shorter than the one in the ground state $L = 4(k)$.

4.5 Vortex states at finite temperature

So far, all our calculations were done at zero temperature, $T/T_c = 0$, where T_c is the bulk critical temperature at zero flux $\Phi/\Phi_0 = 0$. In what follows, we investigate the effect of temperature on the vortex configuration. First, we show all the vortex states for the flux range $\Phi/\Phi_0 \in [0, 10]$, for sample I with size $W/\xi_0 = 10$ at $T/T_c = 0.6$ where the system is NOT in the quantum limit since $T/T_c > 1/k_F\xi_0$. The corresponding free energy curve as a function of flux is presented in Fig. 4.10. Contrary to the results for $T/T_c = 0$, which were shown in Fig. 4.4, the figure looks more conventional (similar to the results obtained by GL theory in Ref. [144]) and there is only one stable state for each winding number L. Moreover, only giant vortex states are found in this case for $L \geqslant 2$. For the size of the square sample considered here, $W \approx 10\xi$, GL theory[144] predicts that multi-vortex states should exist. Here we find instead that multi-vortex states are absent since ξ increases as temperature increases.

In order to see how temperature affects the coherence and the profile of the superconducting order parameter, we show the order parameter for $\Phi/\Phi_0 = 4$ and $L = 1$ in Fig. 4.11. The diagonal profile of $|\Delta|$ at $T/T_c = 0$ shows the strongest Friedel-like oscillations. As temperature increases to $T/T_c = 0.2$, the profile is similar to the one obtained at zero temperature, but with less oscillations at the vortex core. Both cases are in the quantum limit and the order parameter shows rapid variation in the core. When temperature

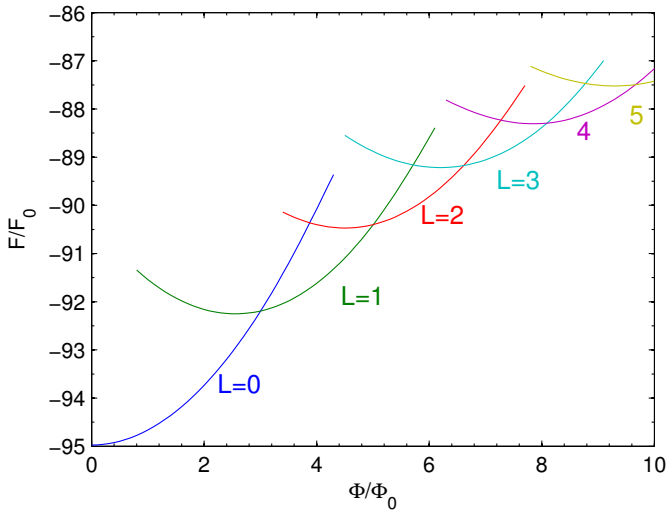

Figure 4.10: Free energy as a function of the magnetic flux through the square sample I for size $W/\xi_0 = 10$ and $T/T_c = 0.6$.

reaches $T/T_c = 0.6$, we find that both the average and the oscillations of the absolute value of the order parameter are suppressed which indicates that the vortex states become more conventional. Finally, the order parameter is smooth at $T/T_c = 0.8$ and the GL results are approached.

As seen from the Fig. 4.11, the coherence length, which represents the vortex core radius, increases with increasing temperature. As defined by Kramer and Pesch[115], we calculate the coherence length ξ_1 as

$$\frac{1}{\xi_1} = \lim_{r\to 0} \frac{\Delta(r)}{r\Delta_0} \tag{4.8}$$

where r is the distance to the vortex core. We plot in Fig. 4.12 $(\xi_0/\xi_1)^2$ as a function of temperature, T/T_c . As discussed in Ref. [120], ξ_1 can be described by $\xi(T) \propto (T_c - T)^{-1/2}$ when T is close to T_c ($T/T_c > 0.5$ in our case). In the intermediate temperature regime, there is a substantial suppression of the coherence length because of the bound states. At low temperature, the shrinkage of the coherence length stops and saturates when the system is in the quantum limit. Note that ξ_1 at $T/T_c = 0.6$ is around three times larger than the one at zero temperature. This explains why only giant vortex states can be found at such temperatures.

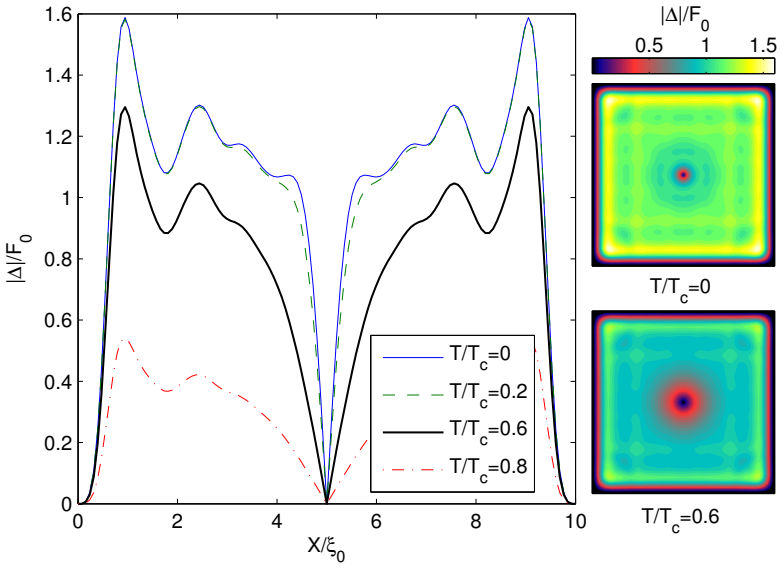

Figure 4.11: The diagonal profile of the order parameter for sample I with size $W/\xi_0 = 10$ for $\Phi/\Phi_0 = 4$ and $L = 1$ at different temperatures. The corresponding contour plots of the order parameter at $T/T_c = 0$ and $T/T_c = 0.6$ are also shown.

Fig. 4.13 shows the order parameter for sample I at $T/T_c = 0.6$ for $L = 2$ in panel (a) and $L = 3$ in panel (b), respectively. Both are giant vortex states and the C_4 symmetry grid pattern is strongly suppressed. As can be seen from the figure, the vortex cores show perfect circular symmetry, which is in agreement with the results from GL theory. Of course, the size of the vortex core shown in panel (b) is larger than the one shown in panel (a) because its vorticity is larger.

Finally, we end this section with the (T-Φ) phase diagram for lower fields for sample I with $W/\xi_0 = 5$. This is shown in Fig. 4.14. The thick black curve indicates the phase boundary between the superconducting and the normal state. When the system is in the quantum limit, for these parameters, only unconventional vortex states, such as asymmetric $L = 1$ and $L = 3$ states and edge-parallel $L = 2$ states, are found as ground states. When temperature increases, the vortex states become conventional and the C_4 symmetry of the states is always preserved. Note that the asymmetric $L = 1$ state goes through a continuous phase transition to the symmetric $L = 1$ state, which

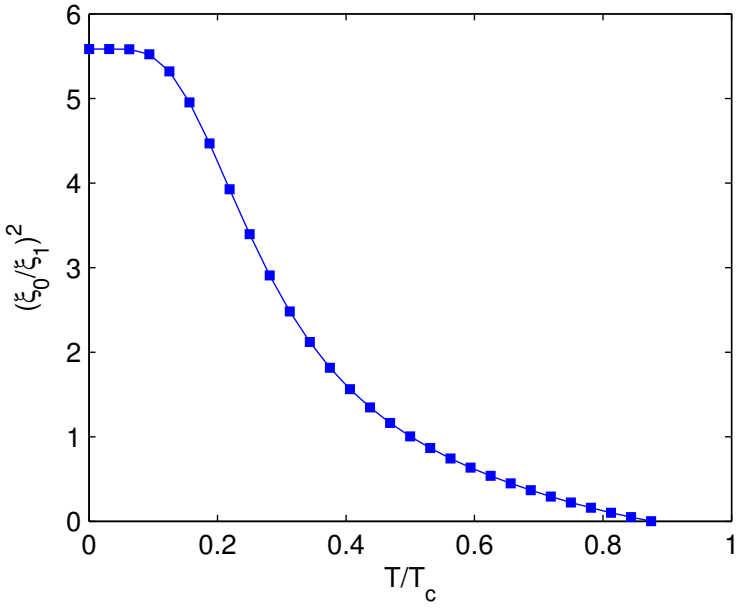

Figure 4.12: Temperature dependence of $(\xi_0/\xi_1)^2$ for sample I with size $W/\xi_0 = 10$ and $\Phi/\Phi_0 = 4$.

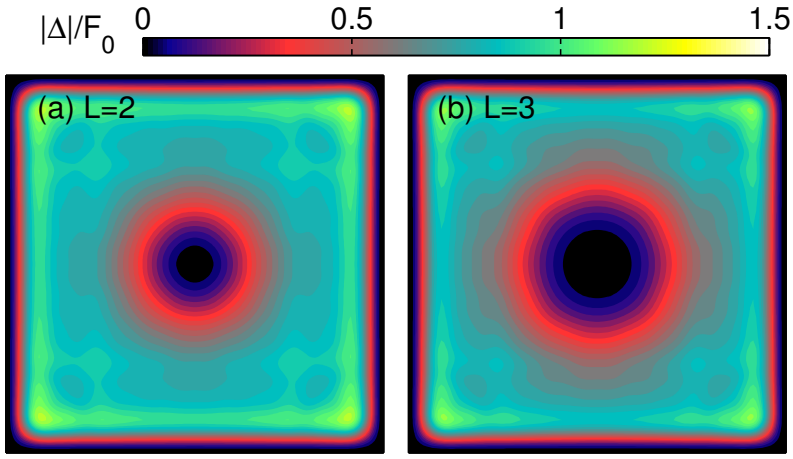

Figure 4.13: The contour plots of the order parameter for sample I with size $W/\xi_0 = 10$ at $T/T_c = 0.6$ for (a) $L = 2$ and (b) $L = 3$.

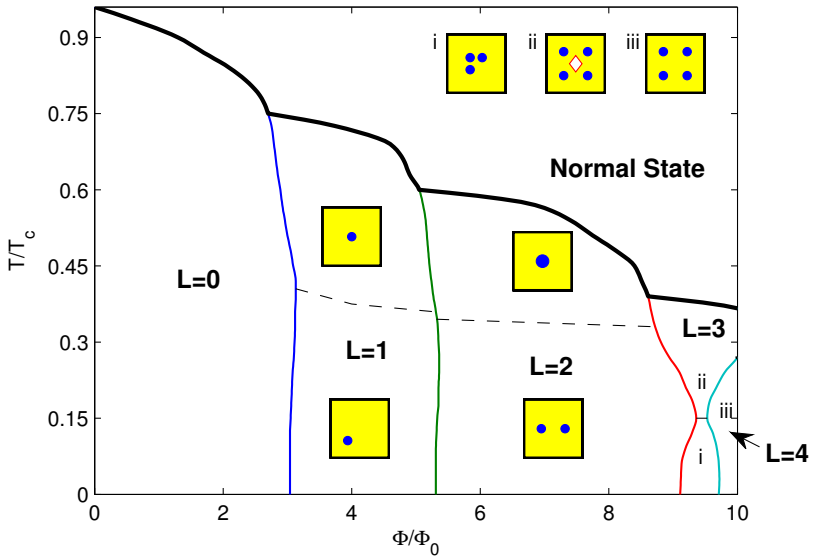

Figure 4.14: Temperature-Flux phase diagram for sample I with size $W/\xi_0 = 5$. The vortex configurations of areas (i-iii) are shown as insets in the upper right corner.

means the vortex moves gradually as the temperature changes. However, for higher winding numbers, the system usually goes through a first order phase transition. For example, the phase transition between the parallel vortex state and the giant vortex state of $L = 2$ is of first order. This is different from the GL result, where vortices merge into a giant vortex through a continuous phase transition[140]. For the $L = 3$ state, we note that the ground state flux range for the four-fold symmetric V-AV state is larger than the asymmetric one due to the compatibility of its symmetry with the geometry of the sample.

Concluding this section, higher temperature: 1) makes vortex states look more conventional (closer to the GL results); 2) smoothens the order parameter; 3) suppresses the influence of the oscillation of the order parameter and 4) increases the superconducting coherence length ξ. As a consequence, the number of metastable states is also lowered. The effect of temperature is very different (more complex) from the effect obtained by simply changing the effective size of the sample as is usually done within the GL theory.

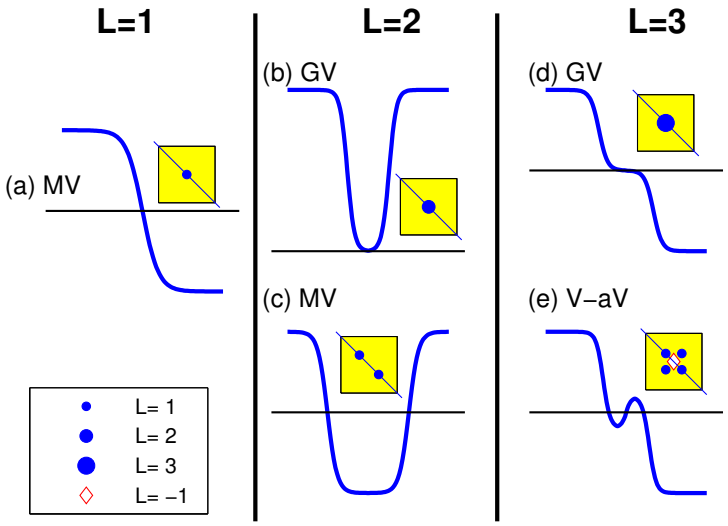

Figure 4.15: Diagonal profile of the order parameter for different vortex states in the GL theory. Blue thick curves represent the order parameter. All the phases have been adjusted such that on the diagonal the order parameter is real. The horizontal line indicates the zero of the order parameter and a vortex appears when it intersects the order parameter. Panels (a) and (c) represent multi-vortex states. Panels (b) and (d) are giant vortex states and (e) is a vortex-antivortex configuration.

4.6 Giant anti-vortex and the structure of the vortex core

In this section, we discuss the appearance and stability of anti-vortex states in the BdG theory in order to explain the existence of the giant antivortex. Actually, such a state was already found in Ref. [33, 130] through the linear GL method by introducing artificial pinning.

From the phase diagram shown in Fig. 4.6, we found that anti-vortex states are surprisingly stable within BdG theory. This is due to the fact that the grid pattern oscillation of the order parameter gives an additional contribution to the symmetry of the vortex states and therefore, in a square sample, the C_4 symmetry is enhanced. The other reason to form an anti-vortex is that the oscillations induced by the order parameter are seen in

the vortex core where the order parameter is already suppressed. These oscillations can easily lead to a shift in the phase of the order parameter by π and, thus, result in the formation of vortex-antivortex molecules.

In order to explain this, we first discuss briefly the vortex profile in the GL theory. Fig. 4.15 shows a schematic diagram of the vortex states for different winding number L in GL theory. The diagonal profiles of the order parameters vary smoothly in space and the vortex emerges where the order parameter vanishes. Note that the phase of the order parameter is adjusted such that along the diagonal the order parameter is real. Panel (a) from Fig. 4.15 shows the simplest case when only one vortex sits at the center. As can been seen from the figure, the order parameter changes sign, which indicates the π phase shift of the order parameter. The profile is an odd function and $\Delta(r) \sim r$ near the vortex core. Panels (b) and (c) from Fig. 4.15 show the diagonal profiles for $L = 2$. Both profiles are even functions due to the 2π phase shift between the opposite corners. The order parameter exhibits $\Delta(r) \sim r^2$ property. When there is only one root, as can be seen from panel (b), the vortex is a giant one. When there are two roots, as shown in panel (c), the configurations are multi-vortex states. Similarly, the profiles of the order parameter shown in panels (d) and (e) from Fig. 4.15 for $L = 3$ show a $\Delta(r) \sim r^3$ spatial dependence. One root means that we have a giant vortex state whereas three roots represent a vortex-antivortex configuration. Note that, in order to generate the central anti-vortex, the order parameter has to oscillate around the center of the square.

Now let us move to nano-size superconductors where the BdG theory has to be used and the spatial oscillation of the order parameter cannot be neglected. As can be seen from Fig. 4.16 the oscillation plays an important role in generating vortices, especially when the value of the order parameter is comparable to the amplitude of the oscillation. For instance, panels (a) and (b) from Fig. 4.16 show the symmetric and the asymmetric $L = 1$ vortex states. The reason for the appearance of the asymmetric vortex state is the fact that the order parameter has an odd number of oscillations across the diagonal. Thus, the vortex can not sit at the center. For the $L = 2$ states, panel (c) shows a giant vortex state where the sign of the profile of the order parameter is always positive across the diagonal. However, due to the oscillations, the case shown in panel (d) of Fig. 4.16 can easily exist and shows a giant anti-vortex ($L = -2$) at the center. Further, the configurations show a large diversity for a fixed winding number L. When $L = 2$, the configuration can be $1 + 1$, $2 + 0$, $3 - 1$, $4 - 2$ and so on. Panels (e) and (f)

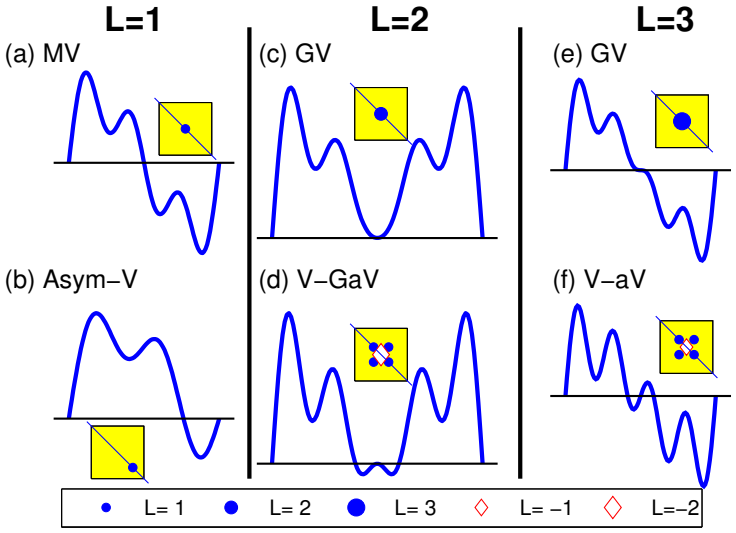

Figure 4.16: Similar as Fig. 4.15 but now for the BdG theory. Panels (a) and (b) show the symmetric and asymmetric $L = 1$ vortex states, respectively. Panels (c) and (d) are the giant vortex and vortex-giant antivortex $L = 2$ states, respectively. Panels (e) and (f) are the giant vortex and vortex-antivortex $L = 3$ configurations, respectively.

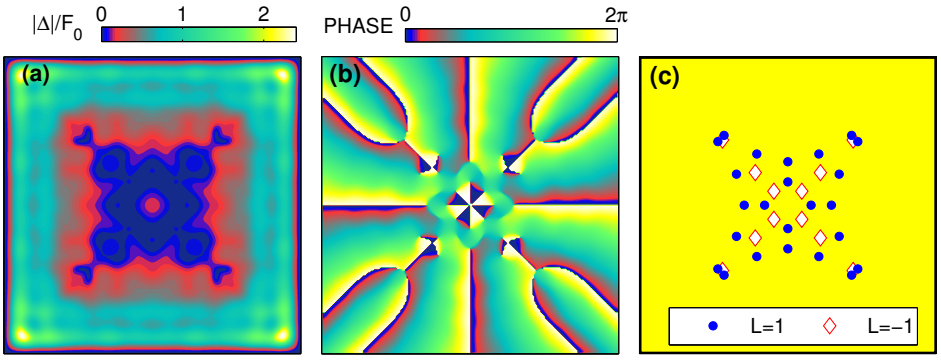

Figure 4.17: Vortex state for sample III with $W/\xi_0 = 7$ at $\Phi/\Phi_0 = 20$ with winding number $L = 12$. Panels (a) and (b) show contour plots of the order parameter and its phase, respectively. Panel (c) shows schematically the vortex configuration. Dark(blue) dots and open diamonds indicate vortices and antivortices, respectively.

from Fig. 4.16 are for $L = 3$ states. Apparently, they are similar to the GL case shown in Fig. 4.15, but the probability of the occurrence of the V-aV state is much larger than in GL case. The reason is that the result with one root is just a special case while the general case shows oscillations at and around the vortex core.

The V-aV molecules do not only exist for smaller winding number L, but they can also appear for large L in the BdG results. Fig. 4.17 shows an example for sample III with W/ξ_0=7 at $\Phi/\Phi_0 = 20$ and with a winding number $L = 12$. We find that vortices concentrate in the central dark (blue) area where the order parameter is strongly suppressed. From the phase of the order parameter, which is shown in Fig. 4.17(b), the total winding number $L = 12$ is found but it is difficult to distinguish each vortex. After a careful analysis, we plot schematic diagram of the vortex configuration in Fig. 4.17(c). The dark(blue) dots and open diamonds indicate vortices and anti-vortices, respectively. As can be seen, the lattices of vortices and antivortices are nested within each other. Since anti-vortices attract vortices, all the vortices (24 vortices and 12 antivortices) can be condensed in the cental area of the sample. This picture becomes more accurate when $k_F\xi_0$ is large. The stronger the oscillations of the order parameter the more V-aV

pairs are generated. However, the size of the V-aV pair can only be of the order of the Fermi wavelength. Thus, it will be very hard to detect them in experiments. This is why these states are mostly treated as a giant vortex in conventional superconductors. In other words, the suppressed central area of the order parameter, after coarse graining, will look like a giant vortex with $L = 12$.

4.7 Conclusions

To summarize, we investigated the vortex states in a nanoscale superconducting square for different sizes W, parameters $k_F\xi_0$, and temperatures T. First, we found that the inhomogeneous pattern of the order parameter in the absence of magnetic field strongly depends on $k_F\xi_0$ and the size W. This oscillation pattern will give an additional contribution to competing effects that determine the vortex configurations when the field is applied. Due to the inhomogeneous order parameter induced by the quantum topological confinement, samples with different $k_F\xi_0$ and W will favor different winding numbers L.

We find unconventional vortex states such as asymmetric, edge-parallel and vortex-antivortex states as the ground state of our nanoscale system. These were never seen in the Ginzburg-Landau approach. The inhomogeneous pattern of the order parameter, especially the strong oscillation at the boundaries causes additional potential wells for vortices which in turn generates a lot of metastable vortex states. Furthermore, in the quantum limit, nano-size superconductors favor vortex-antivortex molecules while disfavoring giant vortex states.

We observe that vortex ground states and the phase transition fields are very sensitive to changes in the parameter $k_F\xi_0$, size W and temperature T. This is a direct consequence of the quantum size effect. However, this effect is suppressed when the size W is large or when temperature is high. In this case most metastable states become unstable and the ground states become compatible with GL theory.

For high magnetic fields, vortex-antivortex pairs can be easily found when $k_F\xi_0$ is large because the absolute value of the order parameter becomes smaller than the amplitude of its oscillations. However, detection of such states is beyond the current experimental abilities.

The peculiar vortex states uncovered in the present work should be ob-

servable in superconducting systems where $k_F\xi_0$ is small. Such systems could be high-T_c superconducting nano-grains for which the coherence length is small or cold-atom condensates with small k_F, i.e. large Fermi wavelength. Of special interest could be hybrid systems made of superconducting substrates and graphene sheets for which the Fermi wavelength is highly tunable near the Dirac point. Future work could also address the fundamental vortex-vortex and vortex-antivortex interactions for systems with a small $k_F\xi_0$, for which the oscillations of the order parameter on the order of λ_F become important.

Chapter 5

Position-dependent effect of non-magnetic impurities on superconducting properties of nanowires

A single non-magnetic impurity has very little effect on the bulk properties of conventional superconductors. However, as the dimensionality is reduced, the effect of impurities becomes more significant. Here we investigate superconducting nanowires with diameter comparable to the Fermi wavelength λ_F (which is less than the superconducting coherence length) by using a microscopic description based on the Bogoliubov-de Gennes method. We find that: 1) impurities strongly affect the superconducting properties, 2) the effect is impurity position-dependent, and 3) it exhibits opposite behavior for resonant and off-resonant wire widths. We show that this is due to the interplay between the shape resonances of the order parameter and the sub-band energy spectrum induced by the lateral quantum confinement. These effects can be used to manipulate the Josephson current, filter electrons by subband and investigate the symmetries of the superconducting subband gaps.

The results of this chapter were published as: L.-F. Zhang, L. Covaci and F. M. Peeters, Europhys. Lett. **109**, 17010 (2015).

5.1 Introduction

The effect of impurities on superconductivity have intrigued scientists for several decades. Adding impurities to a superconductor can not only provide an useful tool to investigate the superconducting state but can also be used to optimize the performance of certain devices. For example, impurities are used to distinguish between various symmetries of the superconducting state[180, 181], to identify topological superconductors[182] or to pin vortices in order to enhance the superconducting critical current[6]. Strong disorder is often used to study the superconducting-insulator transitions and the localization of the Cooper pairs[183–188]. It is well known that magnetic impurities, which are pair breakers, suppress superconductivity. On the other hand, as Anderson's theorem points out[65], for bulk conventional superconductors in the dirty limit, additional non-magnetic impurities have very little effect on the thermodynamic properties of the system, such as the superconducting critical temperature T_c, and that impurities have only local effects[180] on the superconducting order parameter (OP) and the density of states.

On the other hand, quasi-one-dimensional superconducting nanowires show different properties from the bulk and could have wide potential applications in the near future[105]. First, if in some regions, the diameter of the cross section of the wire is shorter than the superconducting coherence length, ξ (also known as the healing length of the OP), superconductivity weakens there, thus affecting transport properties of the wires. Quantum phase slips, leading to the loss of phase coherence, are one of the main reasons for the appearance of normal regions giving rise to a finite resistance below T_c in nanowires[189–195]. Phase slip junctions can be fabricated in order to take advantage of this mechanism[196]. Normal regions can also be caused by interactions with photons and this can be used to build single-photon detectors[197, 198]. Second, surface effects in nanoscale superconductors result in topological superconducting states[199]. Majorana fermions, which are their own anti-particles, were predicted as quasi-particles in such p-wave nanowires[200, 201]. Third, quantum confinement results in quantum size effects[67, 92, 202], quantum-size cascades[95], facilitates the appearance of new Andreev-states[94] and give rise to unconventional vortex states[179, 203] induced by the wavelike inhomogeneous spatial distribution of the OP[67].

Up to now, the theoretical study of superconducting nanowires was limited to defect-free cases in the clean limit or to systems with weak links, which were treated in the one-dimensional limit. However, experiments such

as Scanning Tunneling Microscopy (STM) are nowadays able to measure the local density of states (LDOS) with atomic resolution[46, 53, 112, 137, 204] and consequently the finite width of nanowires can no longer be neglected. It is known that in low dimensional superconductors phase fluctuations should play an important role [205–207]. The calculation presented here is done at zero temperature and at mean-field level, therefore it cannot describe fluctuations. Nevertheless, by calculating the modifications induced by the impurity on the Josephson current we are able to infer the phase robustness of the condensate, therefore indirectly provide information about the enhancement of fluctuations and the appearance of phase slips.

In this chapter, we investigate the effect of a nonmagnetic impurity on superconducting nanowires with diameter comparable to the Fermi wavelength, λ_F. The bulk coherence length at zero temperature, ξ_0, is much larger than λ_F. For such systems, quantum confinement effects dominate and a description based on the microscopic Bogoliubov-de Gennes (BdG) equations is required. The impurity, which induces potential scattering on single electrons, not only affects local properties such as the OP and the LDOS, but also has global effects on the critical supercurrent. Quantum confinement leads to inhomogeneous superconductivity and therefore the effect of the impurity strongly depends on its transverse location.

The chapter is organized as follows: first we briefly present our numerical method and the properties of the nanowires in the clean limit, then we show the effect of non-magnetic impurities on the profile of the order parameter and the local density of states. At the end we investigate the impurity effect on the Josephson critical current.

5.2 Theoretical approach

We start from the well-known BdG equations:

$$\begin{aligned} [K_0 - E_F]\, u_n(\mathbf{r}) + \Delta(\mathbf{r}) v_n(\mathbf{r}) &= E_n u_n(\mathbf{r}), & (5.1)\\ \Delta(\mathbf{r})^* u_n(\mathbf{r}) - [K_0^* - E_F]\, v_n(\mathbf{r}) &= E_n v_n(\mathbf{r}), & (5.2) \end{aligned}$$

where $K_0 = -(\hbar\nabla)^2/2m + U(\mathbf{r})$ is the kinetic energy with U being the potential barrier induced by the impurity and E_F the Fermi energy, $u_n(v_n)$ are electron(hole)-like quasiparticle eigen-wavefunctions, E_n are the quasiparticle eigen-energies. The impurity potential is modeled by a symmetrical Gaussian

function, $U(\mathbf{r}) = U_0 exp[-(\mathbf{r}-\mathbf{r_0})^2/2\sigma^2]$ where U_0 is the amplitude, $\mathbf{r_0}$ is the location of the impurity and σ is the width of the Gaussian.

The pair potential is determined self-consistently from the eigen- wave-functions and eigen-energies:

$$\Delta(\mathbf{r}) = g \sum_{E_n<E_c} u_n(\mathbf{r}) v_n^*(\mathbf{r})[1-2f(E_n)], \tag{5.3}$$

where g is the coupling constant, E_c is the Debye energy, and $f(E_n) = [1+\exp(E_n/k_BT)]^{-1}$ is the Fermi distribution function, where T is the temperature. The local density of states is calculated as usual: $N(\mathbf{r},E) = \sum_n [\delta(E_n-E)|u_n(\mathbf{r})|^2 + \delta(E_n+E)|v_n(\mathbf{r})|^2]$.

For simplicity, we consider a two-dimensional problem and introduce a long unit cell whose area is $S = L_xL_y$ where L_x is the length of the unit cell and L_y is the wire width. Periodic boundary conditions are set in the x direction and L_x is set to be long enough such that physical properties are L_x-independent. Due to quantum confinement in the transverse direction y, we set Dirichlet boundary condition at the surface (i.e. $u_n(\mathbf{r}) = v_n(\mathbf{r}) = 0,\ r \in \partial S$).

In order to solve more efficiently the self-consistent BdG equations (5.1)-(5.3), we expand $u_n(v_n)$ by using a two step procedure. First, in order to get the eigenstates of the single-electron Schrödinger equation $K_0\phi_l = E_l\phi_l$ we Fourier expand ϕ_l:

$$\phi_l(x,y) = \sqrt{\frac{2}{L_xL_y}} \sum_{j>0,k} c_{j,k} \exp(ikx) \sin\left(\frac{\pi jy}{L_y}\right), \tag{5.4}$$

where $c_{j,k}$ are the coefficients of the expansion and wave vector $k = 2\pi m/L_x$, $m \in \mathbb{Z}$. Here we use a large number of basis functions in order to ensure the accuracy of the results. Next, we expand $u_n(v_n)$ in terms of $\phi_l(x,y)$. In this step, only states with energies $E_l < E_F + \varepsilon$ are included. In our calculation, ε is taken to be $30E_c$ and we find that any larger cut-off does not modify the results. We have checked our results, for a specific choice of parameters, against a more computationally intensive finite-difference method approach.

We choose to study $NbSe_2$ nanowires as an example because of the availability of high-quality nanowires with $2-25$nm in diameter [58, 208]. Also, theoretical calculations are in good agreement with experiments, especially, for vortex lines[114, 120, 122]. In addition, the lower Fermi energy makes

the calculations feasible. The parameters of bulk $NbSe_2$ are the following: $m = 2m_e$, $E_F = 40$ meV, $E_c = 3$ meV and coupling constant g is set so that the bulk gap $\Delta_0 = 1.2$ meV, which yields $T_c \approx 8.22K$, $\xi_0 = 14.7$ nm and $k_F\xi_0 = 21.23$. In nanowires, the mean electron density n_e is kept to the value obtained when $L_x, L_y \to \infty$ by using an effective E_F, where $n_e = \frac{2}{S}\sum_n \int \{|u_n|^2 f(E_n) + |v_n|^2[1 - f(E_n)]\}$. All the calculations are performed at zero temperature.

5.3 Numerical results

We first show in Fig. 5.1 important superconducting properties of clean nanowires, i.e. with $U \equiv 0$. The spatially averaged OP, $\bar{\Delta}$, shows quantum size oscillations as a function of the width, L_y, as seen from Fig. 5.1(a). The resonant enhancements appear almost regularly with a period of half the Fermi wavelength, i.e. $\lambda_F/2$. They are due to the fact that the bottom of the relevant single-electron subbands passes through the Fermi surface, which results in a significant increase in the density of states, i.e. in the number of electrons which can form Cooper pairs. The different energy spectra for the resonance and off-resonance cases are the key to understand the behavior of the nanowires. For completeness, we show in Fig. 5.1(b)-(h) more information for the resonance case, with $L_y = 3.4$ nm, intermediate case, with $L_y = 3.8$ nm, and off-resonance case, with $L_y = 5.4$ nm.[1] The energy spectrum for resonance [see Fig. 5.1(c)] shows two energy gaps: a smaller gap for subband $j = 1$ and a larger one for $j = 2$. Most quasiparticle states are just below the Debye energy E_c for subband $j = 2$. This results in an enhancement of the OP, which shows two pronounced peaks and is strongly inhomogeneous in the y direction [see Fig. 5.1(b)]. We consider the spatial positions $\alpha\beta\gamma$ and $\alpha'\beta'$ as given in the insets of Fig. 5.1(d)(h) where the OP has either a maximum or a minimum. The corresponding LDOS at positions α and β are shown in Fig. 5.1(d). We notice that there are two gaps at α and only one gap at β. The smaller sub-gap at α and the gap at β comes from the $j = 1$ subband. The main gap at α comes mostly from the $j = 2$ subband which is indicated by the ratio of the LDOS peaks at the main gap and at the sub-gap. In contrast, the off-resonance case shows the same energy gap

[1] Details for other resonance ($L_y = 5.8$ nm) and off-resonance ($L_y = 7.5$ nm) cases, where there are three peaks in $|\Delta(y)|$, are shown as supplemental materials in arXiv:1401.4319.

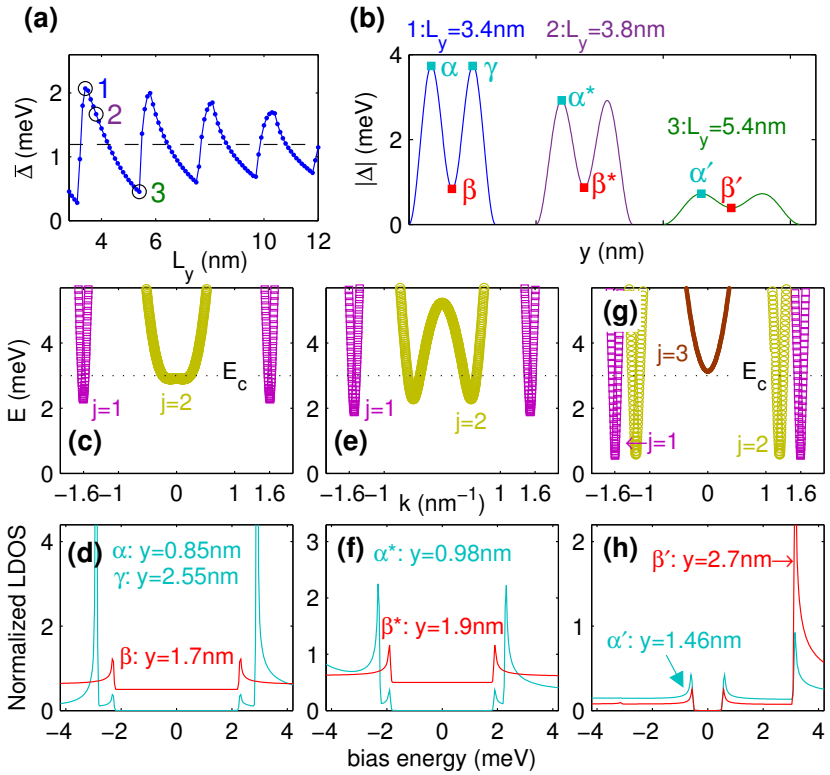

Figure 5.1: Properties of clean $NbSe_2$ nanowires. (a) Spatially averaged $\bar{\Delta}$ as a function of L_y. The open circles $1-3$ indicate the resonance case ($L_y = 3.4$ nm), intermediate case ($L_y = 3.8$ nm) and off-resonance case ($L_y = 5.4$ nm), respectively. (b) OP $|\Delta(y)|$ for the three cases. The $\alpha\beta\gamma$ are defined as the positions where the OP has a local maximum / minimum for resonance, the $\alpha^*\beta^*$ are for intermediate and the $\alpha'\beta'$ are for off-resonance. The value of these positions are shown in the inset of the panels (d),(f) and (h), respectively. (c) and (d) energy spectrum and the corresponding LDOS at positions α, β and γ for resonance. (e) and (f) the same but for the intermediate case and positions α^* and β^*. (g) and (h) the same but for off-resonance and positions α' and β'. Note that in panel (d) and (f) the LDOS for position β and β^* are shifted for clarity.

for $j = 1$ and $j = 2$ [see Fig. 5.1(g)] and the LDOS [see Fig. 5.1(h)] is more conventional: only one superconducting gap and the amplitude of the LDOS is proportional to $|\Delta(y)|$, i.e. the LDOS at α' (local maximum) is larger than the one at β' (local minimum). Besides the sub-gap shift seen in the energy spectrum, another important difference between the two cases is that for resonance there is always a large number of low momentum quasi-particles [see Fig. 5.1(c)] which are involved in pairing, whereas there are no quasi-particles at $k = 0$ in the off-resonance case [see Fig. 5.1(e)]. Note that subband $j = 3$ in off-resonance sits just outside of E_c and generates a large asymmetric peak in the LDOS [see Fig. 5.1(f)]. The intermediate case [see Fig. 5.1(e) and (f)] mixes the characteristic from both resonance and off-resonance cases where it has the intermediate gap difference between subbands $j = 1$ and $j = 2$ and the intermediate k-value for most quasi-particles states with subband $j = 2$.

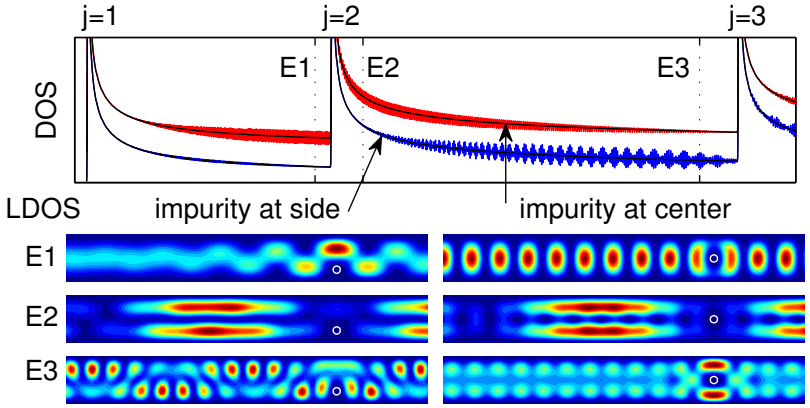

Figure 5.2: Effect of the impurities on the electronic structure when the nanowire is in normal state. (upper panel) DOS as a function of energy for an impurity at sided position (blue solid line) and at centered position (red solid line, shifted up for clarity), respectively. The black solid lines are for $U = 0$ as references. (lower panels) Schematic corresponding LDOS(x, y) at energy $E1$, $E2$ and $E3$, respectively. The open circles indicate impurities' position.

Next, we consider an impurity in the nanowire. The impurity is strong enough to suppress completely the wave-functions of the electronic states locally. Meanwhile, the spread of the impurity is smaller than the width of the nanowire. The effects of the impurity on the electronic structures of normal state are presented in Fig. 5.2. The scattering due to the single

impurity does not change the quasi one-dimensional characteristic seen in the DOS. However, it results in additional small oscillations when comparing with the clean case with $U = 0$. In addition, the oscillations show different pattern for impurity at sided position and at centered position. It indicates the influence of the impurity depending on its position and the quantum number of the electronic state, i.e. j and k. Due to the sine-shaped transverse electronic wave-functions, the impurity at center position affects the states with subband $j = 1$ more than states with subband $j = 2$. Thus, the DOS of the impurity at center position shows stronger oscillations than the one of the impurity at side position between the peaks of $j = 1$ and $j = 2$. For the same reason, it shows opposite behavior in DOS between the peak of $j = 2$ and $j = 3$. Furthermore, the impurity leads to fast oscillations in the LDOS at energies $E1$ and $E3$ [see Fig. 5.2 (lower panels)] because these states have large wave-number, i.e. k. In contrast, the impurity leads to oscillations with long wave-length in the LDOS at energy $E2$, due to the states with small k-value dominating near $E2$.

Now we move on to the superconducting state and consider an impurity at position $(0, \alpha)$ and $(0, \beta)$ for resonance case and at $(0, \alpha')$ and $(0, \beta')$ when off-resonance. We set $U_0 = 20E_F$ and $\sigma = 0.02$ nm so that the impurity strongly suppresses the local OP and the spread of the potential (full width at 1/10th of maximum) is 0.86 nm, which is shorter than the width of the nanowire. We show in Fig. 5.3 the profile of the amplitude of the OP in the presence of the impurity. For the resonance, [see Figs. 5.3(c)(d)], the impurity suppresses the OP over the whole width which is more pronounced when in α than in β. Meanwhile, the asymmetrical impurity, at α, results in a local enhancement at position $(0, \gamma)$, as seen from Fig. 5.3(a). For the impurity sitting in the center, β, the OP oscillates along the wire over a longer distance although the impurity sits at a local minima of the OP which intuitively should have a smaller effect. As seen from Fig. 5.3(b), the OP oscillations extend to $x = \pm 50$ nm, which is much farther than the extent of the oscillations for the impurity at α. The reason is that the centered β impurity strongly affects the $j = 1$ subband quasi-particles due to the sine-shaped transverse wave-function, leaving the $j = 2$ subband unaffected. Moreover, only high k quasi-particles in subband $j = 1$ play a role so that scattering on the impurity results in oscillations of the wave-functions. On the other hand, the impurity at α affects mostly subband $j = 2$ but all states with $j = 2$ have low k so that the OP recovers fast and has longer wave-length oscillations. The local density of states in Figs. 5.4(a-d) show evidence that

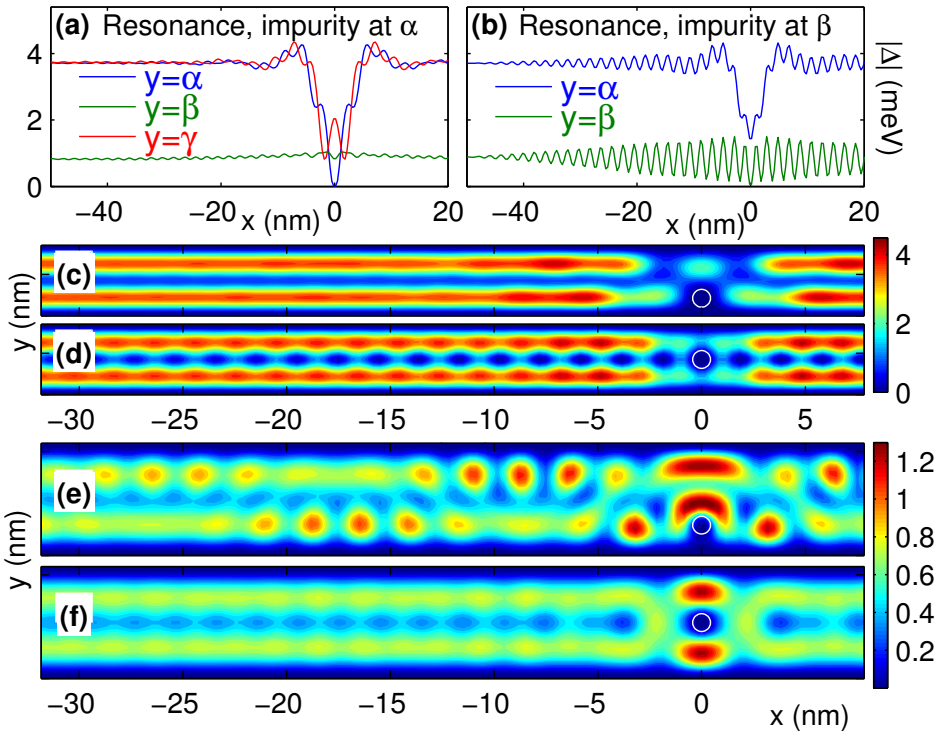

Figure 5.3: OP in the presence of an impurity. (a) and (c) show $|\Delta(x)|$ at y=α, β, γ (defined in Fig. 5.1) and contour plot of $|\Delta(x, y)|$ for an impurity sitting at α in resonance case, respectively. (b) and (d) are the same as (a) and (c) but for the impurity sitting at the center β. (e) and (f) show contour plot of $|\Delta(x, y)|$ for an impurity sitting at α' and β' in off-resonance case, respectively. The white open circles indicate impurities' profile where $U = 0.1U_0$.

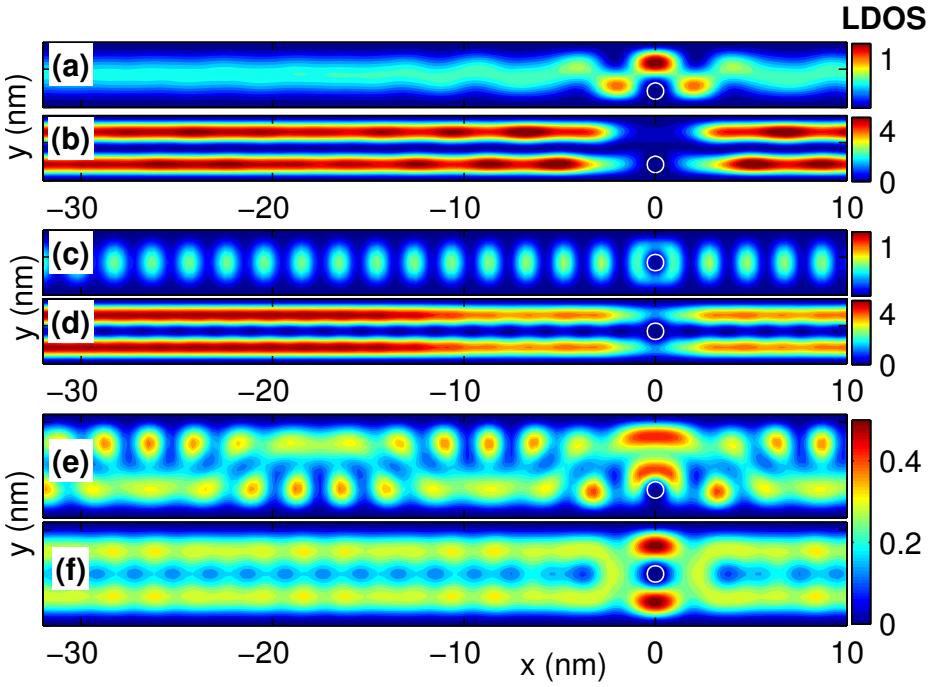

Figure 5.4: Contour plots of LDOS at the energies' (sub-)gap in the presence of an impurity. (a-d) are for the resonance case with an impurity sitting at α at sub-gap (a) $E = 2.32$ meV and gap (b) $E = 2.93$ meV and with an impurity sitting at β at sub-gap (c) $E = 2.36$ meV and gap (d) $E = 2.93$ meV. (e) and (f) are for off-resonance case with the impurity at α' and at β' at gap $E = 0.68$ meV and 0.65 meV, respectively. The open circles indicate impurities' profile where $U = 0.1U_0$.

supports this explanation. For the off-resonance case [see Figs. 5.3 (e-f)], due to the combination of the $j = 1$ and $j = 2$ subbands which now have only high k quasi-particles, the impurity always induces strong oscillations in the OP. Note that the OP is affected more strongly when the impurity sits at a local maximum. The LDOS shown in Figs. 5.4 (e-f) show the same patterns as the OP.

Finally, we study the effect of the impurity on the transport properties such as the Josephson current. In order to do so, we set a junction link of length $L_j = 30$ nm at the center of the nanowire where Δ is obtained self-consistently. Outside the link, we fix the phase of the order parameter and impose a phase difference $\delta\theta$ between the two sides of the link, i.e. $\Delta(x < -15 \text{ nm}) = |\Delta|e^{i0}$ and $\Delta(x > 15 \text{ nm}) = |\Delta|e^{i\theta}$. Then, the supercurrent induced by the phase difference $\delta\theta$ can be calculated as follows:

$$\mathbf{J}(\mathbf{r}) = \frac{e\hbar}{2mi} \sum_{E_n<E_c} \{f(E_n)u_n^*(\mathbf{r}) \bigtriangledown u_n(\mathbf{r}) + [(1 - f(E_n)]v_n(\mathbf{r}) \bigtriangledown v_n^*(\mathbf{r}) - h.c.\}\,.$$

Please note that $\mathbf{J}$ satisfies the continuity condition $\nabla \cdot \mathbf{J} = 0$ in the link due to the self-consistent Δ[143, 209]. Outside the link, $\mathbf{J}$ is discontinuous due to the fixed phase of the order parameter but these areas can be treated as current sources.

Figs. 5.5(a) and (b) show the $J - \theta$ relation for resonant and off-resonant cases, respectively. For resonance, the current increases monotonically with the phase for the impurity at α but it shows a sine-shaped curve for the impurity at β. We find that the critical Josephson current is suppressed dramatically for the impurity at β while the impurity at position α has little effect. The explanation is that when the current is small, only the lowest quasi-particle states are involved. and almost all such states are from the $j = 1$ branch and as a result the current distribution $j(y) \propto \sin(\pi y/L_y)$ is as in the clean limit. This can be seen from Fig. 5.5(d) for x far away from the impurity. Thus, the impurity blocking effect on the current for the impurity at the center β has a larger effect than the off-center position α. In contrast, for the off resonance case, the current with the impurity at α' is more suppressed. The reason is the same but, here, the $j = 1$ and $j = 2$ branches contribute both to the current, and as a consequence the current distribution is $j(y) \propto |\sin(2\pi y/L_y)| + |\sin(\pi y/L_y)|$ and has a maximum at the α' position. This can also be seen from Figs. 5.5(f) far away from

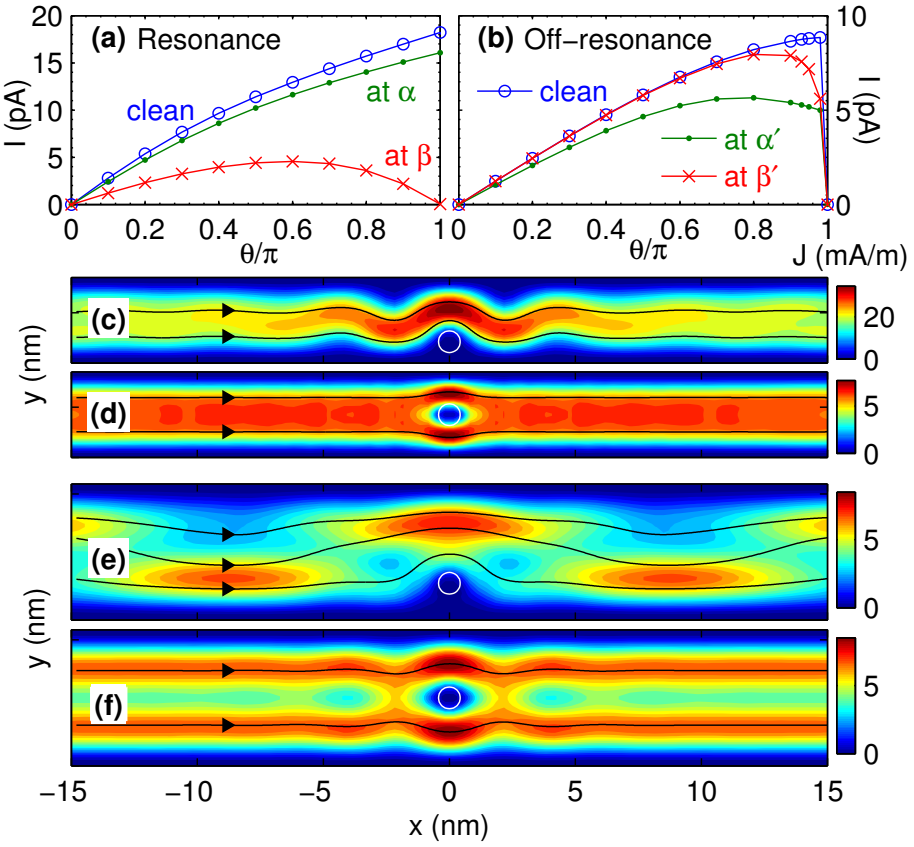

Figure 5.5: Effects of an impurity on Josephson current where the junction length is $L_j = 30$ nm. (a) Current-phase relation in the resonance case for clean limit, with impurity at α and at β. (b) Results in the off-resonance case for clean limit, impurity at α' and at β'. (c)-(f) The spatial distributions of current for an impurity at α, β for resonance case and at α', β' for off-resonance case with phase differences where currents reach their critical Josephson currents. The color indicates the amplitude of the current and the streamlines indicate the direction of the current. The open circles indicate the impurity profile for which $U = 0.1U_0$.

the impurity. This position dependent effect could be used to investigate the nature of the superconducting condensate, e.g. by using Scanning Gate Microscopy(SGM) in order to locally mimic the effect of the impurity and suppress the order parameter. By monitoring the change in the Josephson current, one can map out the symmetry of the order parameter and the distribution of the supercurrent along the y direction.

5.4 Conclusions

In conclusion, we studied the effect of non-magnetic impurities on narrow superconducting nanowires in the clean limit, in which quantum confinement plays an important role. By applying BdG theory to the case of $NbSe_2$, we uncovered several regimes in which the impurity affects the superconducting properties of the nanowire in different ways. First, depending whether the nanowire is in the resonant or off-resonant regime, the OP will show slow or fast oscillations away from the impurity, respectively. This is due to the different nature of the quasi-particles involved in the formation of the Cooper pairs, i.e. small or large momentum. Additionally, the impurity has a strong position-dependent effect on the Josephson critical current with opposite behavior in the resonant and off-resonance cases. In the resonant case an impurity at the center of the wire will strongly suppress the current while for the off-resonance case the current is slightly suppressed for an impurity sitting at an off-center location.

In experiments, the crystal structure of the material, the surface roughness of the specimen and the properties of the substrate will modify the Fermi level, the band structure, the electronic wave functions or the electron mean free path. All these factors could broaden the single-electron levels and modify the specific scattering patterns of the OP and electronic structures (LDOS). However, the superconducting shape resonances are robust, as shown in more realistic theoretical models[85]. In this case, quantum confinement dominates and the position dependence of the amplitude of the electronic wave functions and OP are robust. As a result, our conclusions about the position-dependent impurity effect (especially the effect on the Josephson current) will not be significantly altered, although specific details might change.

We believe that these effects could be used to investigate the nature of the superconducting condensate and the scattering of the various subbands

on the impurity. Also in realistic nanowires, which contain impurities, one should see a strong impurity effect in the resonant case. Although the mean-field calculation presented here cannot describe fluctuations, by showing that the Josephson current can be strongly suppressed in the resonant case, one can infer that fluctuations will become more important. Our calculations could also provide a basis for a phenomenological toy model of a 1D disordered Josephson array with position impurity dependent junction parameters.

Chapter 6

Tomasch effect in nanoscale superconductors

The Tomasch effect (TE) is due to quasiparticle interference (QPI) as induced by a nonuniform superconducting order parameter, which results in oscillations in the density of states (DOS) at energies above the superconducting gap. Quantum confinement in nanoscale superconductors leads to an inhomogeneous distribution of the Cooper-pair condensate, which, as we found, triggers the manifestation of a new TE. We investigate the electronic structure of nanoscale superconductors by solving the Bogoliubov-de Gennes (BdG) equations self-consistently and describe the TE determined by two types of processes, involving two- or three- subband QPIs. Both types of QPIs result in additional BCS-like Bogoliubov-quasiparticles and BCS-like energy gaps leading to oscillations in the DOS and modulated wave patterns in the local density of states. These effects are strongly related to the symmetries of the system. A reduced 4×4 inter-subband BdG Hamiltonian is established in order to describe analytically the TE of two-subband QPIs. Our study is relevant to nanoscale superconductors, either nanowires or thin films, Bose-Einstein condensates and confined systems such as two-dimensional electron gas interface superconductivity.

The results of this chapter were published as: L.-F. Zhang, L. Covaci and F. M. Peeters, Phys. Rev. B. **91**, 024508 (2015).

6.1 Introduction

Electronic structure has always been one of the most important topics in understanding transport properties in condensed matter. A variety of remarkable phenomena, from traditional conducting, semiconducting or insulating behavior to contemporary quantum Hall effect[210] and topological insulator behavior[199], are induced by a diversity of electronic structures.

For conventional superconductors, the well-known BCS theory[11] and its generalization, the Bogoliubov-de Gennes (BdG) equations[34], are the milestones needed to reveal the electronic structure theoretically. An energy gap created around the Fermi level, E_F, in homogeneous superconductivity and low-lying bound states existing in the core of vortex states[114, 116, 119, 120, 122, 141, 175] were successfully predicted and coincide with experimental results from tunneling conductance and scanning tunneling microscopy (STM)[46, 53, 137, 211].

Nanoscale superconductors have also received considerable attention in the last decades due to developments in nanotechnology and their unique properties such as shell effect,[86] quantum-size effect[67, 77, 81, 92, 212] and quantum-size cascades under magnetic field[95]. All these effects are induced by changes in the electronic structure resulting from quantum confinement, such that energy levels are discretized in nanoparticles and single-electron subbands appears in nanowires. In addition, such electronic structure results in a spatially inhomogeneous superconducting order parameter[67], which further induces other effects such as superconducting multi-gap structures,[94, 213] new Andreev-states,[94] unconventional vortex states,[179, 203] and a position-dependent impurity effect[214].

An interesting phenomenon that appears due to inhomogeneous superconductivity is the Tomasch effect (TE), which is a consequence of quasiparticle interference (QPI) due to scattering on a nonuniform energy-gap.[38–40, 215] The underlying process consists in a quasiparticle interacting with, and being condensed into, the sea of Cooper pairs leaving behind a different but degenerate quasiparticle.[40, 215] As a result, Tomasch oscillations appear as periodic oscillations in the density of states (DOS) in superconducting junctions, at energies larger than the superconducting gap.[38, 39, 114, 216] These oscillations could be further enhanced when considering layered structures formed by intercalating successive metallic and superconducting regions. In this case the order parameter is by design non-homogeneous. Theoretically, these oscillations were studied in multi-layer structures by using Green's functions

methods like Gor'kov equations.[217, 218] However, the electronic structure under TE has not been unveiled because a fully self-consistent numerical calculation is required in order to obtain the coherence between quasiparticle states.

QPIs should also be observed in unconventional superconductors[219–221], where the interference should be more pronounced due to the intrinsic inhomogeneous nature of the superconducting order parameter. Theoretically, QPI due to a local superconducting order parameter suppression in large unconventional samples was demonstrated in Ref. [222]. However, in nanoscale structures, quantum confinement modifies the symmetries of the electronic states. Thus, the signatures of QPI in nanoscale superconductors, although of same nature, could be different in manifestation in large samples but with intrinsic inhomogeneities [222].

In this chapter, we investigate the electronic structure of clean nanoscale superconductors by solving the Bogoliubov-de Gennes (BdG) equations self-consistently. We focus on the TE which appears above the superconducting gap. High precision energy excitation spectra are needed in order to see the effect of the QPI processes clearly. Two geometries, nanobelts and nanowires, are used as typical examples in order to unveil the properties of TE resulting from two- and three- subband QPIs. The importance of the sample symmetry is discussed. We find that even in the presence of weak disorder, the Tomasch is robust.

It is important to keep in mind that the mean-field BdG approach has limited validity when describing superconducting nanobelts and nanowires with diameters down to 10 nm.[189, 205, 223, 224] For such nano-scale samples, fluctuations might play an important role, but are totally neglected by a mean-field method. Moreover, the quasi-particles in the Landau-Fermi liquid theory are only well defined near the Fermi level. Therefore, the discussion and results presented in this chapter are valid for larger samples where these effects are not significant.

The chapter is organized as follows. In Sec. 6.2, we first investigate TE of two-subband QPI in nanobelts. The two-dimensional BdG equations are outlined for nanobelts in SubSec. 6.2.1. Properties of the electronic structures under the TE of two-subband QPI are presented in SubSec. 6.2.2. A description based on a reduced 4×4 BdG matrix is next introduced in SubSec. 6.2.3 in order to explain the properties of TE as due to two-subband QPI. A possible observable effect, modulated wave patterns in LDOS, induced by TE of two-subband QPI is discussed in SubSec. 6.2.4. Signatures of QPI

under the influence of weak impurities are discussed in SubSec. 6.2.5. Next, we investigate TE of three-subband QPI in nanowires in Sec. 6.3, where the three-dimensional BdG equations are solved for nanowires in SubSec. 6.3.1. The electronic structure under the influence of TE of three-subband QPI and their symmetry dependent properties are presented in SubSec. 6.3.2. Finally, our conclusions are summarized in Sec. 6.4.

6.2 Tomasch effect in superconducting nanobelts

6.2.1 Bogoliubov-de Gennes equations for two-dimensional nanobelts

For a conventional superconductor in the clean limit, the BdG equations in the absence of a magnetic field can be written as

$$\begin{pmatrix} H_e & \Delta(\mathbf{r}) \\ \Delta(\mathbf{r})^* & -H_e^* \end{pmatrix} \begin{pmatrix} u_n(\mathbf{r}) \\ v_n(\mathbf{r}) \end{pmatrix} = E_n \begin{pmatrix} u_n(\mathbf{r}) \\ v_n(\mathbf{r}) \end{pmatrix}, \tag{6.1}$$

where $H_e = -(\hbar\nabla)^2/2m - E_F$ is the single-electron Hamiltonian with E_F the Fermi energy, $u_n(v_n)$ are electron(hole)-like quasiparticle eigen-wavefunctions and E_n are the quasiparticle eigen-energies. The $u_n(v_n)$ obey the normalization condition

$$\int (|u_n(\mathbf{r})|^2 + |v_n(\mathbf{r})|^2) d\mathbf{r} = 1. \tag{6.2}$$

The superconducting order parameter is determined self-consistently from the eigen-wavefunctions and eigen-energies:

$$\Delta(\mathbf{r}) = g \sum_{E_n < E_c} u_n(\mathbf{r}) v_n^*(\mathbf{r})[1 - 2f(E_n)], \tag{6.3}$$

where g is the coupling constant, E_c is the cutoff energy, and $f(E_n) = [1 + \exp(E_n/k_B T)]^{-1}$ is the Fermi distribution function, where T is the temperature. The core part of Eq. (6.3) is the pair amplitude which is defined as

$$D_n(\mathbf{r}) = u_n(\mathbf{r}) v_n^*(\mathbf{r}). \tag{6.4}$$

The pair amplitude is the key parameter that shows the coupling between electron-like and hole-like quasiparticles for each Bogoliubov quasiparticle.

In this section, we consider a two-dimensional nanobelt. The width is W in the transverse direction, x, and, because of confinement, Dirichlet boundary conditions are used at the surface (i.e. $u_n|_{x=0} = u_n|_{x=W} = 0$, $v_n|_{x=0} = v_n|_{x=W} = 0$). We consider periodic boundary conditions along the y direction, with a unit cell of length L. The length is set to be large enough in order to guarantee that physical properties are L-independent.

In order to solve the BdG equations (6.1-6.3) numerically, we expand $u_n(v_n)$ as

$$\begin{pmatrix} u_n(\mathbf{r}) \\ v_n(\mathbf{r}) \end{pmatrix} = \sum_{j\in\mathbb{N}^+,k} \varphi_{jk}(x,y) \begin{pmatrix} u^n_{jk} \\ v^n_{jk} \end{pmatrix} \tag{6.5}$$

where

$$\varphi_{jk}(x,y) = \sqrt{\frac{2}{W}} \sin\left(\frac{\pi j x}{W}\right) \frac{e^{iky}}{\sqrt{L}} \tag{6.6}$$

are the eigenstates of the single-electron Schrödinger equation $H_e\phi_{jk} = \zeta_{jk}\phi_{jk}$ where the wave vector $k = 2\pi m/L, m \in \mathbb{Z}$. The expansion in Eq.(6.5) has to include all the states with energy in the range $-E_F < \zeta_{jk} < E_F + \epsilon$ in order to allow the emergence of the TE well above the the energy gap. The energy ϵ is taken to be $5E_c$, which guarantees sufficient accuracy. We checked that higher ϵ does not change the results.

We remark that, for the chosen geometry, the order parameter depends only on the transverse variable x, i.e., $\Delta(\mathbf{r}) = \Delta(x)$. This implies no net momentum of the condensate in the y direction and the quasiparticle amplitudes $(u_n,\ v_n)^T$ are k-separated. Then, the summation over k in Eq. (6.5) can be removed and the BdG equation (6.1) is converted into a matrix equation for each k whose contribution to Δ can be calculated independently from the other values of k. This allows us to include millions of quasiparticle states allowing very high resolution in the energy dispersion which is necessary to observe clearly the Tomasch effect.

The local density of states (LDOS) is calculated as usual:

$$A(\mathbf{r},E) = \sum_n [|u_n(\mathbf{r})|^2\delta(E-E_n) + |v_n(\mathbf{r})|^2\delta(E+E_n)], \tag{6.7}$$

and the total density of states (DOS) is obtained as

$$N(E) = \int A(\mathbf{r},E)d\mathbf{r}. \tag{6.8}$$

The spectral weight is

$$Z_n = \int |u_n(\mathbf{r})|^2 d\mathbf{r}, \tag{6.9}$$

which represents the contribution of the electronic part of the wave function of a Bogoliubov quasiparticle state.

In this section, we set the microscopic parameters to be the same as those used in Refs. [114, 120]. These parameters for bulk are the following: effective mass $m = 2m_e$, $E_F = 40$ meV, $E_c = 3$ meV and coupling constant g is set so that the bulk gap at zero temperature is $\Delta_0 = 1.2$ meV, which yields $T_c \approx 8.22$ K, $\xi_0 = \hbar v_F/(\pi\Delta_0) = 14.7$ nm and $k_F\xi_0 = 21.23$. The prototype material can be, e.g., $NbSe_2$.[114, 120] For nanobelts, the mean electron density n_e is kept to the value obtained when $W, L \to \infty$ by using an effective E_F, where

$$n_e = \frac{2}{S}\sum_n \int \left\{|u_n|^2 f(E_n) + |v_n|^2[1 - f(E_n)]\right\} d\mathbf{r}$$

and $S = W \times L$ is the area of the unit cell. All the calculations are performed at zero temperature.

6.2.2 Tomasch effect from two-subband quasiparticle interference

Results for the nanobelt with width $W = 16.8$ nm are presented in Fig. 6.1. We first discuss its general properties which will be used as a reference later on when the system is under the influence of TE.

The width of the nanobelt is about ξ_0 such that the quantum size effect is significant. The spatially averaged order parameter $\bar{\Delta}$ is shown in Fig. 6.1(a) as a function of the width W. This nanobelt with width $W = 16.8$ nm is at resonance and $\bar{\Delta}$ is about 20% higher than the bulk one, Δ_0. As seen from Fig. 6.1(b), the spatial distribution of the order parameter, $\Delta(x)$, is clearly enhanced for most of the x-values and shows strong wave-like oscillations. This enhancement is induced by quasiparticle states from the bottom of subband $j = 8$ which have a large spectral weight as seen from Fig. 6.1(c). For this narrow nanobelt, only a few subbands ($j = 1 - 8$) contribute to the order parameter and are distinguishable from each other in Fig. 6.1(c).

For a superconductor under quantum confinement and thus with inhomogeneous order parameter, a multi-gap structure was predicted.[94, 213]

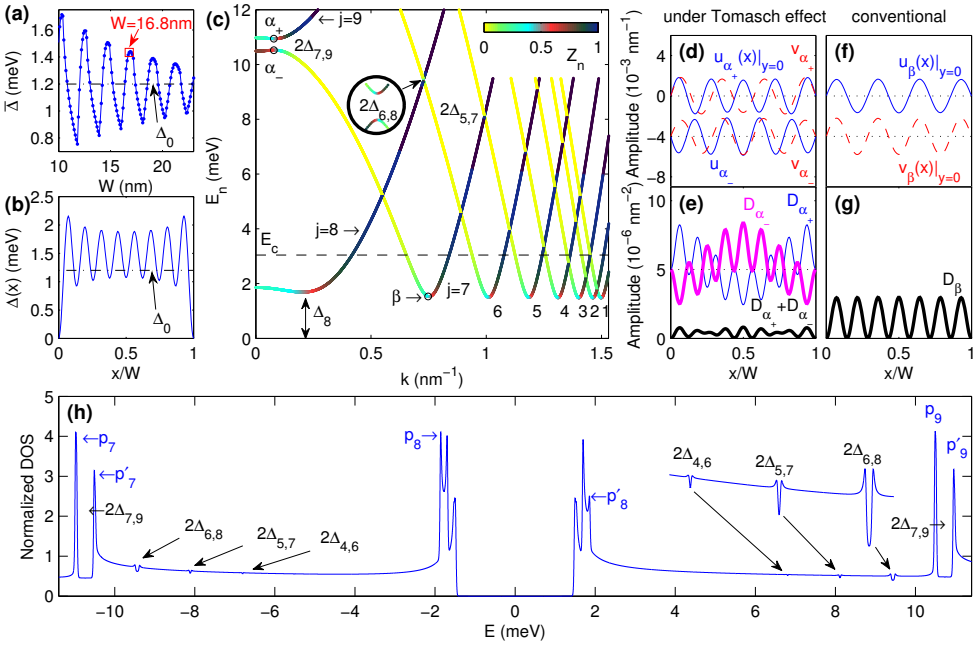

Figure 6.1: Nanobelt in the clean limit. (a) Spatially averaged $\bar{\Delta}$ as a function of width W. In the following we take, $W = 16.8$ nm (marked by an open square), which is in the resonant regime. (b) Order parameter, $|\Delta(x)|$, as a function of x. The horizontal dashed line indicates the bulk value of the order parameter, Δ_0, in panel (a) and (b). (c) Quasiparticle excitation spectrum as a function of positive longitudinal wave vector, k, for the relevant single-electron subband j. The spectral weight of the states is indicated by color. The horizontal dashed line indicates the cutoff energy E_c. Δ_j is the superconducting energy gap for states of subband j and $2\Delta_{jj'}$ is the energy gap between the states of subbands j and j' appearing due to the Tomasch effect. The electron and hole amplitudes, u and v, (at $y = 0$ as a function of x) of states α_+ and α_- [see panel (c)], which are under the influence of the Tomasch effect, are shown in panels (d). Their pair amplitudes, D_{α_+} and D_{α_-}, and the total one, $D_{\alpha_+} + D_{\alpha_-}$, are shown in panel (e). Note that D_{α_+} and D_{α_-} are shifted up for clarity. In panels (f) and (g), we show u, v and D as a function of x for the state β [see panel (c)], respectively. (h) The corresponding density of states. Peaks p_j are due to the contributions from the states of the bottom of the subbands j, while accompanying peaks $p\prime_j$ are due to the formation of the gaps, i.e. electron-hole coupling.

The energy gap Δ_j of the subband j is defined by the lowest energy of that subband. As seen from Fig. 6.1(c), the energy gaps $\Delta_1, ..., \Delta_7$ have almost the same value but are lower than Δ_8. This feature can be seen clearly in the corresponding DOS, in Fig. 6.1(h), where three significant pairs of coherence peaks form around the Fermi level. The lowest energy pair of peaks are less important and are due to the contributions of quasiparticles of subbands $j = 1 - 7$. The second lowest pair of peaks are more significant and most of the contributions are given by quasiparticle states of the subband $j = 8$ around $k = 0.2$ nm^{-1} where it reaches its local minimum, as shown in Fig. 6.1(c). It is worth noting that these two pairs of peaks show electron-hole symmetry in the DOS, whereas the third lowest pair of peaks do not. The latter ones are due to the contribution from states of subband $j = 8$ around $k = 0$. The more significant peak in negative bias is due to: 1) a large number of hole quasiparticle states at the bottom of subband $j = 8$, and 2) the electron-hole coupling asymmetry due to the higher energy level where the Bogoliubov quasiparticle states are formed by the larger weight of the hole component. This can be seen from Fig. 6.1(c) where the spectral weight Z_n represents the color(shade) of the lines.

In an isotropic superconductor, Bogoliubov quasiparticles are well defined only for energies close to the superconducting gap Δ. For such states, the electron and hole components are of the same weight, which maximizes the amplitude of the pair amplitudes that generate the order parameter. With increasing energy, Bogoliubov quasiparticles decompose into dominant electron and hole components, accompanied by a dramatically decreasing pair amplitude. Finally, they decompose into separate electron or hole quasiparticles belonging to the normal state.

For a conventional Bogoliubov quasiparticle, which is well formed for energies near the gap, the electron and hole components belong always to the same subbands j, i.e. $j - j$ coupling. As an example, we show more details of the lowest energy state β of subband $j = 7$ [marked by an open circle in Fig. 6.1(c)] in Figs. 6.1(f) and (g). The electron and hole amplitudes at $y = 0$, i.e. $u_\beta|_{y=0}$ and $v_\beta|_{y=0}$, as a function of x are shown in Fig. 6.1(f). v_β are shifted down for clarity. It can be seen that both components are in phase because they belong to the same subband $j = 7$. Thus, the pair amplitude D_β shown in Fig. 6.1(g) as a function of x, is always positive and shows a regular wave-like pattern with a constant envelope.

We next discuss the influence of the TE on the electronic structure. First, we find that energy gaps are unexpectedly opened between electron and hole

quasiparticle states even well above the Fermi level. As seen from Fig. 6.1(c), the most pronounced energy gap above E_c is generated by states α_+ and α_- (marked by open circles) where subbands $j = 7$ and $j = 9$ were supposed to cross each other in case of a homogeneous superconductor. Here, the states $\alpha_\pm$ have the same k-value and they are chosen because they have the minimal gap $2\Delta_{7,9}$ between the two subbands, i.e., $E_{\alpha_+} - E_{\alpha_-} = 2\Delta_{7,9}$. The energy of state α_+ is higher than the state of α_-. As there are only two quasiparticles that take part in the QPI, we refer to this effect as the Tomasch effect determined by two-subband quasiparticles interference processes.

Second, we find that particle-hole mixing (Bogoliubov quasiparticles) is always significant for states under the influence of the TE. This can be seen from the spectral weight of the related quasiparticle states in Fig. 6.1(c). Their color changes gradually for both the upper and lower energy bands that are associated with this gap. Furthermore, the electron and hole wave-functions of the states under the TE have a different structure because they belong to different subbands, j and j', i.e. $j - j'$ coupling. To see this characteristic, we show electron and hole amplitudes at $y = 0$, $u|_{y=0}$ and $v|_{y=0}$, of the states $\alpha_\pm$ as a function of x in Fig. 6.1(d). Note that the amplitudes of the state α_- are shifted down for clarity. For both states, $\alpha_\pm$, the spectral weights of the electron components are the same as those of the hole components, which resembles the conventional Bogoliubov quasiparticle state β. However, their electron and hole wave-functions show a phase shift because the electron components, $u_{\alpha_\pm}$, belong to subband $j = 9$ and the hole component, $v_{\alpha_\pm}$, to subband $j = 7$. This can be noticed by counting the numbers of nodes of the wave functions in Fig. 6.1(d). The difference between these states is that α_+ is the bonding(symmetric) combination of the electron and hole components while α_- is the antibonding(anti-symmetric) combination, i.e., $|\alpha_\pm >= \pm|u_{j=9} > +|v_{j=7} >$, as seen from Fig. 6.1(d). As a result, their pair amplitudes $D_{\alpha_\pm}$ as a function of x, shown in Fig. 6.1(e) are not positive-definite and exhibit a phase shift in space.

Third, the Bogoliubov quasiparticle states under the influence of TE do not directly affect the order parameter. As seen from Fig. 6.1(e), the pair amplitudes $D_{\alpha_\pm}$ are in anti-phase due to the nature of bonding and anti-bonding combinations. Thus, their net pair amplitude $D_{net} = D_{\alpha_+} + D_{\alpha_-}$ almost cancels out as shown in Fig. 6.1(e). It is worth noting that, as proven in the next subsection, the net pair amplitude of these states have nothing to do with the TE. This contribution is always positive, while the superconducting order parameter is weakly affected by TE even if the energy of this

avoided crossing is below the cutoff energy E_c.

Fourth, TE results in BCS-like pseudo-gaps in the DOS, which are symmetrically located on both positive and negative bias. This is easy to understand because energy gaps are opened for the relevant crossing subbands where particle-hole mixing appears under the influence of the TE. Typically, the gaps induced by the TE are smaller than the main superconducting gap. They will appear as pseudo-gaps because of the underlying background given by the other subbands which are not gapped. For example, as shown in Fig. 6.1(h), the largest gap induced by TE, $2\Delta_{7,9}$ is only about 0.42 meV. However, the effect of the gap resulting from the TE can be seen more clearly from the enhanced peaks appearing at the gap edge when the bottom of one subband touches the top of the other subband. In Fig. 6.1(h), the gap $2\Delta_{7,9}$ is surrounded by the peaks $p_{j=7}$ and $p'_{j=7}$ in DOS for negative bias and by $p_{j=9}$ and $p'_{j=9}$ for positive bias. The generation of the two pair of peaks are similar to the $p_{j=8}$, $p'_{j=8}$ except that they result from the top of the hole-like subband $j = 7$ and from the bottom of the electron-like subband $j = 9$.

For the chosen width, there are more gap structures induced by TE in the excitation spectrum [see Fig. 6.1(c)] and corresponding peaks in the DOS [see Fig. 6.1(h)]. For example, the gap $2\Delta_{6,8}$ appears for the coupling of states from subbands $j = 6$ and $j = 8$ at $E = 9.4$ meV but its influence on the DOS is weak. We also find other gaps such as $2\Delta_{5,7}$, $2\Delta_{4,6}$ and $2\Delta_{3,5}$.

TE is a common effect in inhomogeneous superconductivity and is strongly related to the symmetry, parity and structure of the order parameter. In the case of the clean limit, as we showed here, it is important to realize that avoided crossings exist only between electron and hole quasiparticle states of subbands j and $j + 2n$, where n is an integer. This is because the order parameter has an even function with respect to $y = 0$. Similarly, an odd-functional order parameter would result in TE between states of subbands j and $j + (2n - 1)$. In the arbitrary situation where the order parameter shows a random distribution due to strong disorder, TE should happen between all degenerate electron and hole quasiparticles. All these properties can be explained by a reduced 4×4 BdG matrix as shown in the next subsection.

6.2.3 4×4 BdG matrix for the two-subband quasiparticle interference

Due to the fact that only two subbands are involved in the TE of two-subband QPI, we find it can be qualitatively described by a reduced 4×4 BdG matrix where only the two Bogoliubov quasiparticles and their correlations are considered.

We start from the general BdG equations (6.1) but only keep a hole state of subband j and an electron state of subband j' for a given wave vector k. For the hole state, its energy and wave function are determined by the single-electron Schrödinger equation $H_e|j>=-\zeta_j|j>$. Note that $-\zeta_j<0$ due to the hole excitation. Again, the energy and wave function of the electron state is determined by $H_e|j'>=\zeta_{j'}|j'>$ where $\zeta_{j'}>0$. The orthogonal relation between the hole state $|j>$ and the electron state $|j'>$ yields $<j|j'>=\delta_{jj'}$. For simplicity and fitting the case of previous subsection, $|j>$ and $|j'>$ are chosen as real and to generate the real order parameter $\Delta(\mathbf{r})$. Then, the electron component of a Bogoliubov quasiparticle is $u_n=U_j|j>+U_{j'}|j'>$ and the hole component is $v_n=V_j|j>+V_{j'}|j'>$ where U_j and V_j are the component amplitude of subband j for electron and hole, respectively. The 4×4 BdG matrix reads:

$$\begin{bmatrix} -\zeta_j & 0 & \Delta_j & \Delta_{jj'} \\ 0 & \zeta_{j'} & \Delta_{j'j} & \Delta_{j'} \\ \Delta_j & \Delta_{jj'} & \zeta_j & 0 \\ \Delta_{j'j} & \Delta_{j'} & 0 & -\zeta_{j'} \end{bmatrix} \begin{bmatrix} U_j^n \\ U_{j'}^n \\ V_j^n \\ V_{j'}^n \end{bmatrix} = E_n \begin{bmatrix} U_j^n \\ U_{j'}^n \\ V_j^n \\ V_{j'}^n \end{bmatrix} \tag{6.10}$$

with the matrix elements $\Delta_j=<j|\Delta(\mathbf{r})|j>$ and $\Delta_{jj'}=<j|\Delta(\mathbf{r})|j'>=\Delta_{j'j}$. Note that the $\Delta_{jj'}$ is the exchange integral between the two states from different subbands. In a homogeneous superconductor, the constant order parameter $\Delta(\mathbf{r})\equiv\Delta$ leading to the zero exchange integral, $\Delta_{jj'}=0$, results in the decomposition of Eqs. (6.10) into two sets of general 2×2 BdG matrices for the two states respectively. Thus, there is no TE for this case.

For an inhomogeneous superconductor with a perturbation in the order parameter $\Delta(\mathbf{r})=\Delta+\delta\Delta(\mathbf{r})$, the matrix elements are

$$\Delta_j=<j|\Delta+\delta\Delta(\mathbf{r})|j>\approx\Delta, \tag{6.11}$$

and

$$\Delta_{jj'}=<j|\Delta+\delta\Delta(\mathbf{r})|j'>=<j|\delta\Delta(\mathbf{r})|j'>=\Delta_{j'j}\neq0. \tag{6.12}$$

Note that the non-zero exchange integral $\Delta_{jj'} \neq 0$ in this case is responsible for the TE.

The TE of QPI reaches its maximum when states of two subbands are degenerate in energy, i.e., $\zeta_j = \zeta_{j'} = \zeta$. So Eqs. (6.10) are written as

$$\begin{bmatrix} -\zeta & 0 & \Delta & \Delta_{jj'} \\ 0 & \zeta & \Delta_{jj'} & \Delta \\ \Delta & \Delta_{jj'} & \zeta & 0 \\ \Delta_{jj'} & \Delta & 0 & -\zeta \end{bmatrix} \begin{bmatrix} U_j^n \\ U_{j'}^n \\ V_j^n \\ V_{j'}^n \end{bmatrix} = E_n \begin{bmatrix} U_j^n \\ U_{j'}^n \\ V_j^n \\ V_{j'}^n . \end{bmatrix} \tag{6.13}$$

The eigenvalues and eigenstates of matrix (6.13) are exactly solvable and the four eigenvalues are

$$\pm E_{\pm} = \pm\varepsilon \pm \Delta_{jj'} \tag{6.14}$$

where $\varepsilon = \sqrt{\zeta^2 + \Delta^2}$ is the quasiparticle excitation energy of the isotropic superconducting gap Δ. The gap induced by TE, Δ_{TE}, is the energy difference between the two positive eigenvalues:

$$\Delta_{TE} = \begin{cases} 2\Delta_{jj'} & \text{if } \Delta_{jj'} < \varepsilon \\ 2\varepsilon & \text{if } \Delta_{jj'} \geqslant \varepsilon. \end{cases} \tag{6.15}$$

Typically, the exchange integral $\Delta_{jj'}$ is smaller than the excitation energy gap ε. As a result, $\Delta_{TE} = 2\Delta_{jj'}$ and that is why we labeled the gaps as $2\Delta_{j,j'}$ in Fig. 6.1.

When the exchange integral is positive, i.e., $0 < \Delta_{jj'} < \varepsilon$, the eigenvalues sorted by their values are $\begin{pmatrix} -E_+ & -E_- & E_- & E_+ \end{pmatrix}$ and their corresponding eigenstates are

$$\begin{pmatrix} U_j^n \\ U_{j'}^n \\ V_j^n \\ V_{j'}^n \end{pmatrix} = \begin{pmatrix} A & A & B & B \\ B & -B & -A & A \\ -B & -B & A & A \\ -A & A & -B & B \end{pmatrix} \tag{6.16}$$

where

$$\begin{aligned} A &= \tfrac{1}{2}\left(1 + \tfrac{\zeta}{\varepsilon}\right)^{\frac{1}{2}} \\ B &= \tfrac{1}{2}\left(1 - \tfrac{\zeta}{\varepsilon}\right)^{\frac{1}{2}}. \end{aligned} \tag{6.17}$$

Normalization is chosen to satisfy Eq. (6.2), i.e. $2(A^2 + B^2) = 1$. For both eigenstates with positive eigenvalue E_+ and E_-, their spectral weights $Z_{E_\pm} = 0.5$ indicate that Bogoliubov quasiparticles are well formed by the

coupling between the electron and hole subbands. The difference between the two states are the bonding and anti-bonding combinations of the electron and hole components.

It is interesting to realize that the A and B are $\Delta_{jj'}$-independent and $\sqrt{2}(A\ B)^T$ is the eigenstate of the positive eigenvalue of the general 2×2 BdG equations, i.e.,

$$\begin{pmatrix} \zeta & \Delta \\ \Delta & -\zeta \end{pmatrix} \begin{pmatrix} \sqrt{2}A \\ \sqrt{2}B \end{pmatrix} = \varepsilon \begin{pmatrix} \sqrt{2}A \\ \sqrt{2}B \end{pmatrix}. \tag{6.18}$$

where the eigen-energy is ε and the $\sqrt{2}$ is introduced to satisfy the normalization condition, Eq.(6.2). It turns out that the total pair amplitude of the states E_+ and E_- are the same as the one without TE, i.e.,

$$D_{E_+} + D_{E_-} = 2AB(|j>^2 + |j'>^2) = D_j + D_{j'}. \tag{6.19}$$

Finally, we have to mention that the exchange integral $\Delta_{jj'}$ is sensitive to the symmetry, parity and spatial variation of the order parameter $\Delta(\mathbf{r})$. For the nanobelt in the clean limit, $\Delta(\mathbf{r})$ has a spatial distribution with even-parity with respect to $y = 0$. The exchange integral is exactly zero when both states $|j>$ and $|j'>$ have different parity. This is the reason why TE only appears between electron and hole quasiparticle states of subbands j and $j + 2n$ which have the same parity, resulting in a possible non-zero exchange integral $\Delta_{jj'}$.

6.2.4 Modulated waves in the local density of states due to the Tomasch effect

Previously, we introduced the properties of the TE of two-subband QPIs for a narrow sample. However, the mean field BdG theory is of limited validity in such a case due to the increasing importance of phase fluctuations and, moreover, quasiparticles are not well defined far above the Fermi level. In this subsection, we investigate the TE in wider samples in order to avoid these issues. The results of this subsection show that: 1) properties obtained previously are still valid, and 2) the TE results in a modulated wave structure in the local density of states, which should be observable in experiments.

As an example, we present results for a nanobelt with width $W = 153.3$ nm, which is more than $10\xi_0$. The spatial distribution of the order parameter

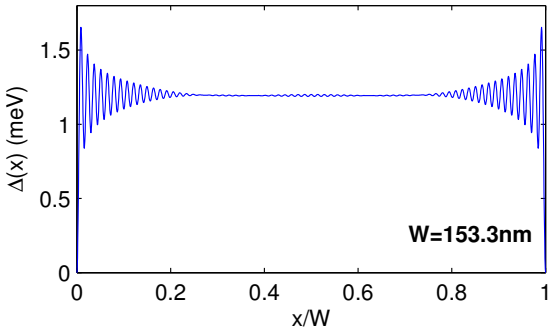

Figure 6.2: Spatial order parameter distribution $|\Delta(x)|$ for a sample with $W = 153.3$ nm. Note that the order parameter converges to Δ_0 in the bulk.

$\Delta(x)$ is shown in Fig. 6.2. It can be seen that the order parameter shows Friedel-like oscillations at both edges but it converges to its bulk value Δ_0 far away from the edges. The flat order parameter in the central area suppresses the TE. Fortunately, the energy gaps induced by TE can still be seen clearly in the corresponding quasiparticle excitation spectrum in the upper panel of Fig. 6.3. Here, we focus on the gaps at the intersection between states of subbands j and $j + 2$, which are indicated by a dashed curve. Due to the smaller energy difference between the adjacent subbands in the wider sample, the gaps appear at energies close to the superconducting gap energy Δ_0 and far below the cutoff energy E_c, where the quasiparticles are well defined.

The TE exhibits all the properties which have been introduced previously except that the quasiparticle states generate considerable net pair amplitude, contributing to the order parameter. To show this feature, we present the electron and hole amplitudes, u and v, and their pair amplitude, D, of selected quasiparticle states γ_+ and γ_- (marked by open circle in the upper panel) as a function of x in the lower panels of Fig. 6.3. Both states have the same wave vector k and are separated by an energy gap due to the influence of TE. It can be seen that u and v exhibit rapid oscillations with slowly varying envelopes. The envelopes show modulated wave structures due to the combination of states of subbands j and $j+2$. The difference in envelope for states γ_+ and γ_- are due to the bonding and antibonding combinations of the two single-electron wave functions, respectively. Meanwhile, the phase shift between the u and v components leads to more complex pattern in their pair amplitude. Finally, the net pair amplitude $D_{\gamma_+} + D_{\gamma_-}$ (shown in

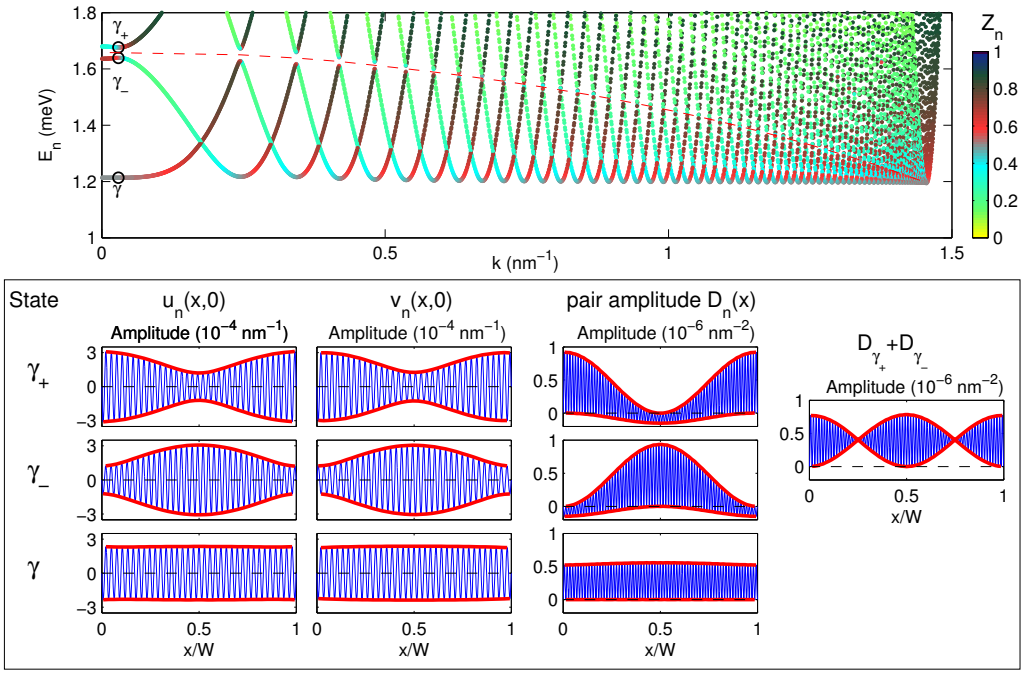

Figure 6.3: (Color online) (Upper panel) Quasiparticle excitation spectrum as a function of positive longitudinal wave vector, k_z, for energies below 1.8 meV for a nanobelt of width $W = 153.3$ nm. The spectral weight of the quasiparticle states are indicated by color. The three quasiparticle states γ_+, γ_- and γ marked by open circle are chosen for showing the electron and hole amplitudes, u and v, as a function of x at $y = 0$ and their pair amplitudes D in the lower panels. The red thick lines are the envelopes of the curves. The quasiparticle states γ_+ and γ_- are under the influence of the Tomasch effect and show a phase difference between their u and v components. The net pair amplitude of the two states $D_{\gamma_+} + D_{\gamma_-}$ is shown in the right-most panel.

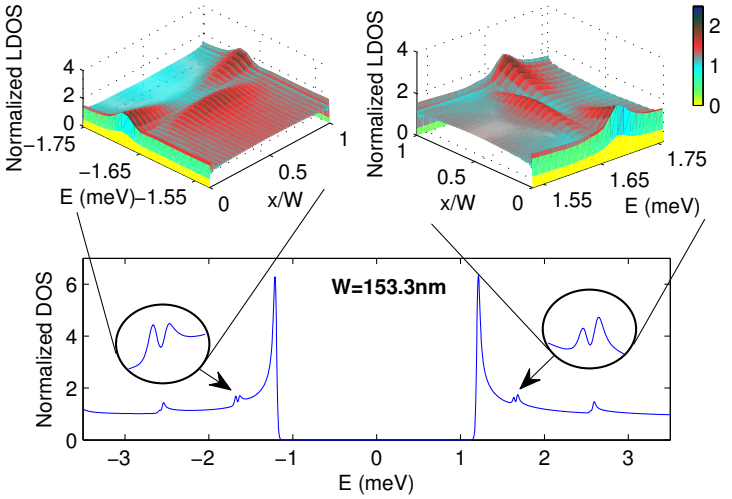

Figure 6.4: DOS and relevant LDOS for the sample with $W = 153.3$ nm. The DOS is shown in the lower panel. The oscillatory structures induced by the Tomasch effect are magnified in the two insets. The corresponding LDOS $A(x, E)$ along the transversal direction are shown in the upper panels.

the lower panel of Fig. 6.3) is large and positive, showing a modulated wave structure.

As a reference, we also present the electron amplitude, u, hole amplitude, v, and its pair amplitude, D, of a conventional Bogoliubov quasiparticle state γ (also marked by open circle in the upper panel) as a function of x in the lower panels of Fig. 6.3. Because u and v belong to the same subband j, they are in phase leading to a positive pair amplitude with a flat envelope.

The states γ_+ and γ_-, which are under the influence of TE, induce peaks in the DOS and modulated wave structures in the LDOS. Fig. 6.4 show the corresponding DOS in the lower panel and the LDOS under the influence of TE in the upper panel. In the DOS, the peaks induced by states $\gamma_\pm$ sit at the symmetrical bias energy $E = \pm 1.65$meV. The insets magnify the relevant areas. In the insets, the outer peaks are induced by the state γ_+ while the inner peaks are induced by the state γ_-. The LDOS shows very different patterns at these two energies, which can be seen from the upper panels. For the outer peaks in DOS, the LDOS is enhanced at the edge whereas, for the inner peaks, it is enhanced at the center. The envelope of LDOS varies slowly as a function of x. Therefore, it may be easily detected by STM.

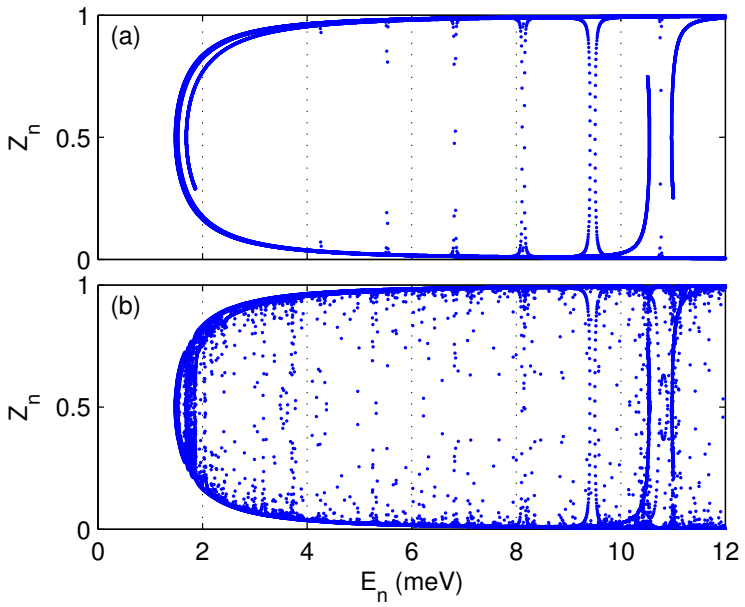

Figure 6.5: (Color online) Spectral weight of quasiparticles, Z_n, as a function of energy of states, E_n, for the nanobelt of width $W = 16.8$ nm (a) in the clean limit ($U = 0$) and (b) under the influence of random impurities.

6.2.5 Discussion on the signature of the Tomasch effect in the presence of disorder

Previously, only the TE in clean superconductors were considered. However, in all experiments, superconductors are rather "dirty", where additional scattering processes of quasiparticles appear due to surface roughness, impurities, substrate and so on. These factors will broaden the single-electron levels, modify electronic wave functions, reduce the electron mean free path and, thus, lead to noise and modifications in DOS and LDOS. In this subsection, we study TE under such additional scattering processes by introducing a random distribution of weak impurities. The results of this subsection show that :1) many more gaps induced by TE are opened in this case, 2) one can still recover the dominant gaps seen the clean limit by comparing the DOS of superconducting and normal states, 3) the LDOS shows more complex scattering patterns but follows the same bonding and antibonding combination of involved quasiparticle wave functions.

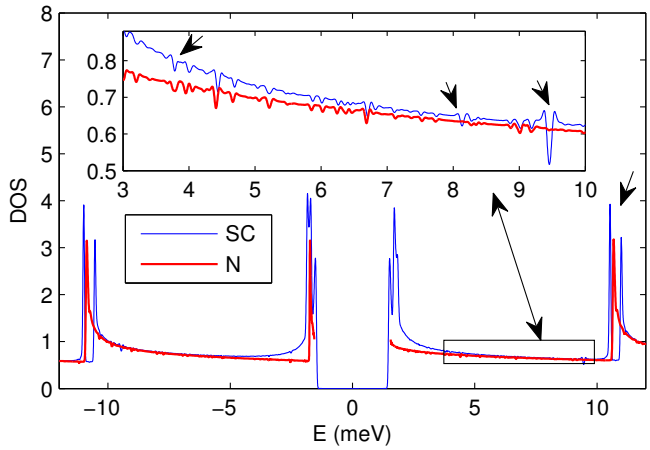

Figure 6.6: (Color online) DOS of the superconducting (blue) and normal (red) states for the nanobelt of width $W = 16.8$ nm under the influence of the random impurities. The inset shows details of the DOS between $E = 3$ meV and 10 meV. The arrows indicate signatures of the TE. Note that the normal DOS is mapped on a new energy scale, in order to match the oscillations in the DOS induced by the impurities. The mapping is done by rescaling, $E_{new} = \sqrt{E_{old}^2 + |\tilde{\Delta}|^2}$, where E_{new} and E_{old} are the new and old energies, and $\tilde{\Delta}$ is a fitting parameter whose value is close to the mean amplitude of the order parameter $|\bar{\Delta}|$.

The random impurities are introduced by using the potential $U(\mathbf{r})$ in the single-electron Hamiltonian defined Eq. (6.1), i.e. $H_e = -(\hbar\nabla)^2/2m + U(\mathbf{r}) - E_F$. As a result, the order parameter, $\Delta(\mathbf{r})$, is no longer longitudinally independent, i.e. $\Delta(\mathbf{r}) = \Delta(x, y)$. Following the numerical approach introduced in Sec. 6.2.1, we take a periodic unit cell with length L and width W and expand the electron(hole)-like quasiparticle wavefunctions $u_n(v_n)$ by using Eq. (6.6). Using Bloch's theorem, the BdG equations will be separated for each reciprocal vector. By considering a large number of k points, we achieve a good resolution in the DOS in order to observe the TE. In this subsection, we take $W = 16.8$ nm and $L = 40$ nm. Such nanobelt in the clean limit ($U = 0$) has been introduced in Sec. 6.2.2. The impurity potential profile is modeled by a random collection of symmetric Gaussian functions, $U(\mathbf{r}) = \sum_i U_i exp[-(\mathbf{r}-\mathbf{r_i})^2/2\sigma^2]$ where U_i is the amplitude, $\mathbf{r_i}$ is the location of the impurity and $\sigma = 0.02$ represents the the spread of the potential (full width at 1/10th of maximum is 0.86 nm). For the situation of weak impurities (disorder), we take 100 impurities in the unit cell with random locations r_i and random amplitude U_i with a maximum $U_i^{max} = 0.1E_F$. After the BdG equations are solved self consistently, as described in the previous sections, the order parameter, Δ, has almost the same distribution as the one with $U = 0$.

We show in Fig. 6.5 the spectral weight of quasiparticles Z_n as a function of energy of states E_n for the case in the clean limit and the case with impurities. In clean bulk superconductors, particles and holes never mix at energies away from the superconducting gap, i.e. $Z_n = 0$ *or* 1, for holes or electrons, respectively. In the case of clean superconductor under quantum confinement, as seen from Fig. 6.5(a), particle-hole mixing indicates the emergence of TE due to the stripe-like inhomogeneity of the order parameter. In the presence of the impurities, as shown in Fig. 6.5(b), TE appears for much wider range of energies due to the symmetry broken of the electronic wave functions. It indicates that many more TE gaps are opened at the crossover of electron and hole subbands for more realistic situations. Nevertheless, for weak disorder, the stronger contribution is still observed at the same energies as obtained in the clean limit.

To find the signature of TE, we show the DOS of both superconducting and normal states in the presence of impurities in Fig. 6.6. The noise-like oscillations in the DOS are imposed over the signature of TE. After matching both oscillations in DOS by mapping the DOS of normal state to a rescale energy range, one can find TE signatures 1) where there are new oscillations in

the superconducting DOS and, 2) where there are different oscillatory structures between DOS of superconducting and normal states. In Fig. 6.6, these signatures are marked by arrows. It is worth noting that the TE modifies the DOS on positive and negative biases symmetrically.

Finally, we have to mention that the LDOS under the influence of random impurities shows much more complex patterns. However, the pattern still follows the bonding and antibonding combination of involved quasiparticle wave functions as described in the previous sections.

As the impurity strength increases, the band structure together with order parameter become strongly affected. In this case, while the TE is also strongly enhanced, it becomes increasingly difficult to compare with results obtained in the clean limit. Depending on the particular impurity distribution, TE contributions to the DOS could be individually recognized but these are of different manifestation, when compared to the DOS modifications obtained in the clean limit.

6.3 Tomasch effect in superconducting nanowires

In this section, we consider superconducting nanowires with square and rectangular cross sections. We find a new type of TE, i.e., TE induced by three-subband QPI. Its influence on the electronic structure and its dependence on the symmetry of the system will be discussed in the following sections.

6.3.1 Bogoliubov-de Gennes theory for three-dimensional nanowires

Here, we consider a three-dimensional superconducting nanowire with rectangular cross section (transverse dimensions L_x and L_y). Due to quantum confinement in the transverse directions, the Dirichlet boundary conditions are taken on the surface (i.e. $u_n(\mathbf{r}) = v_n(\mathbf{r}) = 0,\ \mathbf{r} \in \partial S$). Along the longitudinal direction z, we introduce a periodic computational unit cell with length L_z where periodic boundary conditions are used.

Due to the fact that the order parameter is independent of the longitudinal direction, i.e. $\Delta(\mathbf{r}) = \Delta(x, y)$, the electron-like and hole-like wave functions u_n and v_n can be expanded, for each longitudinal wave vector k_z,

as

$$\begin{pmatrix} u_n(\mathbf{r}) \\ v_n(\mathbf{r}) \end{pmatrix} = \frac{e^{ik_z z}}{\sqrt{L_z}} \sum_{j_x, j_y \in \mathbb{N}^+} \phi_{j_x j_y}(x, y) \begin{pmatrix} u^n_{j_x j_y} \\ v^n_{j_x j_y} \end{pmatrix}, \tag{6.20}$$

where

$$\phi_{j_x j_y}(x, y) = \frac{2}{\sqrt{L_x L_y}} \sin\left(\frac{\pi j_x x}{L_x}\right) \sin\left(\frac{\pi j_y y}{L_y}\right), \tag{6.21}$$

are the eigenstates of the single-electron Schrödinger equation $H_e \phi_{j_x j_y} = \zeta_{j_x j_y} \phi_{j_x j_y}$. The longitudinal momentum, k_z, satisfies the quantization condition, i.e. $k_z \cdot L_z = 2\pi m, m \in \mathbb{Z}$. Following the previous section, the expansion in Eq. (6.20) includes the states with energies $-E_F < \zeta_{j_x j_y} < E_F + \varepsilon$ where $\varepsilon = 5E_c$ is taken sufficiently large in order to guarantee the accuracy.

The pair amplitude $D_n(\mathbf{r})$ and spectral weight Z_n for each state are calculated from the Eqs. (6.4) and (6.9), respectively. The LDOS $A(\mathbf{r}, E)$ and the DOS $N(E)$ are calculated from the Eqs. (6.7) and (6.8), respectively.

We use the same microscopic parameters as the one introduced in Sub-Sec. 6.2.1 for bulk $NbSe_2$. The mean electron density

$$n_e = \frac{2}{V} \sum_n \int \left\{ |u_n|^2 f(E_n) + |v_n|^2 [1 - f(E_n)] \right\} d\mathbf{r}$$

for nanowires with $V = L_x L_y L_z$. n_e is kept to its bulk value obtained when $L_{x,y,z} \to \infty$. All the calculations are performed at zero temperature.

6.3.2 Tomasch effect due to three-subband quasiparticles interference

We first show results in Fig. 6.7 for a nanowire with square cross section ($L_x = L_y = 8$ nm) where the geometry of the sample and the order parameter show C_4 symmetry. Fig. 6.7(a) shows the excitation spectrum as a function of the positive wave vector $k_z > 0$. All the subbands displayed in the panel are distinguishable and labeled by a set of quantum numbers (j_x, j_y). Note that the $(j_x, j_y)^*$ is a shorthand notation for the pairs (j_x, j_y) and (j_y, j_x) because of their overlap due to degeneracy. The spectral weight Z_n is marked by color for each quasiparticle state.

As seen from Fig. 6.7(a), the bottom of the subband $(3, 3)$ lying below the cutoff energy E_c results in a resonant and spatially inhomogeneous order parameter $\Delta(x, y)$, which is shown in Fig. 6.7(b). $\Delta(x, y)$ shows C_4 symmetry

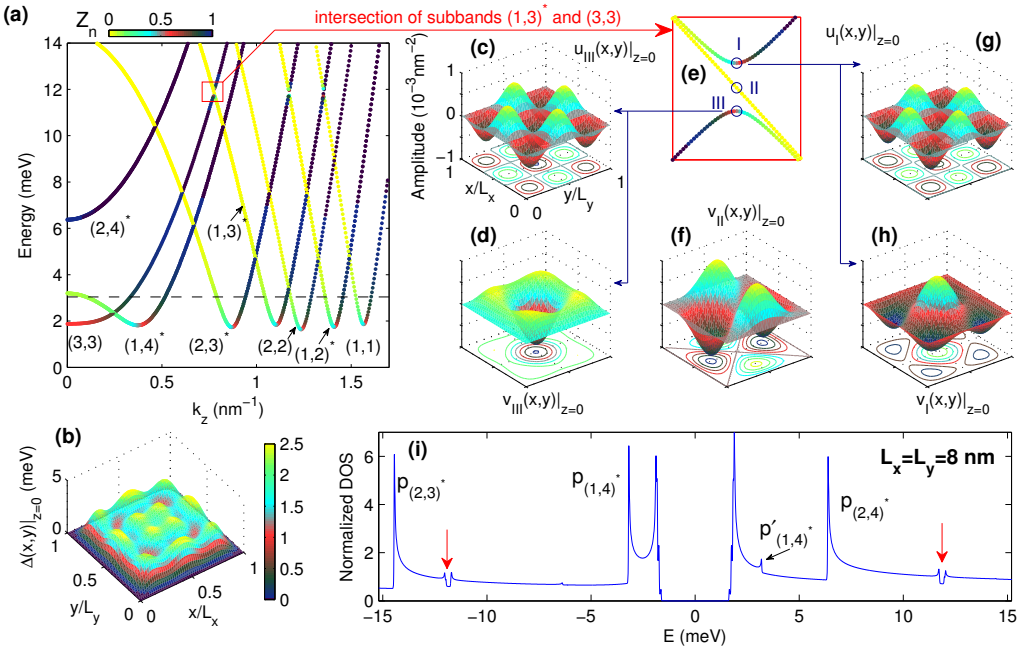

Figure 6.7: Results for the nanowire with a square cross section: $L_x = L_y = 8$ nm. (a) Quasiparticle excitation spectrum as a function of positive longitudinal wave vector k_z for the relevant single-electron subbands (j_x, j_y). Note that the notation $(j_x, j_y)^*$ represents two degenerate subbands (j_x, j_y) and (j_y, j_x). The spectral weight of the quasiparticle states is indicated by color. The excitation spectrum in the red rectangle is magnified in panel (e) in order to show the influence of the Tomasch effect due to three-subband quasiparticle interference. The three quasiparticle states I-III are marked by open circle in panel (e) and their spatial distribution of electron and hole amplitude, u and v, at $z = 0$ are shown in panels (c, d, f-h). Note that the electron amplitude of the state II is not shown because $u_{II}(x, y) = 0$. (b) The spatial distribution of the order parameter $\Delta(x, y)$. (i) The corresponding DOS. The gaps due to the Tomasch effect as determined by three-quasiparticle interference processes are marked by red arrows. Peaks $p_{(j_x,j_y)}$ are due to the contributions from the states of the bottom of the subbands (j_x, j_y), while accompanying peaks $p\prime_{(j_x,j_y)}$ are due to the formation of the gaps, i.e. electron-hole coupling.

due to the square cross section. The symmetry of the system and the order parameter determine the properties of TE and its emergence. For example, two sets of TE from two-subband QPI appear at the intersection of subbands $(1,2)^*$ and $(1,3)^*$, while TE from three-subband QPI appears at the intersection of subbands $(1,3)^*$ and $(3,3)$ or $(1,3)^*$ and $(1,1)$, respectively.

We next investigate the most significant three-QPI appearing at the intersection of two hole quasiparticle states from subbands $(1,3)^*$ and one electron quasiparticle state from subband $(3,3)$. This is indicated by the open red rectangle in Fig. 6.7(a) and the relevant three dispersion relations of the energy bands are amplified in Fig. 6.7(e). It is clearly seen that the upper and lower energy bands exhibit a gap-like structure while the middle energy band crosses the gap diagonally. The Bogoliubov quasiparticles are well formed for the states close to the bottom of the upper band and the top of the lower band. Note that the state pertaining to the middle band are pure hole-like quasiparticles states with zero amplitude of the electron component. This is an interesting phenomenon because if a gap opens between states from subbands $(1,3)$ and $(3,3)$, the other gap was supposed to be opened between states from subbands $(3,1)$ and $(3,3)$. The reason is that the gap induced by the exchange integral only depends on the symmetry of the wave functions of the relevant states.

In fact, this interesting asymmetrical energy band structure is due to the symmetric and anti-symmetric combinations of the two hole states from subbands $(1,3)^*$. To see this, in Figs. 6.7(c, d, f-h), we show the spatial distribution of the hole and the electron amplitude, $u(x,y)$ and $v(x,y)$, of states I-III marked by open circles in Fig. 6.7(e). The three states have the same wave vector k_z, chosen such that the gap has a local minimum [see panel 6.7(e)]. The electron components of the gapped states, u_I and u_{III} [shown in panels 6.7(c) and (g)], have contributions only from the electron state of subband $(3,3)$. Therefore, they show the same pattern as $\phi_{3,3}$, which is the eigenstate of the single-electron Schrödinger equation with quantum numbers $j_x = 3$ and $j_y = 3$. For the corresponding amplitude of hole components, v_I and v_{III} [shown in panels 6.7(d) and (h)], they have the same spatial distribution as the symmetric combination of the two eigenstates, i.e., $\phi_{1,3} + \phi_{3,1}$, but with opposite sign for the two amplitudes I and III.

Clearly, the Bogoliubov quasiparticle states, I and III, are the bonding and anti-bonding combinations of the electron and hole components. The reason is that both the wave-functions and the order parameter exhibit C_4 symmetry and, thus, result in non-zero exchange integrals, which are respon-

sible for TE and generate energy gaps. The quasiparticle state II does not take part in the quasiparticle interference because its hole component, v_{II}, has C_2 symmetry, $(v_{II}(x,y) = -v_{II}(y,x))$, due to the anti-symmetric combination of the two hole eigenstates, i.e., $\phi_{1,3} - \phi_{3,1}$, leading to a vanishing exchange integral.

We now conclude the appearance of TE due to three-subband QPI. First, hole states from subbands $(1,3)$ and $(3,1)$ are combined in order to generate symmetric and anti-symmetric states but which are degenerate in energy. Then, the symmetric combination couples with the electron state from subband $(3,3)$ and forms Bogoliubov quasiparticle states, therefore inducing a gap. Finally, the energy and the wave-function of the anti-symmetric combination is unaffected.

The process results in oscillations in the DOS, which are symmetrical in bias [see Fig. 6.7(i)]. The oscillations induced by TE from the three-QPI are marked by arrows for both positive and negative biases. When comparing with the DOS of a nanobelt shown in Fig. 6.1(h), we notice that there are less oscillations induced by TE. The reason is that TE emerges only in case of a non-zero exchange integral. This becomes harder to achieve for a system with two quantum numbers, (j_x, j_y), because the condition has to be fulfilled by both .

Next we will show that the TE of three-subband QPI in a nanowire depends strongly on the symmetry of the electronic structures and the geometry of the sample. For this purpose, we consider nanowires with rectangular cross section, i.e. $L_x \neq L_y$ where the C_4 symmetry is broken and, more importantly, results in the splitting of the subbands (j_x, j_y) and (j_y, j_x). In Fig. 6.7, we present the appearance of the TE due to three-subband QPI for states of hole subbands $(1,3)$, $(3,1)$ and electron subband $(3,3)$ for nanowires with $L_x = 8$ nm and $L_y = 8.03$ nm, 8.05 nm, 8.07 nm and 8.10 nm, respectively. The spectral weight of the relevant states is indicated by color. The three subbands without TE are shown in the most left panel. As mentioned previously, the two hole subbands $(1,3)$ and $(3,1)$ split while the electron subband $(3,3)$ crosses them. The states of subband $(3,1)$ have higher energy than those of subband $(1,3)$ for a given k_z when $L_y > L_x$. It can be seen that the bottom of the highest energy subband shifts to the right with increasing L_y, while the top of the lowest energy subband shifts to the left. When comparing with the result for a square cross section shown in Fig. 6.7(e), we find that the previously unaffected hole subband becomes and shows mixed electron-hole components, signaling a coupling with the electron subband.

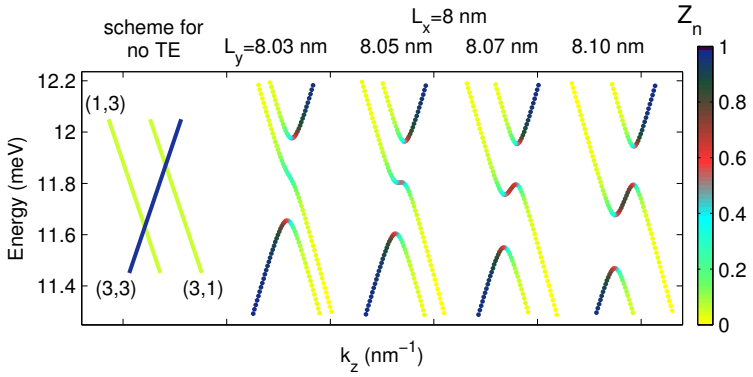

Figure 6.8: Symmetry-dependent Tomasch effect of three-subband quasiparticles interference for states of subbands $(1,3)$, $(3,1)$ and $(3,3)$ for rectangular cross section $L_x < L_y$. The left-most panel shows the band dispersion for the three subbands without Tomasch effect. The other four panels show the band dispersion versus longitudinal wave vector k_z for$L_x = 8$ nm and $L_y = 8.03$ nm, 8.05 nm, 8.07 nm, 8.10 nm, respectively. They are shifted horizontally for clarity. The spectral weight of the quasiparticle states is indicated by color in all panels.

Finally, the three-subband QPI converts into two sets of two-subband QPI, appearing for states from subbands $(1,3)$ and $(3,3)$ and separately from subbands $(3,1)$ and $(3,3)$, as seen in Fig. 6.7 for $L_y = 8.10$ nm.

An interesting phenomenon is noticed for $L_y = 8.05$ nm where the middle energy band exhibits a flat region, as seen in Fig. 6.8. The spectral weight Z_n and the corresponding states [see Fig. 6.9] show that the Bogoliubov quasiparticle states couple the hole and electron components. For the upper energy band L_I, the quasiparticle states are converted from the hole-like states $v_{3,1}$ to the electron-like states $u_{3,3}$ as k_z is increased, as seen in Fig. 6.9(b). The same is true for the lower energy band L_{III} but now from the electron-like states $u_{3,3}$ to the hole-like states $v_{1,3}$, as seen in Fig. 6.9(d). The middle energy band shows a more complex coupling among the three subbands as it is converted from $v_{1,3}$ to $v_{3,1}$ with the help of $u_{3,3}$ due to the compatible symmetry of these states.

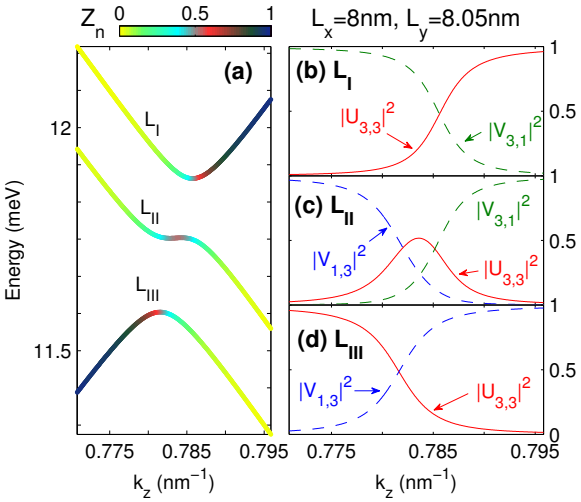

Figure 6.9: (a) Band dispersion for the energy bands (L_I-L_{III}) due to the Tomasch effect of three-quasiparticles interference of the energy subbands $(1,3)$, $(3,1)$ with $(3,3)$ for a rectangular cross section $L_x = 8$ nm and $L_y = 8.05$ nm. The spectral weight of the quasiparticle states are indicated by color. The electron and hole components of these states are shown in panels (b-d), respectively.

6.4 Conclusion and discussion

In conclusion, we investigated the Tomasch effect on the electronic structure in nanoscale superconductors by solving the Bogoliubov-de Gennes equations self-consistently. Here, the Tomasch effect is induced by an inhomogeneous order parameter appearing due to quantum confinement. We found that the Tomasch effect couples degenerate electron and hole states above the superconducting gap due to quasiparticle interference leading to additional pairs of BCS-like Bogoliubov-quasiparticles that generate energy gaps resulting in oscillations in the DOS. When the energies of the paired states are far from the Fermi level, the pair states show pseudo-gap-like structures in the DOS. When they are close to the Fermi level, the pair states result in modulated wave patterns in the local density of states. All these are due to the inter-subband electron-hole coupling and their bonding and anti-bonding combinations generating the pair states.

The Tomasch effect is strongly related to the geometrical symmetry of the system and the symmetry, parity and spacial variation of the order parameter. For the nanobelt, the Tomasch effect only leads to two-subband quasiparticles interference processes. With even-parity order parameter in the clean limit, the Tomasch effect only plays a role for two states with the same parity. A reduced 4×4 BdG matrix can describe well the results. For a nanowire with a square cross section, the Tomasch effect also results in three-subband quasiparticle interference processes due to the higher degree of symmetry. We observe coupling only for the symmetric combination of two hole states, while the anti-symmetric one remains unaffected. This leads to a unique energy band structure, where one of the subband crosses diagonally across the induced gap. For nanowires with rectangular cross section, the three-subband quasiparticles interference is converted into two sets of two-subband quasiparticles interference leading to a distortion of the previously unaffected band.

The Tomasch effect is commonly formed in inhomogeneous superconductivity but it could be difficult to observe it experimentally. One reason is that the effect can be shadowed by other states present at the same energy. Another reason is that the large size of Cooper-pairs may result in a complex global electronic structure. However, the effect can be enhanced in the following ways: 1) by reducing the symmetry of the sample such as realized by surface roughness and by making layered junctions; 2) by breaking the symmetry of the order parameter by e.g. disorder and impurities, and 3)

by designing the sample such that the relevant electron and hole subbands touch each other near their bottom and top, respectively. We have show that for a realistic case, in the presence of weak disorder, the modifications in the DOS due to the TE survive and can be clearly distinguished from oscillations induced by impurity scattering.

Chapter 7

Summary and Outlook

7.1 Summary

Due to quantum confinement, nanoscale superconductivity exhibits richer phenomena than bulk superconductivity. This will allow us to artificially design the electronic properties by changing the size and geometry of the superconductor, leading to the desired control and enhancement of superconductivity. It provides us with a great potential for applications in ultrafast, power-saving electronic devices such as superconducting transistors and single-photon detectors. However, the interplay between superconductivity and quantum confinement effect has not been fully understood yet.

In the present thesis, we theoretically investigated several aspects of nanoscale superconductivity by solving self-consistently the Bogoliubov-de Gennes equations. The topics that are covered range from vortex states under the influence of quantum confinement to the electronic structure in various nano-structures. The density of states obtained in this thesis can be compared with results from STM/STS experiments.

In **Chapter 3**, we studied vortex states under the influence of quantum confinement effect in nanoscale superconductors. We found that nanoscale superconductors with coherence length comparable to the Fermi wavelength, that the shape resonances of the order parameter results in an additional contribution to quantum topological confinement - leading to unconventional vortex configurations. Our results for a square geometry in the quantum limit reveal a plethora of asymmetric, giant multi-vortex, and vortex-antivortex structures, stable over a wide range of parameters and which are very differ-

ent from those predicted by the Ginzburg-Landau theory. Experimentally, these states can be accessed through STM measurements. Additional, competing interactions in the quantum limit for the bound states are different from those for the vortices, so that the conventional picture of a vortex bound to the lowest energy states does not hold. Instead we predict that the maxima in LDOS of the lowest energy states will be observed between vortices and near surfaces. These peculiar phenomena are a consequence of the strong quantum confinement, which induces spatial oscillations in the order parameter. Finally, we proposed that the system consisting of a graphene flake in contact to a superconducting film could be a good candidate to observe experimentally these novel vortex states.

In **Chapter 4**, we investigated the vortex states in a nanoscale superconducting square for different sizes W, parameters $k_F\xi_0$, and temperatures T. It is an extension of the previous study presented in Chapter 3. We found that the inhomogeneous pattern of the order parameter as induced by the quantum confinement effect gives an additional contribution to the competing effects that determine the vortex configurations. Because of this reason, some unconventional vortex states such as asymmetric, edge-parallel and vortex-antivortex states are found as the ground state of our nanoscale system. These were never seen in the Ginzburg-Landau approach. Since the inhomogeneous pattern of the order parameter strongly depends on $k_F\xi_0$ and the size W, the vortex ground states and the magnetic field values of the phase transition are very sensitive to changes in these parameters, which is a direct consequence of the quantum size effect. Finally, we found that, in the quantum limit, nano-size superconductors favor vortex-antivortex molecules while disfavoring giant vortex states, which could be used to observe experimentally the antivortex.

In **Chapter 5**, we studied the effect of non-magnetic impurities on the local density of states and the transport properties in superconducting nanowires with diameter comparable to the Fermi wavelength λ_F (which is less than the superconducting coherence length). Such impurities have very little effect on the bulk properties of conventional superconductors. However, as the dimensionality is reduced, the effect of impurities becomes more significant. By applying the BdG theory to the case of $NbSe_2$, we uncovered several regimes in which the impurity affects the superconducting properties of the nanowire in different ways. First, depending whether the nanowire is in the resonant or off-resonant regime, the order parameter will show slow or fast oscillations away from the impurity, respectively. This is due to the

different nature of the quasi-particles involved in the formation of Cooper pairs, i.e. small or large momentum. Additionally, the impurity has a strong position-dependent effect on the Josephson critical current with opposite behavior in the resonant and off-resonance cases. These effects could be used to investigate the nature of the superconducting condensate and the scattering of the various subbands on the impurity.

In **Chapter 6**, we investigated the Tomasch effect on the electronic structure in nanoscale superconductors. The Tomasch effect is due to quasiparticle interference as induced by a nonuniform superconducting order parameter, which results in oscillations in the density of states at energies above the superconducting gap. Here, the Tomasch effect is induced by an inhomogeneous order parameter appearing due to quantum confinement. We found that the Tomasch effect couples degenerate electron and hole states above the superconducting gap leading to additional pairs of BCS-like Bogoliubov-quasiparticles. When the energies of the paired states are far from the Fermi level, the pair states show pseudo-gap-like structures in the DOS. When they are close to the Fermi level, the pair states result in modulated wave patterns in the local density of states. All these are due to the inter-subband electron-hole coupling.

The Tomasch effect is strongly related to the geometrical symmetry of the system and the symmetry, parity and spacial variation of the order parameter. For the nanobelt, the Tomasch effect only leads to two-subband quasiparticles interference processes. For a nanowire, it also results in three-subband quasiparticle interference processes leading to a unique energy band structure. The study on the Tomasch effect can help us to understand how the inhomogeneous order parameter affects quasiparticle states.

7.2 Outlook

In **Chapter 3** and **Chapter 4**, I investigated the vortex states in nanoscale one-component superconductors. Several novel vortex configurations and their electronic properties were unveiled under the influence of quantum confinement. Recently, by using the GL model in a multi-component superconductor, degenerate ground states with different inter-component phase differences were predicted [225]. It was shown that such systems will possess topological excitations in the form of domain walls separating the different phases of the coupled condensates. Such a domain wall connects fractional-

quantum vortices in the different components and supports the formation of novel broken time-reversal excitations - known as skyrmions [226]. However, the GL model can not provide the electronic structure of these topological excitations. Therefore, as a future continuation of my work it will be interesting to investigate the electronic structure of the domain walls, the fractional-quantum vortices and the skyrmions in multi-component superconductor by using BdG model. Also, it will be interesting to investigate how the properties of the topological excitations change under the influence of quantum confinement.

In **Chapter 5**, I investigated the effect of a non-magnetic impurity on a superconducting nanowire. It was shown that the effect is impurity position dependent so that the impurity can be used to manipulate the electrical properties of the nanowire. Recent advances in nanotechnology enabled the fabrication of nanoscale superconductors with artificial structuring e.g. designed interfaces, impurities, edge steps and other more complex boundary profiles. These factors directly alter the electronic states and the band structure of the material, and result in different superconducting properties, the tuning of which could be purposefully made useful when engineering electronic, fluxonic, or spintronic devices. Therefore, it will be interesting to theoretically investigate the effect of these types of boundary profiles on superconducting nano-structures.

Finally, in **Chapter 6**, I investigated the Tomasch effect (TE) in one-component nanoscale superconductors. The TE is a consequence of quasiparticle interferences in the superconducting side of the interface due to scattering on a non-uniform superconducting energy gap. It results in oscillations appearing in the DOS at energies above the superconducting gap. From the frequency of these oscillations, one can infer the properties of the superconducting gap [227]. Therefore, a straight forward extension of this work is the study of the TE in multi-component superconductors.

Chapter 8

Samenvatting

8.1 Samenvatting

Nanoschaal supergeleiding vertoont, als gevolg van de inperking, een veel uitgebreidere reeks van verschijnselen dan bulk supergeleiding. Dit zal ons toelaten om artificieel de elektronische eigenschappen te manipuleren door de grootte, vorm en structuur van de supergeleider te veranderen, wat leidt tot de controle en verhoging van de supergeleidende toestand. Het biedt een groot potentieël voor toepassingen in ultrasnelle, energie-besparende elektronische apparaten zoals supergeleidende transistoren en enkel-foton detectoren. De interactie tussen supergeleiding en quantum inperking is nog niet volledig begrepen.

In dit proefschrift hebben we theoretisch onderzoek verricht over de verschillende aspecten van nanoschaal supergeleiding en dit door het zelf-consistent oplossen van de Bogoliubov-de Gennes vergelijkingen. De onderwerpen handelen over vortextoestanden onder de invloed van quantum opsluiting tot de elektronische structuur in verschillende nanostructuren. De toestandsdichtheid verkregen in dit proefschrift kan worden vergeleken met de resultaten van STM / STS-experimenten.

In **hoofdstuk 3** onderzochten we vortextoestanden onder de invloed van quantum inperking in nanoschaal supergeleiders. We vonden dat nanoschaal supergeleiders met coherentielengte vergelijkbaar met de Fermi golflengte, dat de vorm resonanties in de ordeparameter resulteert in een extra bijdrage tot de kwantumtopologische inperking – en dit resulteer in onconventionele vortex configuraties. Onze resultaten voor een vierkante geometrie in de

quantum limiet onthullen een overvloed aan asymmetrische, multi-vortex, en vortex-antivortex structuren die stabiel zijn over een breed parameter gebied en welke zeer verschillend zijn van die voorspeld door de Ginzburg-Landau theorie. Experimenteel kunnen deze toestanden worden onderzocht via STM metingen. Additioneel, concurrerende interacties in de quantum limiet voor de gebonden toestanden zijn verschillend van die van de vortices, waardoor het conventionele beeld van een vortex gebonden aan de laagste energie toestanden niet meer opgaat. In de plaats voorspellen wij dat de maxima in de LDOS van de laagste energietoestanden zullen worden waargenomen tussen de vortices en in de buurt van oppervlakken. Deze bijzondere verschijnselen zijn een gevolg van de sterke quantum inperking, welke ruimtelijke oscillaties induceert in de ordeparameter. Tenslotte hebben we voorspeld dat een systeem bestaande uit een grafeenvlok in contact met een supergeleidende film een goede kandidaat kan zijn om deze nieuwe vortextoestanden experimenteel waar te nemen.

In **hoofdstuk** 4 onderzochten we de vortextoestanden in een nanoschaal supergeleidende vierkant van verschillende afmetingen W, verschillende parameter $k_F\xi_0$, en temperatuur T. Deze studie is een uitbreiding van hoofdstuk 3. We vonden dat het inhomogene patroon van de ordeparameter zoals geïnduceerd door de quantum inperking een extra bijdrage geeft aan concurrerende effecten die de vortex configuraties bepalen. Vanwege deze reden, werden er unconventionele vortextoestanden gevonden zoals asymmetrische, rand-parallelle en vortex-antivortex toestanden. Deze waren nooit eerder gevonden in de Ginzburg-Landau benadering. Sinds de inhomogene patronen van de ordeparameter sterk afhankelijk zijn van de waarde van $k_F\xi_0$ en de grootte W, vonden we dat de vortex grondtoestanden en de magnetische veld waarden van de fase-overgang zeer gevoelig zijn voor veranderingen in deze parameters. Uiteindelijk vonden we dat, in de quantum limiet, nanoschaal supergeleiders een voorkeur hebben voor vortex-antivortex moleculen terwijl multi vortextoestanden ongunstig zijn. Dit kan worden gebruikt om experimenteel de antivortex te observeren.

In **hoofdstuk** 5 hebben we het effect van niet-magnetische verontreinigingen op de lokale toestandsdichtheid bestudeerd en de transporteigenschappen in supergeleidende nanodraden met diameter vergelijkbaar met de Fermi golflengte λ_F (die kleiner is dan de supergeleidende coherentielengte). Dergelijke verontreinigingen hebben weinig effect op de bulk eigenschappen van conventionele supergeleiders. Aangezien de dimensionaliteit gereduceerd is, zal het effect van onzuiverheden meer significant zijn. Door de BdG the-

orie toe te passen voor het materiaal $NbSe_2$, ontdekken we verschillende regimes waarin de onzuiverheden een invloed hebben op de supergeleidende eigenschappen van de nanodraad en dit op verschillende manieren. Eerst, naargelang de nanodraad in het resonant of niet-resonant regime bevindt, zal de ordeparameter respectievelijk een langzaam of snel oscillerend gedrag vertonen weg van de onzuiverheid. Dit komt door de verschillende aard van de quasi-deeltjes die betrokken zijn bij de vorming van de Cooper paren, dat wil zeggen, klein of groot momentum. Bovendien, de onzuiverheid heeft een sterk positie-afhankelijke effect op de Josephson kritische stroom met tegengestelde gedrag in de resonante en niet-resonantie gevallen. Deze effecten kunnen worden gebruikt om de aard van het supergeleidende condensaat en de verstrooiing van de verschillende subbanden aan de onzuiverheid te onderzoeken.

In **hoofdstuk 6** hebben we het Tomasch effect onderzocht op de elektronische structuur van nanoschaal supergeleiders. Het Tomasch effect is te wijten aan de interferentie van quasi-deeltjes zoals veroorzaakt door een niet-uniforme supergeleidende ordeparameter, dat resulteert in oscillaties in de toestandsdichtheid bij energieën boven de supergeleidende kloof. Hier wordt het Tomasch effect veroorzaakt door een inhomogene ordeparameter die een gevolg is van kwantum opsluiting. We vonden dat het Tomasch effect ontaarde elektron en holde toestanden boven de supergeleidende kloof met elkaar koppelt, dat leidt tot extra paren van BCS-achtige Bogoliubov-quasideeltjes. Wanneer de energieën van de gepaarde toestanden ver van het Fermi niveau liggen, vertonen de paartoestanden pseudo-gap-achtige structuren in de DOS. Wanneer zij dicht bij het Fermi-niveau liggen, resulteren de paartoestanden in gemoduleerde golf patronen in de lokale toestandsdichtheid. Al deze effecten zijn te wijten aan de inter-subband elektron-gat koppeling.

Het Tomasch effect is sterk gerelateerd aan de geometrische symmetrie van het systeem en de symmetrie, pariteit en ruimtelijke variatie van de ordeparameter. Voor de nanoband, leidt het Tomasch effect slechts tot twee subband quasideeltjes interferentie processen. Voor een nanodraad, resulteert het ook in drie subband quasideeltjes interferentie processen die leiden tot een unieke energie bandstructuur. De studie van het Tomasch effect kan ons helpen om inzicht te krijgen hoe de inhomogene ordeparameter een invloed heeft op de quasideeltjes toestanden.

Bibliography

[1] H. Onnes, "The resistance of pure mercury at helium temperatures," Commun. Phys. Lab. Univ. Leiden. **12**, 120 (1911).

[2] D. van Delft and P. Kes, "The discovery of superconductivity," Physics Today **63**, 38 (2010).

[3] R. A. Serway, "Superconductivity," in *Modern Physics*, edited by R. A. Serway and C. J. Moses (Cengage Learning, 2004) pp. 476–527.

[4] J. File and R. G. Mills, "Observation of persistent current in a superconducting solenoid," Phys. Rev. Lett. **10**, 93 (1963).

[5] W. Meissner and R. Ochsenfeld, "Ein neuer effekt bei eintritt der supraleitfähigkeit," Naturwissenschaften **21**, 787 (1933).

[6] M. Tinkham, *Introduction to superconductivity*, 2nd ed., International series in pure and applied physics (McGraw Hill, 1996).

[7] F. London and H. London, "The electromagnetic equations of the supraconductor," Proceedings of the Royal Society of London A: Mathematical, Physical and Engineering Sciences **149**, 71 (1935).

[8] V. Ginzburg and L. Landau, Zh. Eksp. Teor. Fiz. **20**, 1064 (1950).

[9] A. A. Abrikosov, "On the magnetic properties of superconductors," Sov. Phys. JETP **5**, 1174 (1957).

[10] L. P. Gor'kov, "Microscopic derivation of the ginzburg-landau equations in the theory of superconductivity," Sov. Phys. JETP **36**, 1364 (1959).

[11] J. Bardeen, L. N. Cooper, and J. R. Schrieffer, "Theory of superconductivity," Phys. Rev. **108**, 1175 (1957).

[12] B. Josephson, "Possible new effects in superconductive tunnelling," Physics Letters **1**, 251 (1962).

[13] P. W. Anderson and A. H. Dayem, "Radio-frequency effects in superconducting thin film bridges," Phys. Rev. Lett. **13**, 195 (1964).

[14] J. Bednorz and K. Müller, "Possible high-T_c superconductivity in the Ba-La-Cu-O system," Zeitschrift fur Physik B Condensed Matter **64**, 189 (1986).

[15] M. K. Wu, J. R. Ashburn, C. J. Torng, P. H. Hor, R. L. Meng, L. Gao, Z. J. Huang, Y. Q. Wang, and C. W. Chu, "Superconductivity at 93 K in a new mixed-phase Y-Ba-Cu-O compound system at ambient pressure," Phys. Rev. Lett. **58**, 908 (1987).

[16] H. Maeda, Y. Tanaka, M. Fukutomi, and T. Asano, "A new high-T_c oxide superconductor without a rare earth element," Japanese Journal of Applied Physics **27**, L209 (1988).

[17] L. Gao, Y. Y. Xue, F. Chen, Q. Xiong, R. L. Meng, D. Ramirez, C. W. Chu, J. H. Eggert, and H. K. Mao, "Superconductivity up to 164 K in $HgBa_2Ca_{m-1}Cu_mO_{2m+2+\delta}$ (m=1, 2, and 3) under quasihydrostatic pressures," Phys. Rev. B **50**, 4260 (1994).

[18] Y. Maeno, H. Hashimoto, K. Yoshida, S. Nishizaki, T. Fujita, J. G. Bednorz, and F. Lichtenberg, "Superconductivity in a layered perovskite without copper," Nature (London) **372**, 532 (1994).

[19] T. M. Rice and M. Sigrist, "Sr_2RuO_4: an electronic analogue of ^{3}He?" Journal of Physics: Condensed Matter **7**, L643 (1995).

[20] A. P. Mackenzie and Y. Maeno, "The superconductivity of Sr_2RuO_4 and the physics of spin-triplet pairing," Rev. Mod. Phys. **75**, 657 (2003).

[21] J. Nagamatsu, N. Nakagawa, T. Muranaka, Y. Zenitani, and J. Akimitsu, "Superconductivity at 39 K in magnesium diboride," Nature (London) **410**, 63 (2001).

[22] M. E. Jones and R. E. Marsh, "The preparation and structure of magnesium boride, MgB_2," Journal of the American Chemical Society **76**, 1434 (1954).

[23] A. S. Cooper, E. Corenzwit, L. D. Longinotti, B. T. Matthias, and W. H. Zachariasen, "Superconductivity: The transition temperature peak below four electrons per atom," Proceedings of the National Academy of Sciences of the United States of America **67**, 313 (1970).

[24] L. Leyarovska and E. Leyarovski, "A search for superconductivity below 1 K in transition metal borides," Journal of the Less Common Metals **67**, 249 (1979).

[25] P. C. Canfield and G. W. Crabtree, "Magnesium diboride: Better late than never," Physics Today **56**, 34 (2003).

[26] National Research Council (U.S.), ed., *Opportunities in high magnetic field science* (National Academies Press, Washington, D.C, 2005).

[27] H. Hosono and Z.-A. Ren, "Focus on iron-based superconductors," New Journal of Physics **11**, 025003 (2009).

[28] K. Ishida, Y. Nakai, and H. Hosono, "To what extent iron-pnictide new superconductors have been clarified: A progress report," Journal of the Physical Society of Japan **78**, 062001 (2009).

[29] N. S. Lin, V. R. Misko, and F. M. Peeters, "Unconventional vortex dynamics in mesoscopic superconducting corbino disks," Phys. Rev. Lett. **102**, 197003 (2009).

[30] H. J. Zhao, V. R. Misko, F. M. Peeters, V. Oboznov, S. V. Dubonos, and I. V. Grigorieva, "Vortex states in mesoscopic superconducting squares: Formation of vortex shells," Phys. Rev. B **78**, 104517 (2008).

[31] V. A. Schweigert, F. M. Peeters, and P. S. Deo, "Vortex phase diagram for mesoscopic superconducting disks," Phys. Rev. Lett. **81**, 2783 (1998).

[32] L. F. Chibotaru, A. Ceulemans, V. Bruyndoncx, and V. V. Moshchalkov, "Symmetry-induced formation of antivortices in mesoscopic superconductors," Nature (London) **408**, 833 (2000).

[33] R. Geurts, M. V. Milošević, and F. M. Peeters, "Symmetric and asymmetric vortex-antivortex molecules in a fourfold superconducting geometry," Phys. Rev. Lett. **97**, 137002 (2006).

[34] P. D. Gennes, *Superconductivity of Metals and Alloys* (Westview Press, 1999).

[35] H. Alloul, *Introduction to the Physics of Electrons in Solids*, Graduate Texts in Physics (Springer Berlin Heidelberg, Berlin, Heidelberg, 2011).

[36] J. Q. You and F. Nori, "Atomic physics and quantum optics using superconducting circuits," Nature (London) **474**, 589 (2011).

[37] C. Visani, Z. Sefrioui, J. Tornos, C. Leon, J. Briatico, M. Bibes, A. Barthelemy, J. Santamaria, and J. E. Villegas, "Equal-spin Andreev reflection and long-range coherent transport in high-temperature superconductor/half-metallic ferromagnet junctions," Nat Phys **8**, 539 (2012).

[38] W. J. Tomasch, "Geometrical resonance in the tunneling characteristics of superconducting Pb," Phys. Rev. Lett. **15**, 672 (1965).

[39] W. J. Tomasch, "Geometrical resonance and boundary effects in tunneling from superconducting In," Phys. Rev. Lett. **16**, 16 (1966).

[40] W. L. McMillan and P. W. Anderson, "Theory of geometrical resonances in the tunneling characteristics of thick films of superconductors," Phys. Rev. Lett. **16**, 85 (1966).

[41] J. M. Rowell and W. L. McMillan, "Electron interference in a normal metal induced by superconducting contracts," Phys. Rev. Lett. **16**, 453 (1966).

[42] J. M. Rowell, "Tunneling observation of bound states in a normal metal¯superconductor sandwich," Phys. Rev. Lett. **30**, 167 (1973).

[43] T. Klapwijk, "Proximity effect from an Andreev perspective," Journal of Superconductivity **17**, 593 (2004).

[44] A. A. Abrikosov, "The magnetic properties of superconducting alloys," Journal of Physics and Chemistry of Solids **2**, 199 (1957).

[45] V. V. Schmidt, P. Müller, and A. V. Ustinov, *The Physics of Superconductors Introduction to Fundamentals and Applications* (Springer Berlin Heidelberg, Berlin, Heidelberg, 1997).

[46] T. Nishio, T. An, A. Nomura, K. Miyachi, T. Eguchi, H. Sakata, S. Lin, N. Hayashi, N. Nakai, M. Machida, and Y. Hasegawa, "Superconducting Pb island nanostructures studied by scanning tunneling microscopy and spectroscopy," Phys. Rev. Lett. **101**, 167001 (2008).

[47] L. Kramer, "Thermodynamic behavior of type-II superconductors with small κ near the lower critical field," Phys. Rev. B **3**, 3821 (1971).

[48] E. H. Brandt, "Elastic and plastic properties of the flux-line lattice in type-II superconductors," Phys. Rev. B **34**, 6514 (1986).

[49] A. Chaves, F. M. Peeters, G. A. Farias, and M. V. Milošević, "Vortex-vortex interaction in bulk superconductors: Ginzburg-Landau theory," Phys. Rev. B **83**, 054516 (2011).

[50] C. P. Bean and J. D. Livingston, "Surface barrier in type-II superconductors," Phys. Rev. Lett. **12**, 14 (1964).

[51] I. V. Grigorieva, W. Escoffier, J. Richardson, L. Y. Vinnikov, S. Dubonos, and V. Oboznov, "Direct observation of vortex shells and magic numbers in mesoscopic superconducting disks," Phys. Rev. Lett. **96**, 077005 (2006).

[52] A. Kanda, B. J. Baelus, F. M. Peeters, K. Kadowaki, and Y. Ootuka, "Experimental evidence for giant vortex states in a mesoscopic superconducting disk," Phys. Rev. Lett. **93**, 257002 (2004).

[53] T. Cren, L. Serrier-Garcia, F. Debontridder, and D. Roditchev, "Vortex fusion and giant vortex states in confined superconducting condensates," Phys. Rev. Lett. **107**, 097202 (2011).

[54] V. R. Misko, V. M. Fomin, J. T. Devreese, and V. V. Moshchalkov, "Stable vortex-antivortex molecules in mesoscopic superconducting triangles," Phys. Rev. Lett. **90**, 147003 (2003).

[55] L. F. Chibotaru, V. H. Dao, and A. Ceulemans, "Thermodynamically stable noncomposite vortices in mesoscopic two-gap superconductors," EPL (Europhysics Letters) **78**, 47001 (2007).

[56] L. F. Chibotaru, A. Ceulemans, M. Morelle, G. Teniers, C. Carballeira, and V. V. Moshchalkov, "Ginzburg–landau description of confinement and quantization effects in mesoscopic superconductors," Journal of Mathematical Physics **46**, 095108 (2005).

[57] Y. Wang, M. Chen, Z. Li, L. Wang, K. He, Q.-K. Xue, and X. Ma, "Scanning tunneling microscopy study of the superconducting properties of three-atomic-layer Pb films," Applied Physics Letters **103**, 242603 (2013).

[58] Y. S. Hor, U. Welp, Y. Ito, Z. L. Xiao, U. Patel, J. F. Mitchell, W. K. Kwok, and G. W. Crabtree, "Superconducting $NbSe_2$ nanowires and nanoribbons converted from $NbSe_3$ nanostructures," Applied Physics Letters **87**, 142506 (2005).

[59] P. Zolotavin and P. Guyot-Sionnest, "Meissner effect in colloidal Pb nanoparticles," ACS Nano **4**, 5599 (2010).

[60] N. C. Koshnick, M. E. Huber, J. A. Bert, C. W. Hicks, J. Large, H. Edwards, and K. A. Moler, "A terraced scanning super conducting quantum interference device susceptometer with submicron pickup loops," Applied Physics Letters **93**, 243101 (2008).

[61] M. Tinkham, "Penetration depth, susceptibility, and nuclear magnetic resonance in finely divided superconductors," Phys. Rev. **110**, 26 (1958).

[62] R. W. Cohen and B. Abeles, "Superconductivity in granular aluminum films," Phys. Rev. **168**, 444 (1968).

[63] S. Bose and P. Ayyub, "A review of finite size effects in quasi-zero dimensional superconductors," Reports on Progress in Physics **77**, 116503 (2014).

[64] R. Kubo, A. Kawabata, and S. Kobayashi, "Electronic properties of small particles," Annual Review of Materials Science **14**, 49 (1984).

[65] P. Anderson, "Theory of dirty superconductors," Journal of Physics and Chemistry of Solids **11**, 26 (1959).

[66] A. Romero-Bermúdez and A. M. García-García, "Shape resonances and shell effects in thin-film multiband superconductors," Phys. Rev. B **89**, 024510 (2014).

[67] M. D. Croitoru, A. A. Shanenko, and F. M. Peeters, "Dependence of superconducting properties on the size and shape of a nanoscale superconductor: From nanowire to film," Phys. Rev. B **76**, 024511 (2007).

[68] J. M. Blatt and C. J. Thompson, "Shape resonances in superconducting thin films," Phys. Rev. Lett. **10**, 332 (1963).

[69] A. Perali, A. Bianconi, A. Lanzara, and N. Saini, "The gap amplification at a shape resonance in a superlattice of quantum stripes: A mechanism for high Tc," Solid State Communications **100**, 181 (1996).

[70] A. Bianconi, A. Valletta, A. Perali, and N. Saini, "High Tc superconductivity in a superlattice of quantum stripes," Solid State Communications **102**, 369 (1997).

[71] A. Bianconi, A. Valletta, A. Perali, and N. L. Saini, "Superconductivity of a striped phase at the atomic limit," Physica C: Superconductivity **296**, 269 (1998).

[72] J. J. Hauser, "Enhancement of superconductivity in aluminum films," Phys. Rev. B **3**, 1611 (1971).

[73] J. M. Valles, R. C. Dynes, and J. P. Garno, "Superconductivity and the electronic density of states in disordered two-dimensional metals," Phys. Rev. B **40**, 6680 (1989).

[74] M. S. M. Minhaj, S. Meepagala, J. T. Chen, and L. E. Wenger, "Thickness dependence on the superconducting properties of thin nb films," Phys. Rev. B **49**, 15235 (1994).

[75] J. H. Quateman, "T_c suppression and critical fields in thin superconducting Nb films," Phys. Rev. B **34**, 1948 (1986).

[76] A. F. Hebard and A. T. Fiory, "Microstructure, dimensionality, and depression of the transition temperature in disordered superconducting films," Phys. Rev. Lett. **58**, 1131 (1987).

[77] Y. Guo, Y.-F. Zhang, X.-Y. Bao, T.-Z. Han, Z. Tang, L.-X. Zhang, W.-G. Zhu, E. G. Wang, Q. Niu, Z. Q. Qiu, J.-F. Jia, Z.-X. Zhao, and Q.-K. Xue, "Superconductivity modulated by quantum size effects," Science **306**, 1915 (2004).

[78] M. M. Özer, J. R. Thompson, and H. H. Weitering, "Hard superconductivity of a soft metal in the quantum regime," Nature Physics **2**, 173 (2006).

[79] D. Eom, S. Qin, M.-Y. Chou, and C. K. Shih, "Persistent superconductivity in ultrathin Pb films: A scanning tunneling spectroscopy study," Phys. Rev. Lett. **96**, 027005 (2006).

[80] C. Brun, I.-P. Hong, F. Patthey, I. Y. Sklyadneva, R. Heid, P. M. Echenique, K. P. Bohnen, E. V. Chulkov, and W.-D. Schneider, "Reduction of the superconducting gap of ultrathin Pb islands grown on Si(111)," Phys. Rev. Lett. **102**, 207002 (2009).

[81] S. Qin, J. Kim, Q. Niu, and C.-K. Shih, "Superconductivity at the two-dimensional limit," Science **324**, 1314 (2009).

[82] T. Zhang, P. Cheng, W.-J. Li, Y.-J. Sun, G. Wang, X.-G. Zhu, K. He, L. Wang, X. Ma, X. Chen, Y. Wang, Y. Liu, H.-Q. Lin, J.-F. Jia, and Q.-K. Xue, "Superconductivity in one-atomic-layer metal films grown on Si(111)," Nature Physics **6**, 104 (2010).

[83] Y. Chen, A. A. Shanenko, and F. M. Peeters, "Superconducting transition temperature of Pb nanofilms: Impact of thickness-dependent oscillations of the phonon-mediated electron-electron coupling," Phys. Rev. B **85**, 224517 (2012).

[84] H. M. Jaeger, D. B. Haviland, B. G. Orr, and A. M. Goldman, "Onset of superconductivity in ultrathin granular metal films," Phys. Rev. B **40**, 182 (1989).

[85] A. Romero-Bermúdez and A. M. García-García, "Size effects in superconducting thin films coupled to a substrate," Phys. Rev. B **89**, 064508 (2014).

[86] S. Bose, A. M. Garcia-Garcia, M. M. Ugeda, J. D. Urbina, C. H. Michaelis, I. Brihuega, and K. Kern, "Observation of shell effects in superconducting nanoparticles of Sn," Nature Materials **9**, 550 (2010).

[87] W.-H. Li, C. C. Yang, F. C. Tsao, S. Y. Wu, P. J. Huang, M. K. Chung, and Y. D. Yao, "Enhancement of superconductivity by the small size effect in In nanoparticles," Phys. Rev. B **72**, 214516 (2005).

[88] B. Abeles, R. W. Cohen, and G. W. Cullen, "Enhancement of superconductivity in metal films," Phys. Rev. Lett. **17**, 632 (1966).

[89] K. Ohshima, T. Kuroishi, and T. Fujita, "Superconducting transition temperature of aluminium fine particles," Journal of the Physical Society of Japan **41**, 1234 (1976).

[90] S. Reich, G. Leitus, R. Popovitz-Biro, and M. Schechter, "Magnetization of small lead particles," Phys. Rev. Lett. **91**, 147001 (2003).

[91] W.-H. Li, C. C. Yang, F. C. Tsao, and K. C. Lee, "Quantum size effects on the superconducting parameters of zero-dimensional Pb nanoparticles," Phys. Rev. B **68**, 184507 (2003).

[92] A. A. Shanenko, M. D. Croitoru, and F. M. Peeters, "Oscillations of the superconducting temperature induced by quantum well states in thin metallic films: Numerical solution of the Bogoliubov-de Gennes equations," Phys. Rev. B **75**, 014519 (2007).

[93] A. A. Shanenko, N. V. Orlova, A. Vagov, M. V. Milošević, V. M. Axt, and F. M. Peeters, "Nanofilms as quantum-engineered multiband superconductors: The Ginzburg-Landau theory," EPL (Europhysics Letters) **102**, 27003 (2013).

[94] A. A. Shanenko, M. D. Croitoru, R. G. Mints, and F. M. Peeters, "New Andreev-type states in superconducting nanowires," Phys. Rev. Lett. **99**, 067007 (2007).

[95] A. A. Shanenko, M. D. Croitoru, and F. M. Peeters, "Magnetic-field induced quantum-size cascades in superconducting nanowires," Phys. Rev. B **78**, 024505 (2008).

[96] V. N. Gladilin, J. Tempere, I. F. Silvera, and J. T. Devreese, "Critical temperature and specific heat for cooper pairing on a spherical surface," Phys. Rev. B **74**, 104512 (2006).

[97] J. Tempere, V. N. Gladilin, I. F. Silvera, and J. T. Devreese, "Cooper pairing and superconductivity on a spherical surface: Applying the richardson model to a multielectron bubble in liquid helium," Phys. Rev. B **72**, 094506 (2005).

[98] A. M. García-García, J. D. Urbina, E. A. Yuzbashyan, K. Richter, and B. L. Altshuler, "Bardeen-Cooper-Schrieffer theory of finite-size superconducting metallic grains," Phys. Rev. Lett. **100**, 187001 (2008).

[99] H. Olofsson, S. Åberg, and P. Leboeuf, "Semiclassical theory of Bardeen-Cooper-Schrieffer pairing-gap fluctuations," Phys. Rev. Lett. **100**, 037005 (2008).

[100] J. M. Dickey and A. Paskin, "Phonon spectrum changes in small particles and their implications for superconductivity," Phys. Rev. Lett. **21**, 1441 (1968).

[101] C. R. Leavens and E. W. Fenton, "Superconductivity of small particles," Phys. Rev. B **24**, 5086 (1981).

[102] D. B. Haviland, Y. Liu, and A. M. Goldman, "Onset of superconductivity in the two-dimensional limit," Phys. Rev. Lett. **62**, 2180 (1989).

[103] A. D. Maestro, *The superconductor-metal quantum phase transition in ultra-narrow wires*, Ph.D. thesis, Harvard University, Cambridge, Massachusetts (2008).

[104] N. Giordano, "Evidence for macroscopic quantum tunneling in one-dimensional superconductors," Phys. Rev. Lett. **61**, 2137 (1988).

[105] M. Singh, Y. Sun, and J. Wang, "Superconductivity in nanoscale systems," in *Superconductors - Properties, Technology, and Applications*, edited by Y. Grigorashvili (InTech, 2012).

[106] I. Brihuega, A. M. García-García, P. Ribeiro, M. M. Ugeda, C. H. Michaelis, S. Bose, and K. Kern, "Experimental observation of thermal fluctuations in single superconducting Pb nanoparticles through tunneling measurements," Phys. Rev. B **84**, 104525 (2011).

[107] Ø. Fischer, M. Kugler, I. Maggio-Aprile, C. Berthod, and C. Renner, "Scanning tunneling spectroscopy of high-temperature superconductors," Rev. Mod. Phys. **79**, 353 (2007).

[108] C. J. Chen, *Introduction to scanning tunneling microscopy*, Oxford series in optical and imaging sciences No. 4 (Oxford University Press, 1993).

[109] J. Tersoff and D. R. Hamann, "Theory and application for the scanning tunneling microscope," Phys. Rev. Lett. **50**, 1998 (1983).

[110] H. Suderow, I. Guillamón, J. G. Rodrigo, and S. Vieira, "Imaging superconducting vortex cores and lattices with a scanning tunneling microscope," Superconductor Science and Technology **27**, 063001 (2014).

[111] C. Brun, T. Cren, V. Cherkez, F. Debontridder, S. Pons, D. Fokin, M. C. Tringides, S. Bozhko, L. B. Ioffe, B. L. Altshuler, and D. Roditchev, "Remarkable effects of disorder on superconductivity of single atomic layers of lead on silicon," Nature Physics **10**, 444 (2014).

[112] A. Yazdani, B. A. Jones, C. P. Lutz, M. F. Crommie, and D. M. Eigler, "Probing the local effects of magnetic impurities on superconductivity," Science **275**, 1767 (1997).

[113] Y. Chen, M. D. Croitoru, A. A. Shanenko, and F. M. Peeters, "Superconducting nanowires: quantum confinement and spatially dependent Hartree–Fock potential," Journal of Physics: Condensed Matter **21**, 435701 (2009).

[114] K. Tanaka, I. Robel, and B. Jankó, "Electronic structure of multiquantum giant vortex states in mesoscopic superconducting disks," Proceedings of the National Academy of Sciences **99**, 5233 (2002).

[115] L. Kramer and W. Pesch, "Core structure and low-energy spectrum of isolated vortex lines in clean superconductors at $T \ll T_c$," Z. Physik **269**, 59 (1974).

[116] N. Hayashi, T. Isoshima, M. Ichioka, and K. Machida, "Low-lying quasiparticle excitations around a vortex core in quantum limit," Phys. Rev. Lett. **80**, 2921 (1998).

[117] G. E. Volovik, "Vortex vortex core anomaly from the gapless fermions in the core," JETP Letters **58**, 455 (1993).

[118] M. A. Silaev and V. A. Silaeva, "Self-consistent electronic structure of multiquantum vortices in superconductors at T $\ll$ T_c," Journal of Physics: Condensed Matter **25**, 225702 (2013).

[119] J. Bardeen, R. Kümmel, A. E. Jacobs, and L. Tewordt, "Structure of vortex lines in pure superconductors," Phys. Rev. **187**, 556 (1969).

[120] F. Gygi and M. Schlüter, "Self-consistent electronic structure of a vortex line in a type-II superconductor," Phys. Rev. B **43**, 7609 (1991).

[121] S. Pan, *Effects of a single magnetic impurity on superconductivity*, Master's thesis, University of Saskatchewan (2008).

[122] S. M. M. Virtanen and M. M. Salomaa, "Multiquantum vortices in superconductors: Electronic and scanning tunneling microscopy spectra," Phys. Rev. B **60**, 14581 (1999).

[123] A. K. Geim, I. V. Grigorieva, S. V. Dubonos, J. G. S. Lok, J. C. Maan, A. E. Filippov, and F. M. Peeters, "Phase transitions in individual sub-micrometre superconductors," Nature (London) **390**, 259 (1997).

[124] J. J. Palacios, "Metastability and paramagnetism in superconducting mesoscopic disks," Phys. Rev. Lett. **84**, 1796 (2000).

[125] B. J. Baelus, F. M. Peeters, and V. A. Schweigert, "Saddle-point states and energy barriers for vortex entrance and exit in superconducting disks and rings," Phys. Rev. B **63**, 144517 (2001).

[126] M. V. Milošević, S. V. Yampolskii, and F. M. Peeters, "Vortex structure of thin mesoscopic disks in the presence of an inhomogeneous magnetic field," Phys. Rev. B **66**, 024515 (2002).

[127] C.-Y. Liu, G. R. Berdiyorov, and M. V. Milošević, "Vortex states in layered mesoscopic superconductors," Phys. Rev. B **83**, 104524 (2011).

[128] L. F. Chibotaru, A. Ceulemans, V. Bruyndoncx, and V. V. Moshchalkov, "Vortex entry and nucleation of antivortices in a mesoscopic superconducting triangle," Phys. Rev. Lett. **86**, 1323 (2001).

[129] G. Teniers, L. F. Chibotaru, A. Ceulemans, and V. V. Moshchalkov, "Nucleation of superconductivity in a mesoscopic rectangle," EPL (Europhysics Letters) **63**, 296 (2003).

[130] R. Geurts, M. V. Milošević, and F. M. Peeters, "Stabilization of vortex-antivortex configurations in mesoscopic superconductors by engineered pinning," Phys. Rev. B **75**, 184511 (2007).

[131] G. Blatter, M. V. Feigel'man, V. B. Geshkenbein, A. I. Larkin, and V. M. Vinokur, "Vortices in high-temperature superconductors," Rev. Mod. Phys. **66**, 1125 (1994).

[132] D. Valdez-Balderas and D. Stroud, "Model for vortex pinning in a two-dimensional inhomogeneous d-wave superconductor," Phys. Rev. B **76**, 144506 (2007).

[133] H. B. Heersche, P. Jarillo-Herrero, J. B. Oostinga, L. M. K. Vandersypen, and A. F. Morpurgo, "Bipolar supercurrent in graphene," Nature (London) **446**, 56 (2007).

[134] H. Tomori, A. Kanda, H. Goto, S. Takana, Y. Ootuka, and K. Tsukagoshi, "Fabrication of ultrashort graphene Josephson junctions," Physica C: Superconductivity **470**, 1492 (2010).

[135] A. M. Black-Schaffer and S. Doniach, "Self-consistent solution for proximity effect and Josephson current in ballistic graphene SNS Josephson junctions," Phys. Rev. B **78**, 024504 (2008).

[136] L. Covaci and F. M. Peeters, "Superconducting proximity effect in graphene under inhomogeneous strain," Phys. Rev. B **84**, 241401 (2011).

[137] T. Cren, D. Fokin, F. Debontridder, V. Dubost, and D. Roditchev, "Ultimate vortex confinement studied by scanning tunneling spectroscopy," Phys. Rev. Lett. **102**, 127005 (2009).

[138] A. S. Mel'nikov, D. A. Ryzhov, and M. A. Silaev, "Electronic structure and heat transport of multivortex configurations in mesoscopic superconductors," Phys. Rev. B **78**, 064513 (2008).

[139] C. Berthod, "Vorticity and vortex-core states in type-II superconductors," Phys. Rev. B **71**, 134513 (2005).

[140] B. Xu, M. V. Milošević, S.-H. Lin, F. M. Peeters, and B. Jankó, "Formation of multiple-flux-quantum vortices in mesoscopic superconductors from simulations of calorimetric, magnetic, and transport properties," Phys. Rev. Lett. **107**, 057002 (2011).

[141] A. S. Mel'nikov, D. A. Ryzhov, and M. A. Silaev, "Local density of states around single vortices and vortex pairs: Effect of boundaries and hybridization of vortex core states," Phys. Rev. B **79**, 134521 (2009).

[142] I. Kosztin, Š. Kos, M. Stone, and A. J. Leggett, "Free energy of an inhomogeneous superconductor: A wave-function approach," Phys. Rev. B **58**, 9365 (1998).

[143] A. Spuntarelli, P. Pieri, and G. Strinati, "Solution of the Bogoliubov–de Gennes equations at zero temperature throughout the BCS–BEC crossover: Josephson and related effects," Physics Reports **488**, 111 (2010).

[144] B. J. Baelus and F. M. Peeters, "Dependence of the vortex configuration on the geometry of mesoscopic flat samples," Phys. Rev. B **65**, 104515 (2002).

[145] G. R. Berdiyorov, B. J. Baelus, M. V. Milošević, and F. M. Peeters, "Stability and transition between vortex configurations in square mesoscopic samples with antidots," Phys. Rev. B **68**, 174521 (2003).

[146] R. Geurts, M. V. Milošević, and F. M. Peeters, "Second generation of vortex-antivortex states in mesoscopic superconductors: Stabilization by artificial pinning," Phys. Rev. B **79**, 174508 (2009).

[147] S. Aubin, S. Myrskog, M. H. T. Extavour, L. J. LeBlanc, D. McKay, A. Stummer, and J. H. Thywissen, "Rapid sympathetic cooling to fermi degeneracy on a chip," Nat Phys **2**, 384 (2006).

[148] B. Xu, M. V. Milošević, and F. M. Peeters, "Magnetic properties of vortex states in spherical superconductors," Phys. Rev. B **77**, 144509 (2008).

[149] M. M. Doria, A. R. de C. Romaguera, and F. M. Peeters, "Effect of the boundary condition on the vortex patterns in mesoscopic three-dimensional superconductors: Disk and sphere," Phys. Rev. B **75**, 064505 (2007).

[150] M. A. Engbarth, S. J. Bending, and M. V. Milošević, "Geometry-driven vortex states in type-i superconducting Pb nanowires," Phys. Rev. B **83**, 224504 (2011).

[151] R. Geurts, M. V. Milošević, and F. M. Peeters, "Vortex matter in mesoscopic two-gap superconducting disks: Influence of Josephson and magnetic coupling," Phys. Rev. B **81**, 214514 (2010).

[152] M. V. Milošević, G. R. Berdiyorov, and F. M. Peeters, "Fluxonic cellular automata," Applied Physics Letters **91**, 212501 (2007).

[153] O. Bourgeois, S. E. Skipetrov, F. Ong, and J. Chaussy, "Attojoule calorimetry of mesoscopic superconducting loops," Phys. Rev. Lett. **94**, 057007 (2005).

[154] J. Bonča and V. V. Kabanov, "Phase transitions in the mesoscopic superconducting square," Phys. Rev. B **65**, 012509 (2001).

[155] T. Mertelj and V. V. Kabanov, "Vortex-antivortex configurations and its stability in a mesoscopic superconducting square," Phys. Rev. B **67**, 134527 (2003).

[156] A. S. Mel'nikov, I. M. Nefedov, D. A. Ryzhov, I. A. Shereshevskii, V. M. Vinokur, and P. P. Vysheslavtsev, "Vortex states and magnetization curve of square mesoscopic superconductors," Phys. Rev. B **65**, 140503 (2002).

[157] D. S. Golubović, M. V. Milošević, F. M. Peeters, and V. V. Moshchalkov, "Magnetically induced splitting of a giant vortex state in a mesoscopic superconducting disk," Phys. Rev. B **71**, 180502 (2005).

[158] M. R. Connolly, M. V. Milošević, S. J. Bending, J. R. Clem, and T. Tamegai, "Continuum vs . discrete flux behaviour in large mesoscopic $bi_2sr_2cacu_2o_{8+\delta}$ disks," EPL (Europhysics Letters) **85**, 17008 (2009).

[159] F. R. Ong, O. Bourgeois, S. E. Skipetrov, and J. Chaussy, "Thermal signatures of the Little-Parks effect in the heat capacity of mesoscopic superconducting rings," Phys. Rev. B **74**, 140503 (2006).

[160] P. J. Pereira, V. V. Moshchalkov, and L. F. Chibotaru, "Method for the solution of the nucleation problem in arbitrary mesoscopic superconductors: Theory and application," Phys. Rev. E **86**, 056709 (2012).

[161] A. S. Mel'nikov and V. M. Vinokur, "Mesoscopic superconductor as a ballistic quantum switch," Nature (London) **415**, 60 (2002).

[162] S.-Z. Lin, T. Nishio, L. N. Bulaevskii, M. J. Graf, and Y. Hasegawa, "Thermally assisted penetration and exclusion of single vortex in mesoscopic superconductors," Phys. Rev. B **85**, 134534 (2012).

[163] J. Tóbik, V. Cambel, and G. Karapetrov, "Dynamics of vortex nucleation in nanomagnets with broken symmetry," Phys. Rev. B **86**, 134433 (2012).

[164] P. J. Pereira, L. F. Chibotaru, and V. V. Moshchalkov, "Vortex matter in mesoscopic two-gap superconductor square," Phys. Rev. B **84**, 144504 (2011).

[165] H. T. Huy, M. Kato, and T. Ishida, "Vortex states in de facto mesoscopic $Mo_{80}Ge_{20}$ pentagon plates," Superconductor Science and Technology **26**, 065001 (2013).

[166] X.-H. Hu, A.-C. Ji, X.-G. Qiu, and W.-M. Liu, "Effects of geometrical symmetry on the vortex in mesoscopic superconductors," The European Physical Journal B **79**, 473 (2011).

[167] M. D. Croitoru, A. Vagov, A. A. Shanenko, and V. M. Axt, "The cooper problem in nanoscale: enhancement of the coupling due to confinement," Superconductor Science and Technology **25**, 124001 (2012).

[168] M. Machida and T. Koyama, "Friedel oscillation in charge profile and position dependent screening around a superconducting vortex core," Phys. Rev. Lett. **90**, 077003 (2003).

[169] Y. Chen, M. M. Doria, and F. M. Peeters, "Vortices in a mesoscopic cone: A superconducting tip in the presence of an applied field," Phys. Rev. B **77**, 054511 (2008).

[170] B. Xu, M. V. Milošević, and F. M. Peeters, "Vortex matter in oblate mesoscopic superconductors with a hole: broken symmetry vortex states and multi-vortex entry," New Journal of Physics **11**, 013020 (2009).

[171] B. Xu, M. V. Milošević, and F. M. Peeters, "Second-order multiple-quanta flux entry into a perforated spherical mesoscopic superconductor," Phys. Rev. B **82**, 214501 (2010).

[172] G. R. Berdiyorov, M. V. Milošević, and F. M. Peeters, "Vortex configurations and critical parameters in superconducting thin films containing antidot arrays: Nonlinear Ginzburg-Landau theory," Phys. Rev. B **74**, 174512 (2006).

[173] G. R. Berdiyorov, M. V. Milošević, and F. M. Peeters, "Composite vortex ordering in superconducting films with arrays of blind holes," New Journal of Physics **11**, 013025 (2009).

[174] N. B. Kopnin, I. M. Khaymovich, and A. S. Mel'nikov, "Predicted multiple cores of a magnetic vortex threading a two-dimensional metal proximity coupled to a superconductor," Phys. Rev. Lett. **110**, 027003 (2013).

[175] C. Caroli, P. G. De Gennes, and J. Matricon, "Bound Fermion states on a vortex line in a type II superconductor," Physics Letters **9**, 307 (1964).

[176] A. Mel'nikov and M. Silaev, "Intervortex quasiparticle tunneling and the electronic structure of multivortex configurations in type-II superconductors," JETP Letters **83**, 578 (2006).

[177] A. S. Mel'nikov and V. M. Vinokur, "Quasiparticle excitations and ballistic transport in the mixed state of mesoscopic superconductors," Phys. Rev. B **65**, 224514 (2002).

[178] H. Suematsu, T. Ishida, T. Koyama, M. Machida, and M. Kato, "Vortex molecule in a nanoscopic square superconducting plate," Journal of the Physical Society of Japan **79**, 124704 (2010).

[179] L.-F. Zhang, L. Covaci, M. V. Milošević, G. R. Berdiyorov, and F. M. Peeters, "Unconventional vortex states in nanoscale superconductors

due to shape-induced resonances in the inhomogeneous cooper-pair condensate," Phys. Rev. Lett. **109**, 107001 (2012).

[180] A. V. Balatsky, I. Vekhter, and J.-X. Zhu, "Impurity-induced states in conventional and unconventional superconductors," Rev. Mod. Phys. **78**, 373 (2006).

[181] B. Liu and I. Eremin, "Impurity resonance states in noncentrosymmetric superconductor $CePt_3Si$: A probe for cooper-pairing symmetry," Phys. Rev. B **78**, 014518 (2008).

[182] H. Hu, L. Jiang, H. Pu, Y. Chen, and X.-J. Liu, "Universal impurity-induced bound state in topological superfluids," Phys. Rev. Lett. **110**, 020401 (2013).

[183] M. P. A. Fisher, "Quantum phase transitions in disordered two-dimensional superconductors," Phys. Rev. Lett. **65**, 923 (1990).

[184] A. Ghosal, M. Randeria, and N. Trivedi, "Role of spatial amplitude fluctuations in highly disordered s-wave superconductors," Phys. Rev. Lett. **81**, 3940 (1998).

[185] Y. Dubi, Y. Meir, and Y. Avishai, "Nature of the superconductor–insulator transition in disordered superconductors," Nature (London) **449**, 876 (2007).

[186] K. Bouadim, Y. L. Loh, M. Randeria, and N. Trivedi, "Single- and two-particle energy gaps across the disorder-driven superconductor-insulator transition," Nature Physics **7**, 884 (2011).

[187] M. Mondal, A. Kamlapure, M. Chand, G. Saraswat, S. Kumar, J. Jesudasan, L. Benfatto, V. Tripathi, and P. Raychaudhuri, "Phase fluctuations in a strongly disordered s-wave NbN superconductor close to the metal-insulator transition," Phys. Rev. Lett. **106**, 047001 (2011).

[188] B. Sacépé, T. Dubouchet, C. Chapelier, M. Sanquer, M. Ovadia, D. Shahar, M. Feigel'man, and L. Ioffe, "Localization of preformed cooper pairs in disordered superconductors," Nature Physics **7**, 239 (2011).

[189] C. N. Lau, N. Markovic, M. Bockrath, A. Bezryadin, and M. Tinkham, "Quantum phase slips in superconducting nanowires," Phys. Rev. Lett. **87**, 217003 (2001).

[190] S. Michotte, S. Mátéfi-Tempfli, L. Piraux, D. Y. Vodolazov, and F. M. Peeters, "Condition for the occurrence of phase slip centers in superconducting nanowires under applied current or voltage," Phys. Rev. B **69**, 094512 (2004).

[191] P. Li, P. M. Wu, Y. Bomze, I. V. Borzenets, G. Finkelstein, and A. M. Chang, "Switching currents limited by single phase slips in one-dimensional superconducting Al nanowires," Phys. Rev. Lett. **107**, 137004 (2011).

[192] O. V. Astafiev, L. B. Ioffe, S. Kafanov, Y. A. Pashkin, K. Y. Arutyunov, D. Shahar, O. Cohen, and J. S. Tsai, "Coherent quantum phase slip," Nature (London) **484**, 355 (2012).

[193] M. Vanević and Y. V. Nazarov, "Quantum phase slips in superconducting wires with weak inhomogeneities," Phys. Rev. Lett. **108**, 187002 (2012).

[194] A. Murphy, P. Weinberg, T. Aref, U. C. Coskun, V. Vakaryuk, A. Levchenko, and A. Bezryadin, "Universal features of counting statistics of thermal and quantum phase slips in nanosize superconducting circuits," Phys. Rev. Lett. **110**, 247001 (2013).

[195] A. G. Semenov and A. D. Zaikin, "Persistent currents in quantum phase slip rings," Phys. Rev. B **88**, 054505 (2013).

[196] J. E. Mooij and Y. V. Nazarov, "Superconducting nanowires as quantum phase-slip junctions," Nature Physics **2**, 169 (2006).

[197] C. M. Natarajan, M. G. Tanner, and R. H. Hadfield, "Superconducting nanowire single-photon detectors: physics and applications," Superconductor Science and Technology **25**, 063001 (2012).

[198] G. N. Gol'tsman, O. Okunev, G. Chulkova, A. Lipatov, A. Semenov, K. Smirnov, B. Voronov, A. Dzardanov, C. Williams, and R. Sobolewski, "Picosecond superconducting single-photon optical detector," Applied Physics Letters **79** (2001).

[199] X.-L. Qi and S.-C. Zhang, "Topological insulators and superconductors," Rev. Mod. Phys. **83**, 1057 (2011).

[200] J. G. Rodrigo, V. Crespo, H. Suderow, S. Vieira, and F. Guinea, "Topological superconducting state of lead nanowires in an external magnetic field," Phys. Rev. Lett. **109**, 237003 (2012).

[201] A. Das, Y. Ronen, Y. Most, Y. Oreg, M. Heiblum, and H. Shtrikman, "Zero-bias peaks and splitting in an Al-InAs nanowire topological superconductor as a signature of majorana fermions," Nature Physics **8**, 887 (2012).

[202] Y. Chen, A. A. Shanenko, and F. M. Peeters, "Hollow nanocylinder: Multisubband superconductivity induced by quantum confinement," Phys. Rev. B **81**, 134523 (2010).

[203] L.-F. Zhang, L. Covaci, M. V. Milošević, G. R. Berdiyorov, and F. M. Peeters, "Vortex states in nanoscale superconducting squares: The influence of quantum confinement," Phys. Rev. B **88**, 144501 (2013).

[204] L. Serrier-Garcia, J. C. Cuevas, T. Cren, C. Brun, V. Cherkez, F. Debontridder, D. Fokin, F. S. Bergeret, and D. Roditchev, "Scanning tunneling spectroscopy study of the proximity effect in a disordered two-dimensional metal," Phys. Rev. Lett. **110**, 157003 (2013).

[205] K. Arutyunov, D. Golubev, and A. Zaikin, "Superconductivity in one dimension," Physics Reports **464**, 1 (2008).

[206] A. D. Zaikin, D. S. Golubev, A. van Otterlo, and G. T. Zimányi, "Quantum phase slips and transport in ultrathin superconducting wires," Phys. Rev. Lett. **78**, 1552 (1997).

[207] S. Khlebnikov and L. P. Pryadko, "Quantum phase slips in the presence of finite-range disorder," Phys. Rev. Lett. **95**, 107007 (2005).

[208] P. Sekar, E. C. Greyson, J. E. Barton, and T. W. Odom, "Synthesis of nanoscale $NbSe_2$ materials from molecular precursors," Journal of the American Chemical Society **127**, 2054 (2005).

[209] L. Covaci and F. Marsiglio, "Proximity effect and Josephson current in clean strong/weak/strong superconducting trilayers," Phys. Rev. B **73**, 014503 (2006).

[210] K. von Klitzing, "The quantized Hall effect," Rev. Mod. Phys. **58**, 519 (1986).

[211] H. F. Hess, R. B. Robinson, and J. V. Waszczak, "Vortex-core structure observed with a scanning tunneling microscope," Phys. Rev. Lett. **64**, 2711 (1990).

[212] A. A. Shanenko, M. D. Croitoru, A. V. Vagov, V. M. Axt, A. Perali, and F. M. Peeters, "Atypical BCS-BEC crossover induced by quantum-size effects," Phys. Rev. A **86**, 033612 (2012).

[213] Y. Mizohata, M. Ichioka, and K. Machida, "Multiple-gap structure in electric-field-induced surface superconductivity," Phys. Rev. B **87**, 014505 (2013).

[214] L.-F. Zhang, L. Covaci, and F. M. Peeters, "Position-dependent effect of non-magnetic impurities on superconducting properties of nanowires," EPL (Europhysics Letters) **109**, 17010 (2015).

[215] T. Wolfram, "Tomasch oscillations in the density of states of superconducting films," Phys. Rev. **170**, 481 (1968).

[216] O. Nesher and G. Koren, "Observation of tomasch oscillations and tunneling-like behavior in oxygen-deficient edge junctions," Applied Physics Letters **74**, 3392 (1999).

[217] B. P. Stojković and O. T. Valls, "Density of states in layered short-coherence-length superconducting structures," Phys. Rev. B **50**, 3374 (1994).

[218] B. P. Stojković and O. T. Valls, "Size effects and characteristic lengths in superconducting films and interfaces," Phys. Rev. B **49**, 3413 (1994).

[219] J. E. Hoffman, K. McElroy, D.-H. Lee, K. M. Lang, H. Eisaki, S. Uchida, and J. C. Davis, "Imaging quasiparticle interference in $Bi_2Sr_2CaCu_2O_{8+\delta}$," Science **297**, 1148 (2002).

[220] T. Hanaguri, Y. Kohsaka, J. C. Davis, C. Lupien, I. Yamada, M. Azuma, M. Takano, K. Ohishi, M. Ono, and H. Takagi, "Quasiparticle interference and superconducting gap in $Ca_{2-x}Na_xCuO_2Cl_2$," Nature Physics **3**, 865 (2007).

[221] T. Hänke, S. Sykora, R. Schlegel, D. Baumann, L. Harnagea, S. Wurmehl, M. Daghofer, B. Büchner, J. van den Brink, and C. Hess, "Probing the unconventional superconducting state of lifeas by quasiparticle interference," Phys. Rev. Lett. **108**, 127001 (2012).

[222] J.-X. Zhu, K. McElroy, J. Lee, T. P. Devereaux, Q. Si, J. C. Davis, and A. V. Balatsky, "Effects of pairing potential scattering on fourier-transformed inelastic tunneling spectra of high-T_c cuprate superconductors with bosonic modes," Phys. Rev. Lett. **97**, 177001 (2006).

[223] N. C. Koshnick, H. Bluhm, M. E. Huber, and K. A. Moler, "Fluctuation superconductivity in mesoscopic aluminum rings," Science **318**, 1440 (2007).

[224] K. Y. Arutyunov, T. T. Hongisto, J. S. Lehtinen, L. I. Leino, and A. L. Vasiliev, "Quantum phase slip phenomenon in ultra-narrow superconducting nanorings," Scientific Reports **2**, 293 (2012).

[225] E. Babaev, "Vortices with fractional flux in two-gap superconductors and in extended Faddeev model," Phys. Rev. Lett. **89**, 067001 (2002).

[226] N. Read and D. Green, "Paired states of fermions in two dimensions with breaking of parity and time-reversal symmetries and the fractional quantum Hall effect," Phys. Rev. B **61**, 10267 (2000).

[227] W. J. Gallagher, "Compound geometrical resonances in superconducting proximity-effect sandwiches," Phys. Rev. B **22**, 1233 (1980).

Lingfeng Zhang

✉ *lingfeng.zhang@uantwerpen.be*
Born in Shanghai, China
on Nov 7, 1984

Curriculum Vitae

Education

2011–2015 **PhD**, *University of Antwerp*, Antwerpen, Belgium.

- Thesis Title: Effects of quantum confinement in nanoscale superconductors: from electronic density of states to vortex matter
- Supervisors: Dr. Lucian Covaci, Prof. F. M. Peeters
- Research area: Condensed matter theory

2007–2010 **M.Sc.**, *Shanghai University*, Shanghai, China.

- Thesis Title: Phase transition of vortex states in three-dimensional mesoscopic superconducting rings
- Supervisor: Prof. Shi-Ping Zhou
- Major: Condensed matter physics

2003–2007 **B.Sc.(Eng)**, *Shanghai University*, Shanghai, China.

- Thesis Title: Non-equilibrium transport properties of GaAs/AlGaAs heterostructure
- Supervisor: Prof. Shi-Ping Zhou
- Major: Applied physics

Publications

- **L.-F. Zhang**, L. Covaci and F. M. Peeters, *Tomasch effect in nanoscale superconductors*, Phys. Rev. B **91**, 024508 (2015).
- **L.-F. Zhang**, L. Covaci and F. M. Peeters, *Position-dependent effect of non-magnetic impurities on superconducting properties of nanowires*, Europhysics Letters **109**, 17010 (2015).
- **L.-F. Zhang**, L. Covaci, M. V. Milošević, G .R. Berdiyorov,and F. M. Peeters, *Vortex states in nanoscale superconducting squares: The influence of quantum confinement*, Phys. Rev. B **88**, 144501 (2013).

- **L.-F. Zhang**, L. Covaci, M. V. Milošević, G .R. Berdiyorov,and F. M. Peeters, *Unconventional Vortex States in Nanoscale Superconductors Due to Shape-Induced Resonances in the Inhomogeneous Cooper-pair Condensate*, Phys. Rev. Lett. **109**, 107001 (2012).

Awards

- Chinese Government Award for Outstanding Self-Financed Students Abroad (2014)

Conferences

- **COMA-RUGA 2014** (10th International Workshop on Magnetism and Superconductivity at the Nanoscale), Barcelona, Spain, Jun 2014, Poster: *Position-dependent effect of non-magnetic impurities on superconducting properties of nanowires*.
- **VORTEX VIII** (8th International Conference in School Format on Vortex Matter in Nanostructured Superconductors), Rhodes, Greece, Sep 2013, Poster: *Vortex states in nanoscale superconducting squares: The influence of quantum confinement*.
- **BPS 2013** (Belgian Physical Society General Scientific Meeting), Louvain-la-Neuve, May 2013, Poster: *Unconventional vortex states in nanoscale superconductors due to shape-resonated inhomogeneity of the Cooper-pair condensate*.
- **CCQS 2012** (Workshop on Correlations and Coherence in Quantum Systems), Evora, Potugal, Oct 2012, Poster: *Unconventional vortex states in nanoscale superconductors due to shape-resonated inhomogeneity of the Cooper-pair condensate*.

Skills

Programming: MATLAB, C/C++

Language

Chinese (native), English (fluent), Japanese (basic)